

A DYNAMICAL SYSTEMS PERSPECTIVE FOR
PRELIMINARY LOW-THRUST TRAJECTORY DESIGN
IN MULTI-BODY REGIMES

A Dissertation

Submitted to the Faculty

of

Purdue University

by

Andrew D. Cox

In Partial Fulfillment of the

Requirements for the Degree

of

Doctor of Philosophy

May 2020

Purdue University

West Lafayette, Indiana

THE PURDUE UNIVERSITY GRADUATE SCHOOL
STATEMENT OF DISSERTATION APPROVAL

Dr. Kathleen Howell, Chair

School of Aeronautics and Astronautics

Dr. Martin Corless

School of Aeronautics and Astronautics

Dr. William Crossley

School of Aeronautics and Astronautics

Dr. Carolin Frueh

School of Aeronautics and Astronautics

Approved by:

Dr. Gregory Blaisdell

Associate Head of Graduate Program of Aeronautics and Astronautics

ACKNOWLEDGMENTS

This project has benefited from the support of many people and organizations and I am very grateful for each of them. First, I would like to thank my family and friends. Graduate school can be long and tedious, but your encouragement, support, and friendship have ensured that it is quite the opposite: succinct and interesting! Second, I am extremely grateful to Professor Howell; I could not have completed this project without your guidance and encouragement. Next, I cannot over state my gratitude for my fellow researchers, both at Purdue and throughout the astrodynamics community. Your insightful comments and interesting questions have contributed to this project more than you know. I would also like to acknowledge my committee members: Professors Martin Corless, William Crossley, and Carolin Frueh. Thank you for reviewing this dissertation and for providing valuable feedback.

This research and my time in graduate school have greatly benefited from the support of the NASA Space Technology Research Fellowship, grant number NNX16AM40H. It has been my honor to support NASA's objective of exploring outer space. I have also been incredibly lucky to work with Mr. Dave Folta and Dr. Dan Grebow. Thank you both, as well as your respective branches at NASA Goddard and the Jet Propulsion Laboratory, for hosting me and for collaborating on this project.

Finally, it has been my pleasure to lead the development of the new Adaptive Trajectory Design software architecture. I would like to thank Rolfe Power, David Canales Garcia, Kenza Boudad, Brian McCarthy, Stephen Scheuerle, Juan Ojeda Romero, and Nick LaFarge for your contributions to the software, whether by discussing potential architectures, writing code, testing the code, or creating documentation. This has truly been a group effort! Our efforts to improve the software have greatly benefited from the work completed by Amanda Haapala, Tom Pavlak, Davide Guzzetti, and Natasha Bosanac.

TABLE OF CONTENTS

	Page
LIST OF TABLES	vii
LIST OF FIGURES	viii
SYMBOLS	xiii
ABBREVIATIONS	xviii
ABSTRACT	xix
1 INTRODUCTION	1
1.1 Motivation and Previous Contributions	1
1.2 Research Objectives and Document Overview	4
2 DYNAMICAL MODELS	8
2.1 Circular Restricted 3-Body Problem	8
2.1.1 Newtonian Derivation	10
2.1.2 Hamiltonian Derivation	16
2.2 CR3BP Incorporating Low Thrust	22
2.2.1 Newtonian Derivation	23
2.2.2 Perturbing Accelerations Survey	27
2.2.3 The Perturbed Natural Hamiltonian	30
2.2.4 Pseudo-Separable Control Parameterization	32
2.2.5 A Low-Thrust Hamiltonian System	39
2.2.6 Conservative Model Validation	44
2.2.7 Symmetry	54
2.2.8 Energy Evolution on a Plane	55
3 DYNAMICAL STRUCTURES	61
3.1 Forbidden Regions	62
3.2 Equilibrium Solutions	66
3.2.1 Collinear Solutions	71
3.2.2 Highly Out-of-Plane Solutions	74
3.2.3 Analytical Solutions	76
3.2.4 General Locations	84
3.2.5 ZAS Merge Locations	91
3.2.6 Stability Properties	95
3.2.7 Distinct Solutions	102
3.3 Equilibrium Point Manifolds	115

	Page
3.3.1	Hyperbolic Manifold 115
3.3.2	Center Manifold: Periodic Orbits 126
3.4	Periodic Orbit Manifolds 137
3.4.1	Hyperbolic Manifold 137
3.4.2	Center Manifold: Families 144
4	APPLICATIONS 161
4.1	Gateway Manipulation Using Energy Planes 161
4.2	Gateway Manipulation Using Control Curves 165
4.2.1	Control Points and Control Curves 167
4.2.2	Low-Thrust Control for Partial Capture 169
4.2.3	Control Curves Linking Two Control Points 171
4.2.4	Feasible Regions 173
4.2.5	Low-Thrust Control for Full Capture 176
4.3	P_2 to L_5 Transfer Leveraging Equilibria Manifolds 179
4.3.1	Preliminary Design Generation 179
4.3.2	Poincaré Mapping at Energy Plane Intersections 182
4.3.3	Transfer Construction and Corrections 187
4.4	Low-Thrust Transfer from GTO to P_2 191
4.4.1	\mathbb{E}_1 and \mathbb{E}_2 Planar LTPO Stability Properties 191
4.4.2	Transit Through E_1 193
4.4.3	Capture: Avoiding Transit Through E_2 198
4.5	P_2 Region Transit Through Intersecting LTPO Manifolds 199
4.5.1	A Strategy for Transit Detection 200
4.5.2	Global Transit Search 204
4.5.3	Capture Within Non-Intersecting Manifolds 209
4.6	Strategies for High-Energy Capture 210
4.6.1	Apsis Maps 211
4.6.2	Low-Thrust Apsis Maps 214
4.6.3	Hovering with Low-Thrust 218
4.6.4	Lunar IceCube Reference Trajectory 220
4.6.5	Capture Initiated Near the Moon 220
4.6.6	Capture Initiated Far from the Moon 224
5	INTERACTIVE TRAJECTORY DESIGN SOFTWARE 235
5.1	A New Adaptive Trajectory Design Architecture 236
5.1.1	Java Library: <code>atd-core</code> 237
5.1.2	MATLAB Interface: <code>atd-matlab</code> 239
5.1.3	Plug-ins 241
5.2	Low-Thrust Analyses in ATD V2 243
5.2.1	Java Library: <code>atd-core-low-thrust</code> 243
5.2.2	General Low-Thrust Propagation 244
5.2.3	Equilibrium Point Analyses 245

	Page
5.2.4 Low-Thrust Periodic Orbit Analyses	249
6 CONCLUDING REMARKS	252
6.1 Insights from Dynamical Systems Theory	252
6.2 Novel Dynamical Structures	253
6.3 Interactive Trajectory Design Software	254
6.4 Recommendations for Future Work	255
REFERENCES	257
APPENDICES	264
A. NUMERICAL INTEGRATION	264
B. SYSTEM AND SPACECRAFT PARAMETERS	265
C. MONTE CARLO ANALYSES	267
D. EQUILIBRIUM POINT SEARCH	276
E. MISCELLANEOUS ALGORITHMS	280
VITA	288

LIST OF TABLES

Table	Page
2.1 Low-thrust system comparison	26
2.2 Predicted and computed H_{1t} changes	48
3.1 Earth-Moon $\mathbb{E}_1(0.07, 180^\circ, 0^\circ)$ Eigenvalues	116
5.1 Solutions implemented in ATD v2 to address shortcomings in ATD v1	236
B.1 CR3BP System Parameters	266
B.2 Low-Thrust Spacecraft Parameters	266

LIST OF FIGURES

Figure	Page
1.1 Trajectory design process	1
2.1 CR3BP reference frame definition	9
2.2 Low-thrust force free body diagrams	23
2.3 Acceleration magnitudes near Earth; Earth-Moon rotating frame	29
2.4 Acceleration magnitudes near the EMB; Sun-EMB rotating frame	30
2.5 Low-thrust vector definition	37
2.6 Comparison of \dot{H}_{lt} values across CR3BP+LT systems	47
2.7 Maximum a_{lt} value for approximately conservative system	50
2.8 Comparison of two 2D Sun-EMB LTPOs with constant and variable mass	51
2.9 Comparison of two 3D Sun-EMB LTPOs with constant and variable mass	53
2.10 Energy plane definition	59
3.1 Ballistic zero velocity surface	63
3.2 Earth-Moon CR3BP+LT forbidden regions (Animation)	65
3.3 Vector diagram to locate low-thrust equilibria	78
3.4 Values of μ and a_{lt} that admit solution for $\alpha = 0$ (Animation)	81
3.5 Values of μ and a_{lt} that admit solution for $\alpha = \pm\pi$ (Animation)	82
3.6 Zero acceleration surfaces in the Earth-Moon system for $a_{lt} = 2.5e-1$	86
3.7 Earth-Moon CR3BP+LT equilibria over range of a_{lt} values (Animation)	88
3.8 Earth-Moon low-thrust equilibria for $a_{lt} = 5e-1$	89
3.9 Comparison of Earth-Moon and Sun-EMB ZACs (Animation)	90
3.10 Acceleration magnitude contours in the Earth-Moon CR3BP	92
3.11 Acceleration magnitude surfaces in the Pluto-Charon CR3BP	94
3.12 Earth-Moon low-thrust equilibria stability for $a_{lt} = 7e-2$	100
3.13 Sun-EMB \mathbb{E}_1 stability for $a_{lt} = 3.2e-2$	101

Figure	Page
3.14 Sun-EMB \mathbb{E}_2 stability for $a_{1t} = 3.2e-2$	101
3.15 Distinct planar equilibria in the Earth-Moon system (Animation)	103
3.16 Distinct spatial equilibria in the Earth-Moon system (Animation)	105
3.17 Stability of the Earth-Moon equilibria for $a_{1t} = 7e-2$ and $\beta = 0$	107
3.18 Earth-Moon low-thrust equilibria for $a_{1t} = 7e-2$ colored by $\det \mathbf{A}$	109
3.19 Stability of the Sun-EMB \mathbb{E}_1 and \mathbb{E}_2 for $a_{1t} = 3.2e-2$ and $\beta = 53^\circ$	110
3.20 Stability changes in the Sun-EMB for $a_{1t} = 3.2e-2$ and $\beta = 0$	111
3.21 Number of equilibria in the Earth-Moon system (Animation)	112
3.22 Hyperbolic eigenvectors at Earth-Moon $\mathbb{E}_1(0.07, 180^\circ, 0^\circ)$	117
3.23 Hyperbolic manifolds at Earth-Moon $\mathbb{E}_1(0.07, 180^\circ, 0^\circ)$	119
3.24 Earth-Moon hyperbolic manifolds for $a_{1t} = 7e-2$, $\alpha = 180^\circ$ and $\beta = 0^\circ$	120
3.25 Ballistic hyperbolic manifolds of the Earth-Moon equilibria	120
3.26 Earth-Moon equilibria hyperbolic manifolds for $a_{1t} = 7e-2$, $\beta = 0^\circ$, variable α angle (Animation)	122
3.27 Earth-Moon equilibria hyperbolic manifolds for $a_{1t} = 7e-2$, $\alpha = 180^\circ$, variable β angle (Animation)	123
3.28 Hyperbolic manifolds associated with the ballistic Sun-EMB equilibria	124
3.29 Sun-EMB hyperbolic manifolds for $a_{1t} = 3.2e-2$ and $\beta = 0$ (Animation)	125
3.30 Earth-Moon E_1 center modes for $a_{1t} = 7e-2$ and $\alpha = 180^\circ$	128
3.31 Earth-Moon nonlinear periodic orbit corrections for $a_{1t} = 7e-2$, $\alpha = 180^\circ$, and $\beta = 0$	131
3.32 Broucke stability diagram	136
3.33 Linearized LTPO hyperbolic manifold on the stroboscopic map	139
3.34 Comparison of linear and nonlinear stable and unstable LTPO manifolds	140
3.35 $\mathbb{E}_1 \Gamma(0.07, 180^\circ, 0^\circ, -1.5342)$ stable and unstable manifolds	141
3.36 Tube topology representation of LTPO hyperbolic manifolds	142
3.37 H_{nat} along the $\mathbb{E}_1 \Gamma(0.07, 180^\circ, 0^\circ, -1.5342)$ stable and unstable manifolds	143
3.38 Earth-Moon $\mathbb{Y}_{2D}^H(180^\circ, 0^\circ)$ family (Animation)	150
3.39 Alternate hodograph for the $\mathbb{Y}_{2D}^H(180^\circ, 0^\circ)$ family	151

Figure	Page
3.40 $\mathbb{Y}_{2D}^H(0.001, 180^\circ, 0^\circ)$ vs. ballistic L_1 Lyapunov family	152
3.41 $\mathbb{Y}_{2D}^H(0.01, 180^\circ, 0^\circ)$ vs. ballistic L_1 Lyapunov family	152
3.42 $\mathbb{Y}_{2D}^H(0.03, 180^\circ, 0^\circ)$ vs. ballistic L_1 Lyapunov family	153
3.43 $\mathbb{Y}_{2D}^H(0.07, 180^\circ, 0^\circ)$ vs. ballistic L_1 Lyapunov family	153
3.44 Earth-Moon $\mathbb{Y}_{3D}^H(180^\circ, 0^\circ)$ family (Animation)	154
3.45 Earth-Moon planar $\mathbb{Y}^H(0^\circ, 0^\circ)$ family near E_1 (Animation)	155
3.46 Earth-Moon planar $\mathbb{Y}^\alpha(0^\circ, -1.544)$ family near E_1 (Animation)	156
3.47 Earth-Moon LTPO families bounded by the \mathbb{E}_1 ZAC	157
3.48 Bifurcations at stability changes in the Earth-Moon $\mathbb{Y}^H(0^\circ, 0^\circ)$ family . .	158
3.49 Earth-Moon E_3 $\mathbb{Y}^\alpha(0^\circ, -1.500)$ family (Animation)	159
4.1 Ballistic arc transiting the Earth-Moon L_1 and L_2 gateways	162
4.2 Transit behavior of low-thrust arcs is predicted by energy plane	164
4.3 Ballistic path bounded by natural forbidden regions at $H_{\text{nat}} = -1.55$. .	166
4.4 Comparison of ZAC energy curves and \mathcal{U}_1 to identify α_1	169
4.5 An α value from \mathcal{U}_1 results in partially-captured arc	170
4.6 Feasible regions in (x, y) map to (α, H_{lt})	174
4.7 An $(\alpha_2, H_{\text{lt},2})$ pair is attainable by changing low-thrust parameters at intersections of $\mathcal{P}_{1,2}$ and the low-thrust arc	177
4.8 The low-thrust capture in the Earth-Moon CR3BP+LT for $a_{\text{lt}} = 7\text{e-}2$. .	178
4.9 Ballistic coast following low-thrust capture at the Moon	178
4.10 An $\mathbb{E}_2(-120^\circ)$ manifold does not reach $H_{\text{nat}}(L_5)$	180
4.11 Earth-Moon ZACs colored by stability for $a_{\text{lt}} = 7\text{e-}2$ and $\beta = 0$	181
4.12 Energy planes corresponding to $E_2(-120^\circ)$ and $E_3^1(-60^\circ)$ intersect . . .	182
4.13 Definition of parameters defining energy plane intersection	185
4.14 The W^s manifolds of $E_3^1(-60^\circ)$ and the W^u manifolds of $E_2(-120^\circ)$ are compared at the energy plane intersection	187
4.15 Preliminary design of a transfer from P_2 to an L_5 SPO leveraging equilibria manifolds	188

Figure	Page
4.16 Converged transfer from P_2 to an L_5 SPO leveraging equilibria manifolds is similar to the initial guess	189
4.17 Stability of planar Earth-Moon \mathbb{E}_1 and \mathbb{E}_2 LTPOs for $a_{lt} = 7e-2$ and $\beta = 0$	192
4.18 Control curves corresponding to states on a low-thrust spiral predict transit through E_1	194
4.19 Stable manifold approaching the Earth-Moon $\Gamma_1(76.36^\circ, -1.604)$ orbit . .	195
4.20 A spiral trajectory within the $\Gamma_1(76.36^\circ, -1.604)$ \mathcal{W}^{s-} is identified as a transit arc	197
4.21 Control curves for low-thrust spiral trajectory states plotted with the ZACs	198
4.22 A trajectory that captures near the Moon in the Earth-Moon CR3BP+LT for $a_{lt} = 7e-2$	199
4.23 Intersections between E_1 and E_1 LTPO manifolds are identified in tube topology on a Poincaré map	201
4.24 Intersections between \mathcal{W}_1^{u+} and \mathcal{W}_2^{s-} are apparent in the third map return	202
4.25 Transit, capture, and manifold states are available from the Poincaré maps in a tube topology	203
4.26 Earliest intersections of $\mathbb{M}_{\Sigma_2}^p(\mathcal{W}_1^{u+})$ by $\mathbb{M}_{\Sigma_2}^k(\mathcal{W}_2^{s-})$	206
4.27 Minimum times-of-flight for intersections between $\mathbb{M}_{\Sigma_2}^p(\mathcal{W}_1^{u+})$ and $\mathbb{M}_{\Sigma_2}^k(\mathcal{W}_2^{s-})$ for $k = 1, 2,$ and 3	208
4.28 Non-intersection \mathcal{W}_1^{u+} and \mathcal{W}_2^{s-} manifolds reveal partially captured trajectories	210
4.29 Ballistic lunar periapsis map for $H_{nat} = -1.584$ and $p = 2$	213
4.30 Comparison of low-thrust lunar apsis maps at different thrust magnitudes (Animation)	215
4.31 Low-thrust lunar periapsis map for $H_{nat,0} = -1.584$ and $p = 75$ (Animation)	216
4.32 Eccentricity of captured arcs for $H_{nat,0} = -1.584$ and $p = 75$	217
4.33 Hovering motion occurs between transiting and captured arcs	218
4.34 Lunar IceCube reference trajectory	221
4.35 Apsis maps in the Moon-centered Earth-Moon rotating frame for $H_{nat} = -1.425$, $I_{sp} = 2500$ seconds, and $p = 20$ map returns.	222
4.36 Close-up views of the high-energy apsis maps	223

Figure	Page
4.37 Chaotic motion is apparent in the high-energy low-thrust trajectories . . .	223
4.38 At the Σ_1 hyperplane, low-thrust arcs flow into and onto the ballistic L_2 Lyapunov manifold	226
4.39 Low-thrust trajectories flow into a ballistic manifold while decreasing the H_{nat} value	228
4.40 Ballistic L_2 Lyapunov manifolds overlaid on a low-thrust apsis map	229
4.41 Arcs that reach a low-energy lunar orbit are designed by identifying ap- propriate states on the Σ_2 , Σ_1 , and apsis maps	231
4.42 Sample capture trajectories in configuration space	232
4.43 The H_{nat} energy along the sample arcs and the LIC trajectory decreases to a low-energy lunar orbit	233
5.1 Code coverage report for <code>atd-core</code>	239
5.2 The main <code>atd-matlab</code> GUI	240
5.3 GUI to propagate a trajectory with low-thrust	245
5.4 The low-thrust dynamics plug-in visualizing the stability of the Earth- Moon ZACs for $a_{\text{lt}} = 7\text{e-}2$	246
5.5 View of Earth-Moon ZACs parameter space in ATD	247
5.6 The Earth-Moon $E_3^1(0.07, 57^\circ, 17^\circ)$ hyperbolic manifolds are propagated via a simple GUI	248
5.7 An Earth-Moon LTPO family displayed in ATD	249
5.8 An interface to view families in the context of the ZAC energy curves . . .	250
C.1 Earth-Moon ΔH_{lt} Monte Carlo Results	270
C.2 Pluto-Charon ΔH_{lt} Monte Carlo Results	271
C.3 Sun-EMB ΔH_{lt} Monte Carlo Results	272
C.4 Sun-Mars ΔH_{lt} Monte Carlo Barycenter Results	273
C.5 Sun-EMB ΔH_{lt} Monte Carlo results for $F = 9.2\text{e-}7$ kN	274
E.1 Example of a mesh	284
E.2 Mesh refinement algorithm	285
E.3 Inner loop through cells in mesh refinement	286

SYMBOLS

Operators – *The variable (e.g., x) may be “decorated” by various symbols or font types to denote different types of quantities.*

\bar{z}	complex conjugate
$\text{Re}(z)$	real component of a complex number
$\text{Im}(z)$	imaginary component of a complex number
x_{nat}	quantity associated with the natural CR3BP
x_{lt}	quantity associated with the CR3BP+LT
\dot{x}	derivative with respect to nondimensional time, τ
\ddot{x}	second derivative with respect to nondimensional time, τ
$ x $	absolute value
\vec{x} or $\begin{Bmatrix} a \\ b \end{Bmatrix}$	column vector
\vec{x}^T	transpose, i.e., row vector
$\{a \ b\}$	row vector
\hat{x}	unit vector (column)
$\vec{x} \cdot \vec{y}$	dot product, i.e., inner product
$\vec{x} \times \vec{y}$	cross product (column vector)
$\ \vec{x}\ $	L2 vector norm
\mathbf{X}	matrix
\mathbf{X}^{-1}	matrix inverse
\mathbf{X}^T	matrix transpose
$\text{tr}(\mathbf{X})$	trace of a matrix
\mathbb{X} or $\{a, b, c\}$	set, i.e., a collection of scalars, vectors, or matrices
$\{a \mid b\}$	set of a given condition b

Variables – *When a lowercase and uppercase variable are presented*

together, the lowercase variable represents the nondimensionalized (nd) version of the dimensional uppercase variable; the default units for both variables are listed in square brackets.

\vec{a}	spacecraft acceleration as seen in the rotating frame [nd]
a_{nat}	magnitude of the natural acceleration vector [nd]
\vec{a}_{nat}	natural acceleration vector, rotating frame [nd]
a_{lt}	magnitude of low-thrust acceleration vector [nd]
\vec{a}_{lt}	low-thrust acceleration vector, rotating frame [nd]
\hat{a}_{lt}	low-thrust acceleration orientation, unit length, rotating frame
d, \tilde{d}	tube topology radial metrics [nd]
f, F_{thrust}	thrust force [nd, N or kg·km/s ²]
\vec{g}_{lt}	low-thrust differential equations (vector form)
m_i, M_i	the mass of the i^{th} primary body [nd, km]
n, N	the mean motion of the primary bodies in their orbits about the system barycenter [nd, sec ⁻¹]
\vec{p}	generalized momenta [nd]
\vec{q}	generalized coordinates [nd]
\vec{r}, \vec{R}	spacecraft position relative to the barycenter, rotating coordinates [nd, km]
r, R	distance between spacecraft and system barycenter [nd, km]
\vec{r}_i, \vec{R}_i	position of i^{th} primary body relative to the barycenter, rotating coordinates [nd, km]
r_{i3}, R_{i3}	distance between spacecraft and the i^{th} primary body in rotating coordinates [nd, km]
$\vec{r}_{i3}, \vec{R}_{i3}$	spacecraft position relative to the i^{th} primary body [nd, km]
τ, t	time [nd, sec]
v	spacecraft velocity magnitude [nd]
\vec{v}	spacecraft velocity, rotating frame [nd]

w	imaginary component of an eigenvalue
x, y, z	spacecraft position coordinates, rotating frame [nd]
$\dot{x}, \dot{y}, \dot{z}$	spacecraft velocity coordinates, rotating frame [nd]
$\ddot{x}, \ddot{y}, \ddot{z}$	spacecraft acceleration coordinates, rotating frame [nd]
$\hat{x}, \hat{y}, \hat{z}$	CR3BP rotating frame basis vectors
E_i^j	the j^{th} low-thrust equilibrium point on the i^{th} zero acceleration surface
\mathbb{E}_i	the i^{th} zero acceleration surface
\vec{F}_{ext}	external force, as seen in an inertial frame [N or kg·km/s ²]
\vec{F}_{thrust}	thrust force, as seen in an inertial frame [N or kg·km/s ²]
$\mathbb{F}_{\text{nat}}, \mathbb{F}_{\text{lt}}$	zero velocity surfaces in the CR3BP and CR3BP+LT
\vec{F}	constraint vector
G	universal gravitational constant [km ³ /kg·s ²]
\mathbf{G}	differential corrections Jacobian matrix
H_{nat}	natural Hamiltonian [nd]
H_{lt}	low-thrust Hamiltonian [nd]
\mathbb{I}	inertial frame basis centered on the CR3BP barycenter
\mathbf{J}	Hamiltonian system derivative relationship matrix
\mathcal{L}	the Lagrangian
L_i	the i^{th} Lagrange point
L_*	characteristic length to nondimensionalize distances [km]
M_*	characteristic mass to nondimensionalize masses [kg]
\mathbb{M}	mapping operator
P_i	the i^{th} primary body
\vec{P}_3	linear momentum of P_3 , inertial observer [kg ² ·km/s ²]
\mathbf{Q}	eigenvector matrix
\mathbb{R}	CR3BP rotating frame basis
$\mathcal{T}, \mathcal{T}_{\text{lt}}$	specific kinetic energies in the CR3BP and CR3BP+LT [nd]
T	orbital period [nd]

T_*	characteristic time to nondimensionalize times [sec]
$\mathbf{T}_{\tilde{\omega}}$	Hamiltonian to Lagrangian basis transformation matrix
U	potential function [km^2/s^2]
$\mathcal{V}, \mathcal{V}_{\text{lt}}$	specific potential energies in the CR3BP and CR3BP+LT [nd]
\vec{V}_e	exhaust velocity, inertial frame [km/s]
W	equilibrium point manifold
\mathcal{W}	periodic orbit manifold
\vec{X}_H	CR3BP state vector in the Hamiltonian basis [nd]
$\vec{X}, \vec{X}_{\mathcal{L}}$	CR3BP state vector in the Lagrangian basis [nd]
\vec{X}_{lt}	state vector in the CR3BP+LT, Lagrangian basis [nd]
$\vec{\mathcal{X}}$	free variable vector
$\hat{\mathbf{x}}, \hat{\mathbf{y}}, \hat{\mathbf{z}}$	CR3BP inertial frame basis vectors
\mathbb{Y}	family of low-thrust periodic orbits
α, β	low-thrust acceleration vector orientation angles relative to the rotating frame [radians]
γ	energy plane orientation angle related to a_{lt} [radians]
θ_v	planar velocity angle [radians]
κ	real component of an eigenvalue
λ	an eigenvalue
μ	mass ratio for the CR3BP [nd]
$\vec{\nu}$	an eigenvector
$\vec{\rho}$	a 4-element “control point” vector containing the position and natural Hamiltonian on a trajectory [nd]
$\vec{\phi}$	flow map
$\vec{\varphi}$	the real components of an eigenvector
$\vec{\psi}$	the imaginary components of an eigenvector
$\tilde{\omega}$	rotating frame angular velocity cross product matrix
Γ	low-thrust periodic orbit
Λ	eigenvalue matrix

Σ	hyperplane (e.g., in Poincaré mapping)
Υ	CR3BP+LT pseudopotential [nd]
Ω	CR3BP pseudopotential [nd]

ABBREVIATIONS

ATD	adaptive trajectory design
CR3BP	circular restricted 3-body problem
CR3BP+LT	circular restricted 3-body problem with low thrust
CSI	constant specific impulse
DS1	Deep-Space 1
EMB	Earth-Moon barycenter
EOM	equation of motion
GTO	geostationary transit orbit
GUI	graphical user interface
LIC	Lunar IceCube
LTPO	low-thrust periodic orbit
NASA	National Aeronautics and Space Administration

ABSTRACT

Cox, Andrew D. PhD, Purdue University, May 2020. A Dynamical Systems Perspective for Preliminary Low-Thrust Trajectory Design in Multi-Body Regimes. Major Professor: Kathleen C. Howell.

A key challenge in low-thrust trajectory design is generating preliminary solutions that simultaneously detail the evolution of the spacecraft position and velocity vectors, as well as the thrust history. To address this difficulty, a dynamical model that incorporates a low-thrust force into the circular restricted 3-body problem (CR3BP), i.e., the CR3BP+LT, is constructed and analyzed. Control strategies that deliver specific energy changes (including zero energy change to deliver a conservative system) are derived and investigated, and dynamical structures within the CR3BP+LT are explored as candidate solutions to seed initial low-thrust trajectory designs. Furthermore, insights from dynamical systems theory are leveraged to inform the design process. In the combined model, the addition of a low-thrust force modifies the locations and stability of the equilibrium solutions, resulting in flow configurations that differ from the natural behavior in the CR3BP. The application of simplifying assumptions yields a conservative, autonomous system with properties that supply useful insights. For instance, "forbidden regions" at fixed energy levels bound low-thrust motion, and analytical equations are available to guide the navigation through energy space. Linearized dynamics about the equilibria supply hyperbolic and center manifold structures, similar to the ballistic CR3BP. Low-thrust periodic orbits in the vicinity of the equilibrium solutions also admit hyperbolic and center manifolds, providing an even greater number of dynamical structures to be employed in preliminary trajectory designs. Several applications of the structures and insights derived from the CR3BP+LT are presented, including several strategies for transit and capture near the smaller CR3BP primary body. Finally, an interactive trajectory design

framework is presented to explore and utilize the structures and insights delivered by this investigation.

1. INTRODUCTION

The efficiency of low-thrust propulsion has enabled a variety of ambitious space missions in recent decades. For example, the Deep Space 1 mission to the McAuliffe asteroid and the West-Kohoutek-Ikemura comet [1], the Dawn mission to the dwarf planets Vesta and Ceres [2], and the Hayabusa 1 and 2 missions to the Itokawa and Ryugu asteroids [3, 4] have all employed low-thrust propulsion to reach their destinations. Additionally, numerous current and future missions such as Psyche [5], Lunar IceCube [6], and Gateway [7] plan to leverage a low-thrust force to reach deep-space destinations as well as locations closer to home, e.g., the Moon. As new and improved low-thrust technologies are designed and validated, the number of low-thrust-enabled missions will only increase. Accordingly, resources and strategies that facilitate low-thrust trajectory design are increasingly in demand.

1.1 Motivation and Previous Contributions

The process of designing an end-to-end trajectory for a spacecraft is a nontrivial endeavor. Nevertheless, this task may be distilled into three general steps, illustrated in Figure 1.1. First, an “initial guess” is constructed. This preliminary design may



Figure 1.1.: Trajectory design process

include arcs from a variety of dynamical models such as the 2-body problem (i.e., conic arcs), the 3-body problem, or an ephemeris model. The initial design need not be continuous, nor must it satisfy all mission constraints; it’s main purpose is to guide the second step, corrections and/or optimization. In this step, the preliminary design

is modified (via some iterative process) until it satisfies a set of mission constraints and/or minimizes a cost function. The output of this process is a single *converged* or *optimized* trajectory.

One common strategy for *ballistic* (i.e., without low-thrust) trajectory design is to assemble *dynamical structures* (e.g., periodic orbits, quasi-periodic orbits, or invariant manifolds) from multi-body models. As early as the 1970’s, researchers proposed leveraging periodic halo orbits in the restricted three body problem for translunar communications satellites [8, 9]. Only a few years later, the ISEE-3 spacecraft flew along a Sun-Earth halo orbit [10], validating the theory and paving the way for future Sun-Earth libration point missions such as SOHO [11] and GENESIS [12], and Earth-Moon libration point missions such as ARTEMIS [13]. Multi-body dynamical structures are now a fundamental part of mission design efforts, from small “CubeSat” missions like Lunar IceCube [6] to large, human spaceflight missions like NASA’s Artemis-1 (previously EM-1) mission [7]. One frequently useful model is the circular restricted 3-body problem (CR3BP) which, when formulated in terms of a rotating frame, yields a conservative, autonomous, Hamiltonian system with useful symmetries and an abundance of available structures [14]. Periodic and quasi-periodic motion from the CR3BP such as the halo, quasi-halo, and Lissajous orbits have been employed as initial designs for a number of missions, and manifolds that asymptotically approach these orbits supply useful paths capable of delivering a spacecraft to a corresponding destination orbit without any deterministic maneuvers [15].

Although strategies that assemble dynamical structures into a preliminary trajectory design are very successful for ballistic paths, additional obstacles exist when a low-thrust force is added to the dynamics. For example, when the multi-body dynamics described by the CR3BP are augmented with a low-thrust force, the resulting system (CR3BP+LT) is not generally autonomous or Hamiltonian; thus, many of the useful simplifications and structures from the CR3BP are not immediately available for use in a preliminary design. Additionally, the problem dimension, i.e., the number of design variables, increases with the inclusion of the low-thrust force. To solve this

large, complex problem (and others like it), many authors employ numerical techniques to identify low-thrust control parameters along trajectories that are initialized from ballistic 2-body and 3-body structures. For example, predictor-corrector shooting algorithms are applied to generate control histories along low-thrust transfers between periodic orbits in the CR3BP [16, 17, 18]. Similarly, collocation algorithms, combined with optimization, add low-thrust to ballistic initial guesses, yielding non-intuitive trajectories [19, 20, 21]. Optimization methods without a collocation scheme have also been employed to augment ballistic structures with a low-thrust acceleration [22, 23]. Other authors apply machine learning and pathfinding techniques to construct itineraries from segments of natural arcs, incorporating the capabilities of a low-thrust propulsion system via *attainable sets* [24, 25]. In any of these strategies, the preliminary designs rarely include an initial guess for the low-thrust control parameters; designers rely on the corrections or optimization algorithms to identify suitable control values. Although this approach may succeed in many cases, the chaotic dependency between the initial guess and the converged solution makes it difficult to understand the impact of changes to the control parameters (or other aspects of the preliminary design) on the final result. This lack of intuition only exacerbates the difficulties in designing an initial guess. In short, *the effects of the magnitude, orientation, and duration of a low-thrust force on a trajectory in a multi-body regime are poorly understood*. This investigation seeks to address this difficulty; a systematic and intuitive strategy to generate preliminary low-thrust designs is desired to improve the predictability of these algorithms and to supply an improved understanding of the available trajectory options.

Rather than relying solely on numerical methods and optimization algorithms to select low-thrust control parameters, an increasing number of authors are examining models that incorporate multiple gravitational forces and a low-thrust force to develop preliminary low-thrust control histories for spacecraft trajectories. Exploration of the 3-body dynamics with a radiation pressure force added to both primaries demonstrates the existence of new equilibrium points [26]. Similar analyses of the

effects of solar radiation pressure on solar sail motion in the Sun-Earth CR3BP examine a set of *artificial equilibrium points* (AEPs) and propose strategies to maintain stable orbits about the AEPs [27, 28]. Subsequent investigations of the AEPs explore the linear stability properties of the points and construct periodic orbits in the vicinity of the AEPs [29] for various mission applications, including communications platforms [30], polar observation missions [31], and asteroid hovering operations [32]. The stable and unstable manifolds corresponding to the AEPs may be leveraged in trajectory designs between the CR3BP libration points in the Sun-Earth solar sail model [33, 34] and in the Earth-Moon low-thrust model [35]. Similarly, the stable and unstable manifolds associated with periodic orbits near the AEPs are employed as segments of low-thrust trajectories [36]. Finally, insights from the CR3BP+LT are applied to select control parameters for capture and escape from gravity wells in the Earth-Moon system [37, 38, 39].

1.2 Research Objectives and Document Overview

Building upon the existing literature, the focus of this investigation is the exploration of a model that incorporates both multi-body dynamics and a low-thrust force. By exploring such a model, flow patterns that incorporate low-thrust control can be quantified and categorized for use in multi-body trajectory designs. Accordingly, the goal of this work is a general set of heuristics and properties to aid in the construction of preliminary solutions that include low-thrust arcs in multi-body regimes. This goal is subdivided into the following objectives:

1. Apply dynamical systems techniques to explore the properties and structures within the context of a model that includes both multi-body gravitational dynamics and a low-thrust force.
2. Create a catalog of dynamical structures from the low-thrust, multi-body model that may be incorporated into preliminary trajectory designs.

3. Demonstrate the use of the insights and structures from the low-thrust, multi-body model to design low-thrust trajectories in the Earth-Moon and Sun-Earth systems.

The analyses in support of these objectives supply intuition where little currently exists in the combined multi-body, low-thrust problem. This intuition enables exploration of the design space before optimization or corrections algorithms are applied, and facilitates a greater understanding of converged and/or optimized results.

To address the challenge of determining the relationship between low-thrust control inputs and the evolution of a trajectory, two specific trajectory characteristics are studied:

Energy The energy along a trajectory, i.e., the Hamiltonian or Jacobi constant in the CR3BP, is a scalar quantity that remains constant in the ballistic CR3BP. With the addition of the low-thrust force, this energy value varies along a trajectory. Links between the low-thrust vector and the energy evolution are identified to enable control of the energy in preliminary designs.

Geometry The effects of low-thrust control on the geometry of a trajectory, i.e., the 6D position and velocity of the arc, are more difficult to identify than the relationship with the scalar energy quantity. To supply a global view of the trajectory geometries enabled by the addition of low-thrust to the CR3BP, a variety of dynamical structures such as equilibrium points, equilibrium point manifolds, periodic orbits, and periodic orbit manifolds are constructed across the full range of plausible control parameters. By comparing these structures with ballistic paths, the impact of the low-thrust force on a spacecraft path may be inferred.

The discussion of these contributions is split into three chapters:

Chapter 2 - Dynamical Models The equations of motion governing the CR3BP are derived via a Newtonian and a Hamiltonian approach, and the Hamiltonian (an integral of the motion) is identified. These multi-body dynamics are then

augmented with a low-thrust force in the CR3BP+LT formulation. A brief survey of other perturbing accelerations puts the magnitude of the low-thrust term into perspective. Next, an analysis of the CR3BP Hamiltonian reveals several low-thrust control strategies that govern the evolution of the Hamiltonian. A low-thrust Hamiltonian is also constructed and examined. The conditions under which this Hamiltonian may be assumed constant are then explored and validated via Monte Carlo analyses. Finally, the properties of an autonomous, conservative, and Hamiltonian CR3BP+LT are discussed, revealing a direct relationship between the low-thrust control parameters, the initial and final positions on a trajectory, and the resulting change in the ballistic Hamiltonian value. These properties supply intuition to guide preliminary trajectory design efforts and lay the groundwork for the following two chapters.

Chapter 3 - Dynamical Structures Building upon the models developed in the first chapter, the forbidden regions associated with the CR3BP+LT are constructed and analyzed. These structures supply bounds on the evolution of a low-thrust trajectory with a specific low-thrust acceleration vector. Next, the locations and stability properties of the equilibrium solutions are assessed. As these solutions differ significantly from the ballistic equilibria, many novel structures and characteristics are identified. The hyperbolic manifolds (i.e., the stable and unstable manifolds) associated with the low-thrust equilibria also deliver new paths throughout the 3-body environment. Next, the periodic orbits within the center manifolds of the equilibrium points are computed; by applying continuation methods, entire families of low-thrust periodic orbits are available, supplying a large number of novel solutions. Finally, the stable and unstable manifolds associated with the periodic orbits are constructed. Any of these dynamical structures may be included in an itinerary for a low-thrust spacecraft.

Chapter 4 - Applications In this chapter, the insights and structures from the previous two chapters are applied to trajectory design problems. First, insights

from the energy plane enable modifications to a ballistic path to prohibit passage through gateways in the low-thrust forbidden regions. Next, a more nuanced strategy to control these gateways is developed by relating the control parameters at a point on a ballistic path to the equilibrium point energies. Using this method, a ballistic path is straightforwardly adjusted to capture near the Moon. A more general criteria for transit and capture near the Moon is then developed by leveraging the hyperbolic manifolds associated with low-thrust periodic orbits located in the low-thrust forbidden region gateways. An application linking low-thrust spiral trajectories departing from a geostationary transit orbit to a manifold that approaches the Moon demonstrates this concept. Intersections of the low-thrust manifolds are also employed to identify paths that transit through the lunar region or that fail to transit, i.e., that capture. Finally, apsis maps of anti-velocity-pointing low-thrust arcs are utilized to locate high-energy trajectories capable of capturing into the Moon's gravity well.

Chapter 5 - Interactive Trajectory Design The final chapter briefly discusses the architecture of an interactive trajectory design software suite that has been developed to communicate the results of this investigation to other researchers. Two Java libraries contain object-oriented classes for rapid and flexible analysis while a MATLAB graphical user interface supplies a visual, interactive front-end to the Java libraries. Two plug-ins to the MATLAB interface enable the exploration of the low-thrust insights and dynamical structures.

Finally, a webpage displaying animated versions of some of the figures in this document is hosted at

[https://engineering.purdue.edu/people/kathleen.howell.1/Publications/
Dissertations/2020_Cox](https://engineering.purdue.edu/people/kathleen.howell.1/Publications/Dissertations/2020_Cox)

2. DYNAMICAL MODELS

The first step toward understanding the impact of the magnitude, orientation, and duration of a low-thrust force on a trajectory in a multi-body regime is the definition of a model that incorporates both the multi-body dynamics and the low-thrust force. In this investigation, the multi-body dynamics are modeled via the circular restricted 3-body problem. This *ballistic* model is then augmented with a low-thrust acceleration to form a combined multi-body, low-thrust dynamical system. Following the derivation of a general model, specific low-thrust control parameterizations are discussed from a dynamical systems perspective, yielding insights that enable the control of the energy along the trajectory. One particular parameterization that results in a conservative, autonomous, and Hamiltonian system is explored in more detail and validated with Monte Carlo analyses. A discussion of several useful properties of this simplified model concludes the chapter, including a direct link between the low-thrust control, the initial and final points on a trajectory, and the energy change along the path. These results enable manipulations of the ballistic energy via low-thrust and lay the groundwork for the calculation of dynamical structures in the next chapter.

2.1 Circular Restricted 3-Body Problem

The circular restricted 3-body problem (CR3BP) describes the motion of three barycentric bodies P_1 , P_2 , and P_3 with masses M_1 , M_2 and M_3 , respectively. It is assumed that P_3 possesses negligible mass compared to the other two bodies (i.e., $M_3 \ll M_1, M_2$) and, thus, does not affect their motion. The paths of the two larger bodies, termed *primaries*, are therefore governed by two-body gravitational dynamics and are represented by conic sections. For simplicity, it is assumed that the two primaries move in circular orbits (rather than more general elliptical orbits) about

their mutual barycenter, B , as depicted in Figure 2.1. A right-handed, orthonormal

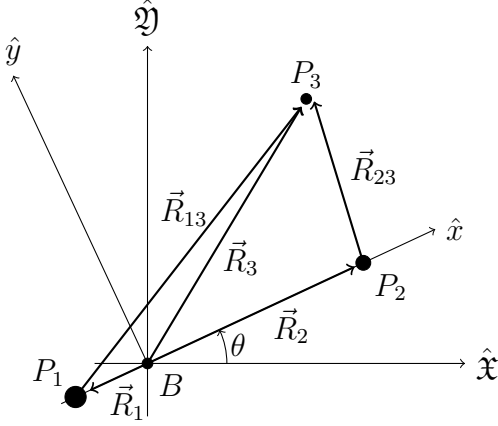


Figure 2.1.: CR3BP reference frame definition

inertial frame, $\mathbb{I} = \{\hat{\mathcal{X}}, \hat{\mathcal{Y}}, \hat{\mathcal{Z}}\}$, is defined such that the $\hat{\mathcal{X}}$ and $\hat{\mathcal{Y}}$ unit vectors span the primaries' orbital plane and $\hat{\mathcal{Z}}$ coincides with their mutual angular momentum vector. The circular motion of the primaries relative to the barycenter is described by simple trigonometric relationships,

$$\vec{R}_1 = R_1 \left[-\cos(Nt)\hat{\mathcal{X}} - \sin(Nt)\hat{\mathcal{Y}} \right], \quad (2.1)$$

$$\vec{R}_2 = R_2 \left[\cos(Nt)\hat{\mathcal{X}} + \sin(Nt)\hat{\mathcal{Y}} \right], \quad (2.2)$$

where \vec{R}_1 and \vec{R}_2 are vectors locating each primary relative to the barycenter and $N = d\theta/dt$ is the mean motion of the primaries in their orbits about B . The position of P_3 is denoted \vec{R}_3 and is measured relative to the inertially-fixed base point B . The equations that govern the motion of P_3 , i.e., the equations for $d\vec{R}_3/dt$ and $d^2\vec{R}_3/dt^2$, may be derived via several methods. A Newtonian approach equates the sum of external forces to the time-varying momentum of the spacecraft. This formulation represents the dynamics in terms of intuitive quantities such as Cartesian position and velocity coordinates and force vectors. Alternatively, a Hamiltonian or Lagrangian derivation may be applied. These energy-balance approaches employ less intuitive generalized coordinates and generalized momenta but offer clear insights into dynam-

ical properties of the system, such as the existence of integrals and the properties of manifolds. Thus, both Newtonian and Hamiltonian derivations are included.

2.1.1 Newtonian Derivation

Newton's second law describes the motion of P_3 as viewed by an inertial observer due to the external forces exerted on P_3 by P_1 and P_2 . Expressed mathematically,

$$\sum \vec{F}_{\text{ext}} = \frac{{}^i d\vec{\mathcal{P}}_3}{dt}, \quad (2.3)$$

where $\vec{\mathcal{P}}_3$ is the linear momentum of P_3 ,

$$\vec{\mathcal{P}}_3 = M_3 \frac{{}^i d\vec{R}_3}{dt}, \quad (2.4)$$

and the i in the left-superscript denotes an inertial observer, i.e., and observer fixed in \mathbb{I} . If M_3 is constant Newton's law simplifies to the familiar form,

$$\sum \vec{F}_{\text{ext}} = M_3 \frac{{}^i d^2 \vec{R}}{dt^2}. \quad (2.5)$$

The external gravitational forces applied to P_3 by P_1 and P_2 are derived from the spatial gradient of the gravitational potential function,

$$U = -G \left(\frac{M_1}{R_{13}} + \frac{M_2}{R_{23}} \right), \quad (2.6)$$

where G is the universal gravitational constant, yielding

$$\sum \vec{F}_{\text{ext}} = GM_3 \vec{\nabla}_r U = -GM_3 \left(\frac{M_1}{R_{13}^3} \vec{R}_{13} + \frac{M_2}{R_{23}^3} \vec{R}_{23} \right) = M_3 \frac{{}^i d^2 \vec{R}_3}{dt^2}. \quad (2.7)$$

In this notation, $\vec{\nabla}_r = \{\partial/\partial x \quad \partial/\partial y \quad \partial/\partial z\}^T$ denotes the gradient with respect to the three Cartesian position coordinates. Removing the mass of P_3 from both sides of this expression yields the acceleration of P_3 as seen by an inertial observer,

$$\frac{{}^i d^2 \vec{R}_3}{dt^2} = -G \frac{M_1}{R_{13}^3} \vec{R}_{13} - G \frac{M_2}{R_{23}^3} \vec{R}_{23}. \quad (2.8)$$

This vector equation is nonautonomous because both \vec{R}_{13} and \vec{R}_{23} explicitly depend on the time-varying positions of P_1 and P_2 as represented in Equations (2.1) and (2.2). To form an autonomous system, reformulate the equations in a rotating frame basis, $\mathbb{R} = \{\hat{x}, \hat{y}, \hat{z}\}$ (pictured in Figure 2.1), defined with \hat{x} directed from P_1 to P_2 and \hat{z} along the angular velocity of the primary orbit; \hat{y} completes the right-handed set. In this rotating frame, both primaries are stationary, removing the explicit functions of time from the equations of motion.

To further simplify notation and reduce round-off error during numerical integration, all variables are nondimensionalized by characteristic quantities. It is convenient to select a characteristic length equal to the constant distance between the two primaries, $L_* = R_1 + R_2$, and a characteristic mass as the total system mass $M_* = M_1 + M_2$. A characteristic time is subsequently deduced from the reciprocal of the mean motion of the primaries $T_* = 1/N = \sqrt{L_*^3/(GM_*)}$. Let the position vectors, masses, and time be nondimensionalized as follows,

$$\vec{R}_i = L_* \vec{r}_i, \quad M_2 = M_* \mu, \quad t = T_* \tau,$$

where uppercase letters generally (time t is an exception) denote dimensional quantities and lowercase letters represent nondimensional quantities. An expression for M_1 is obtained in terms of the system mass ratio μ :

$$M_1 = (1 - \mu)M_*. \quad (2.9)$$

As a result of applying these characteristic quantities, the nondimensional mean motion of the primaries, $n = NT_*$, and the semi-major axis, $r_{12} = (R_1 + R_2)/L_*$, are equal to unity, therefore, the period of primary motion is $2\pi/n = 2\pi$ nondimensional time units. Substituting nondimensional quantities into equation (2.8) results in the following relationship:

$$\begin{aligned} \frac{d^2 \vec{r}_3}{d\tau^2} \left(\frac{L_*}{T_*^2} \right) &= \ddot{\vec{r}}_3 \frac{L_*}{T_*^2} = -G \left[\frac{M_*(1-\mu)L_*\vec{r}_{13}}{r_{13}^3 L_*^3} + \frac{M_*\mu L_*\vec{r}_{23}}{r_{23}^3 L_*^3} \right] \\ \ddot{\vec{r}}_3 &= -G \frac{M_*}{L_*^3} \left(\sqrt{\frac{L_*^3}{GM_*}} \right)^2 \left[\frac{(1-\mu)}{r_{13}^3} \vec{r}_{13} + \frac{\mu}{r_{23}^3} \vec{r}_{23} \right] \\ \ddot{\vec{r}}_3 &= -\frac{(1-\mu)}{r_{13}^3} \vec{r}_{13} - \frac{\mu}{r_{23}^3} \vec{r}_{23}, \end{aligned} \quad (2.10)$$

where \vec{r}_3 is expressed in nondimensional rotating coordinates as $\vec{r}_3 = x\hat{x} + y\hat{y} + z\hat{z}$ and the dots over a vector represent derivatives with respect to nondimensional time, τ . The vectors \vec{r}_{13} and \vec{r}_{23} locate P_3 relative to P_1 and P_2 , respectively, and are evaluated as $\vec{r}_{13} = \vec{r}_3 - \vec{r}_1$ and $\vec{r}_{23} = \vec{r}_3 - \vec{r}_2$. The distance from P_1 to the center of mass along the \hat{x} -axis, r_1 , is derived from the definition of the center of mass:

$$R_1 = \frac{0M_1 + L_*M_2}{M_1 + M_2} \quad \rightarrow \quad r_1 L_* = \frac{L_* M_* \mu}{M_*} \quad \therefore \quad r_1 = \mu. \quad (2.11)$$

As the nondimensional distance between the primaries is unity, the nondimensional distance r_2 is evaluated as $r_2 = 1 - \mu$. Substituting these relationships for r_1 and r_2 into the expressions for \vec{r}_{13} and \vec{r}_{23} yields

$$\vec{r}_{13} = x\hat{x} + y\hat{y} + z\hat{z} - (-\mu)\hat{x} = (x + \mu)\hat{x} + y\hat{y} + z\hat{z}, \quad (2.12)$$

$$\vec{r}_{23} = x\hat{x} + y\hat{y} + z\hat{z} - (1 - \mu)\hat{x} = (x - 1 + \mu)\hat{x} + y\hat{y} + z\hat{z}. \quad (2.13)$$

Accordingly, the location of P_3 relative to the primary bodies is a function only of the nondimensional coordinates and the system parameter, μ .

Recall that Newton's second law (2.10) applies only for derivatives of \vec{r}_3 as seen by an inertial observer and with respect to an inertial base point. The system barycenter, B , serves as a suitable inertial base point and the inertial reference frame, \mathbb{I} , may be employed as the inertial observer. However, it is more convenient to employ the rotating frame, \mathbb{R} , as the working coordinate system as this results in an autonomous system. Thus, to apply Newton's equations, the basic kinematic equation (BKE) is leveraged to compute the derivatives of the spacecraft position as seen by an inertial observer in rotating frame coordinates.

Theorem 2.1.1 (Basic Kinematic Equation (BKE)) *Let \mathbb{I} represent an inertial frame and let \mathbb{R} represent a frame that rotates relative to \mathbb{I} with the constant angular velocity vector, ${}^i\vec{\omega}^r$. Then the derivative of a vector as observed in the \mathbb{I} frame is related to the derivative as observed in the \mathbb{R} frame by the relationship,*

$$\frac{{}^i d\vec{r}}{d\tau} = \frac{{}^r d\vec{r}}{d\tau} + {}^i\vec{\omega}^r \times \vec{r}. \quad (2.14)$$

The vectors may be represented in either working frame, i.e., \mathbb{R} or \mathbb{I} , as long as all of the vectors are expressed in terms of the same working frame.

Proof Define a position vector¹,

$$\vec{r} = x\hat{x} + y\hat{y} + z\hat{z}, \quad (2.15)$$

represented in the $\mathbb{R} = \{\hat{x}, \hat{y}, \hat{z}\}$ working frame. The derivative of this vector as observed in the \mathbb{R} frame is

$$\frac{{}^r d\vec{r}}{d\tau} = \dot{x}\hat{x} + \dot{y}\hat{y} + \dot{z}\hat{z}. \quad (2.16)$$

¹Paraphrased from course notes [40]

Similarly, the derivative as observed from the \mathbb{I} frame is

$$\frac{{}^i d\vec{r}}{d\tau} = \frac{{}^i d}{d\tau} (x\hat{x} + y\hat{y} + z\hat{z}), \quad (2.17)$$

$$= \dot{x}\hat{x} + \dot{y}\hat{y} + \dot{z}\hat{z} + x\frac{{}^i d\hat{x}}{d\tau} + y\frac{{}^i d\hat{y}}{d\tau} + z\frac{{}^i d\hat{z}}{d\tau}, \quad (2.18)$$

$$= \frac{{}^r d\vec{r}}{d\tau} + x\frac{{}^i d\hat{x}}{d\tau} + y\frac{{}^i d\hat{y}}{d\tau} + z\frac{{}^i d\hat{z}}{d\tau}. \quad (2.19)$$

The derivatives of the \mathbb{R} basis vectors as observed in the \mathbb{I} frame are

$$\frac{{}^i d\mathbb{R}_j}{d\tau} = {}^i \vec{\omega}^r \times \mathbb{R}_j, \quad (2.20)$$

where ${}^i \vec{\omega}^r$ is the constant angular velocity of the \mathbb{R} frame relative to the \mathbb{I} frame [41].

Accordingly, Equation (2.19) simplifies to

$$\begin{aligned} \frac{{}^i d\vec{r}}{d\tau} &= \frac{{}^r d\vec{r}}{d\tau} + \left({}^i \vec{\omega}^r \times x\hat{x} \right) + \left({}^i \vec{\omega}^r \times y\hat{y} \right) + \left({}^i \vec{\omega}^r \times z\hat{z} \right), \\ &= \frac{{}^r d\vec{r}}{d\tau} + {}^i \vec{\omega}^r \times \vec{r}. \end{aligned} \quad (2.21)$$

■

The CR3BP rotating frame spins about the $\hat{z} = \hat{Z}$ axis at a constant nondimensional rate, n ; thus, the angular velocity of the CR3BP rotating frame relative to an inertial frame is

$${}^i \vec{\omega}^r = \left\{ \begin{matrix} 0 & 0 & n \end{matrix} \right\}^T. \quad (2.22)$$

Applying the BKE, the kinematic inertial derivative of \vec{r}_3 expressed in rotating coordinates is

$$\begin{aligned} \dot{\vec{r}}_3 &= \frac{{}^i d\vec{r}_3}{d\tau} = \dot{x}\hat{x} + \dot{y}\hat{y} + \dot{z}\hat{z} + [n\hat{z}] \times [x\hat{x} + y\hat{y} + z\hat{z}] \\ &= (\dot{x} - ny)\hat{x} + (\dot{y} + nx)\hat{y} + \dot{z}\hat{z}. \end{aligned} \quad (2.23)$$

Similarly, the second derivative yields

$$\ddot{\vec{r}}_3 = \frac{d^2 \vec{r}_3}{d\tau^2} (\ddot{x} - 2n\dot{y} - n^2 x) \hat{x} + (\ddot{y} + 2n\dot{x} - n^2 y) \hat{y} + \ddot{z} \hat{z}. \quad (2.24)$$

Substituting this expansion, the nondimensional values for r_1 and r_2 , and the nondimensional value $n = 1$ into Equation (2.10) yields three scalar equations describing the motion of P_3 as expressed in terms of the rotating Cartesian coordinates:

$$\ddot{x} - 2\dot{y} = x - (1 - \mu) \frac{x + \mu}{r_{13}^3} - \mu \frac{x - 1 + \mu}{r_{23}^3}, \quad (2.25)$$

$$\ddot{y} + 2\dot{x} = y - (1 - \mu) \frac{y}{r_{13}^3} - \mu \frac{y}{r_{23}^3}, \quad (2.26)$$

$$\ddot{z} = -(1 - \mu) \frac{z}{r_{13}^3} - \mu \frac{z}{r_{23}^3}. \quad (2.27)$$

where

$$r_{13} = \sqrt{(x + \mu)^2 + y^2 + z^2}, \quad (2.28)$$

$$r_{23} = \sqrt{(x - 1 + \mu)^2 + y^2 + z^2}. \quad (2.29)$$

These equations may be written more compactly as the gradient of a *pseudopotential* function, Ω . Recall the inertial potential function, $\tilde{U} = \frac{1-\mu}{r_{13}} + \frac{\mu}{r_{23}}$, now expressed in terms of nondimensional quantities. This inertial potential is augmented with the “potential” of the rotating frame to form the pseudopotential,

$$\Omega = \tilde{U} + \frac{1}{2}(x^2 + y^2) = \frac{1 - \mu}{r_{13}} + \frac{\mu}{r_{23}} + \frac{1}{2}(x^2 + y^2). \quad (2.30)$$

The equations of motion, (2.25) – (2.27), are related to the spatial gradient of Ω :

$$\ddot{x} - 2\dot{y} = \Omega_x, \quad (2.31)$$

$$\ddot{y} + 2\dot{x} = \Omega_y, \quad (2.32)$$

$$\ddot{z} = \Omega_z, \quad (2.33)$$

were the partial derivatives are $\Omega_x = \partial\Omega/\partial x$, $\Omega_y = \partial\Omega/\partial y$, and $\Omega_z = \partial\Omega/\partial z$. In these expressions, the x and y accelerations are decoupled from the z acceleration such that motion that originates entirely in the xy -plane (i.e., $z = \dot{z} = 0$) does not develop any motion in the out-of-plane direction.

2.1.2 Hamiltonian Derivation

Additional insights into the dynamics of the CR3BP are available by applying a Hamiltonian approach.² In contrast to the Newtonian derivation, which relates forces and accelerations, the Hamiltonian method follows an energy balance approach. To begin, define a set of *generalized coordinates*, $\vec{q} = \{q_1 \ q_2 \ q_3\}^T$, where

$$q_1 = x, \tag{2.34}$$

$$q_2 = y, \tag{2.35}$$

$$q_3 = z, \tag{2.36}$$

i.e., $\vec{q} = \vec{r}_3$, the location of P_3 relative to the system barycenter in the rotating frame coordinates. Additionally, define a set of *generalized momenta*, $\vec{p} = \{p_1 \ p_2 \ p_3\}^T$, such that

$$p_1 = \dot{q}_1 - q_2, \tag{2.37}$$

$$p_2 = \dot{q}_2 + q_1, \tag{2.38}$$

$$p_3 = \dot{q}_3. \tag{2.39}$$

These generalized momenta are equivalent to the specific (*specific* here means mass-independent) linear momentum of the spacecraft as seen by an inertial observer, i.e., the inertial velocity,

$$\vec{p} = \frac{{}^i d\vec{r}_3}{d\tau} = \dot{\vec{r}}_3 + {}^i \vec{\omega}^r \times \vec{r}_3 = \dot{\vec{q}} + \tilde{\omega} \vec{q}, \tag{2.40}$$

²Special thanks to Kenza Boudad for inspiring this Hamiltonian approach!

where $\tilde{\omega}$ is the cross-product matrix,

$$\tilde{\omega} = \begin{bmatrix} 0 & -\omega_3 & \omega_2 \\ \omega_3 & 0 & -\omega_1 \\ -\omega_2 & \omega_1 & 0 \end{bmatrix} = \begin{bmatrix} 0 & -1 & 0 \\ 1 & 0 & 0 \\ 0 & 0 & 0 \end{bmatrix}, \quad (2.41)$$

and the ω_1 , ω_2 , and ω_3 terms are the \hat{x} , \hat{y} , and \hat{z} components of ${}^i\tilde{\omega}^r$, respectively, i.e., $\omega_1 = \omega_2 = 0$ and $\omega_3 = n = 1$ as defined in Equation (2.22). Accordingly, the specific kinetic energy associated with P_3 is defined

$$\mathcal{T} = \frac{1}{2} (p_1^2 + p_2^2 + p_3^2), \quad (2.42)$$

and the specific potential energy is

$$\mathcal{V} = -\frac{1-\mu}{r_{13}} - \frac{\mu}{r_{23}}. \quad (2.43)$$

Note that these expressions represent the P_3 energies as viewed by an *inertial* observer; $p_1^2 + p_2^2 + p_3^2$ is equivalent to the squared magnitude of the velocity of P_3 as seen in the inertial frame and the potential energy is a function only of the distances between primaries, values that are equal in both frames. Next, define the Lagrangian as the difference between the two energies,

$$\mathcal{L} = \mathcal{T} - \mathcal{V}. \quad (2.44)$$

The total energy in the system is the Hamiltonian,

$$H = \vec{p} \cdot \dot{\vec{q}} - \mathcal{L}. \quad (2.45)$$

Accordingly, the Hamiltonian in the CR3BP, H_{nat} , is

$$H_{\text{nat}}(\vec{q}, \vec{p}) = \frac{1}{2} (p_1^2 + p_2^2 + p_3^2) + p_1 q_2 - p_2 q_1 - \frac{1-\mu}{r_{13}} - \frac{\mu}{r_{23}}. \quad (2.46)$$

(Throughout this document, the “nat” subscript denotes a quantity associated with the *natural* CR3BP in contrast to a quantity associated with the augmented CR3BP+LT model.) In the H_{nat} expression, the first term represents the kinetic energy of P_3 in the inertial frame, the second and third terms capture the “energy” of the rotating system, and the final two terms represent the potential energy from the gravitational fields. By applying Hamilton’s canonical equations of motion,

$$\dot{\vec{q}} = \left(\frac{\partial H}{\partial \vec{p}} \right)^T, \quad \dot{\vec{p}} = \left(-\frac{\partial H}{\partial \vec{q}} \right)^T,$$

the governing equations are derived,

$$\dot{q}_1 = p_1 + q_2, \tag{2.47}$$

$$\dot{q}_2 = p_2 - q_1, \tag{2.48}$$

$$\dot{q}_3 = p_3, \tag{2.49}$$

$$\dot{p}_1 = p_2 - \frac{1-\mu}{r_{13}^3}(q_1 + \mu) - \frac{\mu}{r_{23}^3}(q_1 - 1 + \mu), \tag{2.50}$$

$$\dot{p}_2 = -p_1 - \frac{1-\mu}{r_{13}^3}q_2 - \frac{\mu}{r_{23}^3}q_2, \tag{2.51}$$

$$\dot{p}_3 = -\frac{1-\mu}{r_{13}^3}q_3 - \frac{\mu}{r_{23}^3}q_3. \tag{2.52}$$

For a more compact form of the equations, define a state vector in the “Hamiltonian basis,”

$$\vec{X}_H = \begin{Bmatrix} \vec{q} \\ \vec{p} \end{Bmatrix}. \tag{2.53}$$

The equations of motion are then

$$\dot{\vec{X}}_H = \mathbf{J} \left(\frac{\partial H_{\text{nat}}}{\partial \vec{X}_H} \right)^T, \tag{2.54}$$

where

$$\mathbf{J} = \begin{bmatrix} \mathbf{0}_{3 \times 3} & \mathbf{I}_{3 \times 3} \\ -\mathbf{I}_{3 \times 3} & \mathbf{0}_{3 \times 3} \end{bmatrix} \quad (2.55)$$

is an orthogonal and skew-symmetric matrix, i.e., $\mathbf{J}^{-1} = \mathbf{J}^T = -\mathbf{J}$. Although these equations leverage a different basis (i.e., the generalized coordinates and generalized momenta) than the Newtonian derivation to describe the dynamics, they are identical to Equations (2.25) – (2.27). Additionally, by employing the Hamiltonian basis and constructing the Hamiltonian, it is immediately clear that H_{nat} is an integral for Equation (2.54) as H_{nat} does not depend on time. In other words, H_{nat} is constant along solutions of Equation (2.54). When scaled by negative two, H_{nat} is equal to the *Jacobi constant*,

$$C = -2H_{\text{nat}}. \quad (2.56)$$

In this investigation, the Hamiltonian is preferred as an integral because it is slightly more intuitive than the Jacobi constant. For example, a Hamiltonian change $\Delta H_{\text{nat}} > 0$ corresponds to an increase in energy but a similar change in the Jacobi constant, $\Delta C > 0$, corresponds to a *decrease* in energy. Regardless of the scaling, the Hamiltonian or Jacobi values are commonly employed to parameterize dynamical structures in the CR3BP.

While the Hamiltonian basis is employed to deliver many dynamical systems results, it is frequently useful to represent the dynamics in a more intuitive basis, i.e., the “Lagrangian basis” employed in the Newtonian approach. In this case, the state vector is denoted

$$\vec{X} = \vec{X}_{\mathcal{L}} = \begin{Bmatrix} \vec{q} \\ \dot{\vec{q}} \end{Bmatrix} = \left\{ x \quad y \quad z \quad \dot{x} \quad \dot{y} \quad \dot{z} \right\}^T, \quad (2.57)$$

where the \mathcal{L} subscript denotes the Lagrangian basis; in most other sections of this document the \mathcal{L} is omitted for brevity as the Lagrangian basis is the default state representation. The generalized momenta can be written in terms of the generalized

coordinates and their derivatives, as in Equation (2.40). When \vec{q} and $\dot{\vec{q}}$ are substituted into Equation (2.46), the natural Hamiltonian is evaluated as

$$\begin{aligned} H_{\text{nat}}(\vec{q}, \dot{\vec{q}}) &= \frac{1}{2} (\dot{q}_1^2 + \dot{q}_2^2 + \dot{q}_3^2) - \frac{1}{2} (q_1^2 + q_2^2) - \frac{1-\mu}{r_{13}} - \frac{\mu}{r_{23}} \\ &= \frac{1}{2} \dot{\vec{q}} \cdot \dot{\vec{q}} - \Omega(\vec{q}). \end{aligned} \quad (2.58)$$

Consistent with the Hamiltonian written in terms of the generalized momenta, the first term in Equation (2.58) represents the kinetic energy of P_3 viewed in the \mathbb{R} rotating frame, the second term incorporates the motion of the frame, and the third and fourth terms capture the potential energy from the gravity fields. However, in contrast to Equation (2.46), the kinetic energy term is expressed in terms of the *rotating* velocity coordinates and the “energy” associated with the rotating frame is written as a function of only the rotating position coordinates. Because the analyses in this investigation are performed in the rotating frame, this representation of the Hamiltonian is employed.

By leveraging the relationship between the generalized momenta and the generalized coordinates in Equation (2.40), dynamical quantities are straightforwardly transformed between the Hamiltonian and Lagrangian bases [42]. First, write the relationship between the generalized momenta and the generalized coordinates more compactly,

$$\vec{p} = \dot{\vec{q}} + \tilde{\omega}\vec{q}. \quad (2.59)$$

Next, this relationship between \vec{p} and \vec{q} is incorporated into the \mathbf{T}_ω transformation matrix to relate vectors in the two bases,

$$\vec{X}_H = \mathbf{T}_\omega \vec{X}_L, \quad (2.60)$$

where

$$\mathbf{T}_\omega = \begin{bmatrix} \mathbf{I}_{3 \times 3} & \mathbf{0}_{3 \times 3} \\ \tilde{\omega} & \mathbf{I}_{3 \times 3} \end{bmatrix}. \quad (2.61)$$

This matrix is invertible,

$$\mathbf{T}_\omega^{-1} = \mathbf{T}_{-\omega}, \quad (2.62)$$

where $\mathbf{T}_{-\omega}$ replaces the $\tilde{\omega}$ submatrix with $-\tilde{\omega}$. Thus, the Lagrangian form of the state vector is also straightforwardly available from the Hamiltonian form,

$$\vec{X}_\mathcal{L} = \mathbf{T}_{-\omega} \vec{X}_H. \quad (2.63)$$

The partial derivatives of the Hamiltonian with respect to the state vectors are similarly related,

$$\frac{\partial H_{\text{nat}}}{\partial \vec{X}_H} = \mathbf{T}_{-\omega}^T \left(\frac{\partial H_{\text{nat}}}{\partial \vec{X}_\mathcal{L}} \right)^T. \quad (2.64)$$

Accordingly, the equations of motion in the Hamiltonian basis are available from the Lagrangian basis,

$$\dot{\vec{X}}_H = \mathbf{J} \mathbf{T}_{-\omega}^T \left(\frac{\partial H_{\text{nat}}}{\partial \vec{X}_\mathcal{L}} \right)^T. \quad (2.65)$$

Transforming the right side of this relationship also yields a matrix form for the governing equations expressed in the Lagrangian basis,

$$\dot{\vec{X}}_\mathcal{L} = \mathbf{T}_{-\omega} \mathbf{J} \mathbf{T}_{-\omega}^T \left(\frac{\partial H_{\text{nat}}}{\partial \vec{X}_\mathcal{L}} \right)^T. \quad (2.66)$$

When expanded, these equations of motion are identical to those derived via the Newtonian approach,

$$\dot{\vec{X}}_{\mathcal{L}} = \begin{bmatrix} \mathbf{0}_{3 \times 3} & \mathbf{I}_{3 \times 3} \\ -\mathbf{I}_{3 \times 3} & -2\tilde{\omega} \end{bmatrix} \begin{Bmatrix} -\frac{\partial \Omega}{\partial \vec{q}} \\ \dot{\vec{q}} \end{Bmatrix} = \begin{Bmatrix} \dot{\vec{q}} \\ \frac{\partial \Omega}{\partial \vec{q}} - 2\tilde{\omega}\dot{\vec{q}} \end{Bmatrix} \quad (2.67)$$

$$= \begin{Bmatrix} \dot{x} \\ \dot{y} \\ \dot{z} \\ 2\dot{y} + x - (1 - \mu)(x + \mu)/r_{13}^3 - \mu(x - 1 + \mu)/r_{23}^3 \\ -2\dot{x} + y - (1 - \mu)y/r_{13}^3 - \mu y/r_{23}^3 \\ -(1 - \mu)z/r_{13}^3 - \mu z/r_{23}^3 \end{Bmatrix}. \quad (2.68)$$

Because these equations cannot be analytically integrated, a numerical integration scheme is employed (see Appendix A for details). Given an initial condition, $\vec{X}_{\mathcal{L}}(\tau_0)$, and some time-of-flight, the $\vec{X}_{\mathcal{L}}$ vector is propagated according to these governing equations. Subsequently, motion throughout the CR3BP may be quantified and analyzed for trajectory design applications.

2.2 CR3BP Incorporating Low Thrust

To gain insights and produce dynamical structures for low-thrust trajectory design in multi-body regimes, the CR3BP dynamics are augmented with the force delivered by a low-thrust propulsion system. Additionally, the spacecraft mass is modeled as a time-varying function to incorporate the effects of propellant expulsion during thrust events. Similar to the CR3BP derivation, both a Newtonian and a Hamiltonian approach are employed to write the governing equations and explore the dynamics of the system. A time-varying low-thrust Hamiltonian is constructed to supply additional insight, and several control strategies are explored. One strategy incorporates assumptions that yield an autonomous system; the dynamics associated with this sim-

plified model are investigated to provide further guidance for preliminary low-thrust trajectory design.

2.2.1 Newtonian Derivation

Consistent with the ballistic CR3BP, the motion of the spacecraft is described by Newton's second law. It is reprinted here for convenience,

$$\sum \vec{F}_{\text{ext}} = \frac{d^i \vec{\mathcal{P}}_3}{dt}. \quad (2.3)$$

The ballistic gravitational forces acting on the spacecraft are augmented with a low-thrust force, yielding a CR3BP model with low-thrust (CR3BP+LT). To derive an expression for this propulsive force, consider a spacecraft at two times: t and $t + dt$ where dt is some infinitesimal time differential.³ At the initial time, depicted in Figure 2.2(a), the spacecraft mass is M_3 and the velocity as observed in the inertial frame is $\vec{V}_3 = d^i \vec{R}_3 / dt$. Accordingly, the momentum of the spacecraft at time t is

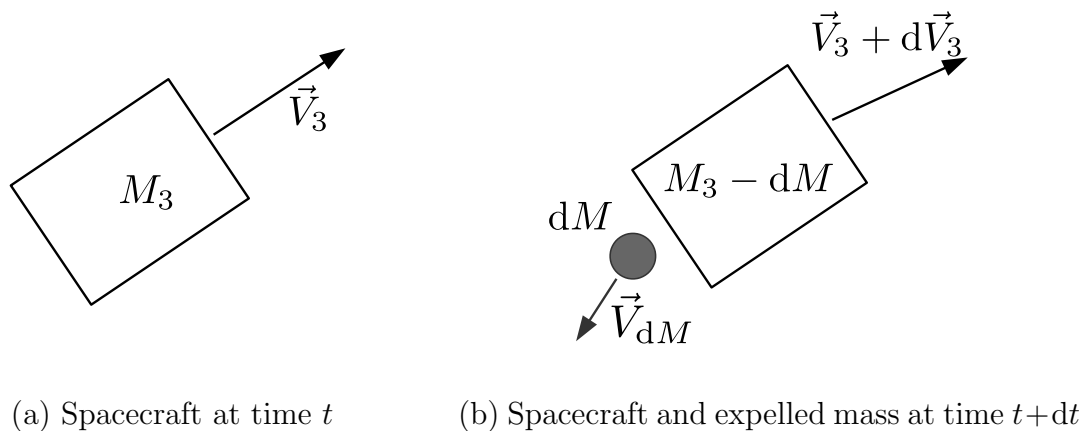


Figure 2.2.: Low-thrust force free body diagrams

$$\vec{\mathcal{P}}_3(t) = M_3 \vec{V}_3. \quad (2.69)$$

³Thanks to Rolfe Power for motivating and assisting with this derivation!

After some infinitesimal time, dt , a small portion of the spacecraft mass, dM , has been expelled by the propulsion system, affecting the spacecraft velocity by $d\vec{V}_3$; similarly, the expelled mass possesses the velocity, \vec{V}_{dM} . Thus, the momentum of the spacecraft and the expelled propellant at time $t + dt$ is

$$\vec{\mathcal{P}}_3(t + dt) = (M_3 - dM)(\vec{V}_3 + d\vec{V}_3) + dM\vec{V}_{dM}. \quad (2.70)$$

The momentum change between the two times is

$$d\vec{\mathcal{P}}_3 = \vec{\mathcal{P}}_3(t + dt) - \vec{\mathcal{P}}_3(t) \quad (2.71)$$

$$= -dM\vec{V}_3 + M_3 d\vec{V}_3 - dM d\vec{V}_3 + dM\vec{V}_{dM}. \quad (2.72)$$

Because dM and $d\vec{V}_3$ are both infinitesimal, their product is assumed to be zero. Substituting the resulting momentum differential into Equation (2.3) yields the expression,

$$\sum \vec{F}_{\text{ext}} = \frac{M_3 d\vec{V}_3}{dt} + \frac{(\vec{V}_{dM} - \vec{V}_3) dM}{dt}. \quad (2.73)$$

The first momentum term on the right side of the equation is the familiar mass times acceleration expression, i.e., $M_3 d\vec{V}_3/dt = M_3 \vec{A}_3$, where \vec{A}_3 is the acceleration of the spacecraft. The second term in the equation is the thrust force; the velocity of the expelled mass relative to the spacecraft is the *exhaust velocity*, $\vec{V}_e = \vec{V}_{dM} - \vec{V}_3$, resulting in the equation for the thrust force,

$$\vec{F}_{\text{thrust}} = -\vec{V}_e \frac{dM}{dt}. \quad (2.74)$$

Rearranging Equation (2.73) results in the vector differential equation,

$$M_3 \frac{d\vec{V}_3}{dt} = M_3 \frac{d^2 \vec{R}_3}{dt^2} = \sum \vec{F}_{\text{ext}} = \vec{F}_{\text{grav}} + \vec{F}_{\text{thrust}}. \quad (2.75)$$

Substitute the gravitational forces, \vec{F}_{grav} , and solve for the spacecraft acceleration vector, i.e.,

$$\frac{d^2 \vec{R}_3}{dt^2} = -G \left(\frac{M_1}{R_{13}^3} \vec{R}_{13} + \frac{M_2}{R_{23}^3} \vec{R}_{23} \right) + \frac{1}{M_3} \vec{F}_{\text{thrust}}. \quad (2.76)$$

When this expression is nondimensionalized using the same procedure as discussed in Section 2.1.1, the thrust force is multiplied by the ratio T_*/L_* . For consistency with the other terms in the equations of motion, nondimensional equivalents are introduced:

$$f = \frac{F_{\text{thrust}}}{M_{3,0}} \left(\frac{T_*^2}{L_*} \right), \quad (2.77)$$

$$m = M_3/M_{3,0}, \quad (2.78)$$

where $M_{3,0}$ is the initial spacecraft mass (i.e., the wet mass), f is the nondimensional thrust magnitude, and m is the nondimensional spacecraft mass. The F_{thrust} value is measured in kilonewtons while M_3 and $M_{3,0}$ are measured in kilograms. The thrust term in Equation (2.76) is rewritten as a nondimensional acceleration,

$$\frac{1}{M_3} \vec{F}_{\text{thrust}} \rightarrow \vec{a}_{\text{lt}} = a_{\text{lt}} \hat{a}_{\text{lt}} = \frac{f}{m} \hat{a}_{\text{lt}}, \quad (2.79)$$

where \vec{a}_{lt} is the low-thrust acceleration vector, which can be decomposed into an acceleration magnitude, a_{lt} , and the acceleration orientation unit vector, \hat{a}_{lt} . A nondimensional thrust magnitude of $f \approx 1\text{e-}2$ in the Earth-Moon and Sun-EMB (Earth-Moon barycenter) CR3BP+LT systems is consistent with current spacecraft capabilities, as listed in Table 2.1 (see Table B.2 for additional spacecraft parameters). Accordingly, a nondimensional f value on the order of $1\text{e-}2$ is frequently employed in this investigation to represent a reasonable low-thrust capability in the Earth-Moon and Sun-EMB systems.

In addition to equations governing the spacecraft acceleration, an equation that models the spacecraft mass over time is required. Several strategies exist to model the mass history and are discussed in later sections. Let the mass rate equation

Table 2.1.: Low-thrust system comparison

Spacecraft	$M_{3,0}$ [kg]	F_{thrust} [mN]	a_{lt} [mm/s ²]	f [nondim]	
				Earth-Moon	Sun-EMB
Deep Space 1 [43]	486	92.0	1.9e-1	7.0e-2	3.2e-2
Hayabusa [44]	510	22.8	4.7e-2	1.6e-2	7.5e-3
Hayabusa 2 [44]	609	27.0	4.4e-2	1.6e-2	7.5e-3
Dawn [45]	1218	91.0	7.6e-2	2.7e-2	1.3e-2
Lunar IceCube [6]	14	1.15	7.1e-2	3.0e-2	1.4e-2

temporarily be written as an arbitrary function, $\dot{m}(\cdot)$. The full set of differential equations governing the motion of P_3 in the CR3BP+LT is then

$$\ddot{x} - 2\dot{y} = \Upsilon_x = x - (1 - \mu)\frac{x + \mu}{r_{13}^3} - \mu\frac{x - 1 + \mu}{r_{23}^3} + \vec{a}_{\text{lt}} \cdot \hat{x}, \quad (2.80)$$

$$\ddot{y} + 2\dot{x} = \Upsilon_y = y - (1 - \mu)\frac{y}{r_{13}^3} - \mu\frac{y}{r_{23}^3} + \vec{a}_{\text{lt}} \cdot \hat{y}, \quad (2.81)$$

$$\ddot{z} = \Upsilon_z = -(1 - \mu)\frac{z}{r_{13}^3} - \mu\frac{z}{r_{23}^3} + \vec{a}_{\text{lt}} \cdot \hat{z}, \quad (2.82)$$

$$\dot{m} = \dot{m}(\cdot), \quad (2.83)$$

where Υ is the low-thrust pseudopotential function,

$$\Upsilon = \frac{1}{2}(x^2 + y^2) + \frac{1 - \mu}{r_{13}} + \frac{\mu}{r_{23}} + \vec{a}_{\text{lt}} \cdot \vec{r} = \Omega + \vec{a}_{\text{lt}} \cdot \vec{r}, \quad (2.84)$$

and Υ_x , Υ_y and Υ_z are the partial derivatives of Υ with respect to the position states. The low-thrust pseudopotential may also be expressed by augmenting the ballistic pseudopotential, Ω , defined in Equation (2.30), with the dot product of the low-thrust acceleration and the spacecraft position vector. The substitution $\vec{r} = \vec{r}_3$ is introduced to simplify the notation as this investigation is focused on the motion of P_3 .

Consistent with the CR3BP, the equations that govern the motion of a spacecraft in the CR3BP+LT are not analytically integrable and are evaluated via numerical integration. For a complete representation of the spacecraft state in the low-thrust

model, the state vector is constructed to include the position vector, velocity vector, and mass, as well as a set of control states that define the low-thrust acceleration vector, \vec{a}_{lt} . If all of these quantities are independent, the problem dimension is 10, dramatically increasing the complexity in comparison to the ballistic CR3BP. Accordingly, one of the primary goals of this investigation is to employ control strategies or other simplifying assumptions that decrease the number of independent variables and enable more intuitive trajectory design. An understanding of the natural Hamiltonian in the CR3BP+LT leads to several relevant control strategies and simplifications to achieve this goal.

2.2.2 Perturbing Accelerations Survey

Before examining the properties of the CR3BP+LT, a survey of the most significant perturbing accelerations is conducted. In the CR3BP+LT derivation, all forces acting on the spacecraft other than the gravitational acceleration of the two primaries and the low-thrust acceleration delivered by the propulsion system are ignored. To understand and validate this assumption, it is useful to inspect the low-thrust acceleration magnitudes within the context of other perturbing accelerations. The acceleration applied to a spacecraft, measured relative to some central body, is available from the equation,

$$\frac{{}^i d^2 \vec{R}_{cs}}{dt^2} = -G \frac{M_c + M_s}{R_{cs}^3} \vec{R}_{cs} + GM_p \left(\frac{\vec{R}_{pc}}{R_{pc}^3} - \frac{\vec{R}_{ps}}{R_{ps}^3} \right) + G \sum_{j=1}^k M_j \left(\frac{\vec{R}_{jc}}{R_{jc}^3} - \frac{\vec{R}_{js}}{R_{js}^3} \right) \quad (2.85)$$

$$= \vec{A}_c + \vec{A}_p + \sum_{j=1}^k \vec{A}_j \quad (2.86)$$

where \vec{R}_{cs} locates the spacecraft, s , relative to the central body, c . As the focus of this investigation is the CR3BP+LT, the central body is selected to be one of the two primaries. The acceleration imparted to the spacecraft by the other primary body is captured by the second set of terms in Equation (2.85); the p subscript represents

this “non-central” primary body. Finally, the accelerations delivered by an arbitrarily large set of k extra perturbing bodies is included in the summation. The masses of the bodies are written as M_c , M_s , M_p , and M_j ; the spacecraft mass, M_s , is assumed to be negligible in comparison to M_c . Written more compactly, the acceleration on the spacecraft (as seen by an inertial observer) is the sum of the central body term, \vec{A}_c , the non-central body term, \vec{A}_p , and the perturbing terms, \vec{A}_j , for $j = 1, \dots, k$. The central body and non-central body terms are combined into a single acceleration vector, $\vec{A}_{c+p} = \vec{A}_c + \vec{A}_p$, to represent the CR3BP acceleration (note that the centripetal acceleration terms from the rotating reference frame are not included).

To construct a general representation of the accelerations delivered throughout the CR3BP+LT regime, a grid of spacecraft states in the xy -plane of the rotating frame are employed. Additionally, the accelerations at each grid point are computed over a range of equally-spaced times between January 1, 2020 and January 1, 2030. The magnitude of the acceleration vector at each point and date is computed and then averaged over time to deliver an average acceleration magnitude for each grid point. These acceleration magnitudes are then plotted as a surface in the rotating frame that is defined by the central and non-central body. For example, the magnitude of the acceleration acting on a spacecraft due to the gravity of the Earth and Moon (i.e., $\|\vec{A}_{c+p}\|$), plotted in Figure 2.3, has peaks at the locations of the Earth and the Moon and a local minimum at a point between the two bodies where the gravitational accelerations sum to zero. Because these accelerations do not include the rotation of the frame, this zero acceleration point (also called a *gravitational saddle point* [46]) is not collocated with the libration points (marked by vertical blue lines). The average magnitude of the solar gravity perturbation in the Earth-Moon rotating frame, depicted by the orange surface, is approximately one order of magnitude smaller than the Earth and Moon gravitational accelerations at the limits of the grid ($x = \pm 2$ and $y = \pm 2$), but the solar gravity is several orders of magnitude less significant than the Earth and Moon gravity when the spacecraft is near either of the primaries. Finally, the acceleration magnitudes delivered by Deep Space 1 (DS1), Hayabusa, and Lunar

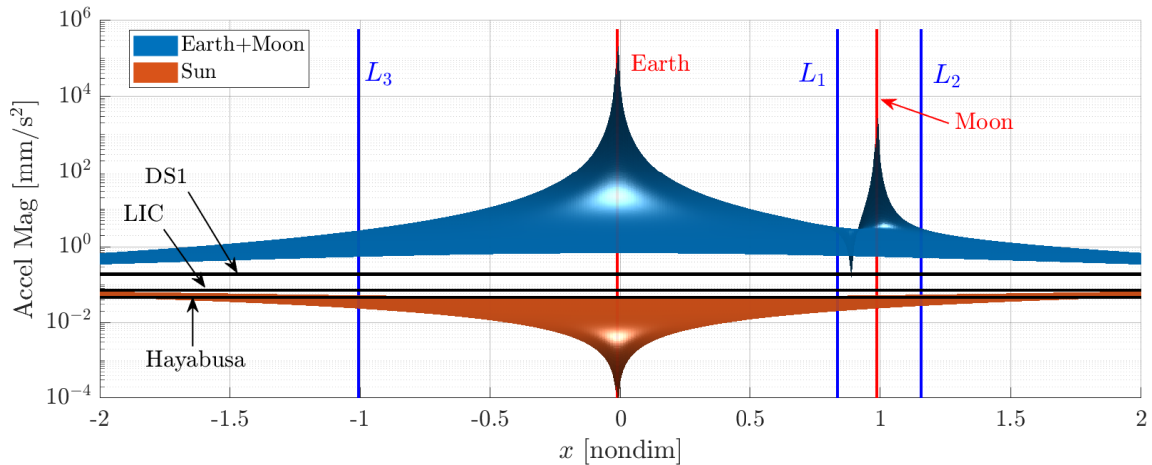


Figure 2.3.: Comparison of acceleration magnitudes near the Earth, viewed in the Earth-Moon rotating frame

IceCube (LIC), plotted as black lines, are generally smaller than the Earth and Moon gravitational accelerations but similar to the solar perturbation, particularly when the spacecraft is far from the Earth and Moon. This result suggests that the design techniques and dynamical structures developed in this investigation for low-thrust applications may also be employed in a model that combines the Sun, Earth, and Moon gravity. This result also reveals that a high-fidelity analysis for low-thrust trajectory design should include the solar gravity perturbation. Regardless, the inclusion of solar gravity in the Earth-Moon system is beyond the scope of this work; only the low-thrust perturbation to the CR3BP is incorporated.

A similar analysis is conducted in the Sun-EMB system. These results, plotted in Figure 2.4, compare the accelerations imparted to a spacecraft located near the Earth due to the combined gravitational pull of the Sun, Earth, and Moon (Sun+EMB) as well as the gravitational accelerations delivered by Jupiter, Saturn, and Venus. Consistent with the Earth-Moon results, these accelerations are averaged over the decade between 2010 and 2020. The Sun+EMB acceleration magnitude peaks at the location of the Earth-Moon Barycenter (EMB) and includes a minimum at a nearby saddle point that is located within the Moon's orbit (a radius of about 0.005 nondimensional units in the Sun-EMB system). The perturbing accelerations of Jupiter, Saturn, and

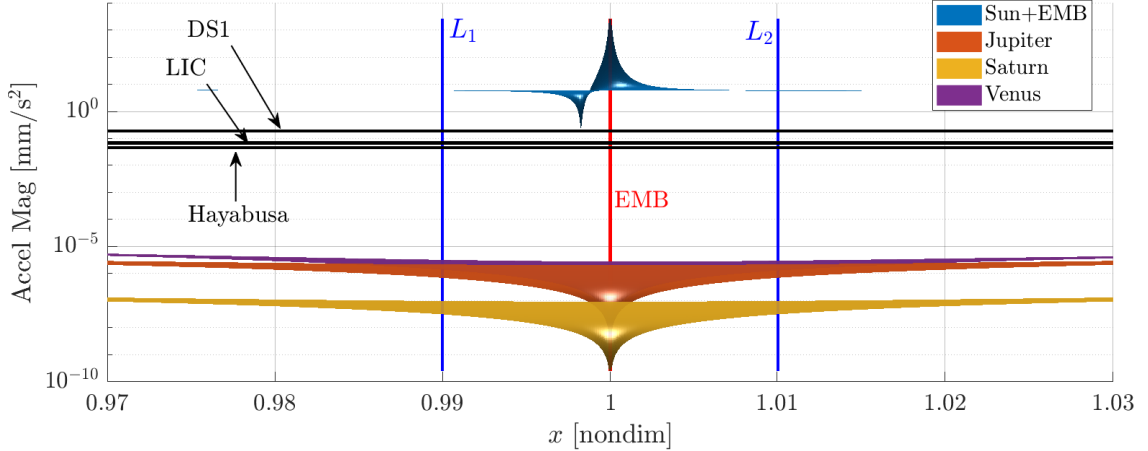


Figure 2.4.: Comparison of acceleration magnitudes near the Earth-Moon Barycenter, viewed in the Sun-EMB rotating frame

Venus are considerably smaller than the Sun, EMB, and low-thrust accelerations. Accordingly, in contrast to the Earth-Moon CR3BP+LT, the Sun-EMB CR3BP+LT is accurately modeled without incorporating extra perturbing accelerations.

A final perturbing acceleration to consider is solar radiation pressure (SRP). The acceleration of a spacecraft due to SRP varies with the Sun-facing area of the spacecraft, its reflectivity properties, as well as with the distance from the Sun. For the sake of a simple comparison, consider an SRP acceleration of $8.7e-5$ mm/s², computed for a 1100 kg GPS IIR satellite at 1 AU [47]. Four orders of magnitude smaller than the low-thrust acceleration, the SRP may be neglected.

2.2.3 The Perturbed Natural Hamiltonian

Returning to a dynamical systems analysis in the CR3BP+LT, recall that the natural Hamiltonian, H_{nat} , is constant in the ballistic problem, supplying an integral of the motion. However, when a low-thrust force is added to the model, H_{nat} is not generally constant. In other words, H_{nat} is not a dynamically significant quantity in the CR3BP+LT. Nevertheless, as thrust is frequently applied to *change* the energy along a trajectory, the variations in H_{nat} may be beneficial. To facilitate informed

preliminary design decisions, it is important to understand the relationships between the natural Hamiltonian and the low-thrust force. This information is available from the time derivative of the natural Hamiltonian, expressed here in terms of the Cartesian coordinates and the pseudopotential spatial gradient rather than the generalized coordinates and momenta,

$$\dot{H}_{\text{nat}} = \frac{dH_{\text{nat}}}{d\tau} = \dot{x}(\ddot{x} - \Omega_x) + \dot{y}(\ddot{y} - \Omega_y) + \dot{z}(\ddot{z} - \Omega_z). \quad (2.87)$$

Substitute the CR3BP+LT equations of motion (2.80) – (2.83) for the terms within the parentheses and simplify:

$$\dot{H}_{\text{nat}} = \dot{x}(2\dot{y} + \vec{a}_{\text{lt}} \cdot \hat{x}) + \dot{y}(-2\dot{x} + \vec{a}_{\text{lt}} \cdot \hat{y}) + \dot{z}\vec{a}_{\text{lt}} \cdot \hat{z} = \vec{v} \cdot \vec{a}_{\text{lt}}, \quad (2.88)$$

where $\vec{v} = \{\dot{x} \ \dot{y} \ \dot{z}\}^T$ is the spacecraft velocity vector in the rotating frame. This simple result supplies significant insight that may be applied when designing a control strategy, i.e., when constructing a preliminary time history for \vec{a}_{lt} . The dot product in Equation (2.88) expands to

$$\vec{v} \cdot \vec{a}_{\text{lt}} = \|\vec{v}\| \|\vec{a}_{\text{lt}}\| \cos \psi = va_{\text{lt}} \cos \psi, \quad (2.89)$$

where ψ is the angle between the \vec{v} and \vec{a}_{lt} vectors. This relationship delivers several insights:

1. The magnitude of \dot{H}_{nat} is greatest when the velocity magnitude, v , is greatest. That is, thrust applied when the velocity magnitude is large will yield a larger energy change than the same thrust applied when the velocity magnitude is smaller. This result is analogous to the Oberth effect [48].
2. The magnitude of \dot{H}_{nat} is greatest when the low-thrust acceleration magnitude is greatest. This result is intuitive; applying a larger acceleration delivers a larger energy change.

3. The magnitude of \dot{H}_{nat} is greatest when the velocity vector (as seen in the *rotating* frame, \mathbb{R}) and the low-thrust acceleration vector are parallel or anti-parallel, i.e., when $\cos\psi = \pm 1$. This result is also consistent with intuition; accelerating along the velocity vector will increase the magnitude of the velocity most rapidly and therefore increase the kinetic energy, one of the components of the Hamiltonian, most rapidly. Similarly, thrusting along the anti-velocity vector ($-\vec{v}$) will decrease the magnitude of the velocity most rapidly.

The first insight provides some guidance when planning the timing or location of maneuvers. If changing the energy, i.e., the H_{nat} value, of a trajectory is the design goal, implementing a low-thrust burn when the spacecraft velocity magnitude is large (e.g., during a flyby of one of the primaries) may be beneficial. Alternatively, if the energy is to be conserved, implementing a low-thrust maneuver when the velocity magnitude is small may enable changes to the trajectory geometry without significantly affecting the energy. The third insight is useful when designing the orientation of the low-thrust acceleration vector. If a large energy increase or decrease is required, the \vec{a}_{lt} vector may be aligned with the \vec{v} or $-\vec{v}$ directions. Alternatively, a low-thrust acceleration vector orientation that results in $\cos\psi = 0$ yields a constant H_{nat} value. Such a control strategy may be leveraged to manipulate the geometry of a trajectory while maintaining the energy. In the next section, several control parameterizations are explored, including strategies that leverage these insights.

2.2.4 Pseudo-Separable Control Parameterization

The orientation and magnitude of the low-thrust acceleration vector are common design variables in low-thrust mission design problems. In fact, the selection of these variables is frequently one of the largest challenges in low-thrust trajectory design as the effects of those variables on the evolution of the trajectory are not well defined. Although it is difficult to predict changes in the geometry of a trajectory (a 6D quantity) due to low-thrust, the impact of the additional force on the energy, i.e., the

Hamiltonian (a 1D quantity), associated with the trajectory is more straightforward. Accordingly, several control strategies are developed to accomplish specific energy goals.

To facilitate the analysis of many different low-thrust control strategies in the CR3BP multi-body environment, a “pseudo-separable” control parameterization is adopted. Recall the definition for the low-thrust acceleration vector,

$$\vec{a}_{1t} = \frac{f}{m} \hat{a}_{1t}. \quad (2.79)$$

The thrust magnitude, f , spacecraft mass, m , and acceleration orientation, \hat{a}_{1t} , are pseudo-separable, i.e., the values of these values are partially or completely independent. Three *control policy* types are defined:

Thrust Magnitude Policy – Supplies the thrust magnitude, f , and an expression that governs the evolution of f , i.e., \dot{f} .

Mass Policy – Supplies the spacecraft mass, m , and a representation of its evolution, i.e., \dot{m} .

Orientation Policy – Supplies the orientation vector, \hat{a}_{1t} , and a vector definition of its evolution, i.e., $\dot{\hat{a}}_{1t}$.

The control state vector, \vec{u} , may be similarly separated into three vector components associated with the policies,

$$\vec{u} = \left\{ \vec{u}_f^T \quad \vec{u}_m^T \quad \vec{u}_o^T \right\}^T, \quad (2.90)$$

where \vec{u}_f , \vec{u}_m , and \vec{u}_o are the control states associated with the thrust magnitude, mass, and orientation policies. Because all of the control policies employed in this investigation rely on constant control states, i.e., $\dot{\vec{u}} = \vec{0}$, or on the spacecraft position or velocity states, the \vec{u} vector is excluded from the state vector and the control “states” are treated as *parameters* instead. This separation effectively reduces the problem dimension by three, leaving the spacecraft position, velocity, and mass as

the only independent states. When differential corrections algorithms are applied, the control parameters may be included in the design variable vector. Thus, the definitions of the \vec{u} components are omitted from this section, which focuses on the dynamics, and are included in later chapters when relevant to differential corrections processes.

To fully define the low-thrust control strategy, a thrust magnitude policy, a mass policy, and an orientation policy are selected from the available options. In general, the thrust magnitude and orientation are completely independent (i.e., separable) of the spacecraft mass and of each other. On the other hand, the spacecraft mass evolution frequently depends on the thrust magnitude. Some specific policies employed in this investigation are detailed below.

Thrust Magnitude Policy

Throughout this investigation, the thrust magnitude is held constant. Thus, only one thrust magnitude policy is employed:

$$\dot{f} = 0. \quad (2.91)$$

As a result, the acceleration magnitude, $a_{lt} = f/m$, is a function of only one variable, the spacecraft mass, m .

Mass Policies

Two policies are leveraged to model the spacecraft mass:

- **Variable Mass Policy** The first policy sets the mass rate, \dot{m} , to a constant value via the relationship,

$$\dot{m} = \frac{-f}{I_{sp}g_0} \left(\frac{L_*}{T_*} \right), \quad (2.92)$$

where the specific impulse, I_{sp} , is a constant measured in seconds, and $g_0 = 9.80665\text{e-}03 \text{ km/s}^2$ is the mean Earth gravitational acceleration. Specific impulse values for low-thrust propulsion systems are generally high, ranging from 1900 to over 3000 seconds (see Table B.2). The I_{sp} is assumed to be constant in this investigation; accordingly, this strategy is termed a *constant specific impulse* (CSI) formulation.

- **Constant Mass Policy** A second mass policy holds the spacecraft mass constant, i.e.,

$$\dot{m} = 0. \quad (2.93)$$

Although a constant mass is not consistent with existing propulsion technologies, the mass rate in Equation (2.92) is generally very small and m may be reasonably approximated as a constant, at least for relatively short times-of-flight. The definitions of “very small” and “relatively short” vary depending on the specific impulse and on the multi-body dynamics; the validity of this constant-mass assumption is later explored for a number of systems.

In either mass policy, the mass rate, \dot{m} , is a constant. As such, the mass equation of motion, Equation (2.83), is easily integrated analytically,

$$m(\tau) = m(\tau_0) + \dot{m}\tau. \quad (2.94)$$

This equation is then incorporated directly into the equations of motion (EOMs), i.e.,

$$\vec{a}_{\text{lt}}(\vec{X}, \tau) = \frac{f}{m(\tau_0) + \dot{m}\tau} \hat{a}_{\text{lt}}(\vec{X}, \tau), \quad (2.95)$$

where \vec{X} is the spacecraft state in the Lagrangian basis, as defined in Equation (2.57).

This substitution removes mass from the states that must be numerically integrated

but also adds an explicit time dependency to the EOMs. Alternatively, mass may be retained in a seven-element “low-thrust state vector”, $\vec{X}_{\text{lt}} = \{\vec{X}^T \quad m\}^T$, yielding

$$\vec{a}_{\text{lt}}(\vec{X}_{\text{lt}}, \tau) = \frac{f}{m} \hat{a}_{\text{lt}}(\vec{X}_{\text{lt}}, \tau). \quad (2.96)$$

In practical terms, the results (e.g., from numerical integration of the governing equations) of the two approaches are identical. However, the former method is preferred from a dynamical systems perspective as it reduces the number of state variables from seven to six and explicitly communicates the time-dependence of the dynamics. Furthermore, the system with seven states cannot be fully represented by Hamilton’s canonical equations and, subsequently, is more difficult to analyze via dynamical systems techniques.

Orientation Policies

In addition to the thrust magnitude and mass policies, an orientation policy is required to specify the pointing direction for the low-thrust acceleration vector. Let the orientation of the acceleration vector in the rotating frame, \hat{a}_{lt} , be defined by two angles, α and β , via the expression,

$$\hat{a}_{\text{lt}} = \left\{ \cos(\alpha) \cos(\beta) \quad \sin(\alpha) \cos(\beta) \quad \sin(\beta) \right\}^T \quad (2.97)$$

where α measures the orientation of the planar projection of \hat{a}_{lt} relative to \hat{x} , and β measures the angle between the planar projection and \hat{a}_{lt} , as illustrated in Figure 2.5. In this investigation, the two angles are described within the ranges $\alpha \in [-\pi, \pi]$ and $\beta \in [-\pi/2, \pi/2]$. A variety of strategies, discussed below, are available to control these orientation angles.

- **Velocity-Aligned Orientation** As discussed in Section 2.2.3, the natural Hamiltonian rate is related to the dot product between the velocity vector

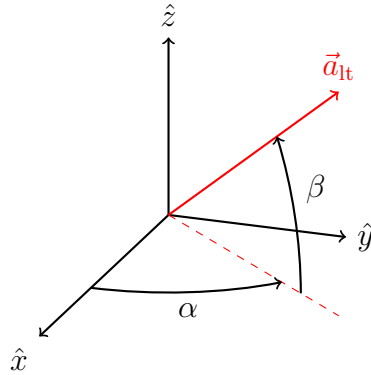


Figure 2.5.: The orientation of the low-thrust acceleration vector relative to the rotating frame

observed in the rotating frame, \vec{v} , and the low-thrust acceleration vector. Accordingly, a strategy to extremize \dot{H}_{nat} is summarized by the expressions,

$$\hat{a}_{1t} = \vec{v}/\|\vec{v}\|, \quad (2.98)$$

$$\hat{a}_{1t} = -\vec{v}/\|\vec{v}\|. \quad (2.99)$$

As these equations are functions only of the velocity states, no control states are required to model the thrust orientation.

- **Velocity-Perpendicular Orientation** In addition to revealing a control strategy to extremize \dot{H}_{nat} , the natural Hamiltonian rate in Equation (2.88) supplies a method to constrain the H_{nat} value along a low-thrust trajectory. Thrusting in a plane orthogonal to the velocity vector, i.e., $\vec{a}_{1t} \perp \vec{v}$, yields $\dot{H}_{\text{nat}} = 0$, preserving the H_{nat} value along the trajectory despite the time-varying spacecraft mass and \hat{a}_{1t} orientation. This control strategy may be employed to manipulate the geometry of a solution while maintaining the energy required to flow onto a ballistic structure. Similar to the velocity-aligned orientation policy, this policy does not require any control states.

Although the velocity-aligned and velocity-perpendicular orientation policies supply useful trends in the H_{nat} value along a low-thrust trajectory, the orientation of \vec{a}_{1t}

must be continuously adjusted to maintain a consistent relationship to the velocity vector. Depending on the evolution of the velocity vector, these strategies may or may not be feasible. Additionally, a forcing term that is a function of the velocity states, as in the two velocity-relative control strategies, generally results in a dynamical system without many useful simplifications. In many applications, such a continuous control strategy may be discretized as a “turn-and-hold” approach where the orientation of \vec{a}_{1t} is updated at discrete time intervals and held constant in between [49]. Accordingly, it is worthwhile to explore the dynamics of the CR3BP+LT when the \vec{a}_{1t} vector orientation is fixed relative to either the rotating frame, \mathbb{R} , or the inertial frame, \mathbb{I} .

- **Fixed Rotating Orientation** When the orientation of \vec{a}_{1t} is fixed in the rotating frame,

$$\dot{\alpha} = 0, \tag{2.100}$$

$$\dot{\beta} = 0. \tag{2.101}$$

Thus, only the magnitude of the \vec{a}_{1t} vector varies as the spacecraft mass evolves with time (recall that f is treated as a constant). However, these magnitude variations are small due to the low mass flow rates typically associated with low-thrust propulsion systems. If the magnitude of \vec{a}_{1t} is assumed constant while the orientation is held fixed, the CR3BP+LT may be modeled as an autonomous, conservative, Hamiltonian system.

While an orientation fixed in the rotating frame is, in fact, a constantly rotating orientation when viewed from an inertial frame, the rotation rate is constant (or nearly constant, in reality) and can be much smaller than the rate at which the spacecraft velocity vector orientation evolves. For instance, many communications and scientific satellites rotate continuously. Thus, a continuously evolving spacecraft orientation is not infeasible.

- **Fixed Inertial Orientation** Finally, an orientation policy that is commonly applied to inter-planetary low-thrust trajectories fixes the acceleration vector

relative to an inertial frame. Recall that the spacecraft velocity as viewed in the inertial frame is identical to the generalized momenta vector, \vec{p} , expanded in Equations (2.37) – (2.39). Although this direction is constant, the resulting dynamical system is nonautonomous (even if the spacecraft mass is assumed constant) due to the movement of the primaries in the inertial frame. Equivalently, an inertially-fixed thrust direction is a time-varying quantity when viewed in the rotating frame that fixes the locations of the primaries. Because this orientation policy introduces nonautonomous terms in addition to the spacecraft mass, complicating rather than simplifying the dynamics, an inertially-fixed thrust is not explored in this investigation.

By selecting a thrust magnitude policy, a mass policy, and an orientation policy, a fully-parameterized control strategy is constructed for a low-thrust trajectory. The orientation policies that orient \vec{a}_{lt} relative to the rotating velocity vector may be applied to manipulate the H_{nat} value along a trajectory. Similarly, when the fixed orientation policy and the constant mass policy are combined, the H_{lt} value may be held constant. The remainder of the chapter discusses the validity and results of this control strategy.

2.2.5 A Low-Thrust Hamiltonian System

In general, the added complexity of the low-thrust acceleration term in the CR3BP+LT prohibits useful insights from Hamiltonian dynamics. However, the selection of a convenient control parameterization and simplifications to the model reduce the number of states and facilitate a Hamiltonian analysis. As discussed in Section 2.2.4, the magnitude of the low-thrust acceleration vector is assumed a constant. Similarly, the mass flow rate, \dot{m} , is modeled as a constant, yielding a mass equation that is linear in time and removing mass from the state vector. Finally, the orientation policies employed in this work are functions of the spacecraft position and velocity states. As a result, the only states required to model the motion of a spacecraft in

the CR3BP+LT are those states employed to describe the spacecraft position and velocity, i.e., \vec{X} . These simplifications reduce the number of independent variables to six but also introduce an explicit function of time into the equations of motion via the mass equation. Before incorporating further simplifications, the Hamiltonian associated with this low-thrust system is derived and analyzed.

To begin a Hamiltonian analysis of the CR3BP+LT, define the specific kinetic and potential energies associated with the motion of the spacecraft. The kinetic energy expression in Equation (2.42) remains unchanged from the CR3BP, repeated here for reference,

$$\mathcal{T}_{\text{lt}}(\vec{p}) = \mathcal{T} = \frac{1}{2} (p_1^2 + p_2^2 + p_3^2), \quad (2.42)$$

with generalized momenta defined identically as in the CR3BP. The potential energy expression incorporates the low-thrust acceleration term, i.e.,

$$\mathcal{V}_{\text{lt}}(\vec{q}, \vec{p}, \tau) = \frac{-(1-\mu)}{r_{13}} - \frac{\mu}{r_{23}} - \vec{q} \cdot \vec{a}_{\text{lt}}(\vec{q}, \vec{p}, \tau), \quad (2.102)$$

where the low-thrust acceleration vector is written as an explicit function of time as in Equation (2.95); the generalized coordinate definitions are consistent with the CR3BP. The low-thrust term propagates through the derivation to yield a low-thrust Hamiltonian,

$$H_{\text{lt}}(\vec{q}, \vec{p}, \tau) = \frac{1}{2} (p_1^2 + p_2^2 + p_3^2) + p_1 q_2 - p_2 q_1 - \frac{1-\mu}{r_{13}} - \frac{\mu}{r_{23}} - \vec{q} \cdot \vec{a}_{\text{lt}}(\vec{q}, \vec{p}, \tau) \quad (2.103)$$

$$H_{\text{lt}}(\vec{q}, \dot{\vec{q}}, \tau) = \frac{1}{2} (\dot{q}_1^2 + \dot{q}_2^2 + \dot{q}_3^2) - \frac{1}{2} (q_1^2 + q_2^2) - \frac{1-\mu}{r_{13}} - \frac{\mu}{r_{23}} - \vec{q} \cdot \vec{a}_{\text{lt}}(\vec{q}, \dot{\vec{q}}, \tau), \quad (2.104)$$

$$= \frac{1}{2} \dot{\vec{q}} \cdot \dot{\vec{q}} - \Omega(\vec{q}) - \vec{q} \cdot \vec{a}_{\text{lt}}(\vec{q}, \dot{\vec{q}}, \tau), \quad (2.105)$$

$$= \frac{1}{2} \dot{\vec{q}} \cdot \dot{\vec{q}} - \Upsilon(\vec{q}, \dot{\vec{q}}, \tau), \quad (2.106)$$

that may be written in terms of the Hamiltonian basis (i.e., the generalized coordinates and momenta) or in the Lagrangian basis (i.e., the generalized coordinates and

their derivatives). The low-thrust Hamiltonian may also be expressed as a function of the natural Hamiltonian, i.e.,

$$H_{\text{lt}}(\vec{q}, \vec{p}, \tau) = H_{\text{nat}}(\vec{q}, \vec{p}) - \vec{q} \cdot \vec{a}_{\text{lt}}(\vec{q}, \vec{p}, \tau). \quad (2.107)$$

In contrast to the ballistic model, the low-thrust Hamiltonian is not generally constant in the CR3BP+LT due to the time-dependency in the \vec{a}_{lt} vector (i.e., in the mass equation). However, Hamilton's canonical equations may still be applied to yield the equations of motion,

$$\dot{q}_1 = \frac{\partial H_{\text{lt}}}{\partial p_1} = p_1 + q_2 - \vec{q} \cdot \frac{\partial \vec{a}_{\text{lt}}}{\partial p_1}, \quad (2.108)$$

$$\dot{q}_2 = \frac{\partial H_{\text{lt}}}{\partial p_2} = p_2 - q_1 - \vec{q} \cdot \frac{\partial \vec{a}_{\text{lt}}}{\partial p_2}, \quad (2.109)$$

$$\dot{q}_3 = \frac{\partial H_{\text{lt}}}{\partial p_3} = p_3 - \vec{q} \cdot \frac{\partial \vec{a}_{\text{lt}}}{\partial p_3}, \quad (2.110)$$

$$\dot{p}_1 = -\frac{\partial H_{\text{lt}}}{\partial q_1} = p_2 - \frac{1-\mu}{r_{13}^3}(q_1 + \mu) - \frac{\mu}{r_{23}^3}(q_1 - 1 + \mu) + (\vec{a}_{\text{lt}} \cdot \hat{x}) + \vec{q} \cdot \frac{\partial \vec{a}_{\text{lt}}}{\partial q_1}, \quad (2.111)$$

$$\dot{p}_2 = -\frac{\partial H_{\text{lt}}}{\partial q_2} = -p_1 - \frac{1-\mu}{r_{13}^3}q_2 - \frac{\mu}{r_{23}^3}q_2 + (\vec{a}_{\text{lt}} \cdot \hat{y}) + \vec{q} \cdot \frac{\partial \vec{a}_{\text{lt}}}{\partial q_2}, \quad (2.112)$$

$$\dot{p}_3 = -\frac{\partial H_{\text{lt}}}{\partial q_3} = -\frac{1-\mu}{r_{13}^3}q_3 - \frac{\mu}{r_{23}^3}q_3 + (\vec{a}_{\text{lt}} \cdot \hat{z}) + \vec{q} \cdot \frac{\partial \vec{a}_{\text{lt}}}{\partial q_3}. \quad (2.113)$$

The partial derivatives of the low-thrust acceleration vector with respect to the generalized coordinates and momenta are determined by the control policies employed to model the low-thrust system. As the thrust magnitude and mass are modeled independently of the other states, the only nontrivial dependencies are between the orientation vector, \hat{a}_{lt} , and the generalized coordinates and momenta. The values of these dependencies vary by the orientation policy, as noted below.

- **Velocity-Aligned** – The orientation vector is a function of the velocity states, i.e., $\dot{\vec{q}}$. These velocities may be expressed as a function of the generalized coordinates and momenta by rearranging Equation (2.59),

$$\dot{\vec{q}} = \vec{p} - \tilde{\omega}\vec{q}.$$

Thus, the orientation of the low-thrust acceleration vector is a unit vector along $\dot{\vec{q}}$, a function of both the generalized momenta and the generalized coordinates, yielding

$$\frac{\partial \vec{a}_{\text{lt}}}{\partial \vec{p}} = \left(\mathbf{I} \|\dot{\vec{q}}\|^2 - \dot{\vec{q}}\dot{\vec{q}}^T \right) / \|\dot{\vec{q}}\|^3, \quad \frac{\partial \vec{a}_{\text{lt}}}{\partial \vec{q}} = \left(-\dot{\vec{q}}^T \dot{\vec{q}} \tilde{\omega} + \dot{\vec{q}}\dot{\vec{q}}^T \tilde{\omega} \right) / \|\dot{\vec{q}}\|^3$$

- **Velocity-Perpendicular** – Similar to the velocity-aligned case; the partial derivatives are nonzero.
- **Fixed Rotating** – The orientation vector is a function of two constant parameters, α and β ; the partial derivatives all evaluate to zero,

$$\frac{\partial \vec{a}_{\text{lt}}}{\partial \vec{p}} = \frac{\partial \vec{a}_{\text{lt}}}{\partial \vec{q}} = \vec{0}$$

- **Fixed Inertial** – The orientation vector is aligned with the general momenta vector. Thus,

$$\frac{\partial \vec{a}_{\text{lt}}}{\partial \vec{p}} = \left(\mathbf{I} \|\vec{p}\|^2 - \vec{p}\vec{p}^T \right) / \|\vec{p}\|^3, \quad \frac{\partial \vec{a}_{\text{lt}}}{\partial \vec{q}} = \mathbf{0}$$

Accordingly, when the orientation of the low-thrust acceleration vector is fixed in the rotating frame, the dependencies between \vec{a}_{lt} and the generalized coordinates and momenta are trivial (i.e., zeros), removing the partial derivative terms from Equations (2.108) – (2.113). Mathematically, the low-thrust acceleration vector is only a function of time, $\vec{a}_{\text{lt}} = f\hat{a}_{\text{lt}}/m(\tau)$; as a result, the pseudopotential simplifies to a function only

of the generalized coordinates and time, $\Upsilon = \Upsilon(\vec{q}, \tau)$. The equations of motion are concisely represented in matrix form,

$$\dot{\vec{X}}_H = \mathbf{J} \frac{\partial H_{\text{lt}}}{\partial \vec{X}_H}, \quad (2.114)$$

consistent with the CR3BP definitions of \mathbf{J} and \vec{X}_H . The vector EOM in (2.114) is transformed into the Lagrangian basis via the same process as in the CR3BP (see Section 2.1.2),

$$\dot{\vec{X}} = \dot{\vec{X}}_L = \mathbf{T}_{-\omega} \mathbf{J} \mathbf{T}_{-\omega}^T \frac{\partial H_{\text{lt}}}{\partial \vec{X}_L} \quad (2.115)$$

$$= \begin{bmatrix} \mathbf{0} & \mathbf{I} \\ -\mathbf{I} & -2\tilde{\omega} \end{bmatrix} \begin{Bmatrix} -\frac{\partial \Upsilon}{\partial \vec{q}} \\ \dot{\vec{q}} \end{Bmatrix} = \begin{Bmatrix} \dot{\vec{q}} \\ \frac{\partial \Upsilon}{\partial \vec{q}} - 2\tilde{\omega} \dot{\vec{q}} \end{Bmatrix} \quad (2.116)$$

These equations are identical to the Newtonian derivation results, (2.80) – (2.82), with the mass equation explicitly integrated and included in the \vec{a}_{lt} vector.

As in the analysis of the natural Hamiltonian in Section 2.2.3, an investigation of H_{lt} supplies insights that may be applied in the preliminary design process. More specifically, an investigation of the time derivative of H_{lt} reveals control strategies that reduce the complexity of the CR3BP+LT. Recall that the low-thrust Hamiltonian may be represented as an augmented natural Hamiltonian, as in Equation (2.107). The time derivative of the first term, H_{nat} , is available from Equation (2.88) and the derivative of the second term is straightforwardly evaluated,

$$\frac{d}{d\tau} [\vec{q} \cdot \vec{a}_{\text{lt}}] = \dot{\vec{q}} \cdot \vec{a}_{\text{lt}} + \vec{q} \cdot \dot{\vec{a}}_{\text{lt}}. \quad (2.117)$$

Combine Equations (2.88) and (2.117) to yield the time derivative of H_{lt} ,

$$\dot{H}_{\text{lt}} = \frac{dH_{\text{lt}}}{d\tau} = -\vec{q} \cdot \dot{\vec{a}}_{\text{lt}} = -\vec{q} \cdot \left[\left(\frac{\dot{f}m(\tau) - f\dot{m}}{m(\tau)^2} \right) \hat{a}_{\text{lt}} + \frac{f}{m(\tau)} \dot{\hat{a}}_{\text{lt}} \right], \quad (2.118)$$

where $m(\tau)$ is evaluated from Equation (2.94). Clearly the evolution of the low-thrust Hamiltonian depends on the evolution of the control parameters, f and \hat{a}_{lt} , as well as the spacecraft mass, $m(\tau)$. A control strategy that delivers a \dot{H}_{lt} value of zero is of particular interest as the resulting system is conservative and admits an integral of the motion, H_{lt} . Within the context of the control policies defined in this chapter, one combination that delivers $\dot{H}_{\text{lt}} = 0$ is apparent. First, the thrust magnitude, f , is constant via the constant thrust magnitude policy, reducing the \dot{f} term to zero. Second, if the fixed rotating orientation policy is selected, the \hat{a}_{lt} derivative also reduces to zero, simplifying the low-thrust Hamiltonian rate to

$$\dot{H}_{\text{lt}} = \vec{q} \cdot \frac{f\dot{m}}{m(\tau)^2} \hat{a}_{\text{lt}} \quad (2.119)$$

Accordingly, the constant mass policy delivers $\dot{H}_{\text{lt}} = 0$ as it assumes $\dot{m} = 0$. This combination of control policies is mathematically equivalent to fixing the magnitude (a_{lt}) and orientation (\hat{a}_{lt}) of the low-thrust acceleration vector. Although a constant mass policy is not as representative of real flight systems as the constant thrust or constant thrust orientation strategies, the high efficiency and small thrust magnitudes associated with low-thrust propulsion systems generally correspond to a very small \dot{m} value. Additionally, the simplifications that result from this combination of control policies enable a plethora of useful results from dynamical systems theory that can be incorporated into preliminary trajectory designs; the majority of the dynamical structures that may be available are a consequence of these simplifications. A detailed exploration of the validity of the constant mass assumption is the next important step. Following the validation, the properties of this simplified model are detailed.

2.2.6 Conservative Model Validation

When the low-thrust acceleration vector, \vec{a}_{lt} , is fixed (both in magnitude and direction) in the rotating frame, the CR3BP+LT becomes a conservative, Hamiltonian system in which the low-thrust Hamiltonian, H_{lt} , is an integral of the motion, as

discussed in Section 2.2.5. While maintaining a fixed thrust orientation is a feasible control strategy, maintaining a constant low-thrust acceleration magnitude may prove more difficult or simply undesirable in practice. In many applications, the thrust magnitude, f , is fixed but the spacecraft mass varies with time. Accordingly, neither the acceleration magnitude, $a_{\text{lt}} = f/m$, nor the acceleration vector, $\vec{a}_{\text{lt}} = a_{\text{lt}}\hat{a}_{\text{lt}}$, are constant. Although the thrust magnitude may be decreased at the same rate as the mass to maintain a constant value of a_{lt} , this strategy further limits the control authority of an already small force, an undesirable outcome from an engineering perspective. Thus, it is prudent to explore the dynamical properties of the CR3BP+LT when the acceleration magnitude is not fixed, i.e., when the spacecraft mass varies.

Hamiltonian Evolution with Variable Mass

One approach to evaluate the validity of a constant mass assumption is to investigate the evolution of the low-thrust Hamiltonian when the mass is *not* held constant. For this analysis, the low-thrust acceleration vector orientation is fixed in the rotating frame ($\dot{\hat{a}}_{\text{lt}} = \vec{0}$) and the thrust magnitude, f , is held constant ($\dot{f} = 0$) while the mass varies according to the CSI policy described in Section 2.2.4. Accordingly, the low-thrust Hamiltonian rate, expressed in Equation (2.118), simplifies to

$$\dot{H}_{\text{lt}}(\vec{q}, \tau) = \vec{q} \cdot \frac{f\dot{m}}{m(\tau)^2} \hat{a}_{\text{lt}}. \quad (2.120)$$

Substitute the CSI mass rate from Equation (2.92) for \dot{m} and the definition of the nondimensional thrust magnitude, f , from Equation (2.77) into the Hamiltonian rate to isolate the physical spacecraft parameters,

$$\dot{H}_{\text{lt}}(\vec{q}, \tau) = \frac{-F^2}{I_{\text{sp}}g_0m(\tau)^2M_{3,0}^2} \vec{q} \cdot \hat{a}_{\text{lt}} \left(\frac{T_*^3}{L_*} \right). \quad (2.121)$$

In this expression the dimensional thrust magnitude, F , is expressed in kilonewtons, I_{sp} is given in seconds, g_0 is measured in km/s^2 , and $M_{3,0}$ is expressed in kilograms.

Several sets of variables impact the magnitude of the Hamiltonian rate. First, the propulsion system parameters (F , I_{sp}) and the spacecraft properties ($M_{3,0}$) scale the magnitude of the rate. Similarly, the distance of the spacecraft from the barycenter (i.e., the magnitude of \vec{q}) is proportional to \dot{H}_{lt} . The less intuitive relationship between the spacecraft position and the orientation of the low-thrust acceleration vector also affects the Hamiltonian rate, as do the characteristic quantities associated with the system (L_* and T_*). To enable a practical comparison across systems, let the spacecraft and propulsion system properties be consistent with the Deep Space 1 spacecraft [43]: $F = 92\text{e-}4$ kN, $I_{sp} = 1900$ sec, and $M_{3,0} = 486$ kg. Furthermore, to increase the magnitude of the rate, let the spacecraft mass be $m = 0.9$, representing a scenario when 10% of the spacecraft wet mass has been depleted. This mass is consistent with the spacecraft capabilities, as Deep Space 1 was equipped with 82 kg of Xenon propellant for maneuvers, i.e., about 17% of the spacecraft wet mass.⁴ Finally, let $\|\vec{q}\| = 1$, a radius that includes the dynamically interesting P_2 vicinity, and let the angle between \vec{q} and \hat{a}_{lt} be zero to maximize the dot product. Together, these selected parameters supply a large but reasonable static \dot{H}_{lt} value that is employed to compare various CR3BP+LT systems.

To supply context within a specific system, the \dot{H}_{lt} values are compared to the difference in natural Hamiltonian values between the L_1 and L_5 Lagrange points. This differential,

$$\Delta H_{\text{nat}} = H_{\text{nat}}(L_5) - H_{\text{nat}}(L_1), \quad (2.122)$$

represents the significant energy change required to transition between a forbidden region geometry that separates the P_1 , P_2 , and exterior regions to a forbidden region geometry that allows unrestricted motion throughout the xy -plane [50]. The value of this differential varies considerably between systems. For example, in the Earth-Moon system, $\Delta H_{\text{nat}} \approx 1\text{e-}1$ while in the Sun-EMB system, $\Delta H_{\text{nat}} \approx 4.5\text{e-}4$. Because the scaling of H_{lt} is consistent with the scaling of H_{nat} , the ratio of the two quantities

⁴See the Deep Space 1 Asteroid Flyby press kit, https://www.jpl.nasa.gov/news/press_kits/dslasteroid.pdf

$\dot{H}_{\text{lt}}/\Delta H_{\text{nat}}$ communicates the significance of a particular change in the H_{lt} value. A small ratio, e.g., $\dot{H}_{\text{lt}}/\Delta H_{\text{nat}} = 3.3\text{e-}3$ for the Deep Space 1 spacecraft in the Earth-Moon system, as plotted in Figure 2.6, indicates that the change in the low-thrust Hamiltonian per unit of nondimensional time is approximately 1000 times smaller than the energy change between L_1 and L_5 . Similarly, a large ratio, e.g., $\dot{H}_{\text{lt}}/\Delta H_{\text{nat}} =$

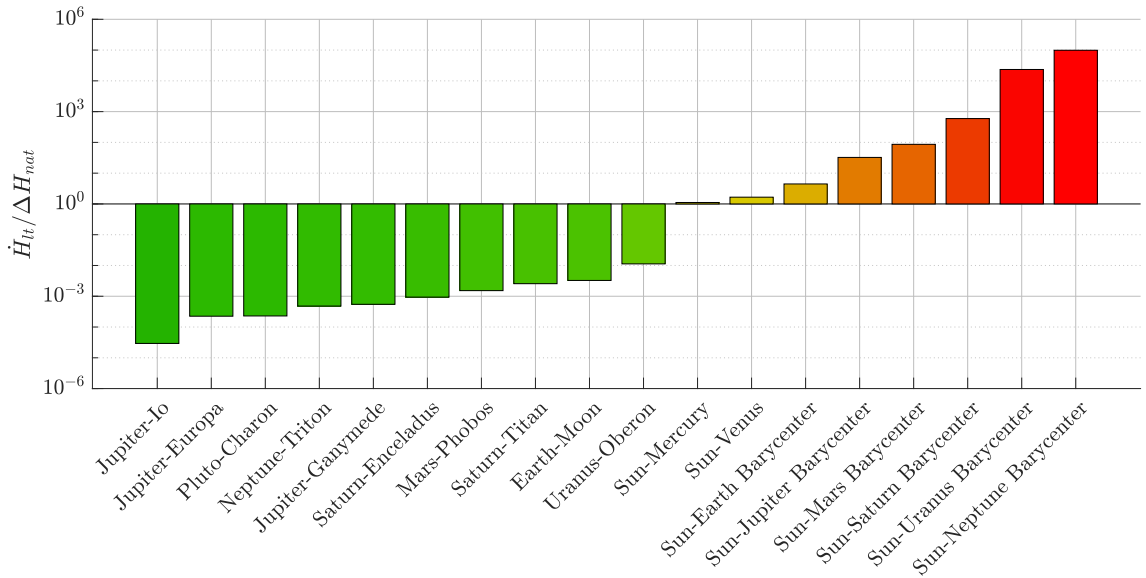


Figure 2.6.: Scaled \dot{H}_{lt} values for the Deep Space 1 spacecraft across CR3BP+LT systems

4.46 in the Sun-EMB system, indicates that the low-thrust Hamiltonian varies by much more than the ΔH_{nat} value in a single unit of nondimensional time. All of the Sun-planet systems in the solar system are characterized by similarly large ratios, as seen in Figure 2.6. (All of the “barycenter” labels indicate the inclusion of the specified body and its satellites, e.g., “Earth Barycenter” is equivalent to the Earth and Moon.) In contrast, many planet-moon systems possess small $\dot{H}_{\text{lt}}/\Delta H_{\text{nat}}$ ratios. Although not a guarantee due to the assumptions employed in computing this static ratio (i.e., $m = 0.9$, and $\vec{q} \cdot \hat{a}_{\text{lt}} = 1$), these values predict that low-thrust arcs propagated with a fixed thrust orientation, fixed thrust magnitude, and variable spacecraft mass are reasonably approximated as conservative in planet-moon systems.

To validate the energy changes predicted by the static \dot{H}_{lt} value, a Monte Carlo analysis is performed. The goal of this analysis is to measure the variations in the H_{lt} value along a low-thrust arc in the CR3BP+LT. To obtain a measure of this variation across an entire system, 100,000 arcs are propagated. The initial conditions (position, velocity, and thrust orientation) are selected at random from uniform distributions and the thrust magnitude and specific impulse are consistent with the Deep Space 1 capabilities, as in the static computation. Each arc is propagated for a half-period of the system or until the spacecraft mass decreases by 17%, consistent with the Deep Space 1 spacecraft capabilities. The propagation is also stopped if the trajectory escapes the the system or passes too close to one of the primaries (Appendix C.1 includes more details about the Monte Carlo analysis). The low-thrust Hamiltonian time profile is computed for each propagated arc and the maximum deviation from the initial H_{lt} value is stored. This maximum deviation,

$$\max|\Delta H_{\text{lt}}| = \max_{\tau} |H_{\text{lt}}(\tau) - H_{\text{lt}}(0)|, \quad (2.123)$$

is then scaled by the time-of-flight along the arc, $\Delta\tau$, and by ΔH_{nat} to supply a metric for each individual arc that is unbiased by the time-of-flight or the system properties. The mean and standard deviation of the $\max|\Delta H_{\text{lt}}|/\Delta H_{\text{nat}}/\Delta\tau$ values for the set of arcs propagated in each Monte Carlo trial is then compared to the energy change predicted by the static \dot{H}_{lt} value, as summarized in Table 2.2. The static Hamiltonian

Table 2.2.: Predicted and computed H_{lt} changes

System	$\dot{H}_{\text{lt}}/\Delta H_{\text{nat}}$	$\max \Delta H_{\text{lt}} /\Delta\tau/\Delta H_{\text{nat}}$	
		Mean	Std
Sun-Mars Barycenter	6.45×10^1	4.58×10^1	3.30×10^1
Sun-EMB	4.43×10^0	2.26×10^0	1.60×10^0
Earth-Moon	2.82×10^{-3}	1.50×10^{-3}	1.09×10^{-3}
Pluto-Charon	1.99×10^{-4}	1.05×10^{-4}	7.64×10^{-5}

rate values, listed in the second column, are within one or two standard deviations of

the experimentally-obtained mean in each of the systems. Accordingly, the \dot{H}_{lt} value, as computed above, is a suitable proxy for the integrated $\max|\Delta H_{\text{lt}}|/\Delta\tau$ value, at least within the context of the average behavior across the system. Thus, the results displayed in Figure 2.6 suggest that the low-thrust Hamiltonian may be reasonably assumed to be constant in the planet-moon systems when the low-thrust acceleration magnitude is similar to that delivered by Deep Space 1. In contrast, the Hamiltonian changes rapidly in many of the Sun-planet systems; assuming that the Hamiltonian is a constant in these systems is not justified.

The non-conservative nature of the low-thrust motion through the Sun-planet systems poses a challenge as many low-thrust missions transit through these regimes. For example, Deep Space 1, the spacecraft frequently used as a baseline in this investigation, visited an asteroid, a comet, and Mars [1], all located in dynamical regimes where the low-thrust Hamiltonian cannot be assumed to be constant. Thus, it is not prudent to simply ignore Sun-planet systems. One strategy to maintain a simplified model in these systems is to decrease the low-thrust acceleration magnitude. Given a specified $\dot{H}_{\text{lt}}/\Delta H_{\text{nat}}$ ratio, a maximum value for the acceleration, $F/M_{3,0}$, may be computed for each system by rearranging Equation (2.121). In this example, $\dot{H}_{\text{lt}}/\Delta H_{\text{nat}} = 0.01$ is deemed a ratio that can be reasonably approximated as zero, yielding the maximum accelerations plotted in Figure 2.7. In the figure, the maximum low-thrust acceleration magnitude for each system is compared to the Deep Space 1 (DS1) capability of approximately 0.019 mm/s^2 for reference. An acceleration magnitude larger than the DS1 magnitude may be employed in the planet-moon systems while maintaining $\dot{H}_{\text{lt}}/\Delta H_{\text{nat}} \leq 0.01$. In contrast, the acceleration magnitude must be decreased in the Sun-planet systems to deliver the same $\dot{H}_{\text{lt}}/\Delta H_{\text{nat}}$ value. For instance, an acceleration magnitude of $F/M_{3,0} = 0.01 \text{ mm/s}^2$ in the Sun-EMB system will deliver a maximum $\dot{H}_{\text{lt}}/\Delta H_{\text{nat}}$ value near 0.01 (confirmed via Monte Carlo analysis in Appendix C.2). Although the DS1 low-thrust acceleration magnitude is nearly 20 times this value, the Hayabusa and Hayabusa 2 spacecraft accelerate at the much smaller rates of 0.047 and 0.044 mm/s^2 , respectively. Thus, it may be rea-

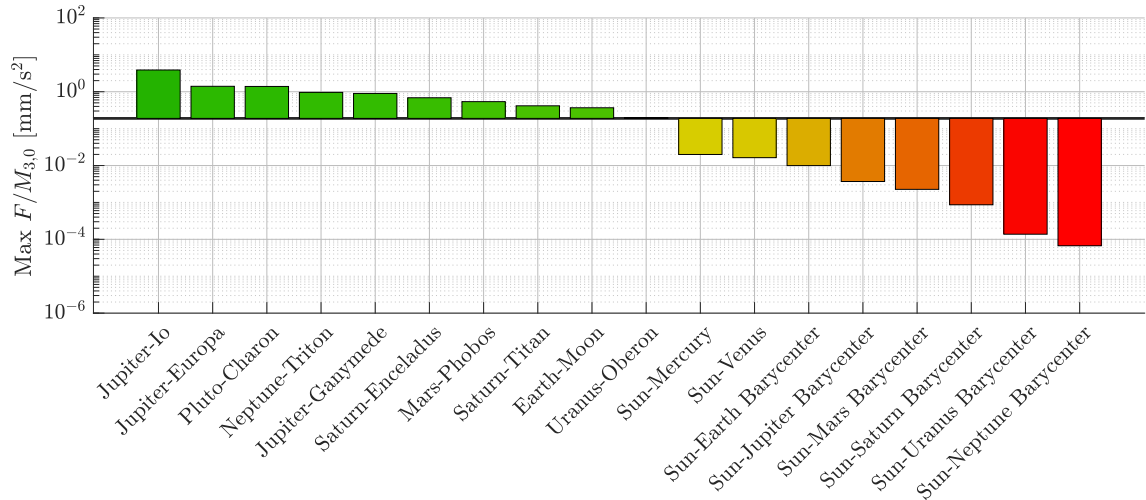


Figure 2.7.: Maximum acceleration magnitudes to achieve $\dot{H}_{\text{lt}}/\Delta H_{\text{nat}} \leq 0.01$ compared to the Deep Space 1 (DS1) capability

sonable to approximate low-thrust paths for particularly small acceleration values as conservative in the Sun-EMB regime.

Trajectory Geometry Comparisons

While the change in the low-thrust Hamiltonian due to a time-varying spacecraft mass in Sun-planet systems is generally non-negligible, the scalar Hamiltonian quantity is not the only parameter of interest. Recall from the [introduction](#) that the effects of a low-thrust force on both the *energy* (i.e., H_{nat} and/or H_{lt}) and the *geometry* of a trajectory are notable. Thus, it is prudent to determine if the effects of a low-thrust control policy with constant mass on the trajectory geometry are similar to the effects of a low-thrust control policy with variable mass on the trajectory geometry. If the results of the two control policies are “sufficiently similar”, the simplified model with a constant mass serves as a valuable proxy for the more complex model with variable mass. The most common metrics of interest when comparing trajectory geometries are the position and velocity histories. For low-thrust paths, the control parameter time histories (i.e., the “geometry” of the low-thrust acceleration vector) are also

an important consideration. Accordingly, the constant-mass model may be deemed suitable for preliminary low-thrust trajectory design if the trajectories are similar to a model that incorporates variable spacecraft mass.

To enable a straightforward comparison, a periodic orbit in the Sun-EMB model is employed. The orbit is first constructed in a CR3BP+LT that incorporates the constant mass assumption, plotted in blue in Figure 2.8. The orbit is composed of

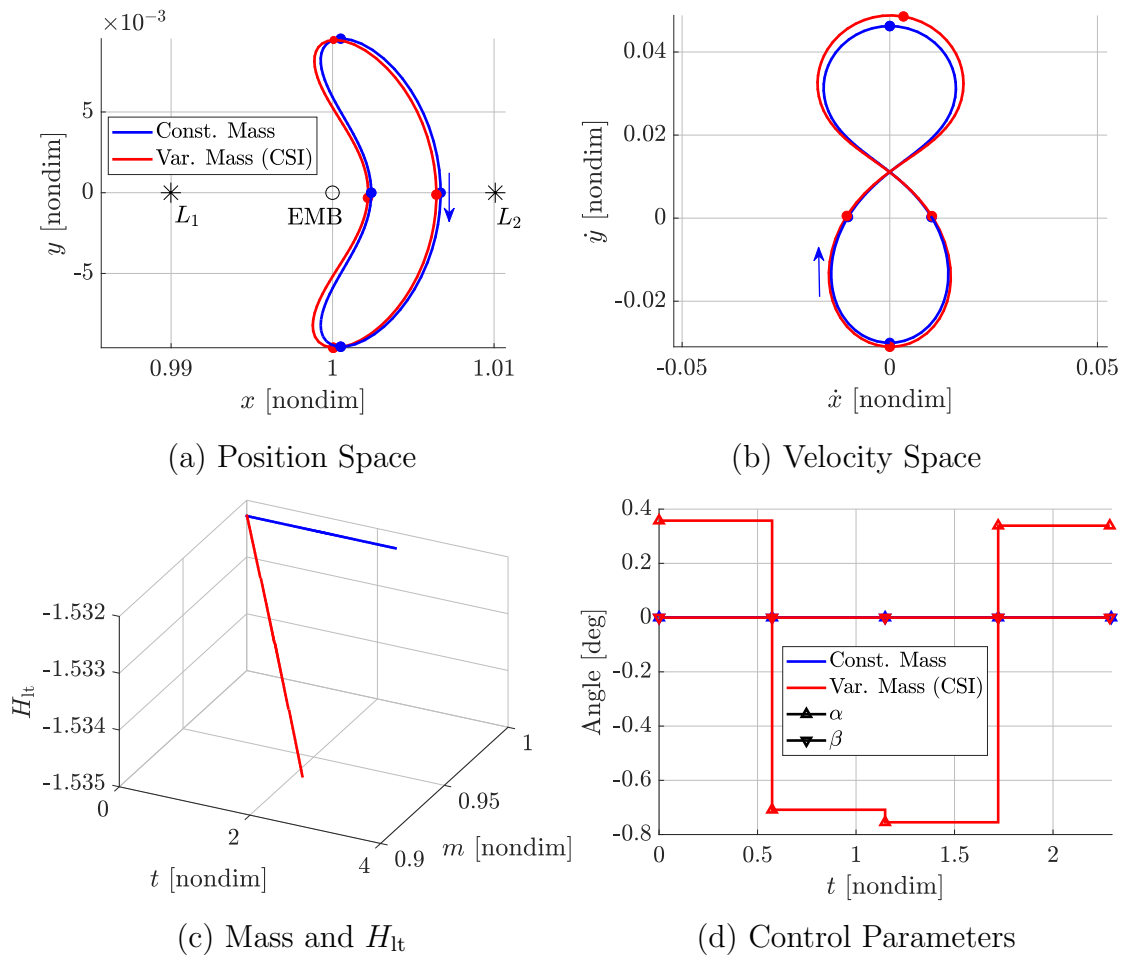


Figure 2.8.: Comparison of two planar Sun-EMB low-thrust periodic orbits in a constant mass model (blue) and in a model with a CSI mass policy ($I_{sp} = 3000$ sec). The thrust magnitude is fixed at $f = 3.2e-2$, consistent with the Deep Space 1 capability.

four segments, separated by circular node markers, with equal times-of-flight. The

preliminary solution in the constant-mass model is parameterized by $f = 3.2\text{e-}2$, (consistent with the Deep Space 1 capability in the Sun-EMB system) $\alpha = 0$ and $\beta = 0$. Due to the constant mass assumption, $m = 1$ along the entire orbit and the low-thrust Hamiltonian is conserved, as represented by the blue line in Figure 2.8(c). The orbit from the constant-mass model is transitioned into a variable mass model that employs a CSI mass policy with a specific impulse of $I_{\text{sp}} = 3000$ sec. Without any modifications, the segments are discontinuous in this higher-fidelity model. A differential corrections process is leveraged to adjust the low-thrust orientation angles (α and β) and enforce continuity in the position and velocity states between the arcs, yielding a similar periodic orbit that is plotted in red. As depicted in Figure 2.8, the geometry of the converged orbit in the variable mass model is very similar to the geometry of orbit in the constant mass model. The position and velocity histories along the trajectory remain very close to one another, and the α angle varies by less than one degree from the baseline while the β angle remains fixed at zero for both orbits as the trajectory is completely planar. Finally, observe that the H_{lt} value along the variable-mass path decreases by about $2.5\text{e-}3$, a full order of magnitude larger than the ΔH_{nat} value of $4.5\text{e-}4$ in the Sun-EMB system. This large shift in the H_{lt} value is consistent with the discussion earlier in this section. However, it is clear that the changes in the geometry – the position states, velocity states, and control parameters – are small. Similar results are available for other trajectories, including the 3D periodic orbit plotted in Figure 2.9. Like the planar periodic orbits in Figure 2.8, the two 3D orbits have very similar geometries in position and velocity space. Additionally, the low-thrust orientation angles, α and β , change by less than one degree relative to the constant-mass baseline to accommodate the nonautonomous dynamics in the variable mass model.

Although only two examples are included in this section, they are representative of other trajectory comparisons in the system. The selected periodic orbits are located near the smaller primary (the Earth-Moon barycenter (EMB) in this case), a sensitive and dynamically important region of the CR3BP. While the nonlinearities in the

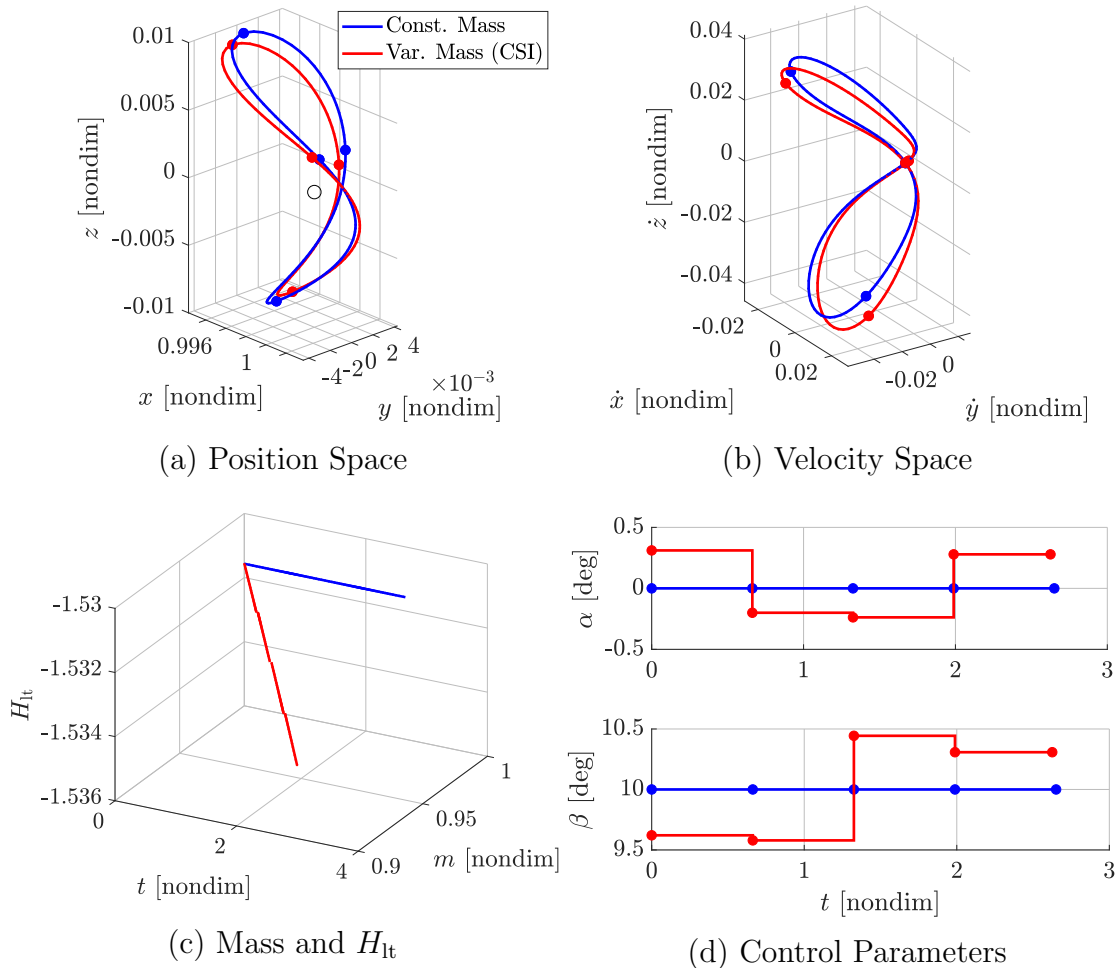


Figure 2.9.: Comparison of two 3D Sun-EMB low-thrust periodic orbits in a constant mass model (blue) and in a model with a CSI mass policy ($I_{sp} = 3000$ sec). The thrust magnitude is fixed at $f = 3.2e-2$, consistent with the Deep Space 1 capability.

system dynamics may make corrections more difficult in some regimes than others, a suitably discretized solution can generally be adjusted to preserve the geometry of the initial guess. Accordingly, it is reasonable to generalize these results and assert that the constant mass control policy is a suitable approximation for the variable mass policy in the Sun-EMB system within the context of the trajectory geometries. As a result, dynamical structures from a constant mass Sun-EMB CR3BP+LT may be employed to construct low-thrust trajectories despite the variable H_{lt} value.

2.2.7 Symmetry

As derived and validated in the previous sections, a CR3BP+LT system that employs a control policy with a fixed thrust magnitude, a fixed thrust orientation, and a constant spacecraft mass simplifies to an autonomous, conservative system. One of the many useful insights that is available due to this simplification is a set of symmetry conditions. When the aforementioned control policies are utilized, the equations of motion (EOMs) in (2.80) – (2.82) may be written as

$$\frac{d^2x}{d\tau^2} - 2 \frac{dy}{d\tau} = x - (1 - \mu) \frac{x + \mu}{r_{13}^3} - \mu \frac{x - 1 + \mu}{r_{23}^3} + a_{lt} \cos(\alpha) \cos(\beta), \quad (2.124)$$

$$\frac{d^2y}{d\tau^2} + 2 \frac{dx}{d\tau} = y - (1 - \mu) \frac{y}{r_{13}^3} - \mu \frac{y}{r_{23}^3} + a_{lt} \sin(\alpha) \cos(\beta), \quad (2.125)$$

$$\frac{d^2z}{d\tau^2} = -(1 - \mu) \frac{z}{r_{13}^3} - \mu \frac{z}{r_{23}^3} + a_{lt} \sin(\beta), \quad (2.126)$$

where the low-thrust acceleration magnitude, a_{lt} , and the orientation angles, α and β , are constant parameters. Define a “standard” state vector,

$$\vec{X}_0 = \left\{ x \quad y \quad z \quad \dot{x} \quad \dot{y} \quad \dot{z} \right\}^T$$

with time, τ , and control parameters α and β . Substituting the transformed coordinates

$$\vec{X}_1 = \left\{ x \quad -y \quad z \quad -\dot{x} \quad \dot{y} \quad -\dot{z} \right\}^T$$

with transformed time, $\tau_1 = -\tau$, and transformed control parameters, $\alpha_1 = -\alpha$, $\beta_1 = \beta$, into the EOMs will, after some rearrangement of the negative signs, yield an identical set of equations. This transformation is equivalent to mirroring a state over the xz -plane, reversing the time direction, and mirroring the low-thrust acceleration vector over the xz -plane. Similarly, substituting

$$\vec{X}_2 = \left\{ x \quad y \quad -z \quad \dot{x} \quad \dot{y} \quad -\dot{z} \right\}^T$$

with $\tau_2 = \tau$ and $\alpha_2 = \alpha$ and $\beta_2 = -\beta$ also results in the same equations. This latter transformation mirrors a trajectory and the low-thrust acceleration vector over the xy -plane. The two transformations may be combined to mirror a state and \vec{a}_{1t} over the x -axis while simultaneously reversing the direction of time.

The symmetry properties of the CR3BP+LT supply insights and also simplify computations. For example, a trajectory that passes through either the xy -plane, the xz -plane, or the x -axis twice with velocity vectors orthogonal to the plane or axis will be mirrored (given the appropriate mirroring of the α and β angles), supplying a periodic solution. In the special case when $\alpha = \beta = 0$, two “perpendicular crossings” of the planes or axis is sufficient to guarantee a periodic solution without any change in the control orientation. By leveraging these properties, the evolution of a trajectory can be forecast into the future or the past (i.e., negative time). Additionally, a solution or set of solutions can be rapidly transformed via these symmetries to yield new trajectories. Similar to the symmetries available in the ballistic CR3BP, these CR3BP+LT properties improve the predictability of motion within the system, facilitating rapid preliminary trajectory design.

2.2.8 Energy Evolution on a Plane

Another useful property of CR3BP+LT with an \vec{a}_{1t} vector fixed in the rotating frame relates the changes in the H_{nat} value along a low-thrust arc to \vec{a}_{1t} and the end points of the arc. As discussed previously, the natural Hamiltonian is an integral of the motion in the ballistic CR3BP but is no longer constant when low-thrust is added to the dynamics in the CR3BP+LT. However, when \vec{a}_{1t} is fixed (in both magnitude and orientation) in the rotating frame, the change in H_{nat} due to the low-thrust acceleration is available from a simple relationship. To derive this result, the natural Hamiltonian rate is once again inspected. Recall that \dot{H}_{nat} is identical to

the dot product between the velocity vector as viewed in the rotating frame and the low-thrust acceleration vector,

$$\dot{H}_{\text{nat}} = \vec{v} \cdot \vec{a}_{\text{lt}}. \quad (2.88)$$

Accordingly, if $\dot{\vec{a}}_{\text{lt}} = \vec{0}$ the natural Hamiltonian rate in Equation (2.88) may be integrated to obtain a relationship between the H_{nat} evolution and the control parameters,

$$\int_{\tau_0}^{\tau_f} \dot{H}_{\text{nat}} d\tau = \int_{\tau_0}^{\tau_f} \vec{v} d\tau \cdot \vec{a}_{\text{lt}} = [\vec{r}(\tau_f) - \vec{r}(\tau_0)] \cdot \vec{a}_{\text{lt}} = H_{\text{nat}}(\tau_f) - H_{\text{nat}}(\tau_0). \quad (2.127)$$

This integral demonstrates that the change in the natural Hamiltonian over a low-thrust arc is a function only of the low-thrust acceleration vector and the change in position between the initial and final times. In other words, the change in the H_{nat} value is independent of the path between the initial and final locations. This property is not surprising and is consistent with other idealized physical systems; the change in energy (H_{nat}) due to a conservative perturbing force (\vec{a}_{lt}) is path-independent. Several trajectory design applications benefit from this insight.

The path-independent property of the natural Hamiltonian in the CR3BP+LT with $\dot{\vec{a}}_{\text{lt}} = \vec{0}$ can be interpreted geometrically:

Lemma 2.2.1 *When \vec{a}_{lt} is constant in the rotating frame, H_{nat} evolves along a hyperplane oriented by the α and β angles as well as by the low-thrust acceleration magnitude, a_{lt} .*

Proof Let $\{\hat{x}, \hat{y}, \hat{z}, \hat{H}\}$ be a right-handed orthonormal basis of the four-dimensional vector space that includes position and natural Hamiltonian and let the spacecraft position and energy in this space be described by the vector,

$$\vec{\rho} = x\hat{x} + y\hat{y} + z\hat{z} + H_{\text{nat}}\hat{H}. \quad (2.128)$$

The change relative to the initial condition on the trajectory is denoted $\Delta\vec{\rho} = \vec{\rho}(\tau) - \vec{\rho}(\tau_0)$. To construct a basis for the hyperplane that contains $\Delta\rho$, three simple rotations

are implemented successively. First, rotate in the xy -plane by the α angle to an intermediate basis, $\{\hat{x}', \hat{y}', \hat{z}', \hat{H}'\}$. This rotation is concisely expressed by the matrix,

$$\mathbf{R}_\alpha = \begin{bmatrix} C_\alpha & S_\alpha & 0 & 0 \\ -S_\alpha & C_\alpha & 0 & 0 \\ 0 & 0 & 1 & 0 \\ 0 & 0 & 0 & 1 \end{bmatrix} \rightarrow \begin{pmatrix} x' \\ y' \\ z' \\ H' \end{pmatrix} = \mathbf{R}_\alpha \begin{pmatrix} x \\ y \\ z \\ H \end{pmatrix},$$

where S_α represents $\sin(\alpha)$ and C_α represents $\cos(\alpha)$. Next rotate in the $x'z'$ -plane by the $-\beta$ angle, described by the matrix,

$$\mathbf{R}_\beta = \begin{bmatrix} C_\beta & 0 & S_\beta & 0 \\ 0 & 1 & 0 & 0 \\ -S_\beta & 0 & C_\beta & 0 \\ 0 & 0 & 0 & 1 \end{bmatrix}.$$

(Note that this right-handed rotation by $-\beta$ is a result of the definition in Equation (2.97) that measures β from the xy -plane rather than from the \hat{z} -axis.) As a result of the second rotation, another intermediate basis, $\{\hat{x}'', \hat{y}'', \hat{z}'', \hat{H}''\}$, is reached. The final rotation takes place in the $x''H''$ -plane and is measured by an arbitrary angle γ ,

$$\mathbf{R}_\gamma = \begin{bmatrix} C_\gamma & 0 & 0 & -S_\gamma \\ 0 & 1 & 0 & 0 \\ 0 & 0 & 1 & 0 \\ S_\gamma & 0 & 0 & C_\gamma \end{bmatrix},$$

and yields the $\{\hat{x}''', \hat{y}''', \hat{z}''', \hat{H}'''\}$ basis. Accordingly, the final basis is expressed in terms of the original basis by combining the rotations,

$$\begin{pmatrix} x''' \\ y''' \\ z''' \\ H''' \end{pmatrix} = \mathbf{R}_\gamma \mathbf{R}_\beta \mathbf{R}_\alpha \begin{pmatrix} x \\ y \\ z \\ H \end{pmatrix} = \begin{bmatrix} C_\gamma C_\beta C_\alpha & C_\gamma C_\beta S_\alpha & C_\gamma S_\beta & -S_\gamma \\ -S_\alpha & C_\alpha & 0 & 0 \\ -S_\beta C_\alpha & -S_\beta S_\alpha & C_\beta & 0 \\ S_\gamma C_\beta C_\alpha & S_\gamma C_\beta S_\alpha & S_\gamma S_\beta & C_\gamma \end{bmatrix} \begin{pmatrix} x \\ y \\ z \\ H \end{pmatrix}. \quad (2.129)$$

Express the $\Delta\vec{\rho}$ vector in the rotated basis; the \hat{H}''' component is equal to

$$\Delta\vec{\rho} \cdot \hat{H}''' = S_\gamma [C_\alpha C_\beta \Delta x + S_\alpha C_\beta \Delta y + S_\beta \Delta z] + C_\gamma \Delta H_{\text{nat}}.$$

If this component is set equal to zero, the terms may be rearranged to form

$$\Delta H_{\text{nat}} = -T_\gamma [C_\alpha C_\beta \Delta x + S_\alpha C_\beta \Delta y + S_\beta \Delta z], \quad (2.130)$$

where $T_\gamma = \tan(\gamma)$. If $T_\gamma = -a_{1t}$, then this expression is identical to Equation (2.127). Thus, the \hat{H}''' component of $\Delta\vec{\rho}$ is zero and the trajectory evolves in a three-dimensional hyperplane spanned by \hat{x}''' , \hat{y}''' , and \hat{z}''' , constant directions that depend only on α , β , and a_{1t} . ■

Because the three-dimensional hyperplane is difficult (arguably impossible) to visualize, consider the planar case when $\beta = 0$. As a result, the third column and row in the $\mathbf{R}_\gamma \mathbf{R}_\beta \mathbf{R}_\alpha$ rotation matrix in Equation (2.129) contain only zeros and the number of rotations to construct a basis fixed in the energy hyperplane is reduced from three to two: a rotation in the xy -plane by α and a rotation in the $x''H''$ -plane (identical to the $x'H'$ -plane in this case) by $\gamma = \arctan(-a_{1t})$, as depicted in Figure 2.10(b). In this two-dimensional form, the relationship between the *energy plane* and the low-thrust acceleration parameters is more straightforward: the energy plane is oriented by the α angle and inclined by the γ angle. Note that because $a_{1t} > 0$ and $\gamma = \arctan(-a_{1t})$, the γ angle is negative (in all practical cases, $a_{1t} < \pi/2$). Thus,

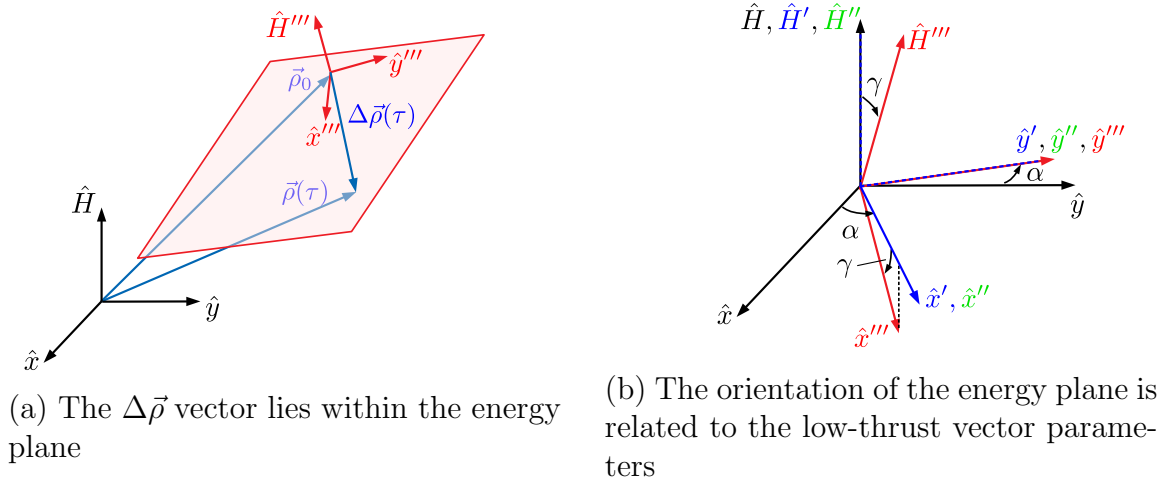


Figure 2.10.: Energy plane definition for $\beta = 0$. Though not shown, $\hat{z} = \hat{z}' = \hat{z}'' = \hat{z}'''$.

the energy plane slopes “uphill”, i.e., toward increasing H_{nat} values in the direction specified by α . For example, if $\alpha = \beta = 0$, the H_{nat} value on a trajectory increases as x increases and decreases as x decreases; the H_{nat} evolution is independent of Δy and Δz . Similar relationships are available in other special cases. If $\alpha = 0$ but $\beta \neq 0$, the H_{nat} evolution along a trajectory depends only on Δx and Δz , yielding a similar two-dimensional energy plane as in the $\beta = 0$ case. Even in the general, three-dimensional case, the energy plane slopes toward increasing H_{nat} values in the direction of the \hat{a}_{lt} vector. As such, when $\vec{v} \parallel \hat{a}_{\text{lt}}$, the spacecraft moves “up” the slope and H_{nat} increases. Similarly, when $\vec{v} \perp \hat{a}_{\text{lt}}$, the spacecraft contours “across” the slope and H_{nat} remains constant. While many of the insights discussed in this chapter consider only the effects of the low-thrust force on the trajectory energy (i.e., the H_{nat} evolution), this result defines a clear relationship between geometry and energy. Given an initial and final location, common constraints in a mission design problem, low-thrust control parameters may be selected to orient the energy plane such that the energy change between the two points is as desired. Alternatively, given an initial location and a desired energy change, a set of possible final locations and associated low-thrust control parameters are available. These direct links between the

change in H_{nat} , the change in position, and the control parameters along a low-thrust arc enable a designer to simultaneously specify an initial guess for a control history and the trajectory geometry, demonstrated in later sections.

3. DYNAMICAL STRUCTURES

To supplement the energy-related insights obtained from the analysis of the dynamical models, tools from dynamical systems theory (DST, an area of mathematics used to explore and analyze the behavior of complex dynamical systems such as the CR3BP and CR3BP+LT) are applied to construct dynamical structures that facilitate preliminary low-thrust trajectory design. A *dynamical structure* is defined here as a solution or set of solutions to the equations of motion. Structures constructed in the CR3BP+LT include position, velocity, mass, and control histories, supplying links between control inputs and the geometry of the solutions. Therefore, a survey of dynamical structures offers an overview of the flow patterns available throughout the system and reveals paths that might not otherwise be considered.

In this chapter, a variety of dynamical structures are investigated. Bounds on the spacecraft motion, i.e., *forbidden regions*, are constructed and parameterized by the natural and/or low-thrust Hamiltonian values along a trajectory. Gateways through these forbidden regions are located at the equilibrium solutions to the governing equations. Flow throughout the system is influenced by the *invariant manifolds* associated with the equilibria, including hyperbolic manifolds that asymptotically approach and depart from the equilibrium points, forming a topological saddle, and center manifolds that contain oscillatory solutions such as periodic and quasi-periodic orbits. An expanded portrait of the global dynamics is revealed by constructing the invariant manifolds associated with the periodic orbits. Each of these entities – a forbidden region, equilibrium point, periodic orbit, and invariant manifold – is a dynamical structure that may be included in or serve as a guide for a low-thrust trajectory design. These structures are identified within the autonomous, conservative system with a constant the low-thrust acceleration vector. However, they also approximate the time-varying dynamics when the orientation of \vec{a}_{lt} is fixed

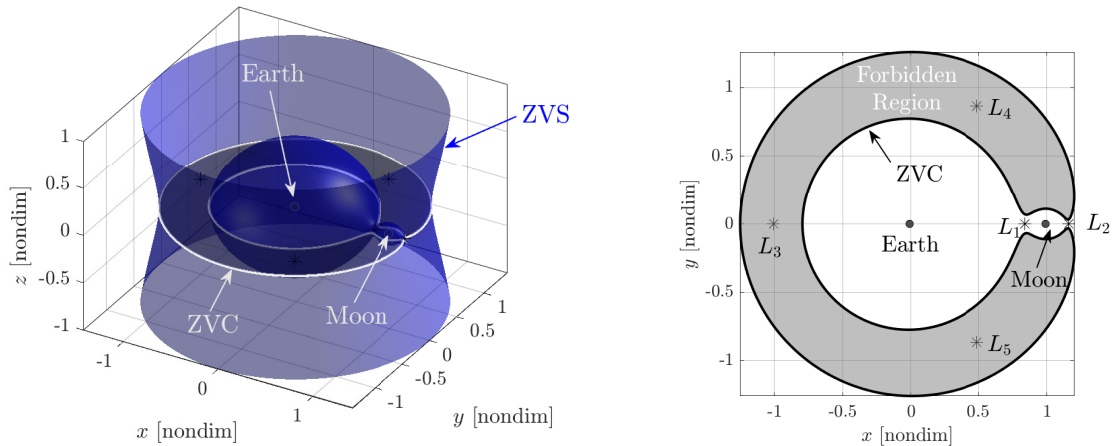
in the rotating frame but the mass is allowed to vary, as demonstrated in Section 2.2.6.

3.1 Forbidden Regions

In a Hamiltonian system with an integral of the motion, a solution to the equations of motion, i.e., a trajectory, exists within a level set with dimension $m - 1$, where m is the number of state variables or degrees of freedom [51]. In the CR3BP, the integral of the motion is H_{nat} and $m = 6$; thus, every ballistic trajectory is part of a 5D level set. Physical bounds on trajectories within the level set are parameterized by the H_{nat} value,

$$\mathbb{F}_{\text{nat}}(H_{\text{nat}}) = \left\{ \{x \quad y \quad z\}^T \mid -\frac{1}{2}(x^2 + y^2) - \frac{1-\mu}{r_{13}} - \frac{\mu}{r_{23}} = H_{\text{nat}} \right\}, \quad (3.1)$$

i.e., the collection of all points that possess the specified natural Hamiltonian value. This set is identical to the group of state vectors that possess the specified natural Hamiltonian value when the velocity components are zero. Accordingly, this surface is frequently called the *zero velocity surface* (ZVS) [50]. The surface, illustrated in Figure 3.1(a), is the boundary between the forbidden region and the *permissible region*, i.e., the region of space in which all trajectories with the associated H_{nat} value may exist. The permissible region always includes the locations of the two primaries as the H_{nat} value associated with the primary positions is $-\infty$. When the motion of the spacecraft is constrained to the xy -plane, a lower-dimensional representation of the ZVS is employed. This *zero velocity contour* (ZVC), depicted in black in Figure 3.1(b), is the intersection of the xy -plane with the ZVS, as shown in Figure 3.1(a). Additional ZVCs may be constructed on other intersecting planes, but the $z = 0$ ZVC is frequently employed because it bounds planar motion. For low H_{nat} values (i.e., for $H_{\text{nat}} \rightarrow -\infty$), the ZVS and ZVC enclose each primary in a distinct “bubble.” Thus, transit between the two bodies is not permitted. As the H_{nat} value increases,



(a) The zero velocity surface (ZVS) bounds the spacecraft motion in 3D space (b) The zero velocity contour (ZVC) at $z = 0$ bounds planar motion

Figure 3.1.: The zero velocity surface (ZVS) separates the forbidden and permissible regions in the Earth-Moon system for $H_{\text{nat}} = -1.585$

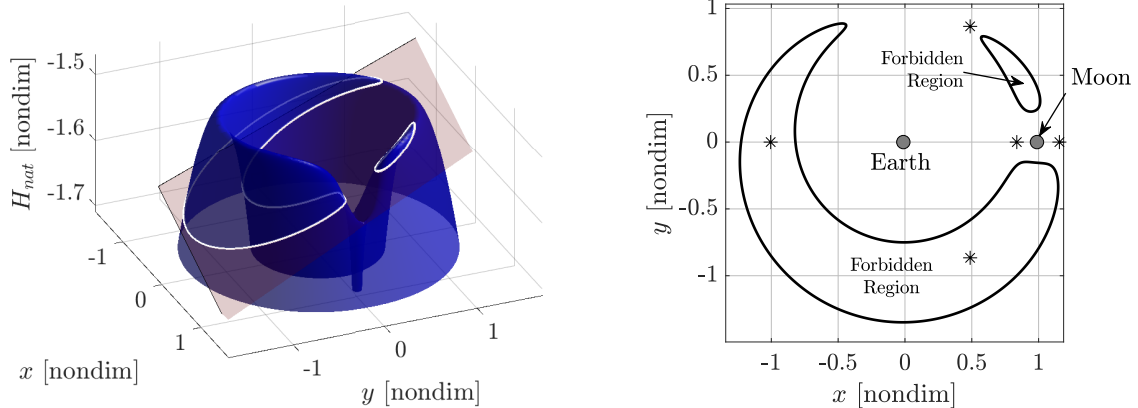
the ZVS recedes from the primaries and a gateway between P_1 and P_2 opens at the location of the L_1 Lagrange point (one of five equilibrium solutions to the ballistic CR3BP [50]) and at the energy associated with that point, i.e., $H_{\text{nat}}(L_1)$. At the $H_{\text{nat}}(L_2)$ value, a gateway between P_2 and the exterior region opens at the location of the L_2 point. With further increases in H_{nat} to $H_{\text{nat}}(L_3)$, a similar gateway opens at L_3 . The L_4 and L_5 points are the final points in the xy -plane that remain within the forbidden region; for H_{nat} values higher than $H_{\text{nat}}(L_{4/5})$, the ZVS does not intersect the xy -plane. Because the natural Hamiltonian is constant along ballistic arcs in the CR3BP, the ZVS and ZVC are static, bounding the evolution of a trajectory for all time. This insight facilitates trajectory design by supplying minimum energy requirements to transit between regions in the system. For example, a spacecraft on a path departing P_1 must achieve an H_{nat} value greater than the L_1 “gateway energy,” $H_{\text{nat}}(L_1)$, to reach P_2 . Although this energy requirement is not sufficient to guarantee transit (a trajectory may remain near P_1 even with an energy greater than $H_{\text{nat}}(L_1)$), it is a necessary condition.

Trajectories that leverage a low-thrust force in the CR3BP+LT are also bounded by the ballistic ZVS, \mathbb{F}_{nat} . However, because H_{nat} varies along low-thrust trajectories, as established in Section 2.2.3, \mathbb{F}_{nat} changes size and shape as H_{nat} evolves. While these pulsating boundaries do represent the instantaneous bounds on the spacecraft path, they are more difficult to employ in the design process than a static boundary set. To construct such a fixed surface, the low-thrust Hamiltonian, H_{lt} , is employed. Recall from Section 2.2.6 that H_{lt} is approximately constant (in planet-moon systems) when the orientation of the low-thrust acceleration vector, \vec{a}_{lt} , is fixed in the rotating frame. Furthermore, H_{lt} is exactly constant if the magnitude of the vector is also constant. Accordingly, a low-thrust zero velocity surface, \mathbb{F}_{lt} , remains static when a control strategy that fixes the magnitude and orientation of \vec{a}_{lt} in the rotating frame is employed. Similar to the ballistic ZVS, the low-thrust surface is the set of points that possess a specified H_{lt} value, i.e.,

$$\mathbb{F}_{\text{lt}}(H_{\text{lt}}, \vec{a}_{\text{lt}}) = \left\{ \{x \ y \ z\}^T \left| -\frac{1}{2} (x^2 + y^2) - \frac{1 - \mu}{r_{13}} - \frac{\mu}{r_{23}} - \vec{r} \cdot \vec{a}_{\text{lt}} = H_{\text{lt}} \right. \right\}, \quad (3.2)$$

where $\vec{r} = \{x \ y \ z\}^T$. The evolution of \mathbb{F}_{lt} with increasing values of H_{lt} is qualitatively identical to the evolution of \mathbb{F}_{nat} . At very low H_{lt} values, \mathbb{F}_{lt} separates P_1 and P_2 . As H_{lt} grows, gateways in \mathbb{F}_{lt} appear at the locations and H_{lt} values of the low-thrust equilibrium points. However, as the locations of the low-thrust equilibria vary significantly from the ballistic equilibria (as discussed in the next section), many novel gateway geometries are possible.

The static \mathbb{F}_{lt} is related to the variable H_{nat} value along a low-thrust trajectory by the energy hyperplane defined in Section 2.2.8. This relationship is most easily explained when the problem is reduced to four-dimensional motion, i.e., $z = \dot{z} = 0$ and $\beta = 0$. In this scenario, a low-thrust arc with a constant \vec{a}_{lt} vector exists in a 3D level set parameterized by the H_{lt} value associated with the trajectory. Additionally, the 3D energy hyperplane simplifies to a 2D plane in x - y - H_{nat} space, as illustrated by the maroon plane in Figure 3.2(a). A 2D “ballistic energy surface,” plotted in blue,



(a) The intersection of an energy plane (maroon) and the ballistic energy surface (blue) defines the low-thrust forbidden regions (white)

(b) A projection of the low-thrust forbidden regions (black contours) into the xy -plane; the Lagrange points (black asterisks) are included for reference

Figure 3.2.: Earth-Moon CR3BP+LT forbidden regions for $a_{lt} = 7e-2$, $\alpha = 80^\circ$, and $H_{lt} = -1.5561$. An Animation of this figure is available [online](#)¹.

represents the planar ZVCs in the same space; each horizontal slice of the energy surface is a ZVC at the corresponding H_{nat} value. As a low-thrust trajectory moves on the energy plane, the H_{nat} value (i.e., the out-of-plane coordinate in this space) and the ballistic ZVC geometry evolve. The intersection of the maroon energy plane with the blue energy surface is the set of points where the spacecraft encounters the instantaneous \mathbb{F}_{nat} contour, i.e., where the spacecraft reaches a velocity magnitude of zero. Accordingly, this intersection is the low-thrust ZVC.

The geometry of the low-thrust forbidden regions may be manipulated by adjusting the low-thrust acceleration magnitude and orientation. Recall that the inclination of the energy plane is a function of the low-thrust acceleration magnitude. When $a_{lt} = 0$, the energy plane has an inclination of zero and slices the ballistic energy surface horizontally, yielding the planar \mathbb{F}_{nat} contour. For larger values of a_{lt} , the plane is inclined by a larger angle. Additionally, the orientation of the plane is determined

¹<https://engineering.purdue.edu/people/kathleen.howell.1/Publications/Dissertations/2020-Cox/#ltzvc>

by the α angle; thus, changes to α rotate the energy plane relative to the ballistic energy surface, yielding different intersection geometries. The Animation of Figure 3.2 (see the link in the figure caption) illustrates the changes in the low-thrust forbidden region as both a_{lt} and α vary in the Earth-Moon system. The higher-dimensional low-thrust ZVS, \mathbb{F}_{lt} , is similarly related to the energy plane and ballistic energy surface. In the spatial problem ($z \neq 0, \dot{z} \neq 0, \beta \neq 0$), the energy plane and ballistic energy surface are both 3D structures; their intersection is the 2D low-thrust zero velocity surface.

3.2 Equilibrium Solutions

While the low-thrust forbidden regions bound trajectories within a level set, the CR3BP+LT equilibrium solutions supply an initial characterization of the local and global dynamics within the level set that may be utilized for low-thrust path planning. Manipulations of the low-thrust acceleration vector directly influence the number and location of equilibrium solutions in the CR3BP+LT, which subsequently affects the existence and characteristics of nearby dynamical structures. Accordingly, the equilibrium solutions in the CR3BP+LT are important to low-thrust mission applications, particularly as the equilibria locations evolve relative to the familiar CR3BP equilibrium points, i.e., the *Lagrange points*.

In general, the full set of low-thrust equations of motion (EOMs), given by Equations (2.108) – (2.113), does not admit invariant equilibria due to the time-varying low-thrust acceleration vector, \vec{a}_{lt} . However, when the constant mass policy and fixed rotating orientation policies are employed, as described in Section 2.2.4, the \vec{a}_{lt} vector is constant and a set of invariant equilibrium points is available to characterize the system dynamics. If other policies are used to model the spacecraft mass, these equilibria remain a useful approximation to the time-varying dynamics due to the small mass flow-rate associated with a low-thrust propulsion system. On the other hand, if the orientation of \vec{a}_{lt} varies rapidly, as in the orientation policies that align

\vec{a}_{lt} relative to \vec{v} , the locations and properties of the equilibrium solutions vary with \vec{a}_{lt} and a static snapshot of the dynamical environment is unavailable. Accordingly, a constant \vec{a}_{lt} vector is utilized to compute the equilibrium solutions.

Every equilibrium point is located where the gradient of the Hamiltonian is zero. Mathematically, an equilibrium point satisfies the equation

$$\frac{\partial H_{\text{lt}}}{\partial \vec{X}_H} = \vec{0}. \quad (3.3)$$

Alternatively, the equilibria also satisfy $\dot{\vec{X}}_H = \vec{0}$ by Equation (2.114) or $\dot{\vec{X}}_L = \vec{0}$ by (2.115). As the majority of this investigation leverages the Lagrangian basis to represent the states, $\vec{X} = \vec{X}_L$, the latter condition for an equilibrium solution is used. The $\dot{\vec{X}}_L = \vec{0}$ relationship yields six scalar equations: the first three simplify to $\dot{\vec{r}} = \vec{v} = \vec{0}$, i.e., the velocity states (as seen in the rotating frame) are all zero at the equilibrium points. As a result, the low-thrust Hamiltonian simplifies to $H_{\text{lt}}(\vec{q}, \tau) = \Upsilon(\vec{q}, \tau)$ and the equilibrium points solve $\vec{\nabla}_r \Upsilon = \vec{\nabla}_q \Upsilon = \vec{0}$. These final three equations are less straightforward to solve than the first three; this section is dedicated to identifying and characterizing the solutions.

In an effort to maintain generality, the \vec{a}_{lt} vector is parameterized by the α and β angles, as described in Equation (2.97), and by the acceleration magnitude, a_{lt} . For a mission design perspective, let a_{lt} be a constant value consistent with the propulsion system capability and let the α and β angles be “design variables” that may be selected to achieve some configuration of the equilibria. Because the velocity states are all zero and the low-thrust acceleration magnitude is fixed, five independent variables are required to isolate an equilibrium point: the 3D location, $\vec{r} = \{x \ y \ z\}^T$ and the corresponding low-thrust acceleration vector orientation, α , and β . These variables are collected together into a *free variable vector*, $\vec{\mathcal{X}} = \{x \ y \ z \ \alpha \ \beta\}^T$, that solves the equation

$$\vec{\nabla}_r \Upsilon(a_{\text{lt}}, \vec{\mathcal{X}}) = \vec{0}, \quad (3.4)$$

at the locations of the equilibrium points.

Without solving Equation (3.4), insights about the locations of the low-thrust equilibria are available from the natural acceleration field. This field is described by the vector,

$$\vec{a}_{\text{nat}} = \left\{ 2\dot{y} + \Omega_x \quad -2\dot{x} + \Omega_y \quad \Omega_z \right\}^T, \quad (3.5)$$

the acceleration imparted on the spacecraft due to the gravitational interactions between the spacecraft and the two primaries as well as the motion of the rotating frame. As established above, the velocity states (\dot{x} , \dot{y} , and \dot{z}) are zero; thus, the natural acceleration at an equilibrium point is equivalent to the spatial gradient of the natural pseudopotential,

$$\vec{a}_{\text{nat}}|_{\text{eq}} = \vec{\nabla}_r \Omega. \quad (3.6)$$

When Υ is expressed as a function of the natural pseudopotential, Ω , as in Equation (2.84), the gradient in Equation (3.4) that locates the low-thrust equilibria may be written,

$$\vec{\nabla}_r \Upsilon = \vec{\nabla}_r \Omega + \vec{\nabla}_r (\vec{r} \cdot \vec{a}_{\text{lt}}) = \vec{\nabla}_r \Omega + \vec{a}_{\text{lt}} = \vec{0}, \quad (3.7)$$

because \vec{a}_{lt} is independent of \vec{r} when parameterized by α , β , and a_{lt} . Combining Equations (3.6) and (3.7), the low-thrust acceleration and natural acceleration vectors are related at the locations of the low-thrust equilibria,

$$\vec{a}_{\text{lt}} = -\vec{\nabla}_r \Omega = -a_{\text{nat}}|_{\text{eq}}. \quad (3.8)$$

The \vec{a}_{lt} vector at an equilibrium point is simply the $\vec{a}_{\text{nat}}|_{\text{eq}}$ vector scaled by -1, i.e., rotated by 180°. Accordingly, every spatial location is an equilibrium solution corresponding to an \vec{a}_{lt} vector with a magnitude equal to the natural acceleration vector at that location and the opposite orientation. Put another way, a set of low-thrust equilibria parameterized by a consistent low-thrust acceleration magnitude, a_{lt} , represents an isosurface in the $\|\vec{a}_{\text{nat}}\|$ field at the a_{lt} value. As a result of this relationship, a set of low-thrust equilibria is termed a *zero acceleration surface* (ZAS) since the

surface represents the locations where \vec{a}_{lt} balances \vec{a}_{nat} when the velocity is zero in the rotating frame.

While numerical methods to construct the low-thrust equilibrium point isosurfaces are available in packages such as MATLAB, an analysis of the equations themselves supplies information that is unavailable from numerical methods and facilitates the construction of the ZAS's with greater accuracy. Given an arbitrary position in space, \vec{r} , the low-thrust acceleration parameters associated with a low-thrust equilibrium point at that location are available directly from the gradient of Ω ,

$$a_{\text{lt}} = \left\| \vec{\nabla}_{\vec{r}} \Omega \right\|, \quad (3.9)$$

$$\alpha = \arctan \left(-\Omega_y / -\Omega_x \right), \quad (3.10)$$

$$\beta = \arcsin \left(-\Omega_z / \left\| \vec{\nabla}_{\vec{r}} \Omega \right\| \right), \quad (3.11)$$

where

$$\Omega_x = x - (1 - \mu) \frac{x + \mu}{r_{13}^3} - \mu \frac{x - 1 + \mu}{r_{23}^3}, \quad (3.12)$$

$$\Omega_y = y \left[1 - \frac{1 - \mu}{r_{13}^3} - \frac{\mu}{r_{23}^3} \right], \quad (3.13)$$

$$\Omega_z = z \left[-\frac{1 - \mu}{r_{13}^3} - \frac{\mu}{r_{23}^3} \right]. \quad (3.14)$$

Several insights result from these expressions:

Lemma 3.2.1 $\left[-\frac{1-\mu}{r_{13}^3} - \frac{\mu}{r_{23}^3} \right] < 0$ for all μ and all finite values of x , y , and z .

Proof The mass ratio, μ , is bounded by $0 < \mu \leq 0.5$; thus, the numerators of the two fractions are positive. Additionally, r_{13} and r_{23} are both L2 norms of the \vec{r}_{13} and \vec{r}_{23} vectors and are positive numbers. Subsequently, both fractions represent positive numbers, equaling zero only as $r_{13} \rightarrow \infty$ and $r_{23} \rightarrow \infty$; multiplying the sum of the two positive numbers by -1 yields a negative number. ■

Lemma 3.2.2 All low-thrust equilibria in the xz -plane correspond to \vec{a}_{lt} vectors that are also located in the xz -plane.

Proof The Ω_y expression in Equation (3.13) is the product of y and another set of terms. When $y = 0$ (i.e., a point located in the xz -plane), $\Omega_y = 0$; thus, Equation (3.10) dictates that $\alpha = 0$ when $\Omega_x < 0$ or $\alpha = \pi$ when $\Omega_x > 0$. (Recall that α is bounded by $[-\pi, \pi]$.) ■

Lemma 3.2.3 *All low-thrust equilibria in the xy -plane correspond to \vec{a}_{lt} vectors that are also planar and all equilibria not in the xy -plane correspond to \vec{a}_{lt} vectors with nonzero out-of-plane components.*

Proof Because Ω_z , given in Equation (3.14), is the product of z and a negative number (the terms in the square brackets, by Lemma 3.2.1), $\Omega_z = 0$ if and only if $z = 0$. Subsequently, β , defined in Equation (3.11), is zero if and only if $z = 0$, ignoring the infeasible limit $a_{\text{lt}} \rightarrow \infty$. ■

Lemma 3.2.4 *All low-thrust equilibrium points located with $z > 0$ are associated with an \vec{a}_{lt} vector with $\beta > 0$, and vice versa.*

Proof Equation (3.11) guarantees that $\text{sgn}(\beta) = -\text{sgn}(\Omega_z)$. Additionally, $\text{sgn}(\Omega_z)$ is the product of $\text{sgn}(z)$ and the sign of the terms in the square brackets in Equation (3.14). By Lemma 3.2.1, these terms are negative; thus, the sign of Ω_z is opposite the sign of z , indicating that β and z have the same sign. (Recall that β is bounded by $[-\pi/2, \pi/2]$.) ■

Additional insights are available from the equations that directly describe the low-thrust equilibria, i.e., the gradient of Υ ,

$$\Upsilon_x = x \left[1 - \frac{1-\mu}{r_{13}^3} - \frac{\mu}{r_{23}^3} \right] + \mu \left[-\frac{1-\mu}{r_{13}^3} - \frac{\mu}{r_{23}^3} \right] + \frac{\mu}{r_{23}^3} + a_{\text{lt}} C_\alpha C_\beta = 0, \quad (3.15)$$

$$\Upsilon_y = y \left[1 - \frac{1-\mu}{r_{13}^3} - \frac{\mu}{r_{23}^3} \right] + a_{\text{lt}} S_\alpha C_\beta = 0, \quad (3.16)$$

$$\Upsilon_z = z \left[-\frac{1-\mu}{r_{13}^3} - \frac{\mu}{r_{23}^3} \right] + a_{\text{lt}} S_\beta = 0, \quad (3.17)$$

where $C_\alpha = \cos \alpha$, $S_\alpha = \sin \alpha$, $C_\beta = \cos \beta$, and $S_\beta = \sin \beta$. Only the nontrivial low-thrust equilibria ($a_{\text{lt}} > 0$) are considered; the ballistic Lagrange points solve

these equations for $a_{1t} = 0$. Useful symmetry conditions are available from these expressions,

Lemma 3.2.5 *If $\vec{\mathcal{X}}_0 = \{x \ y \ z \ \alpha \ \beta\}^T$ is a solution to Equations (3.15) – (3.17), then $\vec{\mathcal{X}}_1 = \{x \ -y \ z \ -\alpha \ \beta\}^T$ and $\vec{\mathcal{X}}_2 = \{x \ y \ -z \ \alpha \ -\beta\}^T$ are also solutions.*

Proof Substitute $\vec{\mathcal{X}}_1$ or $\vec{\mathcal{X}}_2$ into Equations (3.15) – (3.17). Apply trigonometric identities and multiply entire equations by -1 to arrive at identical expressions; thus, both vectors yield the same solution as $\vec{\mathcal{X}}_0$, consistent with the symmetry properties discussed in Section 2.2.7. ■

This symmetry reduces the number of computations required to construct a full ZAS; a subset of the solutions may be mirrored across the xy - and xz -planes (with the corresponding angle changes) to yield a full set of equilibria.

In contrast to the ballistic equilibrium solutions that are located analytically or via a one-dimensional root-finding search [50], the low-thrust equilibrium points cannot generally be located via analytical or simple root-finding processes. However, by fixing specific angle values and constraining the locations of the equilibrium solutions, several analytical and one-dimensional functions are available to yield distinct solutions. Continuation methods may then be employed to construct the full sets of equilibria. In the following sections, specific values of α and β are leveraged to supply a one-dimensional equation for solutions located on the x -axis, i.e., *collinear points*, and a strategy to locate equilibria far above and below the xy -plane is described. Additionally, two analytical expressions for solutions located off of the x -axis are derived. For completeness, the lack of solutions at other combinations of α and β values are described in Appendix D.

3.2.1 Collinear Solutions

As the solutions to Equations (3.15) – (3.17) are under-constrained (i.e., there are more variables than equations), several variables may be fixed to yield distinct

solutions. Reducing any of the equations to a product of terms (rather than a sum) offers insight and permits further simplification. Accordingly, let $\alpha = 0$ or π , setting the $\sin(\alpha)$ term in Equation (3.16) equal to zero. The resulting equation is solved if $y = 0$, as noted in Lemma 3.2.2, reducing the number of equations to two and the number of variables to three (x , z , and β remain). To further reduce the degrees of freedom, let $\beta = 0$. As outlined in Lemma 3.2.3, z must also equal zero. Thus, the system is reduced to a single equation, Equation (3.15), that is a function of a single variable, x ,

$$x - (1 - \mu) \frac{x + \mu}{A(x + \mu)^3} - \mu \frac{x - 1 + \mu}{B(x - 1 + \mu)^3} + a_{1t} \cos(\alpha) = 0, \quad (3.18)$$

where $A = \text{sgn}(x + \mu)$ and $B = \text{sgn}(x - 1 + \mu)$ result from the cancellation of the square roots in r_{13} and r_{23} . This cubic function includes asymptotes at $x = -\mu$ and $x = 1 - \mu$, the locations of P_1 and P_2 , respectively. Between these asymptotes, the function increases monotonically with an increasing value of x , including limits at $\pm\infty$ at the asymptotes and at $x \rightarrow \pm\infty$. Accordingly, exactly three solutions exist, with one in each of the three regions: (i) $-\mu < x < 1 - \mu$; (ii) $x > 1 - \mu$; and (iii) $x < -\mu$. These solutions exist regardless of the values for μ or a_{1t} with no additional roots. Thus, exactly three equilibria exist at $(\alpha = \beta = 0, y = z = 0)$, and another three exist at $(\alpha = \pi, \beta = 0, y = z = 0)$. Because these solutions are located on the x -axis and at α angles of 0 and π , the symmetry conditions expressed in the previous section guarantee that nearby solutions off of the x -axis are symmetric across the xz - and xy -planes.

The precise locations of the collinear points are computed by applying a root-finding algorithm to Equation (3.18). Define a transformed x -coordinate, \tilde{x} , for each of the three regions, $x_1 = 1 - \mu - \tilde{x}_1$, $x_2 = 1 - \mu + \tilde{x}_2$, and $x_3 = -\mu - \tilde{x}_3$. Substituting

these relationships into Equation (3.18) yields three expressions that may be solved iteratively for \tilde{x}_i :

$$h(\tilde{x}_1) = 1 - \mu - \tilde{x}_1 - \frac{1 - \mu}{(1 - \tilde{x}_1)^2} + \frac{\mu}{\tilde{x}_1^2} + a_{\text{lt}} \cos(\alpha) = 0, \quad (3.19)$$

$$h(\tilde{x}_2) = 1 - \mu + \tilde{x}_2 - \frac{1 - \mu}{(1 + \tilde{x}_2)^2} - \frac{\mu}{\tilde{x}_2^2} + a_{\text{lt}} \cos(\alpha) = 0, \quad (3.20)$$

$$h(\tilde{x}_3) = -\mu - \tilde{x}_3 + \frac{1 - \mu}{\tilde{x}_3^2} + \frac{\mu}{(-\tilde{x}_3 - 1)^2} + a_{\text{lt}} \cos(\alpha) = 0. \quad (3.21)$$

The iterative Newton-Raphson root-finding algorithm,

$$\tilde{x}_i[k + 1] = \tilde{x}_i[k] - \frac{h(\tilde{x}_i[k])}{h'(\tilde{x}_i[k])}, \quad (3.22)$$

also employs the partial derivatives of the h function with respect to the independent variable, \tilde{x}_i ,

$$h'(\tilde{x}_1) = \frac{-2(1 - \mu)}{(1 - \tilde{x}_1)^3} - \frac{2\mu}{\tilde{x}_1^3} - 1, \quad (3.23)$$

$$h'(\tilde{x}_2) = \frac{2(1 - \mu)}{(1 + \tilde{x}_2)^3} + \frac{2\mu}{\tilde{x}_2^3} + 1, \quad (3.24)$$

$$h'(\tilde{x}_3) = \frac{-2(1 - \mu)}{\tilde{x}_3^3} - \frac{2\mu}{(1 + \tilde{x}_3)^3} - 1. \quad (3.25)$$

The locations of the ballistic CR3BP collinear points serve as suitable initial guesses for these one-dimensional searches. Following the convergence of the Newton-Raphson method, the location of one of the collinear points is available,

$$\vec{\mathcal{X}} = \left\{ x_i \quad 0 \quad 0 \quad \alpha = (0 \text{ or } \pi) \quad 0 \right\}^T. \quad (3.26)$$

Once a set of collinear, low-thrust equilibrium points have been located, a continuation process may be employed to compute the locations of nearby equilibria that correspond to other α or β angles.

3.2.2 Highly Out-of-Plane Solutions

An analysis of the isosurfaces in the ballistic pseudopotential gradient magnitude, $\left\| \vec{\nabla}_r \Omega \right\|$, reveals solutions far above and below the xy -plane, e.g., for $|z| > 1$. To identify a point on one of these surfaces, consider the $\vec{\nabla}_r \Omega$ equations for large z values as compared to the x and y values. When the z magnitude is much larger than the x or y magnitudes (i.e., $|z| \gg \{ |x|, |y| \}$), the centripetal acceleration dominates the Ω_x and Ω_y terms and the gravitational acceleration only appears in the Ω_z term, as listed in Lemma 3.2.6.

Lemma 3.2.6 For $|z| \gg \{ |x|, |y| \}$: $\Omega_x \approx x$, $\Omega_y \approx y$, $\Omega_z \approx \frac{z}{|z|^3} = \frac{1}{z^2}$

Proof When the magnitude of z is very large compared to the magnitudes of x and y , the r_{13} and r_{23} distances each approximate to the z -displacement,

$$\begin{aligned} r_{13} &= \sqrt{(x + \mu)^2 + y^2 + z^2} \approx |z|, \\ r_{23} &= \sqrt{(x - 1 + \mu)^2 + y^2 + z^2} \approx |z|. \end{aligned}$$

Substituting these approximations into Equations (3.12) – (3.14) and noting that the fractions in Equations (3.12) and (3.13) may be approximated as zero yields the expressions in the lemma. ■

This result is consistent with intuition from the basic physics of the gravitational and centripetal accelerations. Because the system rotates about the \hat{z} axis, the centripetal acceleration scales with the planar position components, x and y , but is independent of z . Additionally, the centripetal acceleration is always oriented normal to the \hat{z} axis. On the other hand, when $|z|$ is large and $|x|$ and $|y|$ are small the gravitational acceleration is inversely proportional to the squared distance to the system barycenter and aligned with the vector to the barycenter. Subsequently, when $|z|$ is significantly larger than $|x|$ or $|y|$, the gravitational acceleration is approximately aligned with the $\pm \hat{z}$ -axis while the centripetal acceleration remains planar.

In the mission design context employed in this investigation, a set of low-thrust equilibrium points is parameterized by a β angle and an a_{lt} magnitude. Substituting the approximate Ω gradient from Lemma 3.2.6 into Equations (3.15) – (3.17) yields

$$\Upsilon_x \approx x + a_{\text{lt}} \cos \alpha \cos \beta = 0, \quad (3.27)$$

$$\Upsilon_y \approx y + a_{\text{lt}} \sin \alpha \cos \beta = 0, \quad (3.28)$$

$$\Upsilon_z \approx \frac{1}{z^2} + a_{\text{lt}} \sin \beta = 0. \quad (3.29)$$

Solve Equation (3.29) for z ,

$$z = \frac{\text{sgn } \beta}{\sqrt{a_{\text{lt}} |\sin \beta|}}, \quad (3.30)$$

leveraging Lemma 3.2.4 to resolve the sign of z . Accordingly, the solution to this system for a pair of β and a_{lt} values is a circle centered on the \hat{z} -axis at the z value described by Equation (3.30) with a radius of $a_{\text{lt}} \cos \beta$, as defined by the relationship between x , y , and α in Equations (3.27) – (3.28). This circle is the intersection between two surfaces parameterized by the planar and out-of-plane low-thrust acceleration components. The first surface is a cylinder of constant centripetal acceleration magnitude equal to the planar low-thrust acceleration magnitude, $a_{\text{lt}} \cos \beta$; the axis of the cylinder is the \hat{z} -axis. The second surface is approximated by a plane centered on the \hat{z} axis and located at a z -coordinate where the gravitational acceleration balances the out-of-plane component of the low-thrust acceleration vector, $a_{\text{lt}} \sin \beta$; the plane normal vector is equal to \hat{z} .

Because the relationships in Equations (3.27) – (3.29) rely on approximate values of the Ω gradient, the solutions to these equations are not exact solutions to the full nonlinear relationships expressed in Equations (3.15) – (3.17). Thus, a point on the circle of approximate solutions,

$$\vec{\mathcal{X}}(\alpha) = \left\{ -a_{\text{lt}} \cos \alpha \cos \beta \quad -a_{\text{lt}} \sin \alpha \cos \beta \quad \frac{\text{sgn } \beta}{\sqrt{a_{\text{lt}} |\sin \beta|}} \quad \alpha \quad \beta \right\}, \quad (3.31)$$

is employed as an initial guess for a differential corrections and/or continuation process that constructs the set of equilibria at the specified β and a_{lt} values. For consistency with the collinear solutions, a point for $\alpha = 0$ or $\alpha = \pi$ may be employed.

Additional topological information about the set of the solutions located far above and below the xy -plane is available from Equation (3.31). First, the z -coordinate tends to $\pm\infty$ as β tends to zero. More specifically, $z \rightarrow -\infty$ as $\beta \rightarrow 0^-$ ($\beta < 0$) and $z \rightarrow \infty$ as $\beta \rightarrow 0^+$ ($\beta > 0$). This result is consistent with Lemma 3.2.3, i.e., all solutions for $\beta = 0$ are located in the xy -plane, insofar as there is no solution on this out-of-plane structure for $\beta = 0$. Second, the z -coordinate reaches a minimum magnitude at $z = \pm a_{\text{lt}}^{-1/2}$ when $\beta = \pm\pi/2$. Thus, the surface of equilibrium points does not reach the xy -plane (besides the infeasible limit $a_{\text{lt}} \rightarrow \infty$) and, for practical magnitudes on the order of 10^{-2} to 10^{-1} , remain higher than $|z| = 3$. Finally, observe that the radius of the circle increases as $|\beta|$ decreases from $\pi/2$ to zero. That is, when $\beta = \pi/2$, the radius is zero and the circle collapses to a single point. On the other hand, as $|\beta|$ approaches zero, the radius of the circle approaches a_{lt} . Combining these topological observations, the surface of equilibrium points for a fixed a_{lt} value and the full range of β values is qualitatively similar to two parabolic dishes, symmetric over the xy -plane and centered on the \hat{z} -axis. Plots of these surfaces are included in Section 3.2.4 (e.g., see Figure 3.6).

3.2.3 Analytical Solutions

In contrast to the collinear points and highly out-of-plane solutions, some low-thrust equilibrium points can be located entirely via analytical methods. To simplify Equations (3.15) – (3.17), let $\alpha = 0$ or π , reducing the $\sin(\alpha)$ term in Equation (3.16) to zero. While setting $y = 0$ solves the resulting equation and yields the collinear points described in Section 3.2.1 as well as two highly out-of-plane points described in Section 3.2.2, the equation is also solvable when $y \neq 0$. In this latter case, an analytical expression for the locations of two symmetric sets of equilibria is derived

as a function of β . Additionally, four point-solutions are derived for $\beta = \pm\pi/2$ and $y \neq 0$ independently of the α angle (when $\beta = \pm\pi/2$, the \vec{a}_{1t} vector orientation is independent of α).

Solutions for $\alpha = 0$ and $\alpha = \pi$

Consistent with the assumptions above, set $\alpha = 0$ or $\alpha = \pi$ and constrain $y \neq 0$. Under these constraints, the terms within the square brackets in Equation (3.16) must sum to zero. As these terms also appear in Equations (3.15) and (3.17), the EOMs simplify to

$$-\mu + \frac{\mu}{r_{23}^3} + a_{1t} \cos(\alpha) \cos(\beta) = 0, \quad (3.32)$$

$$1 - \frac{1 - \mu}{r_{13}^3} - \frac{\mu}{r_{23}^3} = 0, \quad (3.33)$$

$$z - a_{1t} \sin(\beta) = 0. \quad (3.34)$$

Equation (3.32) is solved for r_{23} , yielding

$$r_{23} = \left[\frac{\mu}{\mu - a_{1t} \cos(\alpha) \cos(\beta)} \right]^{1/3}. \quad (3.35)$$

Substitute this expression into Equation (3.33) and solve for r_{13} ,

$$r_{13} = \left[\frac{1 - \mu}{1 - \mu + a_{1t} \cos(\alpha) \cos(\beta)} \right]^{1/3}. \quad (3.36)$$

Finally, Equation (3.34) is straightforwardly solved for z . Given the two radial distances from the primaries and the z -coordinate, up to two equilibrium solutions are located via the intersection between the r_{13} and r_{23} spheres centered on P_1 and P_2 , respectively, and the plane $z = a_{1t} \sin(\beta)$, as depicted in Figure 3.3. To identify the x - and y -coordinates of the equilibrium point, project the r_{13} - r_{23} - r_{12} triangle into the

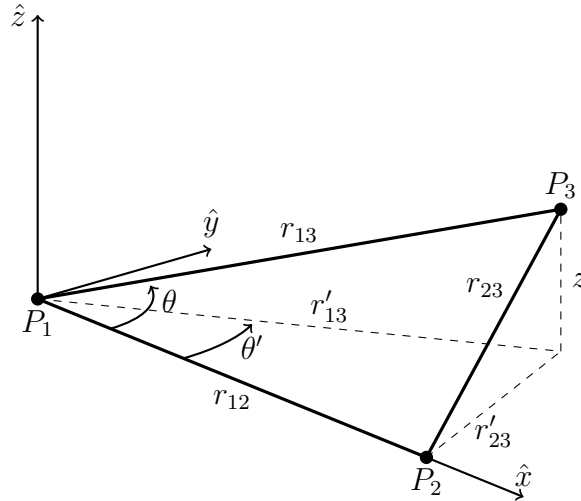


Figure 3.3.: An equilibrium point is located by the intersection r_{13} and r_{23} spheres at the specified z coordinate

xy -plane, resulting in a new triangle with projected side lengths r'_{13} and r'_{23} , as in Figure 3.3. These projected lengths are available from the Pythagorean theorem,

$$r'_{13} = \sqrt{r_{13}^2 - z^2}, \quad (3.37)$$

$$r'_{23} = \sqrt{r_{23}^2 - z^2}. \quad (3.38)$$

Apply the law of cosines to compute two angles within the triangles,

$$\theta = \arccos \left[\frac{1 + r_{13}^2 - r_{23}^2}{2r_{13}} \right], \quad (3.39)$$

$$\theta' = \arccos \left[\frac{1 + r_{13}^2 - r_{23}^2}{2r'_{13}} \right], \quad (3.40)$$

where θ is the angle between the positive \hat{x} -axis and the \vec{r}_{13} vector and θ' is the corresponding angle in the projected triangle. (In these expressions, the unit values represent the r_{12} distance, a convenient value that results from the nondimensional-

ization of the problem.) Using trigonometry, the locations of two solutions are given by

$$\vec{r} = \left\{ -\mu + r'_{13} \cos(\theta') \quad \pm r'_{13} \sin(\theta') \quad a_{\text{lt}} \sin(\beta) \right\}^T. \quad (3.41)$$

The symmetry of these solutions is apparent from the geometry; the intersection between two spheres centered on P_1 and P_2 is a circle orthogonal to and centered on the x -axis, and the intersection between that circle and the plane at z yields two solutions symmetric about the xz -plane. This mirroring is also available from the symmetry conditions discussed at the beginning of the section. Because $\alpha = 0$ or $\alpha = \pi$ at these solutions, the change of coordinates to $-\alpha$ does not affect the orientation of \hat{a}_{lt} and the remaining symmetry is the $y \rightarrow -y$ change. To express these coordinates in terms of the non-projected quantities, apply the identities $\cos(\arccos(b)) = b$ and $\sin(\arccos(b)) = \sqrt{1 - b^2}$. Accordingly, the locations of the equilibria are

$$\vec{\mathcal{X}} = \left\{ \begin{array}{c} -\mu + \frac{1}{2}(1 + r_{13}^2 - r_{23}^2) \\ \pm \sqrt{r_{13}^2 - a_{\text{lt}}^2 \sin^2(\beta) - \frac{1}{4}(1 + r_{13}^2 - r_{23}^2)^2} \\ a_{\text{lt}} \sin(\beta) \\ 0 \text{ or } \pi \\ \beta \end{array} \right\}. \quad (3.42)$$

where r_{13} and r_{23} are functions of μ , a_{lt} , α , and β , as expressed in Equations (3.35) and (3.36). Note that Equation (3.42) is a continuous function of β , yielding a continuum of equilibrium points for $\beta \in [-\pi/2, \pi/2]$. Additionally, the solutions are mirrored over the xy -plane, i.e., over $\beta = 0$.

Because the low-thrust acceleration level, a_{lt} , and the out-of-plane orientation angle, β , may vary over a wide range of values, it is prudent to determine the limits of validity of the equations that deliver these equilibrium locations. As r_{13} and r_{23}

must be positive, the cubed distances, i.e., the arguments within the square brackets in Equations (3.35) and (3.36), must also be positive; the conditions

$$\mathcal{F}_1 = a_{lt} \cos(\alpha) \cos(\beta) + 1 - \mu > 0, \quad (3.43)$$

$$\mathcal{F}_2 = a_{lt} \cos(\alpha) \cos(\beta) - \mu < 0 \quad (3.44)$$

satisfy these constraints. Additionally, the argument of the arccosine function in Equation (3.39) is constrained,

$$\frac{1 + r_{13}^2 - r_{23}^2}{2r_{13}} \leq 1, \quad (3.45)$$

$$\frac{1 + r_{13}^2 - r_{23}^2}{2r_{13}} \geq -1. \quad (3.46)$$

Rearrange the terms in these inequalities and simplify expanded quadratic terms to yield

$$(r_{13} - 1)^2 \leq r_{23}^2, \quad (3.47)$$

$$(r_{13} + 1)^2 \geq r_{23}^2. \quad (3.48)$$

Equation (3.48) may be simplified as the terms on both sides of the inequality are always positive. However, Equation (3.47) cannot be simplified further because $r_{13} - 1$ is not always positive. Accordingly, two constraints are written,

$$\mathcal{F}_3 = (r_{13} - 1)^2 - r_{23}^2 \leq 0, \quad (3.49)$$

$$\mathcal{F}_4 = r_{13} - r_{23} + 1 \geq 0. \quad (3.50)$$

Finally, a constraint that enforces the *triangle inequality*² is written,

$$\mathcal{F}_5 = r_{13} + r_{23} - 1 \geq 0. \quad (3.51)$$

² The sum of two sides of a triangle must exceed the third side

A visual inspection of these inequalities over a range of a_{1t} and μ values, as depicted in Figure 3.4, reveals the active and inactive constraints. Each small plot at the

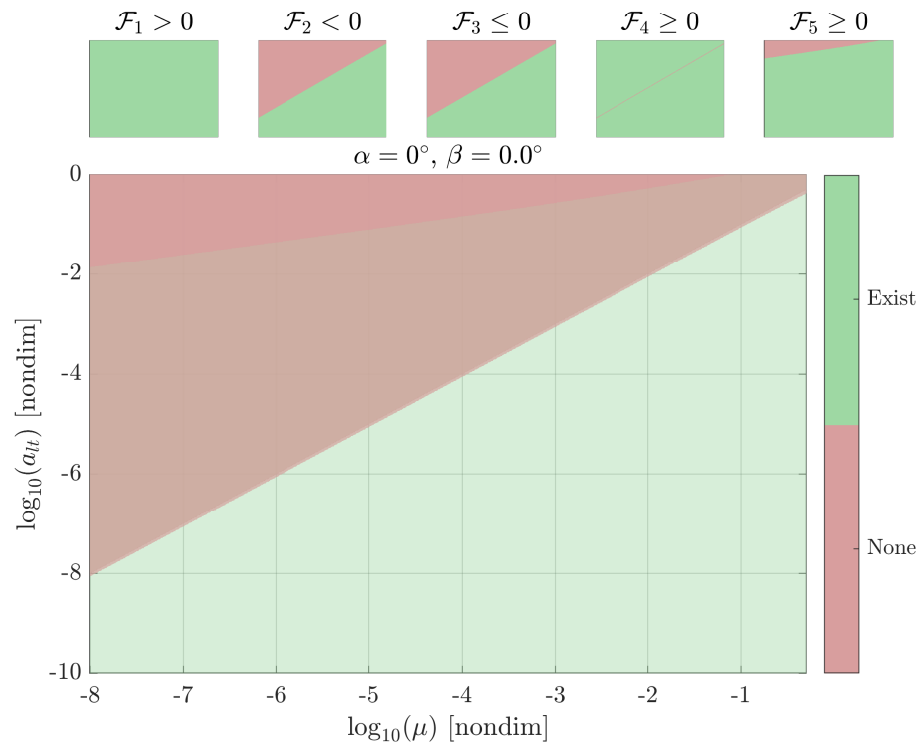


Figure 3.4.: For some μ values, there is no analytical solution for the equilibria at $\alpha = 0$ and $y \neq 0$ ([Animation](https://engineering.purdue.edu/people/kathleen.howell.1/Publications/Dissertations/2020_Cox/#analyticalEqPts)³)

top of the figure represents one of the inequalities, with green regions representing a satisfied inequality and red regions representing an unsatisfied inequality; the axes of the small plots are identical to the larger plot below them. The superposition of the individual inequalities, depicted in the large plot, shows all combinations of μ and a_{1t} for which an analytical solution is available in green and all other combinations (i.e., with no analytical solution) in red. As seen in the smaller inequality plots, the \mathcal{F}_2 , \mathcal{F}_3 , and \mathcal{F}_4 inequalities are active constraints on the availability of the analytical solution over large sections of the the solution space. The \mathcal{F}_4 constraint is active in a thin diagonal strip near $a_{1t} = \mu$, overlapping with the other inequalities and slightly further

³https://engineering.purdue.edu/people/kathleen.howell.1/Publications/Dissertations/2020_Cox/#analyticalEqPts

restricting the set of μ and a_{lt} combinations that admit a solution. For $\alpha = \beta = 0$, as in the plot, the equilibria with $y \neq 0$ generally exist when $a_{lt} < \mu$. For example, in the Earth-Moon system ($\mu \approx 10^{-2}$), these equilibria only exist for $a_{lt} < 10^{-2}$, i.e., these equilibrium solutions do not exist when the low-thrust magnitude is as high as delivered by the spacecraft listed in Table 2.1.

The solutions for $\alpha = \pi$ and $\beta = 0$ are less restrictive than the solutions for $\alpha = 0$. The visualization of the constraints in Figure 3.5 demonstrates this contrast, with a much larger green region representing the existence of the equilibrium points with $y \neq 0$. In this latter case, only the \mathcal{F}_1 and \mathcal{F}_3 constraints are active. Solutions

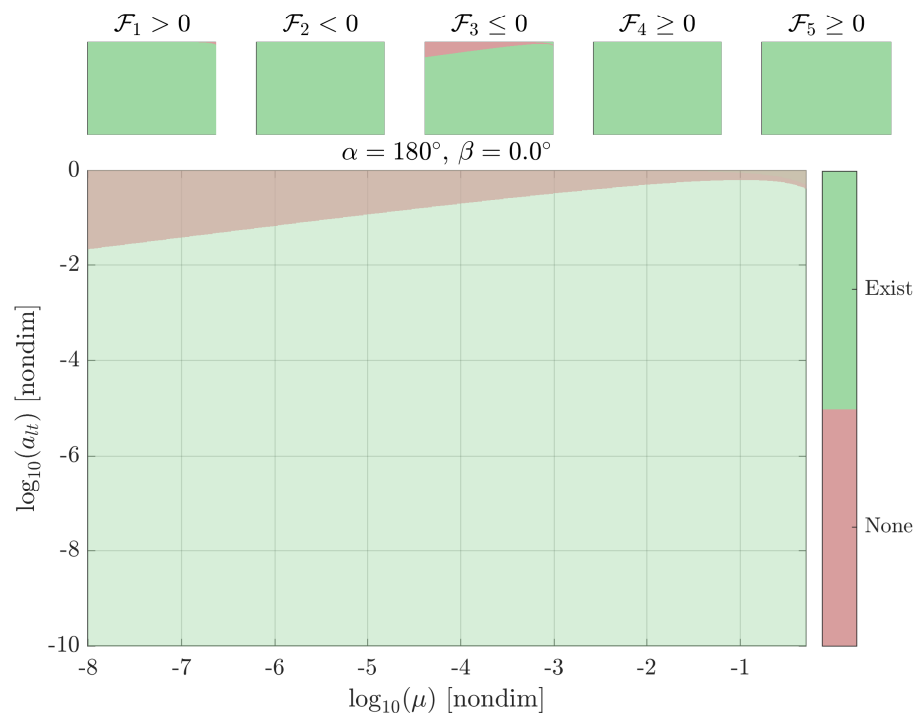


Figure 3.5.: For some μ values, there is no analytical solution for the triangular equilibria at $\alpha = \pm\pi$ (Animation⁴)

are available in the Earth-Moon system for low-thrust acceleration values as high as $a_{lt} = 0.537$, a very large magnitude. Due to the significantly increased region of

⁴https://engineering.purdue.edu/people/kathleen.howell.1/Publications/Dissertations/2020_Cox/#analyticalEqPts

validity compared to $\alpha = 0$, the analytical solutions for the equilibria with $\alpha = \pi$ serve as excellent seed solutions for continuation processes that construct the full set of equilibrium points in the CR3BP+LT. For both $\alpha = 0$ and $\alpha = 180^\circ$, the $\mathcal{F}_1 - \mathcal{F}_5$ constraints are most restrictive when $\beta = 0$. As $|\beta|$ increases, the red, constrained regions of the μ vs. a_{lt} space shrink (see the linked animations to visualize these changes); for $\beta = \pm\pi/2$, solutions exist for every practical combination of μ and a_{lt} , as discussed in the next section

Solutions for $\beta = \pm\pi/2$

The analytical solutions derived in the previous section may be simplified further in the special case when $\beta = \pm\pi/2$. When this β angle is substituted into Equations (3.35) and (3.36), the two distances reduce to unity, $r_{23} = 1$ and $r_{13} = 1$ and Equation (3.34) is straightforwardly solved for z . Accordingly, two equilibria are located at the vertices of two inclined equilateral triangles with the other two vertices located at P_1 and P_2 . Projecting these triangles into the xy -plane yields isosceles triangles with side lengths

$$r'_{13} = r'_{23} = \sqrt{1 - a_{\text{lt}}^2}, \quad (3.52)$$

and $r_{12} = 1$, similar to the more general depiction in Figure 3.3. Consistent with the process employed previously, the x - and y -coordinates are located by computing an angle in the projected triangle, θ' ,

$$\theta' = \arccos \left[\frac{1 + r'_{13}{}^2 - r'_{23}{}^2}{2r'_{13}} \right] = \arccos \left[\frac{1}{2} \sqrt{1 - a_{\text{lt}}^2} \right]. \quad (3.53)$$

The locations of the equilibrium points are given by the vector,

$$\vec{r} = \left\{ -\mu + r'_{13} \cos(\theta') \quad \pm r'_{13} \sin(\theta') \quad a_{\text{lt}} \sin(\beta) \right\}^T. \quad (3.54)$$

By again applying trigonometric identities, this expression is simplified to

$$\vec{\mathcal{X}} = \left\{ -\mu + \frac{1}{2} \quad \pm \sqrt{\frac{3}{4} - a_{\text{lt}}^2} \quad a_{\text{lt}} \sin(\beta) \quad \alpha \quad \beta = \pm\pi/2 \right\}^T. \quad (3.55)$$

Unlike the solutions for $\alpha = 0$ and $\alpha = \pi$, the validity of these solutions is consistent across all systems (i.e., across all μ values). The only constraint on the existence of these solutions is $a_{\text{lt}} \leq \sqrt{3}/2$. As the a_{lt} value increases, the solutions move further from the xy -plane and closer to the xz -plane. Additionally, these solutions are independent of α . This property follows intuitively from the geometry of \vec{a}_{lt} ; when $\beta = \pm\pi/2$, the \vec{a}_{lt} vector is oriented along the $\pm\hat{z}$ vector. Accordingly, the in-plane orientation of the vector, i.e., α , is undefined.

3.2.4 General Locations

In general, Equations (3.15) – (3.17) possess no “simple” solutions, i.e., no analytical expression or one-dimensional function locates the equilibrium points for arbitrary α and β angles. Thus, continuation methods are employed to compute the locations of all of the equilibrium points. Given a low-thrust acceleration magnitude, a_{lt} , the three collinear solutions for $\alpha = 0$ or $\alpha = \pi$ and $\beta = 0$ are quickly located via the one-dimensional root finding algorithms described in Section 3.2.1. Additionally, the approximate locations of four points on the highly out-of-plane ZAS’s are computed for $\alpha = 0$ and $\alpha = \pi$ for any $\beta \neq 0$ angle as outlined in Section 3.2.2. If a_{lt} satisfies the $\mathcal{F}_1, \dots, \mathcal{F}_5$ constraints in Section 3.2.3, additional solutions are available for $\alpha = 0$ and $\alpha = \pi$ and an arbitrary β value. All of these solutions may be used to initialize continuation processes that evolve the initial equilibrium point solutions along single-parameter *families*. In this investigation, the β angle is fixed and the families, or *sets*, of equilibrium points are parameterized by α . The opposite configuration – fixing α and evolving the families along β – may also be employed but is not explored in this investigation. Due to the symmetry described at the beginning of Section 3.2, a full set of equilibrium points (i.e., solutions for all values of $\alpha \in [-\pi, \pi]$) is available by

computing a subset of the equilibrium points for $\alpha \in [0, \pi]$. Thus, given the solutions that have been derived thus far, it is possible to construct a set of equilibria across the full range of α at a specified a_{lt} magnitude and β angle. Performing this computation over the half range of β values, i.e., $\beta \in [0, \pi/2]$, yields all of the equilibrium points associated with the specified low-thrust acceleration magnitude (symmetry over $\beta = 0$ yields the other half of the points without further calculations). Additional details about the equilibrium point computation algorithm are supplied in Section E.1.

To identify these structures independently of the natural equilibrium points, the low-thrust equilibria are described via set notation,

$$\mathbb{E}_i(a_{lt}) = \left\{ \vec{\mathcal{X}} \mid \vec{\nabla}_r \Upsilon(a_{lt}, \vec{\mathcal{X}}) = \vec{0} \right\}, \quad (3.56)$$

where i is an index that identifies a set of solutions (i.e., a ZAS), similar to the indices of the Lagrange points. Each set is a two-dimensional surface of equilibrium solutions that is parameterized by α and β and is spatially distinct from other sets, as illustrated by the zero acceleration surfaces (ZAS's) in the Earth-Moon system for $a_{lt} = 2.5e-1$ in Figure 3.6. This large (larger than is technologically feasible at the time of writing) low-thrust acceleration magnitude is selected to aid in the visualization; smaller a_{lt} values correlate to smaller surfaces that are more difficult to see but qualitatively similar to the surfaces in Figure 3.6. At this acceleration magnitude, four distinct surfaces exist: two ellipsoidal surfaces, \mathbb{E}_1 and \mathbb{E}_2 centered on the L_1 and L_2 points, a large C-shaped surface denoted \mathbb{E}_3 that encompasses L_3 , L_4 , and L_5 , and the two-sided parabolic dish \mathbb{E}_4 surface. Although the \mathbb{E}_4 set is discontinuous, each ‘‘hemisphere’’ represents only half of the β angle range. Thus, the two halves together represent the set of highly out-of-plane equilibria over the full range of β values and are collectively denoted \mathbb{E}_4 without any ambiguity.

The symmetries described in Lemma 3.2.5 are illustrated by the surfaces in Figure 3.6. The simplest symmetry to observe is the mirroring over the xy -plane and over $\beta = 0$, as seen in Figure 3.6(b); all solutions for $\beta = 0$ are located on the xy -plane

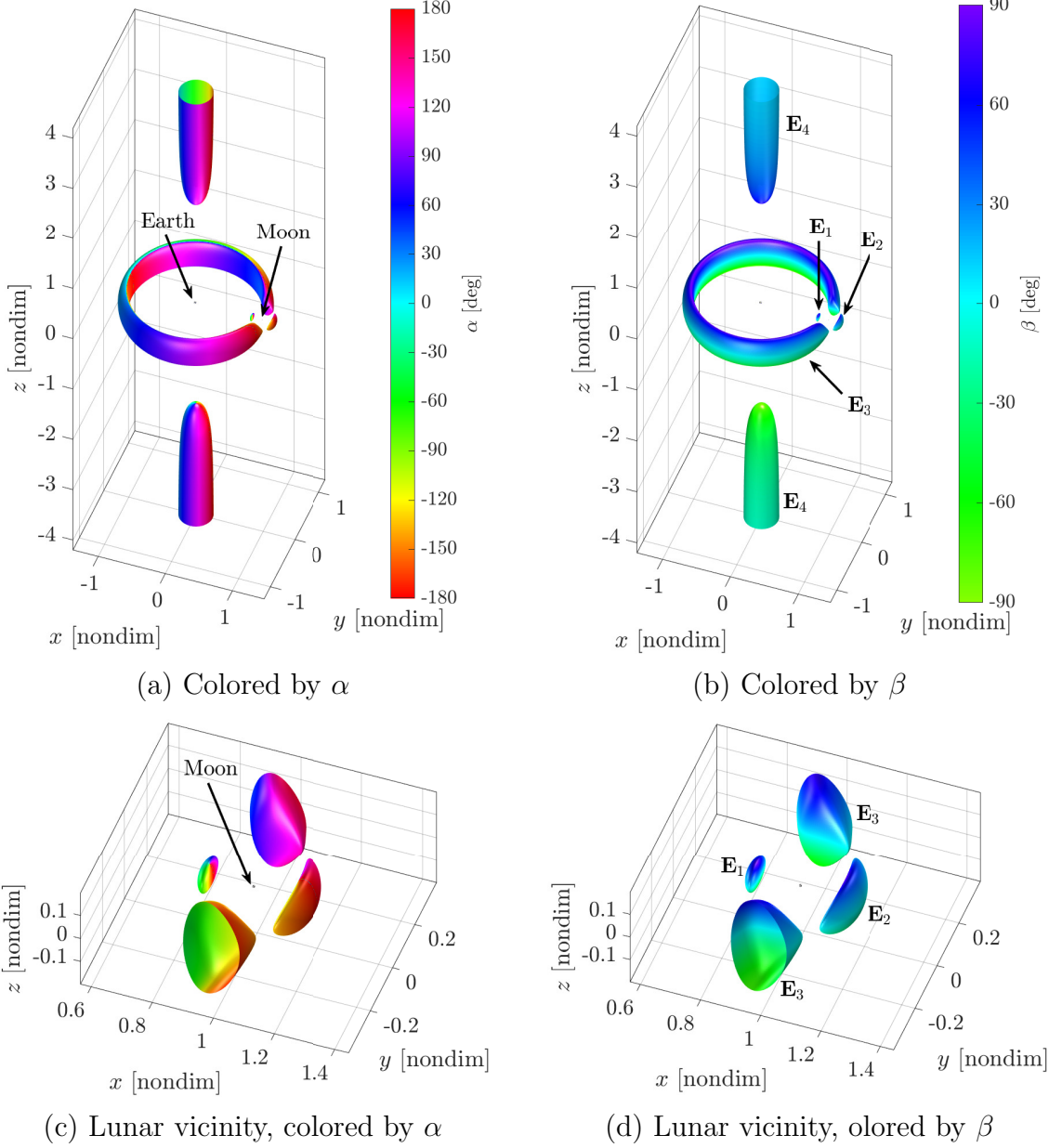


Figure 3.6.: Four sets of low-thrust equilibria, $\mathbb{E}_1 - \mathbb{E}_4$, are isosurfaces matching an acceleration magnitude of $a_{lt} = 2.5e-1$ in the Earth-Moon CR3BP+LT

and solutions for $\beta \neq 0$ are mirrored over that plane, consistent with Lemmas 3.2.3 and 3.2.4. Additionally, note that the points on \mathbb{E}_4 , i.e., the highly out-of-plane solutions, trend toward a β angle of zero as $|z|$ trends toward $\pm\infty$, as predicted by the approximate solutions derived in Section 3.2.2. The symmetry over the xz -plane is

also apparent in the geometry of the surfaces. The relationship between this symmetry and the α angle is more difficult to discern from the plot, but available nonetheless. Solutions for $\alpha = 0$ (colored cyan in Figure 3.6(a)) and for $\alpha = 180^\circ$ (red) are located on the xz -plane, as predicted by Lemma 3.2.2. Solutions for $y \neq 0$ are mirrored across this plane with α angles mirrored over $\alpha = 0$. For a more straightforward visualization of this symmetry, see the planar slice of these surfaces depicted in Figure 3.7.

The number of equilibria sets (i.e., the maximum value of i) varies with a_{1t} and the system mass ratio, μ . In general, when the a_{1t} is “small” six sets exist (i.e., $i = 1, 2, \dots, 6$). As a_{1t} increases, these sets evolve and merge, yielding fewer distinct surfaces. To illustrate this evolution, consider the one-dimensional *zero acceleration contours* (ZACs), subsets of the zero acceleration surfaces at specific β values,

$$\mathbb{E}_i(a_{1t}, \beta) \subset \mathbb{E}_i(a_{1t}). \quad (3.57)$$

For $\beta = 0$ and a small acceleration magnitude of $a_{1t} = 8.00\text{e-}3$, five distinct contours exist in the Earth-Moon system, as illustrated in Figure 3.7(a). Note that the highly out-of-plane equilibrium points do not exist when $\beta = 0$ and, thus, are not included in the figure. The ZAC contours (equivalently, the surfaces that the contours are a subset of) remain near the natural CR3BP equilibrium points, marked by black asterisks; the low-thrust equilibria librate about the Lagrange points as α varies. Though not pictured, similar librations occur out of the plane as β varies. For consistency with the ballistic equilibria, the five sets of low-thrust equilibrium solutions are numbered by their proximity to the ballistic points, i.e., \mathbb{E}_1 surrounds L_1 , \mathbb{E}_2 surrounds L_2 , etc. For nonzero β values at this small a_{1t} value, the highly out-of-plane solutions are denoted \mathbb{E}_6 .

As a_{1t} increases, the location differences between the CR3BP+LT equilibria and the CR3BP equilibria increase. Additionally, the surfaces begin to merge (see the linked animation in the figure caption). For example, when the low-thrust acceleration

⁵https://engineering.purdue.edu/people/kathleen.howell.1/Publications/Dissertations/2020_Cox/#zacs2D

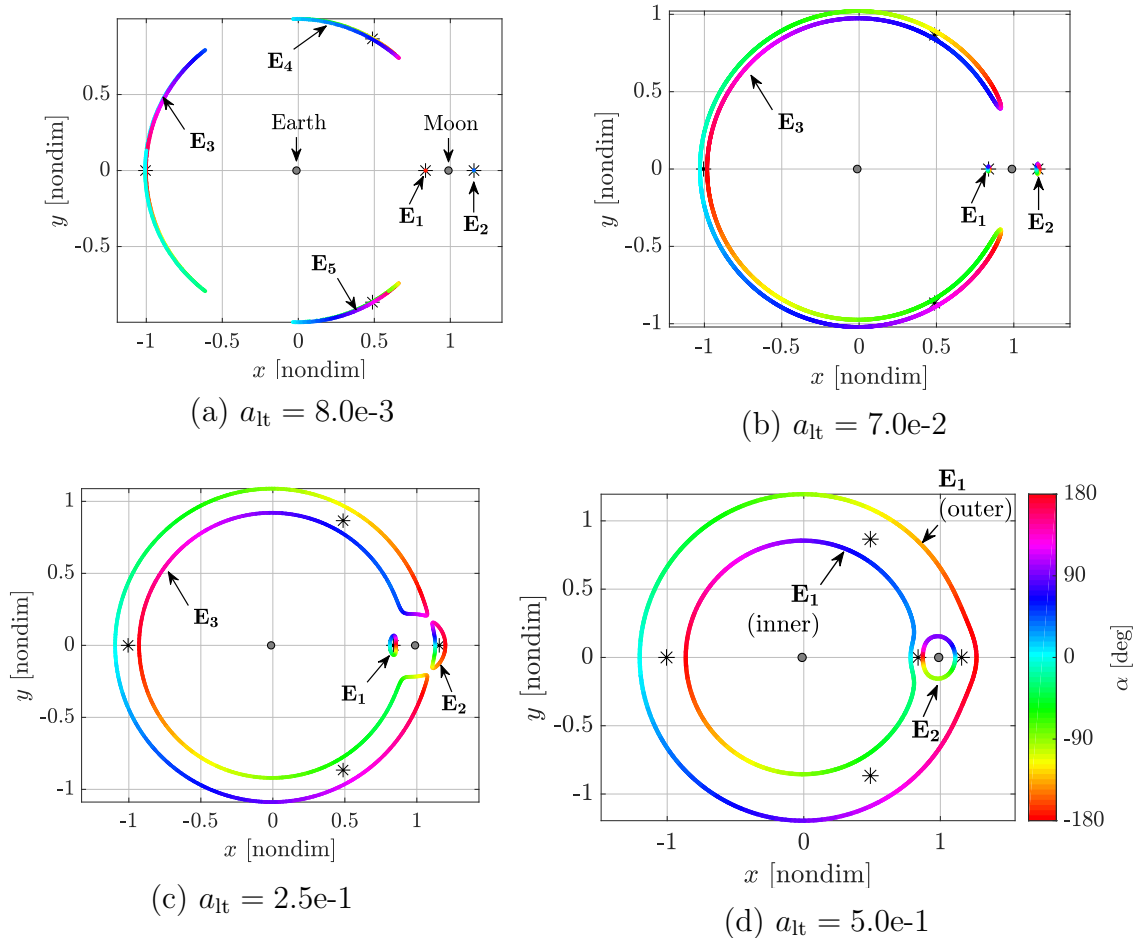
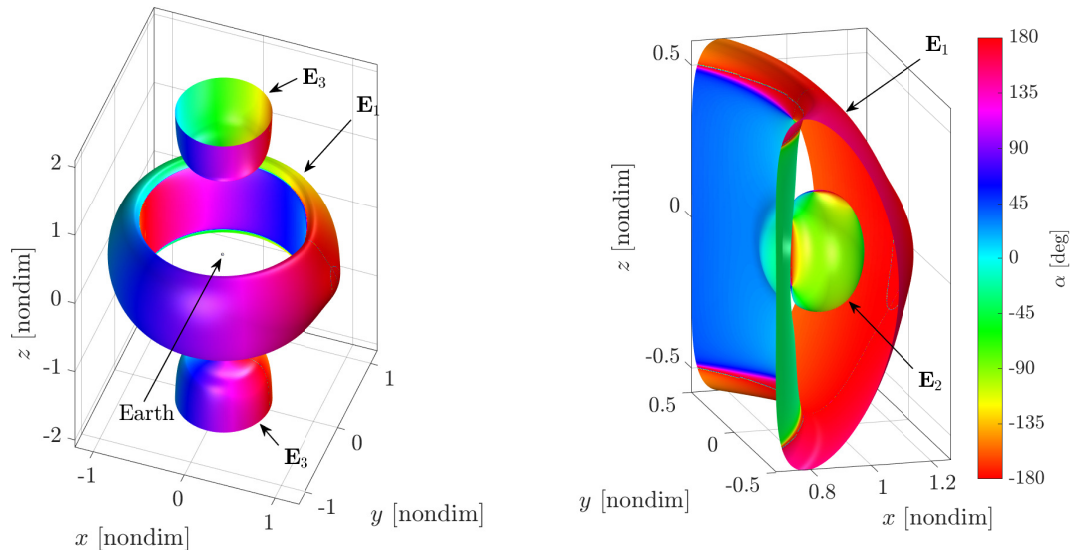


Figure 3.7.: Earth-Moon CR3BP+LT equilibrium points over a range of a_{lt} values, plotted as colored points for $\alpha \in [-\pi, \pi]$ and $\beta = 0$; black asterisks mark the CR3BP Lagrange points, and the primaries are located by gray circles ([Animation](#)⁵)

magnitude increases to $a_{lt} = 7e-2$, as in Figure 3.7(b), the \mathbb{E}_3 , \mathbb{E}_4 and \mathbb{E}_5 surfaces merge into one large C-shaped surface that surrounds L_3 , L_4 and L_5 and is labeled \mathbb{E}_3 . At the larger a_{lt} value of $2.5e-1$, depicted in Figures 3.6 and 3.7(c), the ZACs (and ZAS's) continue to expand. With further increases in thrust magnitude, the \mathbb{E}_3 and \mathbb{E}_2 surfaces merge. At even higher a_{lt} values, another merge occurs, resulting in the structures plotted in Figure 3.7(d). At this large a_{lt} value, the three distinct ZACs actually correspond to *two* distinct ZAS's, as seen in Figure 3.8. The two \mathbb{E}_1 ZACs, labeled “inner” and “outer”, are the inner and outer “walls” of the \mathbb{E}_1 surface that



(a) System view; \mathbb{E}_1 and \mathbb{E}_3 are visible

(b) The \mathbb{E}_2 structure is surrounded by the \mathbb{E}_1 structure

Figure 3.8.: Earth-Moon low-thrust equilibria for $a_{1t} = 5e-1$, colored by α angle; three distinct surfaces exist for this thrust magnitude

encompasses all five ballistic equilibrium points, the Moon, and the \mathbb{E}_2 structure. A close up view of the lunar vicinity, depicted in Figure 3.8(b), reveals the ellipsoidal \mathbb{E}_2 ZAS surrounding the Moon. To maintain consistent labeling of the zero acceleration surfaces (ZAS's), a few simple rules are proposed:

1. The indices begin at 1 and increase with no gaps (e.g., \mathbb{E}_4 cannot exist without \mathbb{E}_3).
2. A ZAS that surrounds a single Lagrange point is identified by the matching index (e.g., \mathbb{E}_1 and \mathbb{E}_2 surround L_1 and L_2 in Figure 3.7(b)).
3. A ZAS that surrounds a single primary is identified by the matching index (e.g., \mathbb{E}_1 and \mathbb{E}_2 surround P_1 and P_2 in Figures 3.7(d) and 3.8).
4. When rules 2 and 3 do not apply or are ambiguous, the index increases with size as measured by the distance from the barycenter and the highly out-of-plane equilibria always receive the largest index.

Although these rules are arbitrary, they link the novel configurations of the ZAS's to the more intuitively known locations of the Lagrange points and primary bodies.

Similar structures are observed in different systems, although not necessarily at the same nondimensional thrust magnitudes. For example, the ZACs for a low-thrust acceleration of 0.19 mm/s^2 in the Earth-Moon and Sun-EMB systems (EMB here represents the Earth-Moon barycenter) systems possess very different geometries, as seen in Figure 3.9. The nondimensional value of this acceleration, consistent with

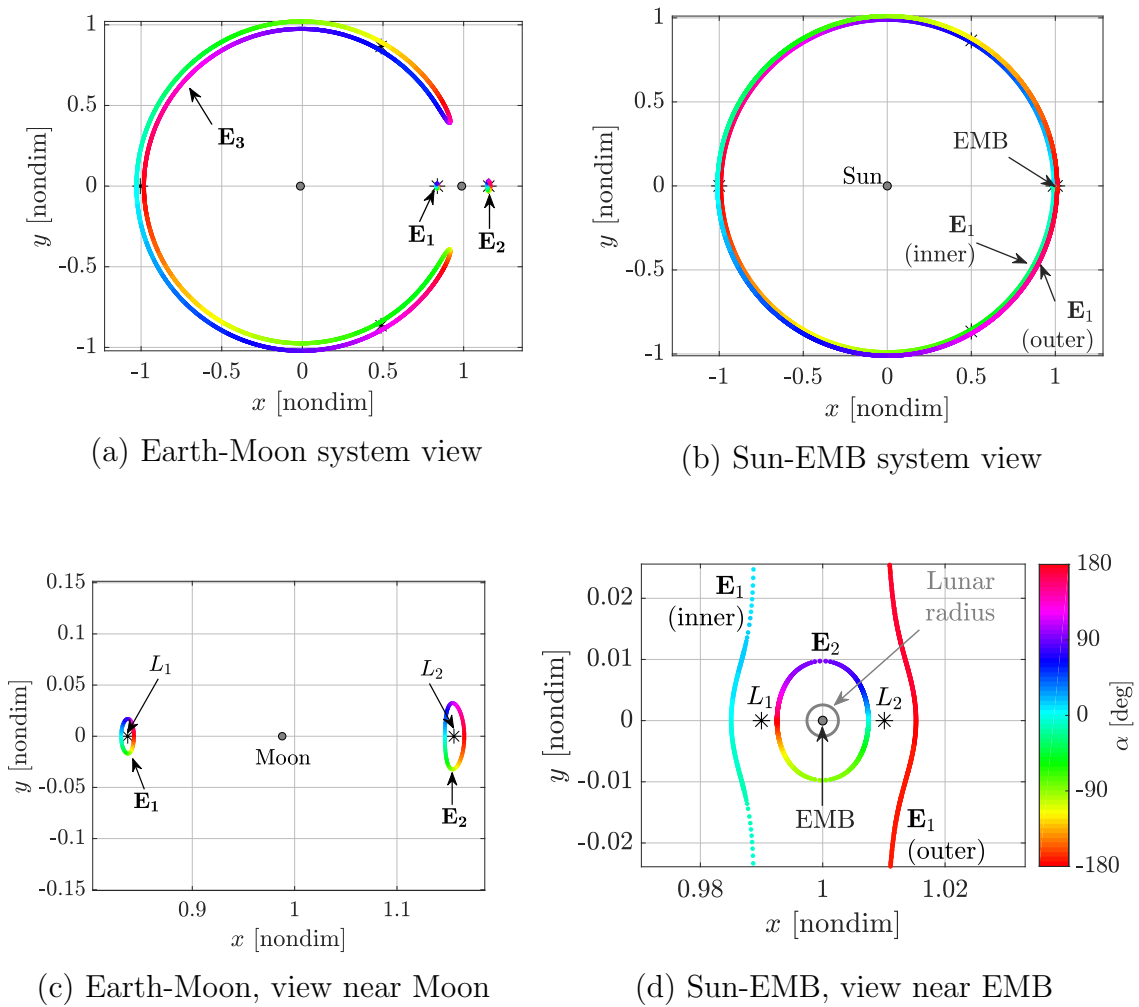


Figure 3.9.: Comparison of Earth-Moon and Sun-EMB ZACs for $a_{lt} = 0.19 \text{ mm/s}^2$ and $\beta = 0$ ([Animation](#)⁶)

the Deep Space 1 capability, varies between the two systems: $7e-2$ in the Earth-Moon system and $3.2e-2$ in the Sun-EMB system. Despite the fact that the nondimensional acceleration magnitude is larger in the Earth-Moon system than in the Sun-EMB system, the Earth-Moon ZACs are *more* similar to the ballistic equilibrium points than the Sun-Earth ZACs. In fact, the structures in the Sun-EMB system resemble the ZACs in the Earth-Moon system for a_{lt} magnitudes an order of magnitude larger, such as those depicted in Figure 3.7(d) for $a_{lt} = 5e-1$. In other words, the low-thrust acceleration delivered by the Deep Space 1 propulsion system influences the dynamics of the Sun-EMB system more dramatically than the dynamics of the Earth-Moon system. This observation is consistent with the analysis conducted in Section 2.2.6 where the low-thrust Hamiltonian rate is compared between systems.

While the ZACs plotted in Figures 3.7 and 3.9 appear similar in geometry to the CR3BP forbidden regions (often called *zero velocity contours* or ZVCs), the ZACs do not bound the spacecraft motion. For every \vec{a}_{lt} vector, there exist a set of three to six distinct equilibria across the ZACs; the full contours represent the equilibria for every orientation of \vec{a}_{lt} . Accordingly, the locations of the equilibria are shifted as rapidly as the thrust vector is reoriented, e.g., via engine gimbaling or spacecraft reorientation. Similarly, throttling the low-thrust propulsion system to modify the delivered acceleration affects the size and geometry of the ZAS's and ZACs. Thus, the low-thrust acceleration vector may be leveraged to adjust the equilibrium solutions and the associated dynamical structures to achieve a specific mission design goal.

3.2.5 ZAS Merge Locations

For further insight into the ZAS geometries, a representation of the natural acceleration magnitude field is constructed. Specifically, the acceleration magnitude field,

$$a_{\text{nat}}(x, y, z) = \left\| \vec{a}_{\text{nat}} \Big|_{\text{eq}} \right\| = \left\| \vec{\nabla}_r \Omega \right\|,$$

⁶https://engineering.purdue.edu/people/kathleen.howell.1/Publications/Dissertations/2020_Cox/#zacs2DSE

is employed, where $\vec{a}_{\text{nat}}|_{\text{eq}}$ is defined in Equation (3.6). As the ZAS's represent iso-surfaces in this field, a range of ZAS geometries may be represented by a contour plot of a_{nat} , as depicted in Figure 3.10. Three slices are utilized: the xy -plane ($z = 0$), the

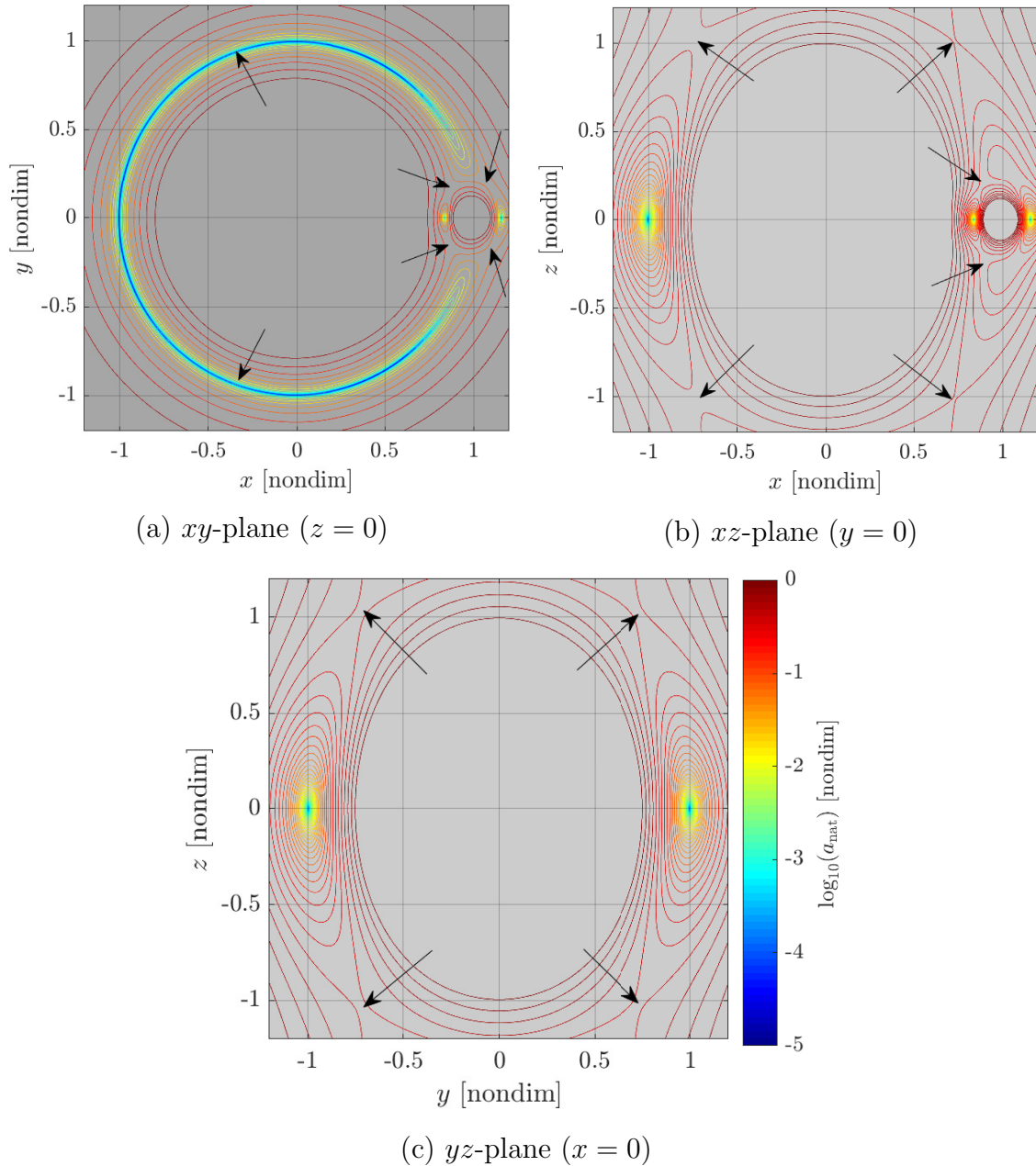


Figure 3.10.: Contours of constant acceleration magnitude, A , in the Earth-Moon CR3BP in the three principal planes; arrows locate topological saddles in the field

xz -plane ($y = 0$), and the yz -plane ($x = 0$). The planar ZACs shown in Figure 3.7 are depicted in the xy -plane contours in Figure 3.10(a), with blue contours corresponding to small a_{lt} values and warmer (yellow, orange, red) colors corresponding to higher a_{lt} magnitudes. The other two slices in Figures 3.10(b) and 3.10(c) supply additional information about the 3D ZAS's. For example, the ellipsoidal shape of the \mathbb{E}_1 and \mathbb{E}_2 ZAS's in Figure 3.6 is apparent from the contours in the xy - and xz -slices of the a_{nat} field. Similarly, the ellipsoidal cross-section of the C-shaped \mathbb{E}_3 ZAS is captured in the contours near $x = -1$ in the xz -plane representation and the contours near $y = \pm 1$ in the yz -plane.

Besides depicting the geometry of the ZAS's across a wide range of acceleration magnitudes, the a_{nat} field contours clearly show the locations and acceleration magnitudes where the ZAS's merge. These merges, introduced in the previous section and illustrated in Figure 3.7, occur at topological saddles in the natural acceleration magnitude field, marked by arrows in Figure 3.10. For a more intuitive understanding of the relationship between ZAS merges and the acceleration magnitude field, consider the planar dynamics ($\beta = 0$) represented by the xy -slice of the a_{nat} field in Figure 3.10(a). A 3D representation of the planar acceleration magnitude field for the Pluto-Charon system, plotted in Figure 3.11, displays qualitatively identical contours as the Earth-Moon field in Figure 3.10(a), but with more pronounced curvature due to the higher mass ratio in the Pluto-Charon System ($\mu = 0.1085$). The curvature of the surface is further accentuated for visualization by applying a base- b logarithmic scale to the acceleration magnitude, where $b > 1$ is an arbitrary scalar. In the planar projection of the 3D acceleration magnitude surface, displayed in Figure 3.11(a), small acceleration magnitudes, colored blue, surround the five CR3BP equilibrium points. Large acceleration magnitudes, colored red, occur near the two primaries due to the gravitational force as well as far from the primaries due to centripetal forces. Between the two extremes, a smooth acceleration magnitude surface is depicted via colors in the visible light spectrum between blue and red. In the 3D representation, depicted in Figure 3.11(b), an identical color scheme is employed with

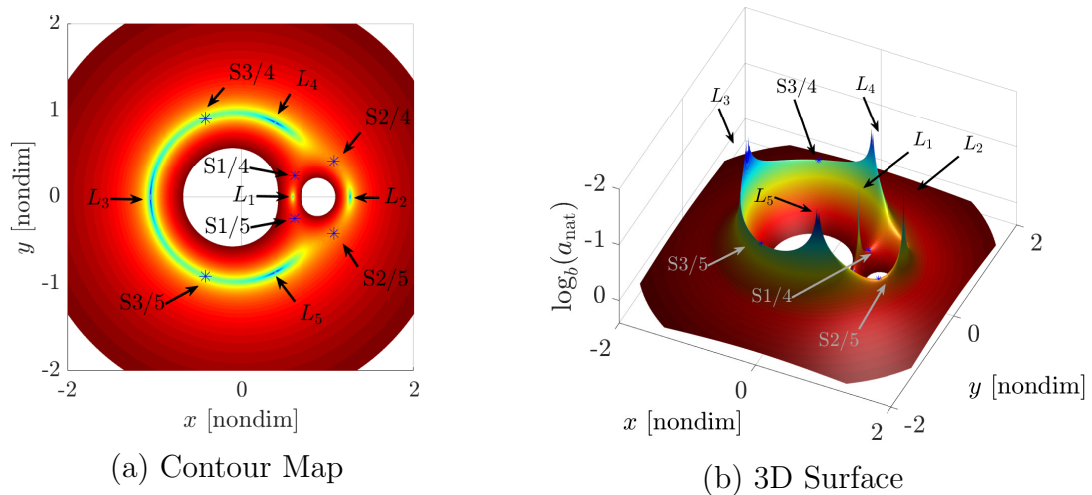


Figure 3.11.: A global portrait of the scaled natural acceleration magnitudes, $\log_b(a_{\text{nat}})$, in the xy -plane for the Pluto-Charon CR3BP with $b = 1000$

low acceleration magnitudes represented by peaks in the surface and large acceleration magnitudes represented by the valleys. The ZACs for $\beta = 0$, plotted in Figure 3.7 for the Earth-Moon system, are identified as the intersection of a horizontal plane of constant low-thrust acceleration magnitude with this 3D natural acceleration magnitude surface. The ZAS's are identified in an analogous manner as the intersection of an acceleration magnitude plane with the 3D hypersurface that maps spatial coordinates to the a_{nat} value.

The distinct ZAC structures merge at the six saddles in the natural acceleration magnitude surface. Each saddle, marked with an asterisk in Figure 3.11, is denoted $S_{i/j}$ where i and j identify the Lagrange points that border the saddle. These merges are observed by moving a horizontal plane of constant low-thrust acceleration magnitude through the 2D $\|\vec{a}_{\text{nat}}\|$ surface in Figure 3.11(b). When the low-thrust acceleration magnitude, a_{lt} , is very small the slicing plane is located near the peaks of the surface; the intersection of the plane and the surface forms small ZACs in the vicinity of the CR3BP Lagrange points, as plotted in Figure 3.7(a). As the thrust magnitude increases from a negligible perturbation to a significant one, the a_{lt} plane descends through the natural acceleration magnitude surface. At the precise acceleration value

and location of a saddle in the a_{nat} field, ZACs merge. For example, when this plane is just above the S2/4 and S2/5 saddles, the \mathbb{E}_1 , \mathbb{E}_2 , and \mathbb{E}_3 structures form the contours depicted in Figure 3.7(c). As the slicing plane descends through the surface to higher a_{lt} values, additional merges occur. This link between these merge locations, both in configuration space and in acceleration magnitude, and the natural dynamics supplies a more intuitive understanding of the CR3BP+LT equilibrium solution landscape.

3.2.6 Stability Properties

As noted previously, many dynamical structures exist in the vicinity of the equilibrium solutions. The number and types of structures available near an equilibrium point are determined by the stability properties of the point. This stability information originates from a linear analysis of the dynamics; the CR3BP+LT is governed by a set of nonlinear differential equations that possess no analytical solution but are approximated by *variational* equations. If higher-order terms are neglected, these equations are reduced to a linear form that is analytically solvable and offers insight into the stability of the reference solution (e.g., an equilibrium point) and predicts nearby behavior. For example, the existence of a 4-dimensional center mode in the vicinity of the CR3BP collinear equilibrium points predicts the existence of nearby planar and spatial periodic orbits [50].

To explore the stability properties of the CR3BP+LT equilibria and identify new dynamical structures, the variational equations are constructed. Only variations in the position and velocity states are considered; the low-thrust acceleration magnitude, a_{lt} , orientation angles, α and β , are all constrained to the values associated with the equilibrium point. If these quantities do not match the reference solution, the solutions to the variational equations will not necessarily reflect the dynamics associated with the reference, failing to supply the desired insight about nearby solutions. Accordingly, the variations in the CR3BP state vector, \vec{X} , are considered.

In general, the nonlinear system of equations is expressed by the vector differential equation,

$$\dot{\vec{X}}(\tau) = \vec{g}_{\text{lt}}(\vec{X}, \tau, a_{\text{lt}}, \alpha, \beta), \quad (3.58)$$

where \vec{g}_{lt} represents the low-thrust equations of motion, τ is the time along the solution, and a_{lt} , α , and β are constant parameters; for brevity, the parameters are omitted from the rest of this discussion. Let the reference solution be denoted $\vec{X}_*(\tau)$ and let a nearby solution be $\vec{X}(\tau) = \vec{X}_*(\tau) + \delta\vec{X}(\tau)$ where $\delta\vec{X}(\tau)$ is a small isochronous variation from the reference solution. Substituting this perturbed solution into (3.58) yields

$$\dot{\vec{X}}(\tau) = \dot{\vec{X}}_*(\tau) + \delta\dot{\vec{X}}(\tau) = \vec{g}_{\text{lt}}(\vec{X}_* + \delta\vec{X}, \tau). \quad (3.59)$$

A linear relationship between the reference and nearby solution is constructed by forming a Taylor Series expansion of \vec{g}_{lt} about the reference solution,

$$\dot{\vec{X}}_*(\tau) + \delta\dot{\vec{X}}(\tau) \approx \vec{g}_{\text{lt}}(\vec{X}_*, \tau) + \frac{\partial \vec{g}_{\text{lt}}(\vec{X}_*, \tau)}{\partial \vec{X}} \delta\vec{X}(\tau) + \text{HOTs}. \quad (3.60)$$

By ignoring all higher-order terms (HOTs), the Taylor Series expansion is reduced to the linear, first order differential equation

$$\delta\dot{\vec{X}}(\tau) \approx \frac{\partial \vec{g}_{\text{lt}}(\vec{X}_*, \tau)}{\partial \vec{X}} \delta\vec{X}(\tau) = \mathbf{A} \Big|_{\vec{X}_*, \tau} \delta\vec{X}(\tau), \quad (3.61)$$

where the \mathbf{A} matrix is related to the Hessian of the low-thrust Hamiltonian,

$$\mathbf{A} = \frac{\partial \vec{g}_{\text{lt}}}{\partial \vec{X}} = \frac{\partial}{\partial \vec{X}} \left(\mathbf{T}_{-\omega} \mathbf{J} \mathbf{T}_{-\omega}^T \frac{\partial H_{\text{lt}}}{\partial \vec{X}} \right) = \mathbf{T}_{-\omega} \mathbf{J} \mathbf{T}_{-\omega}^T \frac{\partial^2 H_{\text{lt}}}{\partial \vec{X}^2} \quad (3.62)$$

$$= \begin{bmatrix} \mathbf{0} & \mathbf{I} \\ -\mathbf{I} & -2\tilde{\omega} \end{bmatrix} \begin{bmatrix} -\vec{\nabla}_r^2 \Upsilon & \mathbf{0} \\ \mathbf{0} & \mathbf{I} \end{bmatrix} \quad (3.63)$$

$$= \begin{bmatrix} \mathbf{0} & \mathbf{I} \\ \vec{\nabla}_r^2 \Upsilon & -2\tilde{\omega} \end{bmatrix}. \quad (3.64)$$

Equivalently, the \mathbf{A} matrix is the Jacobian of the nonlinear differential equations. Because the low-thrust acceleration vector is constant in the rotating frame, the Hessian of the low-thrust pseudopotential, Υ , is equal to the Hessian of the ballistic pseudopotential, Ω , i.e., $\vec{\nabla}_r^2 \Upsilon = \vec{\nabla}_r^2 \Omega$. Subsequently, the \mathbf{A} matrix is a function only of equilibrium point location and does not directly incorporate the low-thrust control parameters. While this may seem unintuitive, the equilibrium point location is an explicit function of the control parameters, so the \mathbf{A} matrix is implicitly related to the control parameters.

To obtain an expression for the relative solution, $\delta\vec{X}(\tau)$, rather than the derivative of the relative solution, $\dot{\delta\vec{X}}(\tau)$, the first order differential equation (3.61) is integrated. Since the reference solution is selected to be one of the equilibrium points in the autonomous system that results from the constant \vec{a}_{lt} control policy, the \mathbf{A} matrix is constant and the integration yields

$$\delta\vec{X}(\tau) = \exp(\mathbf{A}\tau)\delta\vec{X}(0), \quad (3.65)$$

where $\delta\vec{X}(0)$ is the perturbation from the reference solution at the initial time, $\tau = 0$. The \mathbf{A} matrix is decomposed into the form $\mathbf{A} = \mathbf{Q}\mathbf{\Lambda}\mathbf{Q}^{-1}$, where \mathbf{Q} is a square matrix with columns equal to the eigenvectors, \vec{v}_j of \mathbf{A} and $\mathbf{\Lambda}$ is a diagonal matrix containing the corresponding eigenvalues, λ_j . Substituting this eigendecomposition into the integrated solution yields

$$\delta\vec{X}(\tau) = \mathbf{Q} \exp(\mathbf{\Lambda}\tau) \mathbf{Q}^{-1} \delta\vec{X}(\tau_0). \quad (3.66)$$

When the matrix form is expanded, the solution is revealed to be the superposition of the *linear modes*,

$$\delta\vec{X}(\tau) = \sum_{j=1}^6 c_j \exp(\lambda_j \tau) \vec{v}_j, \quad (3.67)$$

where c_j are constant scalars selected to satisfy the boundary condition at $\tau = 0$.

A qualitative analysis of the low-thrust equilibria stability is initiated by identifying the types of linear modes associated with each equilibrium point. Due to the structure of the \mathbf{A} matrix,

Lemma 3.2.7 *The eigenvalues of \mathbf{A} occur in real ($\pm\lambda$) or complex conjugate ($\lambda, \bar{\lambda}$) pairs.*

Proof The eigenvalues are calculated by evaluating solving the equation

$$\begin{aligned} \det(\lambda\mathbf{I} - \mathbf{A}) &= 0 \\ \lambda^6 + b\lambda^4 + c\lambda^2 + d &= 0 \end{aligned} \tag{3.68}$$

for λ where

$$\begin{aligned} b &= 4 - \Omega_{xx} - \Omega_{yy} - \Omega_{zz}, \\ c &= \Omega_{xx}\Omega_{yy} + \Omega_{xx}\Omega_{zz} + \Omega_{yy}\Omega_{zz} - 4\Omega_{zz} - \Omega_{xy}^2 - \Omega_{xz}^2 - \Omega_{yz}^2, \\ d &= -\Omega_{xx}\Omega_{yy}\Omega_{zz} + \Omega_{xx}\Omega_{yz}^2 + \Omega_{zz}\Omega_{xy}^2 + \Omega_{yy}\Omega_{xz}^2 - 2\Omega_{xy}\Omega_{xz}\Omega_{yz}. \end{aligned}$$

Equation (3.68) can be rewritten as

$$\Lambda^3 + b\Lambda^2 + c\Lambda + d = 0, \tag{3.69}$$

where $\Lambda = \lambda^2$. The six roots of (3.68) are then $\pm\sqrt{\Lambda_1}$, $\pm\sqrt{\Lambda_2}$ and $\pm\sqrt{\Lambda_3}$, where Λ_1 , Λ_2 , and Λ_3 are the roots of (3.69). ■

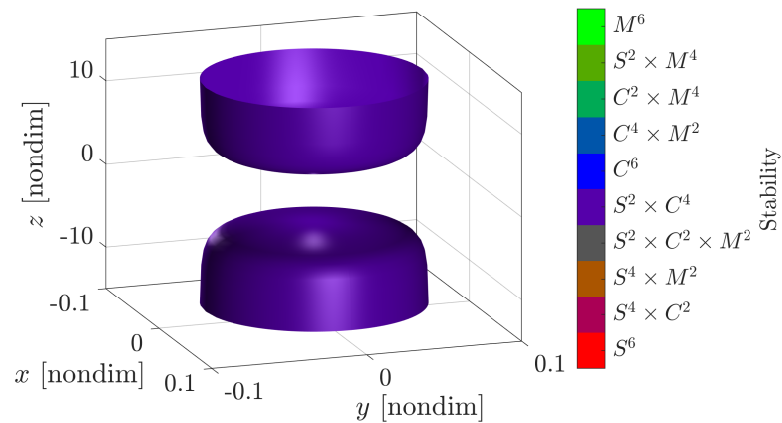
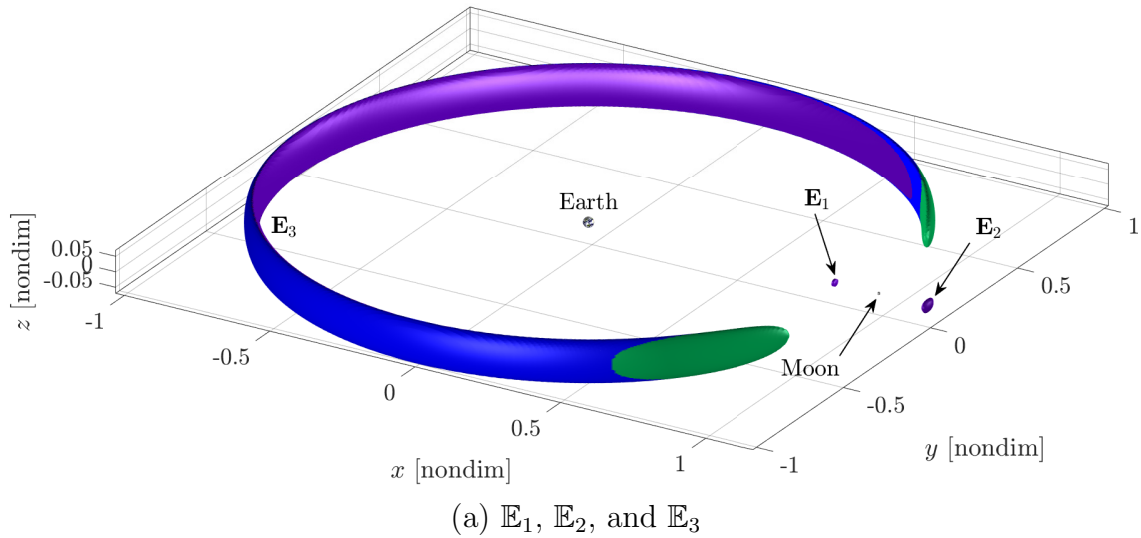
Thus, the linear modes occur in pairs. In this investigation, the modes are characterized as follows:

- $\text{Im}(\lambda) = 0$ – An eigenvalue pair, $\pm\lambda$, on the real axis corresponds to a *saddle* mode; the *stable subspace* grows exponentially relative to the equilibrium point in negative time while the *unstable subspace* grows exponentially in positive time.

- $\text{Re}(\lambda) = 0$ – An eigenvalue pair, $\pm\lambda i$, on the imaginary axis corresponds to a *center* mode, i.e., oscillatory motion about the equilibrium point.
- $\text{Im}(\lambda) \neq 0$ and $\text{Re}(\lambda) \neq 0$ – A complex conjugate eigenvalue pair, λ and $\bar{\lambda}$, represent a *mixed* mode, i.e., oscillatory motion with a stable and unstable component. Like the saddle mode, this mode contains a stable and unstable subspace that each grow exponentially relative to the equilibrium point in negative and forward time, respectively.

To describe a single equilibrium point, the types of modes and their dimensions are collected into a string of the form $S^{n_s} \times C^{n_c} \times M^{n_m}$ where S represents a topological saddle, C represents a topological center, and M represents a mixture of the saddle and center topology (i.e., a spiral). The superscripts n_s , n_c , and n_m denote the dimension of each subspace and sum to six. By coloring equilibrium points by their associated stability types, as seen in Figure 3.12 for the Earth-Moon low-thrust equilibria parameterized by $a_{\text{lt}} = 7\text{e-}2$, a qualitative description of the equilibria is available. At this low-thrust acceleration magnitude, the \mathbb{E}_1 , \mathbb{E}_2 , and \mathbb{E}_4 equilibria are described by the $S^2 \times C^4$ stability type, i.e., these points possess a 2D saddle mode and a 4D center mode, consistent with the stability characteristics of the ballistic L_1 and L_2 points. In contrast, the \mathbb{E}_3 structure is characterized by several stability types. A large portion of the interior (relative to the Earth) of this C-shaped structure is characterized by $S^2 \times C^4$, while the majority of the exterior of the ring is C^6 ; the “tips” of the ring are characterized by $C^2 \times M^4$ motion. These stability characteristics on \mathbb{E}_3 are similar to the stability properties of L_3 , L_4 , and L_5 : the L_3 point is characterized by an $S^2 \times C^4$ linearization while the dynamics near $L_{4/5}$ are described by a C^6 linearization.

The low-thrust equilibrium points in the Sun-EMB system for an equivalent low-thrust acceleration magnitude are characterized by similar stability properties. For a direct comparison with the equilibria in the Earth-Moon system, the dimensional low-thrust acceleration value is set to 0.19 mm/s^2 (a nondimensional value of $7\text{e-}2$ in the Earth-Moon system and $3.2\text{e-}2$ in the Sun-EMB system; see Table 2.1). The resulting



(b) \mathbb{E}_4 ; x and y are scaled differently than z to enable visualization. The minimum $|z|$ coordinate is approximately 3.8

Figure 3.12.: Stability of low-thrust equilibria in the Earth-Moon system for $a_{1t} = 7e-2$

zero acceleration surfaces (ZAS's), displayed in Figure 3.13 and 3.14, differ somewhat from the structures in the Earth-Moon system. Whereas the Earth-Moon equilibria are located on four distinct surfaces, the Sun-EMB equilibria are located on only three (\mathbb{E}_3 is far from the xy -plane and is not depicted), similar to the configuration of the Earth-Moon ZAS's for $a_{1t} = 5e-1$. The Sun-EMB \mathbb{E}_1 surface encompasses all five Lagrange points as well as the Earth-Moon barycenter (EMB). Additionally, \mathbb{E}_1 surrounds the \mathbb{E}_2 structure (as seen in Figure 3.14(a)), which itself surrounds the

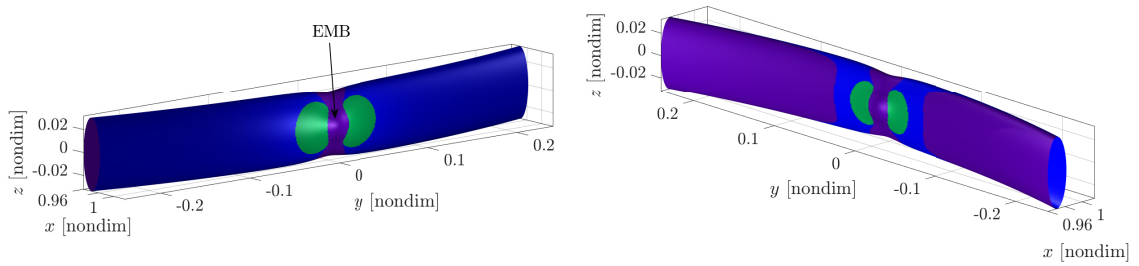
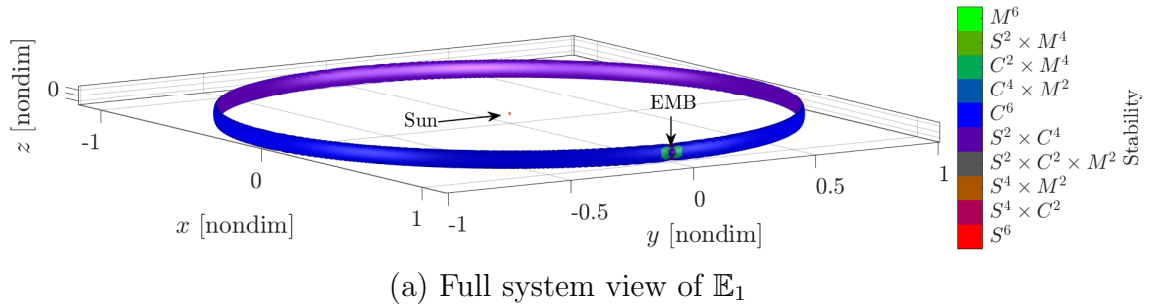


Figure 3.13.: Stability of the \mathbb{E}_1 low-thrust equilibria in the Sun-EMB system for $a_{lt} = 3.2e-2$

EMB but not the L_1 or L_2 points; the planar cross-section of these surfaces presented in Figure 3.9 clarifies the extents of these structures. The stability properties on the

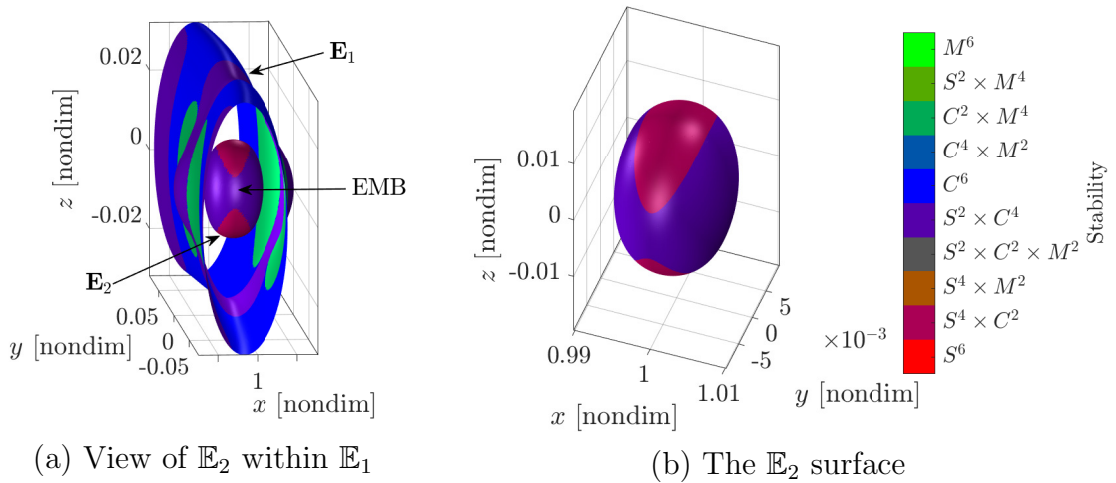


Figure 3.14.: Stability of the \mathbb{E}_2 low-thrust equilibria in the Sun-EMB system for $a_{lt} = 3.2e-2$

Sun-EMB \mathbb{E}_1 structure are similar to the stability properties on the Earth-Moon \mathbb{E}_3 set. The interior of the ring is predominantly characterized by $S^2 \times C^4$ motion while the exterior of the ring is characterized by C^6 motion. Near P_2 , i.e., the EMB, more nuanced behaviors are apparent, as depicted in Figures 3.13(b) and 3.13(c). The blue C^6 behavior wraps from the exterior of the ring to the interior, and two small islands of $C^2 \times M^4$ motion exist on either side of the yz -plane on both the interior and exterior sides. The Sun-EMB \mathbb{E}_2 surface, shown in Figure 3.14, also possesses similar stability characteristics as the Earth-Moon low-thrust \mathbb{E}_1 and \mathbb{E}_2 , i.e., $S^2 \times C^4$ dynamics. However, two large regions of the Sun-EMB surface are characterized by $S^4 \times C^2$ behavior, a mode that is not observed in the Earth-Moon equilibria at the equivalent low-thrust acceleration magnitude.

Correlations between the α and β angles and these stability types supply another criteria that may be employed when constructing preliminary low-thrust trajectories. For example, a spacecraft traveling to the L_4 or L_5 point may leverage the saddle manifold of a low-thrust equilibrium located nearby. However, for the selected low-thrust acceleration magnitude, only a subset of the equilibria near L_4 or L_5 possess such saddle motion. Thus, the set of control parameters for the transfer are limited to those associated with these equilibrium points.

3.2.7 Distinct Solutions

While the zero acceleration surfaces and contours supply a global overview of the equilibria locations, distinct sets of equilibria for specific, static \vec{a}_{lt} configurations are also of interest. Let a set of equilibrium points on a ZAS associated with a specific low-thrust orientation (i.e., α and β angles) and magnitude be notated by the set

$$\mathbb{E}_i(a_{lt}, \alpha \beta) \subset \mathbb{E}_i(a_{lt}, \beta) \subset \mathbb{E}_i(a_{lt}) \quad (3.70)$$

where $\mathbb{E}_i(a_{\text{lt}}, \beta)$ is the ZAC and $\mathbb{E}_i(a_{\text{lt}})$ is the ZAS on which the points exist. To distinguish between distinct solutions in this set, the equilibria,

$$E_i^1(a_{\text{lt}}, \alpha, \beta), E_i^2(a_{\text{lt}}, \alpha, \beta), \dots, E_i^j(a_{\text{lt}}, \alpha, \beta), \quad (3.71)$$

are indexed by their relative low-thrust Hamiltonian values such that

$$H_{\text{lt}} \left(E_i^j(a_{\text{lt}}, \alpha, \beta) \right) \leq H_{\text{lt}} \left(E_i^{j+1}(a_{\text{lt}}, \alpha, \beta) \right). \quad (3.72)$$

Accordingly, $E_i^j(a_{\text{lt}}, \alpha, \beta)$ is the j^{th} equilibrium point with the specified α and β angles on the i^{th} ZAS that exists at the specified a_{lt} magnitude. (A simple algorithm to compute the locations of these solutions is provided in Section E.1.) To illustrate these distinctions, consider the set of low-thrust equilibrium points for $a_{\text{lt}} = 7\text{e-}2$, $\beta = 0$, and $\alpha = 90^\circ$, as in Figure 3.15. Five distinct solutions exist: one on the \mathbb{E}_1

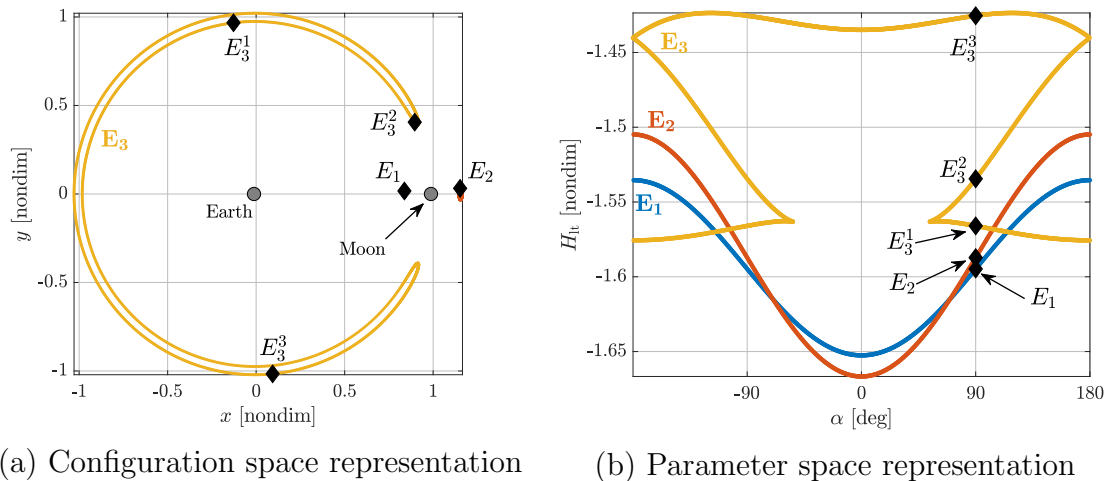


Figure 3.15.: Distinct equilibria (black diamonds) in the Earth-Moon system for $a_{\text{lt}} = 7\text{e-}2$, $\alpha = 90^\circ$, $\beta = 0$; the ZACs for all α values are shown as colored contours (Animation⁷)

ZAC (colored blue), one on the \mathbb{E}_2 ZAC (red), and three on the \mathbb{E}_3 ZAC (yellow). The locations of these solutions in configuration space, depicted in Figure 3.15(a), vary

⁷https://engineering.purdue.edu/people/kathleen.howell.1/Publications/Dissertations/2020_Cox/#eqPts2D

from the ballistic Lagrange points, particularly on the \mathbb{E}_3 set. The novel locations of these equilibrium points offer new flow patterns that may be leveraged for trajectory designs, a topic that is explored in detail in later sections.

In addition to the spatial visualization of the equilibrium points, a *parameter space* view supplies useful insights. Each set of equilibria for a specified a_{1t} magnitude and β angle, i.e., each ZAC, is a 1D curve that is a continuous function of a single parameter. In some cases the α angle parameterizes a ZAC, such as the \mathbb{E}_1 and \mathbb{E}_2 ZACs visualized in Figure 3.15(b). However, the α angle is not generally sufficient to fully parameterize a ZAC, i.e., multiple equilibria exist for a single α value, as in the \mathbb{E}_3 ZAC in Figure 3.15(b). Nevertheless, a visualization that employs α as one coordinate remains useful. The number of distinct points at any α angle is straightforwardly available by counting the number of times a vertical line at that α value intersects the \mathbb{E}_i contours. For example, in Figure 3.15(b), the $\alpha = 90^\circ$ line intersects \mathbb{E}_1 once, \mathbb{E}_2 once, and \mathbb{E}_3 three times, consistent with the equilibria viewed in configuration space. The energy order of these equilibria is straightforwardly determined by their location along the vertical axis; the equilibria with the smallest H_{1t} values are located near the bottom of the plot while the equilibria associated with larger H_{1t} values appear higher on the plot.

Recall from Section 3.1 that the equilibria locate gateways through the forbidden regions. Subsequently, the H_{1t} values associated with the equilibria are equivalent to the H_{1t} values at which the gateways open and close and the equilibria energy order identifies the sequence of gateway openings with increasing H_{1t} values. In the ballistic CR3BP, the equilibrium point energy order is consistently $L_1 \rightarrow L_2 \rightarrow L_3 \rightarrow L_{4/5}$. However, the low-thrust equilibrium point energy order is not generally consistent with the ballistic energy order and can vary with α , β , and a_{1t} . For example, the energy order of the equilibria for $a_{1t} = 7e-2$, $\alpha = 180^\circ$, and $\beta = 0^\circ$, seen in Figure 3.15(b), is $E_3^1 \rightarrow E_1 \rightarrow E_2 \rightarrow E_3^2 \rightarrow E_3^3$. A similarly inconsistent gateway order occurs near $\alpha = 0$, when the low-thrust gateway order is $E_2 \rightarrow E_1 \rightarrow E_3$. These energy orders are straightforwardly available from the parameter space view across

the entire range of α values. These differences between the low-thrust and ballistic problems can be exploited for low-thrust trajectory design and are discussed in more detail later in the document.

The locations and energies of distinct equilibrium points also vary with the β angle. Additionally, because the ZACs are constructed as families parameterized by α , the number and geometry of the ZACs also varies with β . As noted earlier in this section, a ZAC located far from the xy -plane exists for $\beta \neq 0$. For example, for $a_{lt} = 7e-2$ and $\beta = -75^\circ$ in the Earth-Moon system, as in Figure 3.16, a fourth ZAC exists at $z \approx -4$. In this configuration, up to six distinct solutions may exist:

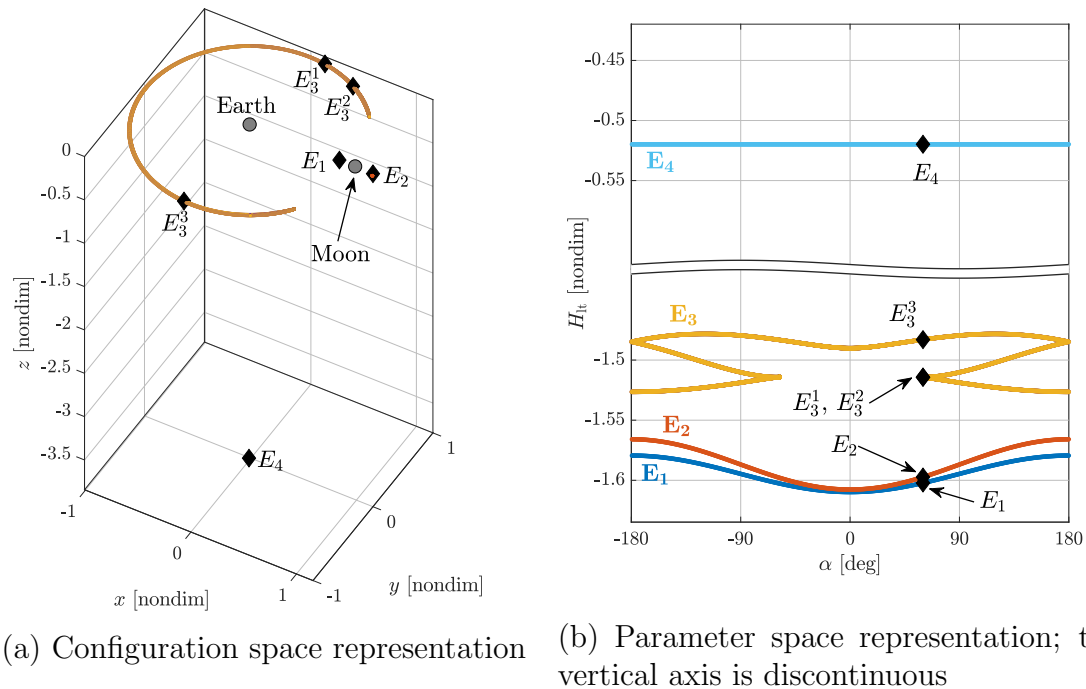


Figure 3.16.: Distinct equilibria (black asterisks) in the Earth-Moon system for $a_{lt} = 7e-2$, $\alpha = 60^\circ$, $\beta = -75^\circ$; the ZACs for all α values are shown as colored contours (Animation⁸)

one on each of the \mathbb{E}_1 , \mathbb{E}_2 , and \mathbb{E}_4 contours, and up to three on the \mathbb{E}_3 contour. However, this arrangement is not consistent across the range of β values. As β varies,

⁸https://engineering.purdue.edu/people/kathleen.howell.1/Publications/Dissertations/2020_Cox/#eqPts3D

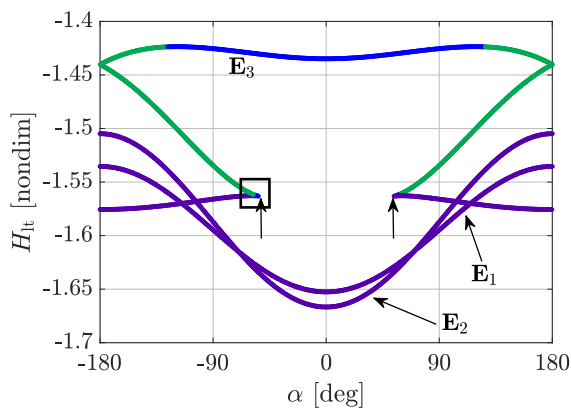
the H_{lt} values associated with the points vary, as do the number of solutions for a fixed α value; the Animation of this figure illustrates this evolution of the distinct equilibria at $\alpha = 60^\circ$ while β varies. Additionally, note that the energy order of the equilibria also depends on β (and on a_{lt}). For example, for $\beta = -75^\circ$, the energy order is consistently $E_1 \rightarrow E_2 \rightarrow E_3^j \rightarrow E_4$ regardless of the α angle, as illustrated in Figure 3.16(b). While the highly-out-of-plane equilibria (\mathbb{E}_4 in this case) are likely too distant from the system to prove useful in trajectory design applications, variations in β may be employed to adjust the gateway order, the number of equilibrium points, or simply to shift the locations of the low-thrust equilibria out of the xy -plane.

Solution Count as a Function of α

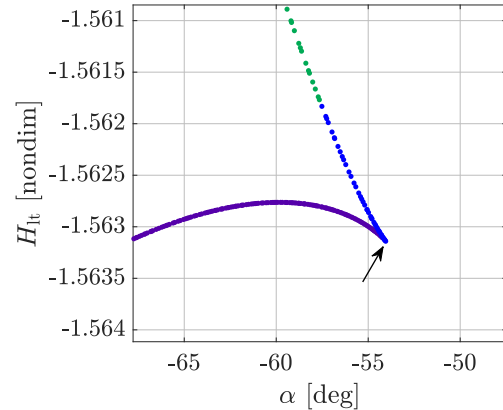
In many scenarios, the number of distinct equilibrium solutions changes across a ZAC. In other words, the number of equilibrium points parameterized by a specified a_{lt} value and β angle is a function of the α angle. For example, as α varies from -180° to 180° in Figure 3.15 (see the animation), five distinct equilibria exist for $|\alpha| > 54^\circ$ and three distinct solutions exist for $|\alpha| < 54^\circ$. The transition between three and five solutions at $\alpha \approx \pm 54^\circ$ is located at a cusp in the parameter space representation plotted in Figure 3.15(b); at the exact point of this cusp, four distinct solutions exist. Note that the apparent cusps at $\alpha = \pm 180^\circ$ are an artifact of the plotting; the branches of the \mathbb{E}_3 ZAC intersect at $\alpha = \pm 180^\circ$ but continue smoothly. Accordingly, five solutions exist at $\alpha = \pm 180^\circ$, with $H_{\text{lt}}(E_2^3) = H_{\text{lt}}(E_3^3)$.

One way to identify the α values where the number of equilibria change is to overlay the stability properties of the equilibria onto the parameter space representation. A cusp that corresponds to a stability change is always such a transition point.⁹ For example, the cusps at $\alpha \approx \pm 54^\circ$, marked by arrows in Figure 3.17, coincide with a change between $S^2 \times C^4$ stability and C^6 . At the precise point of the cusp, i.e., the location where the equilibria appear or disappear (depending on the direction α

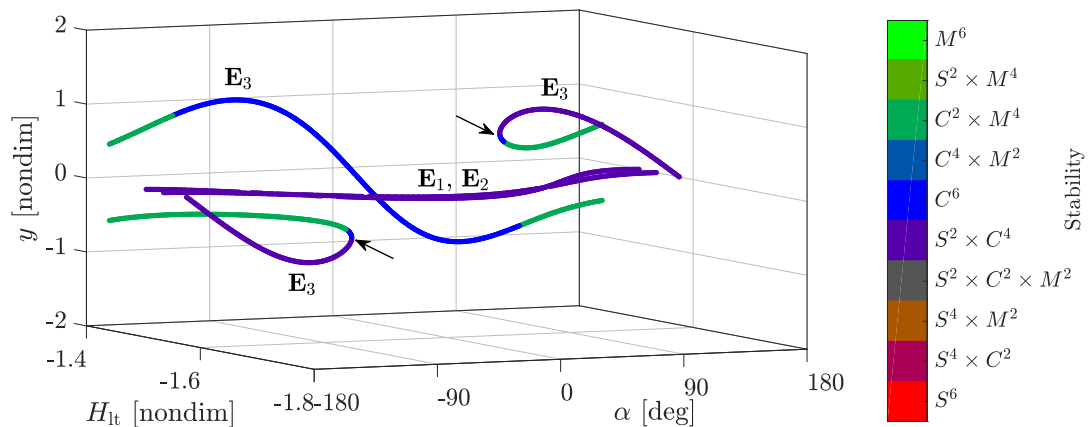
⁹Dr. Dan Grebow deserves credit for sparking this realization



(a) In the parameter space projection, the ZAC appears to have cusps at $\alpha \approx \pm 54^\circ$



(b) A close up view of the apparent cusp at $\alpha \approx 54^\circ$ corresponds to a change between $S^2 \times C^4$ and C^6 stability modes



(c) When additional states are included in the ZAC visualization, the stability change no longer appears at a cusp; the ZAC evolution is smooth

Figure 3.17.: The number of distinct equilibria changes at a stability bifurcation on the \mathbb{E}_3 ZAC in the Earth-Moon CR3BP+LT for $a_{lt} = 7e-2$ and $\beta = 0$

is evolving in), the \mathbf{A} matrix is degenerate and the stability properties are poorly defined as at least one pair of eigenvalues are equal to zero. The conjunction of a stability change with this appearance or disappearance of equilibrium solutions is the subject of *catastrophe theory* [52, 53].

While the finer details of catastrophe theory and their implications for the low-thrust equilibria are beyond the scope of this investigation, a few interesting obser-

vations are available. First, catastrophe theory predicts that these bifurcations in the stability properties of the equilibria occur as part of a well-defined geometric structure that is related to a potential function. By *unfolding* the degeneracy of the critical point, additional insights may be available. Second, the behavior evident in Figure 3.17 appears to be a *cuspl catastrophe*. By adding an extra dimension to the parameter space projection, e.g., the x -, y -, or z -coordinate of the equilibria, the cusp geometry is viewed as part of a continuous, well-defined geometric structure. For example, when the α vs. H_{1t} projection is augmented with the equilibria y -coordinate, as in Figure 3.17(c), the cusps in the projection are revealed to be local extrema on the \mathbb{E}_3 ZAC. In fact, there are no cusps in this higher-dimensional representation of \mathbb{E}_3 . Additionally, this representation of the ZACs demonstrates that the \mathbb{E}_3 structure evolves smoothly without a local extrema or a stability change through $\alpha = \pm 180^\circ$. Finally, while the existence of a stability change is necessary to identify the location where equilibria appear or disappear, it is not sufficient. A second stability change between C^6 and $C^2 \times M^4$ occurs near $H_{1t} = -1.562$ and $\alpha = \pm 57^\circ$ on the \mathbb{E}_3 contour, as seen in Figure 3.17(b), but does not coincide with a degenerate \mathbf{A} matrix.

In contrast to the stability bifurcation criteria, a defective \mathbf{A} matrix is necessary and sufficient to identify the location where equilibria appear or disappear. Subsequently, the cusp catastrophe locations are straightforwardly identified for all β angles (i.e., for all ZACs) by coloring the ZAS's by the determinant of \mathbf{A} , as in Figure 3.18 for the Earth-Moon system and $a_{1t} = 7e-2$. In this representation, dark colors represent a large matrix determinant (order zero or higher) while light colors represent increasingly small determinants. Thus, the white contour apparent on the \mathbb{E}_3 ZAS marks the locations where equilibria appear or disappear. The stability bifurcations identified for $\beta = 0$ are located where the white contour intersects the xy -plane, at the maximum x -value along the contour in this scenario. As all of the equilibria on \mathbb{E}_1 and \mathbb{E}_2 are characterized by $S^2 \times C^4$ motion (for $a_{1t} = 7e-2$ in the Earth-Moon system), no stability bifurcations exist. The lack of white contours on these surfaces

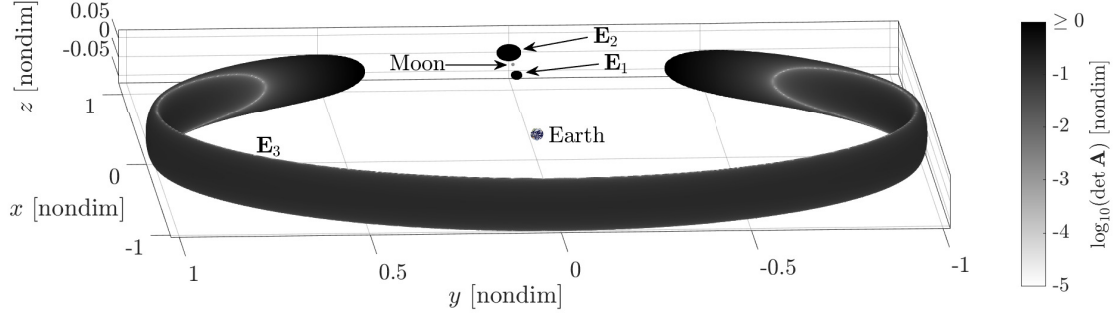
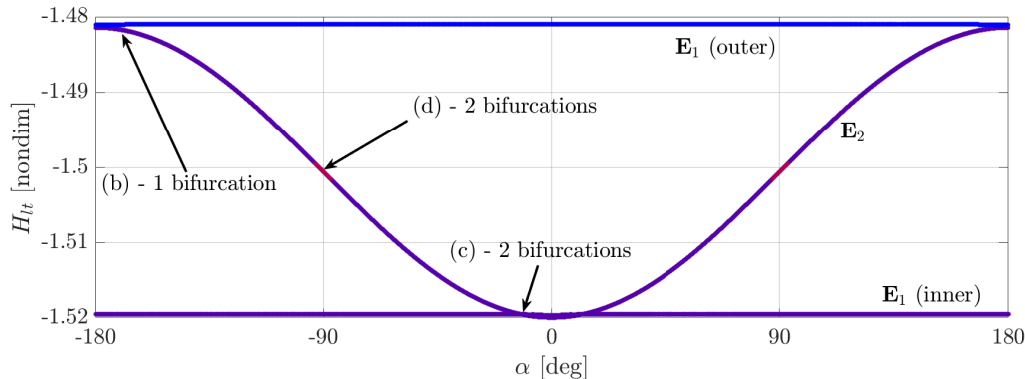


Figure 3.18.: The locations where equilibria appear and disappear in the Earth-Moon CR3BP+LT for $a_{lt} = 7e-2$ are identified by small values of $\det \mathbf{A}$ (marked in white)

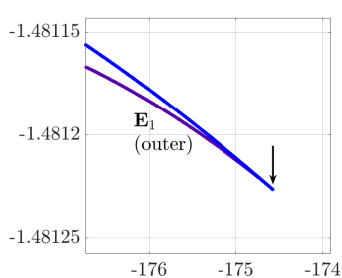
further confirms that the number of equilibrium points on \mathbb{E}_1 and \mathbb{E}_2 is consistent across all values of α and β in this scenario.

Although the locations where equilibria appear and disappear in the Earth-Moon system for $a_{lt} = 7e-2$ correspond to the interface between C^6 (blue) and $S^2 \times C^4$ (purple) modes for all α and β values, other stability bifurcations yield similar cusp catastrophes for different a_{lt} values or in different systems. For example, several bifurcations between the $S^4 \times C^2$ (magenta) and $S^2 \times C^4$ (purple) stability types are apparent in the Sun-EMB ZACs for $a_{lt} = 3.2e-2$ and $\beta = 53^\circ$, as seen in Figure 3.19. Consistent with the cusps observed along the Earth-Moon ZACs, the cusps along the Sun-EMB ZACs appear as local extrema when an additional coordinate (in this case, z) is included in the ZAC visualization, as depicted in Figure 3.19(e). All ten of these stability bifurcations occur near the EMB on the ZAS surfaces visualized in Figure 3.14.

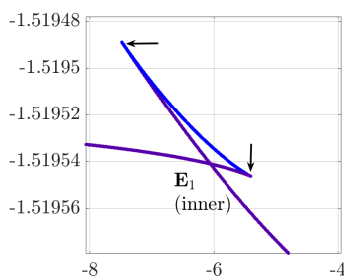
The stability changes in the Sun-EMB system for $\beta = 0^\circ$ also vary from the stability changes observed in the Earth-Moon system. The position space view of the ZACs near the EMB, visualized in Figure 3.20(b), depicts stability changes between $S^2 \times C^4$ (purple), C^6 (blue), and $C^2 \times M^4$ (green) modes; in particular, the $C^2 \times M^4$ mode is not observed on the Earth-Moon ZAS's at the equivalent low-thrust acceleration magnitude. The transitions between $C^2 \times M^4$ (green) and C^6 (blue) modes do not correspond to a cusp in the parameter space view of the ZAC, as seen



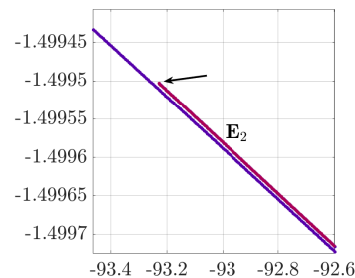
(a) Ten stability bifurcations in the ZAC projections are apparent; the five for $\alpha < 0$ are labeled, the remaining five are mirrored over $\alpha = 0$



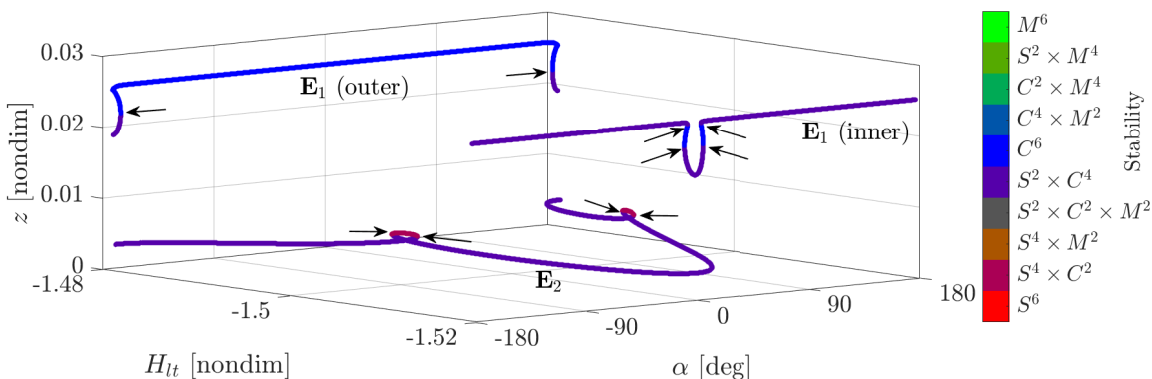
(b) $C^6 \leftrightarrow S^2 \times C^4$, one bifurcation



(c) $C^6 \leftrightarrow S^2 \times C^4$, two bifurcations



(d) $S^4 \times C^2 \leftrightarrow S^2 \times C^4$, one bifurcation



(e) The inclusion of z in the ZAC visualization reveals that the cusps are local extrema

Figure 3.19.: Stability bifurcations, marked by arrows, in the parameter space projections of \mathbb{E}_1 and \mathbb{E}_2 correspond to the locations where number of equilibrium points change; the \mathbb{E}_3 contour lies far from the xy -plane and is not shown; Sun-EMB system for $a_{lt} = 3.2e-2$ and $\beta = 53^\circ$

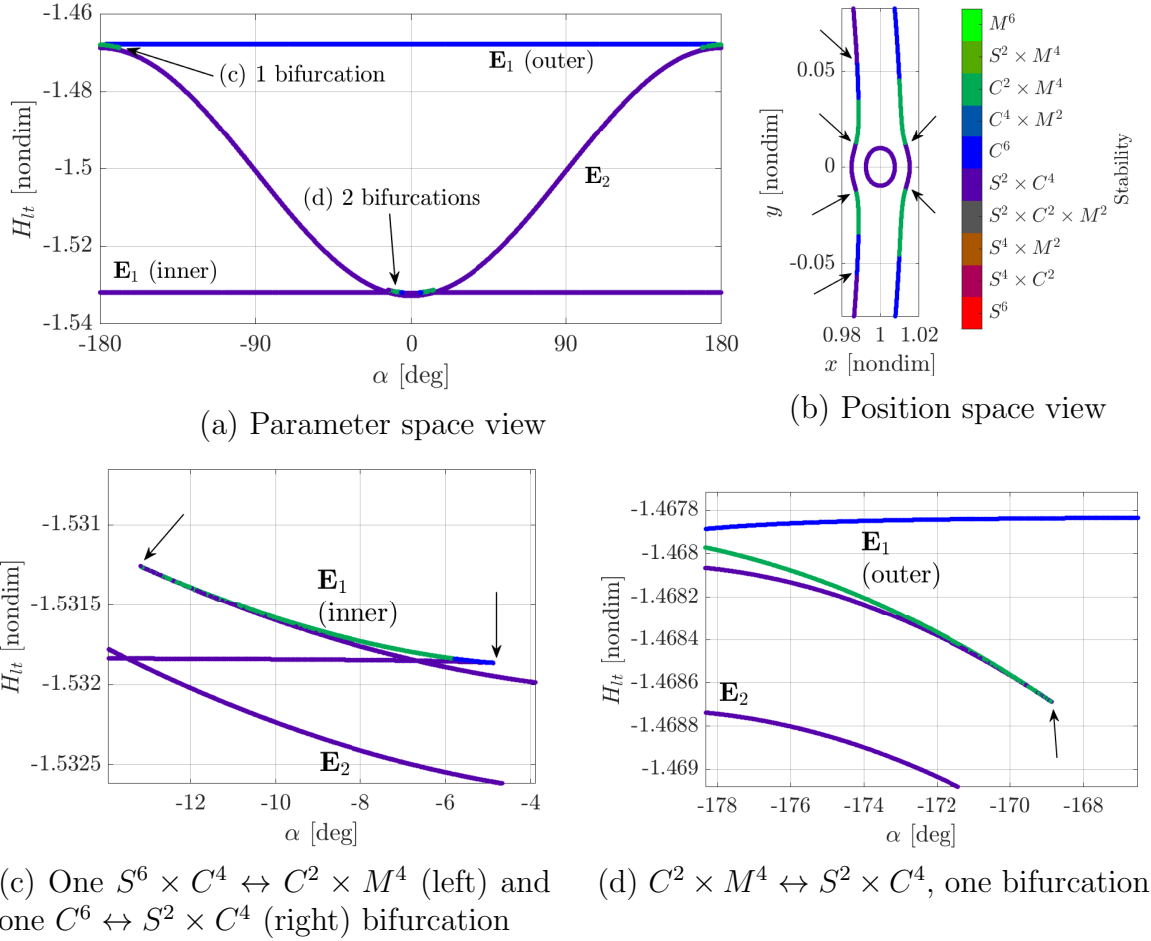


Figure 3.20.: Stability changes, marked by black arrows, in the Sun-EMB for $a_{1t} = 3.2e-2$ and $\beta = 0$

in Figure 3.20(c), thus, these stability bifurcations do not represent locations where the number of equilibria change. Consistent with the ZACs for $\beta = 53^\circ$ in Figure 3.19, only a few small ranges of α values yield more than three distinct equilibria for $\beta = 0^\circ$. Five distinct solutions exist in the approximate ranges $169^\circ < |\alpha| < 180^\circ$ and $5^\circ < |\alpha| < 13^\circ$, with four solutions existing at the bifurcations, and three solutions existing for all other α values. Unlike the ZACs for $\beta = 53^\circ$, the planar ($\beta = 0^\circ$) \mathbb{E}_2 ZAC does not include any stability changes and is entirely characterized by $S^2 \times C^4$ motion. In this respect, the planar \mathbb{E}_2 ZAC is similar to the Earth-Moon \mathbb{E}_1 and \mathbb{E}_2 ZACs. Finally, although all of the stability bifurcations are located on the \mathbb{E}_1

ZAC, which spans the entire Sun-EMB system, all of the bifurcations are located close to the EMB. Accordingly, the low-thrust dynamical environment in the region of interest (i.e., near the Earth) contains novel characteristics to be employed for trajectory design.

Solution Count as a Function of a_{lt}

While the stability bifurcation analysis supplies information about the number of distinct equilibria across values of α and β , it does not capture variations in a_{lt} ; to explore these variations, a global portrait is constructed. The Earth-Moon CR3BP+LT ZACs are computed over a range of a_{lt} and β angles. For each α angle, the number of distinct equilibrium points is assessed. The results, plotted in Figure 3.21 for $\beta = 0$, illustrate the boundaries between the numbers of distinct solutions as a function of α and a_{lt} . Yellow points represent magnitude-angle combinations for which five distinct

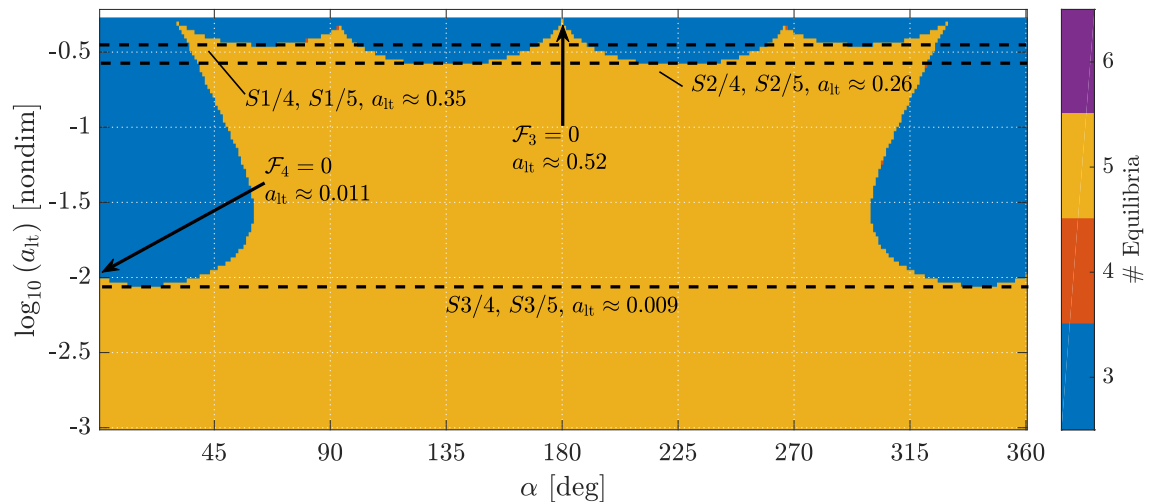


Figure 3.21.: The number of equilibrium solutions in the Earth-Moon CR3BP+LT vary with low-thrust acceleration magnitude, a_{lt} , and angle, α ([Animation](#)¹⁰)

solutions exist while blue points reflect the combinations with only three distinct solutions. A boundary line of orange points, representing four distinct solutions, exists

¹⁰https://engineering.purdue.edu/people/kathleen.howell.1/Publications/Dissertations/2020_Cox/#eqPtCounts

between the two at the exact a_{1t} and α coordinates of equilibria merges, though this boundary is generally not visible in the figure due to the discrete nature of the computation. Several insights are available from this graphic. First, when the magnitude of a_{1t} (displayed on a logarithmic scale) is small, all α angles (for $\beta = 0$) are associated with five distinct equilibria. Recall that, at these small acceleration levels, five distinct ZACs exist near each of the five Lagrange points. As the acceleration level increases, the earliest merges between equilibria correspond to the thrust magnitudes associated with the saddles in the natural acceleration field, as discussed in Section 3.2.5. For example, at the a_{1t} value corresponding to the S3/4 and S3/5 saddles, marked by a black, dashed line, the set of equilibria at roughly $\alpha = \pm 18^\circ$ transitions from five distinct solutions to four distinct solutions. Because the saddle acceleration magnitude corresponds to the smallest a_{1t} magnitude at which two equilibria merge (i.e., appear or disappear), the saddle location corresponds to a defective \mathbf{A} matrix (in fact, all of the saddles in the acceleration magnitude field coincide with defective \mathbf{A} matrices). At a higher acceleration magnitude, the number of distinct equilibria at this α angle decreases to three. In this scenario, all a_{1t} magnitudes larger than the S3/5 saddle value yield a set of three distinct solutions for $\alpha = \pm 18^\circ$. However, it is not always true that the number of distinct solutions decreases as a_{1t} increases. For instance, when $\alpha = 45^\circ$, five distinct equilibrium solutions exist for small and large acceleration magnitudes.

The points at which \mathcal{F}_3 and \mathcal{F}_4 , two constraints on the analytical solutions at $\alpha = 0$ or $\alpha = 180^\circ$, transition between being satisfied and unsatisfied also locate local maxima in the number of equilibrium points as a_{1t} increases. For example, $\mathcal{F}_4 \geq 0$ is required for an analytical solution; this constraint is equal to zero when $\alpha = 0$ and $a_{1t} \approx 0.011$ (in the Earth-Moon system for $\beta = 0$). For larger a_{1t} values, $\mathcal{F}_4 < 0$; thus, the analytical solution for $\alpha = 0$ and $y \neq 0$ is not available at larger a_{1t} values. This point corresponds to the transition from five to three distinct solutions at $\alpha = 0$. A similar transition is marked where $\mathcal{F}_3 = 0$ for $\alpha = 180^\circ$. However, observe that the other constraints (\mathcal{F}_1 , \mathcal{F}_2 , and \mathcal{F}_5) are not associated with changes in the number

of equilibria. For $\alpha = 0$, the \mathcal{F}_3 and \mathcal{F}_4 constraints are violated at lower a_{lt} values than the other constraints across all values of μ , as seen in Figure 3.4. Similarly, when $\alpha = 180^\circ$, only the \mathcal{F}_3 constraint is violated for $a_{\text{lt}} < 1$ (see Figure 3.5); thus, the \mathcal{F}_3 constraint is the limiting condition for analytical solutions for $\alpha = 180^\circ$ and $y \neq 0$. These results suggest that the constraints on the analytical solutions are directly related to the annihilation or merge of equilibria at $\alpha = 0$ and $\alpha = 180^\circ$.

Although the maximum number of distinct equilibrium solutions is five for $\beta = 0$, a total of six distinct solutions exist for $\beta \neq 0$, with the additional solution located far above or below the xy -plane. For small β magnitudes near but not equal to zero the geometry of the regions is very similar to the geometry depicted in Figure 3.21 for $\beta = 0$ (see the linked animation for Figure 3.21). However, the regions with three distinct points have four distinct solutions for $\beta \neq 0$ and the regions with five distinct points for $\beta = 0$ have six distinct solutions for $\beta \neq 0$. As the magnitude of β increases toward 90° , the number of distinct solutions for all a_{lt} values and α angles tends to six. Additionally, the results are mirrored over $\beta = 0$, i.e., the number of equilibria for a given a_{lt} and α combination is identical for $\pm\beta$.

The detailed understanding of the low-thrust equilibria developed in this section facilitates the prediction of the global dynamics. For instance, because the equilibrium points locate gateways in the low-thrust forbidden regions, the annihilation of a particular point indicates that a gateway no longer exists. Furthermore, dynamical structures associated with the annihilated point(s), such as the invariant saddle manifolds and structures within the center subspace (discussed in the next section), disappear with the equilibrium solution. In short, by studying the properties of the CR3BP+LT equilibria, tools to control and leverage dynamical structures in the vicinity of the equilibrium points may be developed.

3.3 Equilibrium Point Manifolds

Once the location and stability properties of the CR3BP+LT equilibrium points have been determined, additional dynamical structures in the vicinity of the equilibria are constructed. One method to initialize these nearby structures leverages the linearized dynamics about an equilibrium point. Different types of structures are available from different stability types, e.g., a hyperbolic mode yields stable and unstable solutions while a center mode yields oscillatory solutions. In general, these solutions are termed *manifolds* and are associated with a particular equilibrium point (i.e., a fixed point). Thus, the stable and unstable solutions are collectively called the *hyperbolic manifold* and the oscillatory solutions are said to be within the *center manifold* [54].

3.3.1 Hyperbolic Manifold

The hyperbolic manifold, represented by a topological saddle, includes flow patterns that asymptotically approach and depart from the equilibrium point. Flow that asymptotically approaches an equilibria is termed *stable* while motion that asymptotically departs is termed *unstable*. When these manifolds are viewed in reverse time, the opposite trends are apparent, i.e., the stable manifold asymptotically departs the equilibrium point and the unstable manifold asymptotically approaches the point. Each manifold is straightforwardly initialized from the linear dynamics near an equilibrium point and then transitioned to the full, nonlinear dynamics by employing numerical integration.

Initialization from Linear Modes

The nonlinear dynamics, i.e., solutions to the equations of motion (2.115), are approximated by a *linearization* of the dynamics about a reference solution. As each equilibrium point is a solution to the nonlinear dynamics, a linearization about an

equilibrium solution supplies insights about nearby motion. Recall from Section 3.2.6 that the linearized dynamics are the superposition of the linear modes, and that the full set of non-trivial linear modes are available from the \mathbf{A} matrix defined in Equation (3.64). Accordingly, the linear dynamics near an equilibrium point, \vec{X}_e , are given by the superposition of the modes,

$$\delta\vec{X}(\tau) = \sum_{j=1}^6 c_j \exp(\lambda_j \tau) \vec{v}_j, \quad (3.67)$$

where λ_j and \vec{v}_j are eigenvalues and eigenvectors of \mathbf{A} when \mathbf{A} is evaluated at \vec{X}_e , c_j is an arbitrary constant, and $\delta\vec{X}(\tau)$ is a linear solution relative to \vec{X}_e . The eigenvalues, which always occur in pairs (see Lemma 3.2.7), determine the types of modes that are available while the eigenvectors give direction (in 6D space) to each mode. Individual modes may be isolated by setting the c_j values of the other modes to zero. To illustrate this strategy, consider the \mathbb{E}_1 equilibrium point in the Earth-Moon system for $a_{\text{lt}} = 7\text{e-}2$, $\alpha = 180^\circ$ and $\beta = 0^\circ$, i.e., $\mathbb{E}_1(0.07, 180^\circ, 0^\circ)$. The eigenvalues of the \mathbf{A} matrix (evaluated at the location of this \mathbb{E}_1 point), listed in Table 3.1, reveal that the linear dynamics include a 2D hyperbolic mode and a 4D center mode, i.e., the $S^2 \times C^4$ stability type as identified in Section 3.2.6. The hyperbolic mode includes the stable

Table 3.1.: Earth-Moon $\mathbb{E}_1(0.07, 180^\circ, 0^\circ)$ Eigenvalues

Eigenvalue	Eigenvector
$\lambda_s = -3.0731$	\vec{v}_s
$\lambda_u = 3.0731$	\vec{v}_u
$\lambda_{c1} = \pm 2.4236i$	$\vec{v}_{c1}, \bar{\vec{v}}_{c1}$
$\lambda_{c2} = \pm 2.3600i$	$\vec{v}_{c2}, \bar{\vec{v}}_{c2}$

manifold, described by λ_s and \vec{v}_s , and the unstable manifold, described by λ_u and \vec{v}_u . Similarly, the 4D center manifold is characterized by the two center eigenvalue pairs, λ_{c1} and λ_{c2} , and their eigenvectors, \vec{v}_{c1} and \vec{v}_{c2} (these occur in complex conjugate pairs). To isolate the unstable mode, all of the c_j values in Equation (3.67) are set to

zero except for the coefficient that corresponds to λ_u ; the resulting linear solution is given by

$$\vec{X}_e + \delta\vec{X}(\tau) = \vec{X}_e + c \exp(\lambda_u \tau) \vec{v}_u, \quad (3.73)$$

where c is a scalar “step size.” As λ_u and \vec{v}_u are constant, this solution describes a line that originates at \vec{X}_e for $\tau = -\infty$ and grows exponentially along the \vec{v}_u vector as $\tau \rightarrow \infty$. A mirrored solution, seen in Figure 3.22, is also available as the eigenvector may be multiplied by a negative scalar. Substituting λ_s and \vec{v}_s into (3.73) yields

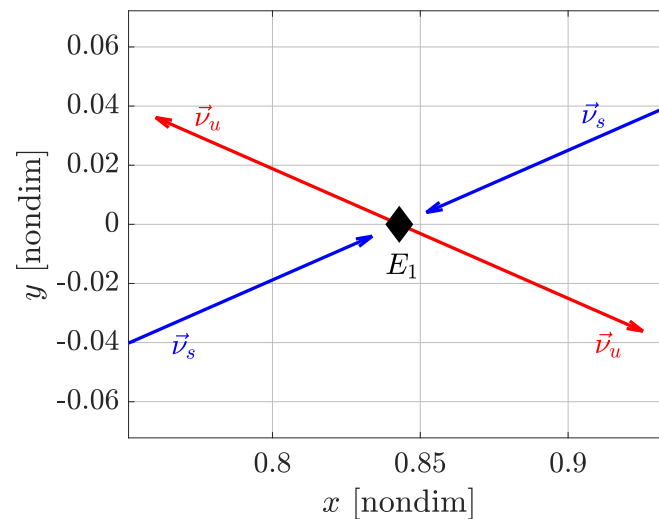


Figure 3.22.: The stable (blue) and unstable (red) eigenvectors associated with the Earth-Moon $\mathbb{E}_1(0.07, 180^\circ, 0^\circ)$ equilibrium point

a similar solution for the stable manifold. However, because $\lambda_s < 0$, the linear solution asymptotically approaches \vec{X}_e along the \vec{v}_s vector as $\tau \rightarrow \infty$; conversely, the stable solution grows exponentially from the equilibrium point state as $\tau \rightarrow -\infty$. While these linearized dynamics supply a useful approximation of the motion near the equilibrium point, they do not necessarily reflect the behavior of the nonlinear flow, particularly as the distance from the equilibrium point increases. In other words, there is some neighborhood around an equilibrium point for which the linear dynamics match the nonlinear dynamics, but the size of the neighborhood can be quite small. To explore the behavior of the stable and unstable manifolds at greater distances from

the equilibrium point, the linear solutions must be transitioned, or “globalized,” to the nonlinear dynamics.

Globalization to Nonlinear Dynamics

The linear dynamics in the vicinity of the low-thrust equilibrium points are straightforwardly transitioned to the full nonlinear model to supply insight into global flow patterns in the CR3BP+LT. The stable and unstable manifolds are initialized by selecting a point on the corresponding linearized solution near the equilibrium point as the initial state for a nonlinear propagation. For example, an initial state on the unstable manifold is computed by adding the scaled unstable eigenvector to the equilibrium point state,

$$\vec{X}^{u+}(0) = \vec{X}_e + c\vec{v}_u; \quad (3.74)$$

an initial state on the stable manifold, $\vec{X}^{s+}(0)$, is similarly computed. Additionally, two more initial states on the manifolds are available by choosing the opposite sign for c , yielding $\vec{X}^{u-}(0)$ and $\vec{X}^{s-}(0)$. The scalar constant, c , should be “small enough” such that an arc propagated in reverse time from $\vec{X}^{u\pm}(0)$ (or in forward time from $\vec{X}^{s\pm}(0)$) asymptotically approaches \vec{X}_e . However, this asymptotic behavior must be balanced with practical considerations such as numerical integrator error buildup; if c is *too* small, the manifold will only depart the vicinity of the equilibrium point as $|\tau|$ grows large, incurring significant numerical errors along the way. An appropriate magnitude for the step size also depends on the system, as different mass ratios and characteristic lengths affect the sensitivity and scaling.

Once the initial state for the low-thrust equilibrium point manifold has been selected from the linearized dynamics, a nonlinear propagation is performed. The low-thrust control parameters are set to be identical to the equilibrium point parameters, e.g., $a_{1t} = 7e-2$, $\alpha = 180^\circ$ and $\beta = 0^\circ$. Two stable manifolds, W_1^{s-} and W_1^{s+} , are propagated in reverse time from \vec{X}^{s-} and \vec{X}^{s+} while two unstable manifolds, W_1^{u-} and W_1^{u+} , are propagated in forward time from \vec{X}^{u-} and \vec{X}^{u+} , yielding the arcs

plotted in Figure 3.23. The manifold notation communicates three characteristics to

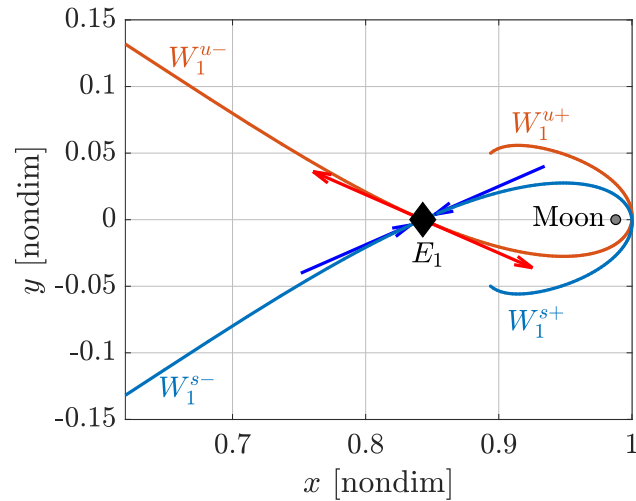


Figure 3.23.: The stable (blue) and unstable (red) manifolds associated with the Earth-Moon $\mathbb{E}_1(0.07, 180^\circ, 0^\circ)$ equilibrium point are tangent to the linear modes (the eigenvectors) at the equilibrium point

distinguish between manifolds. First, the subscript denotes the fixed point, \mathbb{E}_1 in this case. Second, the superscript describes the type of manifold, e.g., s for stable and u for unstable, as well as the direction along the x -axis the manifold flows relative to the fixed point: the $u-$ manifold departs toward $-\hat{x}$ while $u+$ departs toward $+\hat{x}$. When these manifolds are close to the equilibrium point, marked by a black diamond, the manifolds are tangent to the linear dynamics, i.e., the eigenvectors (plotted as arrows). However, as the manifolds evolve away from the equilibrium point, they are no longer tangent to the linear predictions.

By leveraging the globalization method, all of the hyperbolic manifolds associated with the CR3BP+LT equilibria for $a_{lt} = 0.07$, $\alpha = 180^\circ$, and $\beta = 0^\circ$ are computed. The low-thrust hyperbolic manifolds for E_1 , E_2 , and E_3^1 , plotted in Figure 3.24, appear very similar to the ballistic L_1 , L_2 , and L_3 hyperbolic manifolds in the Earth-Moon system, as seen in Figure 3.25, at least for the times of flight represented in these plots. The E_1 and E_2 manifolds appear particularly similar to the L_1 and L_2 manifolds, while the E_3 and L_3 manifolds demonstrate slightly different geometries.

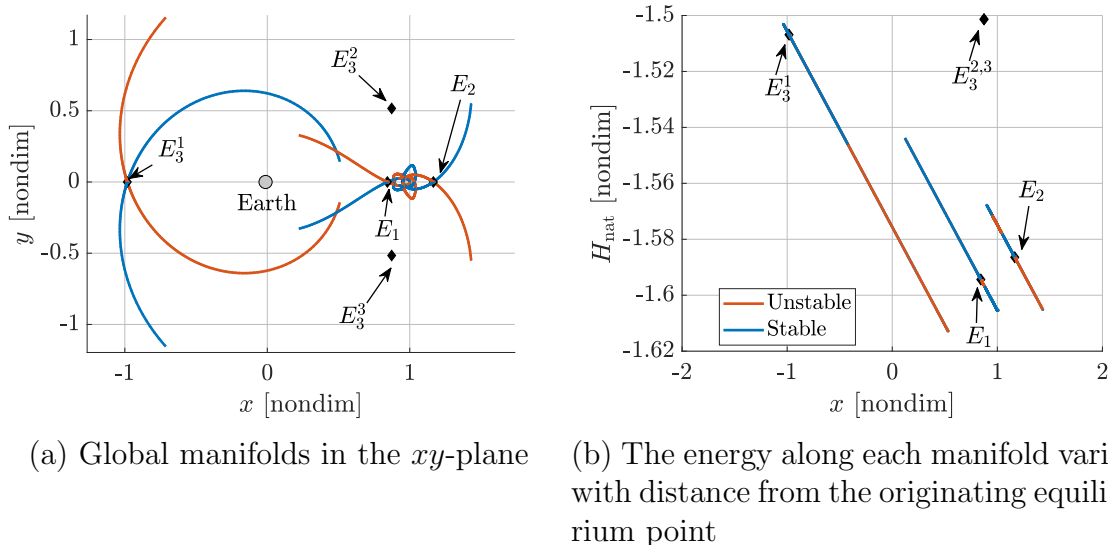


Figure 3.24.: Hyperbolic manifolds of the Earth-Moon CR3BP+LT equilibria for $a_{lt} = 7e-2$, $\alpha = 180^\circ$ and $\beta = 0^\circ$

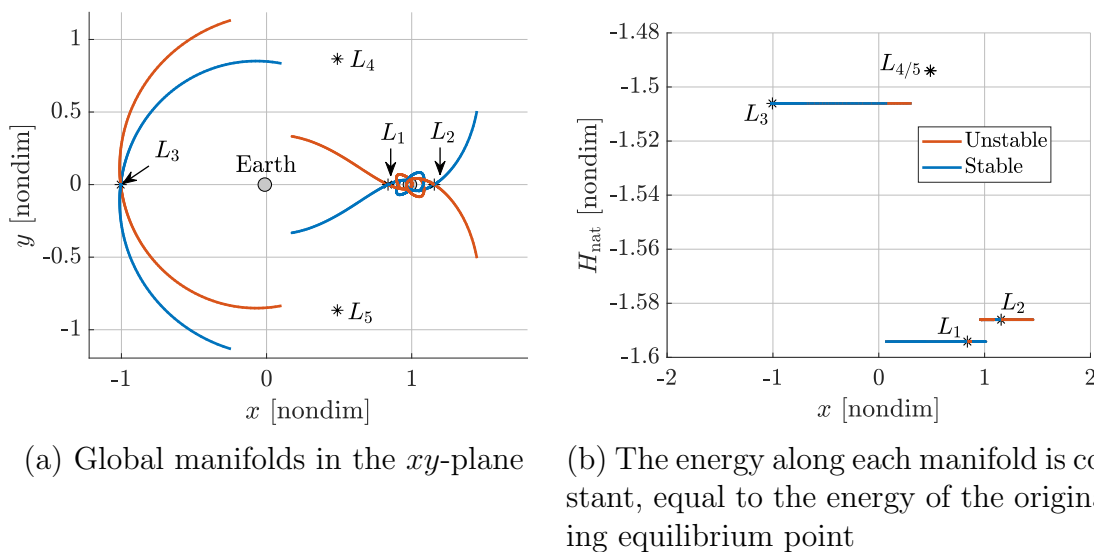


Figure 3.25.: Ballistic hyperbolic manifolds of the Earth-Moon equilibria

In both models, the “triangular points”, i.e., $E_3^{2/3}$ and $L_{4/5}$, are characterized by C^6 motion and do not possess a hyperbolic manifold. Despite the similar geometries in the xy -plane, the velocities along these manifolds vary significantly, as revealed by the differences in energy, i.e., in H_{nat} values, in Figures 3.24(b) and 3.25(b). Whereas

the ballistic manifolds maintain a constant energy, the H_{nat} value along the low-thrust manifolds evolves on the energy plane defined in Section 2.2.8. Recall that, for $\beta = 0$, the energy plane is oriented by the α angle and inclined by the a_{lt} magnitude. Thus, the energy plane tilts “upward” (i.e., toward increasing H_{nat} values) in the $-\hat{x}$ direction for $\alpha = 180^\circ$, as seen in the plot of H_{nat} vs x in Figure 3.24(b). All four manifolds for each equilibrium point exist in the same energy plane because each manifold includes the equilibrium point. Accordingly, the low-thrust equilibrium point manifolds can deliver similar geometric paths as the ballistic manifolds while simultaneously delivering a change in H_{nat} .

Although the geometry of the low-thrust and ballistic hyperbolic manifolds appear similar for $a_{\text{lt}} = 0.07$, $\alpha = 180^\circ$, and $\beta = 0^\circ$, these similarities do not persist for all values of the control parameters. For example, when the α angle is changed, as in Figure 3.26, the location of the E_3^1 point changes and its manifolds vary significantly. For some α angles, such as $\alpha = 0^\circ$ and $\alpha = -40^\circ$, the single E_3 point does not possess hyperbolic manifolds at all. (The parameter-space view of the equilibria for $a_{\text{lt}} = 7\text{e-}2$ and $\beta = 0$ in Figure 3.17 shows the precise range of α values for which an E_3 point possesses hyperbolic manifolds.) As the E_3^1 point moves relative to the Lagrange points (marked by black asterisks), the geometry of the hyperbolic manifolds associated with that point adjusts to match.

The manifold geometry also changes when the β angle is adjusted. While the planar projections of these spatial manifolds appear similar to the manifolds for $\beta = 0^\circ$ (at least for $\alpha = 180^\circ$), the out-of-plane components of the manifolds are strongly affected by the β angle, as depicted in Figure 3.27. Because $\sin(\alpha) = 0$ in this scenario, a 2D energy plane in x - z - H_{nat} space may be constructed to visualize the energy change along the manifolds. In other words, the H_{nat} value along these manifolds evolves with x and z , but is independent of y , as described by Equation (2.130). Animations of the planar and spatial Earth-Moon low-thrust manifolds, available online, show how the manifolds vary for the full range of α and β angles. Due to

¹¹https://engineering.purdue.edu/people/kathleen.howell.1/Publications/Dissertations/2020_Cox/#2dEqPtManifolds

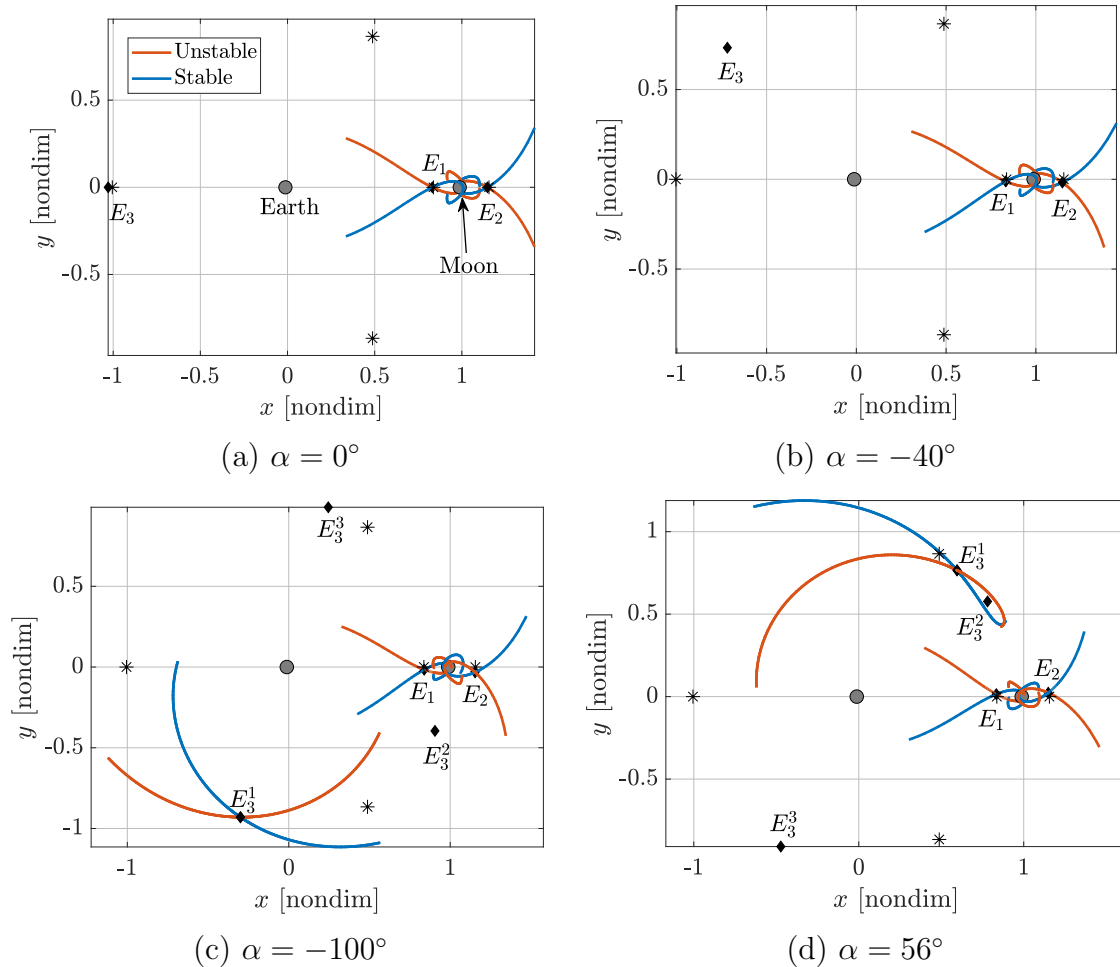


Figure 3.26.: Earth-Moon CR3BP+LT equilibrium point hyperbolic manifolds for $a_{lt} = 7e-2$ and $\beta = 0^\circ$ with different α angles ([Animation](#))¹¹

the significant differences in geometry and energy evolution between the low-thrust equilibrium point manifolds and the ballistic equilibrium point manifolds, novel trajectory options are available when low-thrust is applied. The Earth-Moon \mathbb{E}_3 points supply particularly interesting manifold geometries, especially when the \mathbb{E}_3 points are located near $L_{4/5}$. In the ballistic model, $L_{4/5}$ do not possess hyperbolic manifolds; thus, no natural flow exists to guide a spacecraft toward or away from those points.

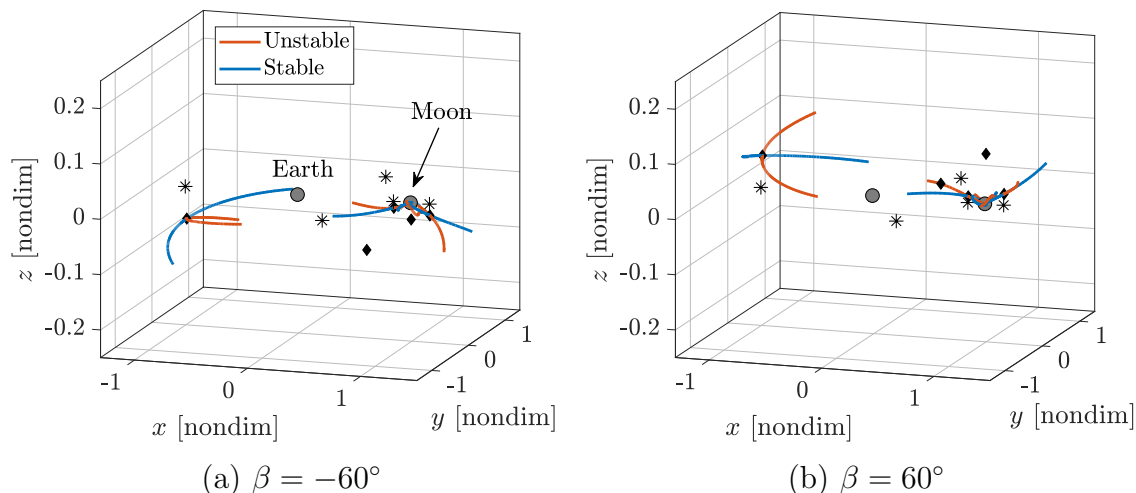


Figure 3.27.: Earth-Moon CR3BP+LT equilibrium point hyperbolic manifolds for $a_{lt} = 7e-2$ and $\alpha = 180^\circ$ with different β angles ([Animation](#))¹²

In contrast, some of the low-thrust equilibria located near $L_{4/5}$ do possess hyperbolic manifolds that may be employed to design a trajectory to the vicinity of L_4 or L_5 .

Similar to the low-thrust equilibria manifolds in the Earth-Moon system, manifolds associated with the low-thrust equilibrium points in the Sun-EMB system possess different geometries compared to the ballistic Sun-EMB manifolds. Like the Earth-Moon system, the Sun-EMB L_1 , L_2 , and L_3 points possess hyperbolic manifolds while L_4 and L_5 do not, as depicted in Figure 3.28. When the low-thrust acceleration is incorporated into the model, the equilibrium solutions shift significantly compared to the ballistic points, as discussed in Section 3.2.4 (see Figure 3.9). The manifolds associated with these points, pictured in Figure 3.29 for $a_{lt} = 3.2e-2$ and $\beta = 0^\circ$, also shift significantly relative to the ballistic manifolds. For instance, when $\alpha = 0^\circ$, only three low-thrust equilibria exist, two near L_1 and L_2 , and one near L_3 , as depicted in Figures 3.29(a) and 3.29(b). Only the points near L_1 and L_2 possess hyperbolic manifolds in this configuration; the low-thrust equilibrium solution near L_3 is characterized entirely by a 6D center manifold. The two hyperbolic manifolds that exist

¹²https://engineering.purdue.edu/people/kathleen.howell.1/Publications/Dissertations/2020_Cox/#3dEqPtManifolds

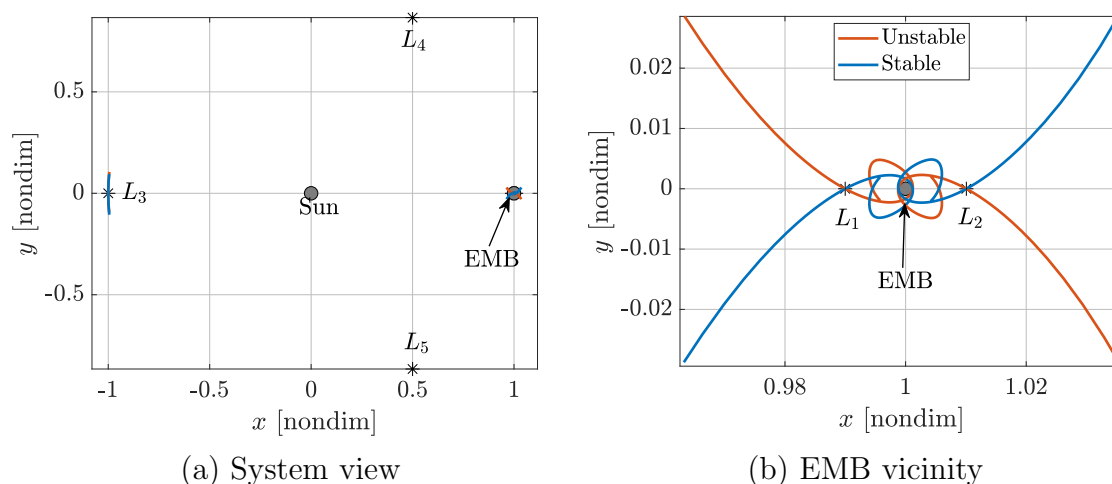


Figure 3.28.: Hyperbolic manifolds associated with the ballistic Sun-EMB equilibria

near L_1 and L_2 have very different geometries than the ballistic L_1 and L_2 manifolds. The E_1^1 manifolds do not approach the EMB, in contrast to the L_1 manifolds, while the E_2 manifolds wrap more “tightly” around the EMB than the corresponding ballistic L_2 manifolds. The structure of the \mathbb{E}_2 manifolds is similar across the full range of α values, including $\alpha = -169^\circ$ in Figure 3.29(d) and $\alpha = 11^\circ$ in Figure 3.29(f). One branch of the \mathbb{E}_2 manifolds approaches the EMB while the other branch departs the vicinity, reflecting similar geometries as the L_1 and L_2 manifolds depending on the α angle. On the other hand, the geometry of the manifolds associated with the \mathbb{E}_1 points varies considerably with α . For example, the two of the manifolds associated with the E_1^2 point for $\alpha = -169^\circ$ converge upon the other two manifolds after wrapping around the E_1^3 point. At this same α angle, the \mathbb{E}_1 point located near L_3 possesses a hyperbolic mode, in contrast to the \mathbb{E}_1 point in the same region for $\alpha = 0^\circ$. In an additional scenario, the hyperbolic manifold geometries for $\alpha = 11^\circ$, seen in Figures 3.29(e) and 3.29(f), appear similar to the manifold geometries for $\alpha = 0^\circ$, but an extra equilibrium point located near $x = 1$ and $y = 0.2$ admits a hyperbolic subspace, supplying additional manifolds to guide flow throughout the region. An animation of Figure 3.29, available online, shows the evolution of the Sun-EMB hyperbolic manifolds for the full range of α values. Although the geometries

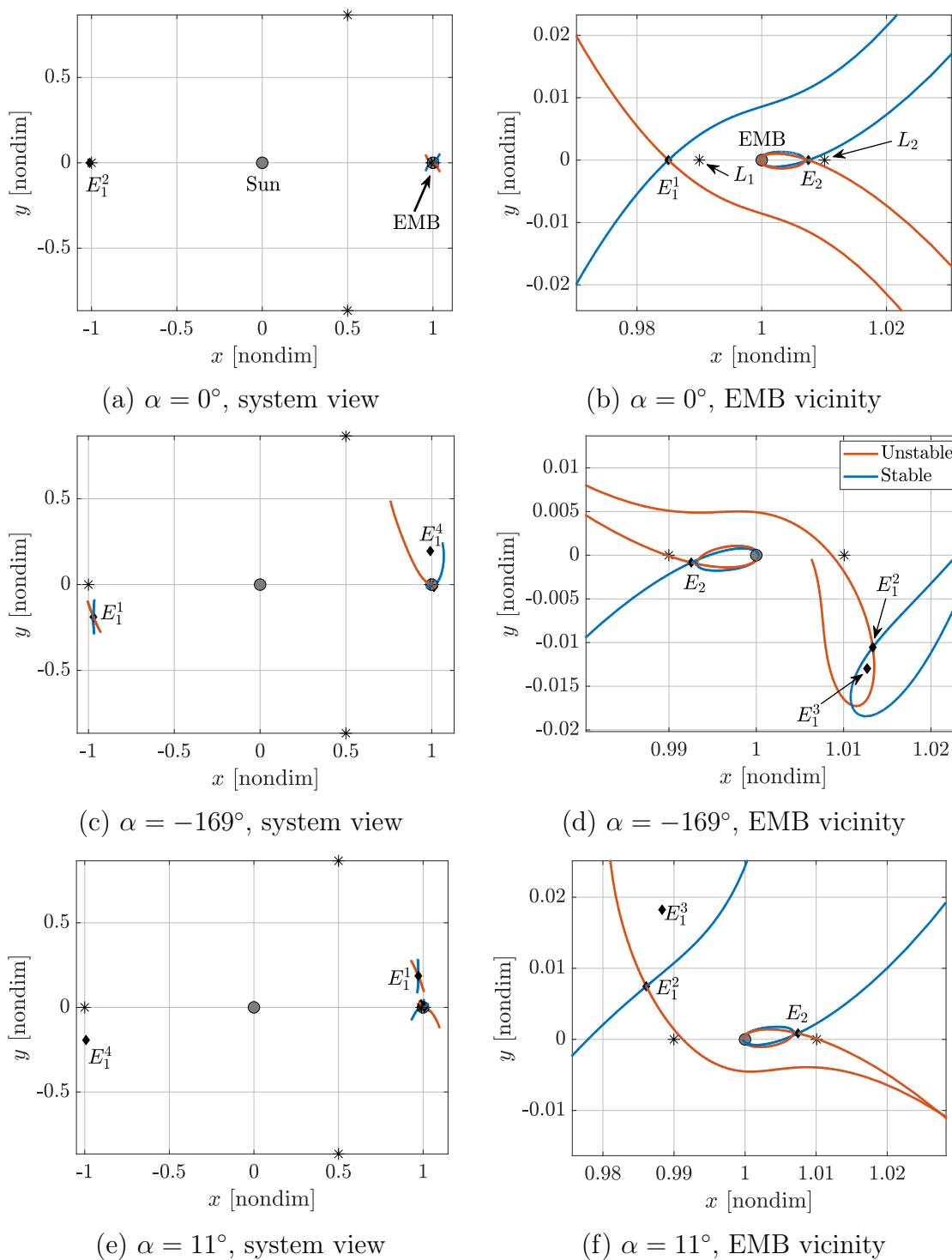


Figure 3.29.: Saddle manifolds in the Sun-EMB system for $a_{1t} = 3.2e-2$ and $\beta = 0$ ([Animation](#)¹³)

and energy profiles of the low-thrust equilibrium point hyperbolic manifolds vary significantly with the low-thrust control parameters, this diversity of solutions supplies novel options for preliminary trajectory designs. The variety of manifold geometries and energy profiles also facilitates an increased understanding of the effects of the low-thrust acceleration on the dynamics in the CR3BP, the primary objective of this investigation.

3.3.2 Center Manifold: Periodic Orbits

The center manifold describes flow patterns that oscillate relative to a fixed point (e.g., an equilibrium solution) and, similar to the hyperbolic manifolds, supplies useful structures to be employed in the trajectory design process. An oscillatory solution that repeats exactly is termed a *periodic orbit* while a solution that nearly repeats but never quite returns to the initial state is called a *quasi-periodic orbit*. Periodic orbits may be computed directly from the equilibrium point center manifold while the quasi-periodic solutions are more straightforwardly initialized from the center manifold of one of the periodic solutions. In this investigation, only the periodic orbits are explored in detail. However, the initialization of the center manifold from linear modes is derived in a general way to facilitate the construction of the other oscillatory solutions, such as the mixed mode solutions, i.e., *stable* and *unstable spirals*. Finally, in contrast to the equilibrium point hyperbolic manifolds, structures within the center manifold of an equilibrium solution exist in *families*. Continuation algorithms are employed to explore several families of periodic orbits.

¹³https://engineering.purdue.edu/people/kathleen.howell.1/Publications/Dissertations/2020_Cox/#2dSEMBEqPtManifolds

Initialization from Linear Modes

As discussed in the previous section, the nonlinear dynamics are approximated by a linearization about a reference solution. Mathematically, the linearized dynamics are represented by the superposition of the linear modes,

$$\delta\vec{X}(\tau) = \sum_{j=1}^6 c_j \exp(\lambda_j \tau) \vec{v}_j, \quad (3.67)$$

where λ_j and \vec{v}_j are the eigenvalues and eigenvectors of the \mathbf{A} matrix evaluated at the equilibrium solution, and $\delta\vec{X}$ represents the linear solution relative to the equilibrium state, \vec{X}_e . To isolate the center mode(s), the c_j coefficients corresponding to the non-center eigenvalues and eigenvectors are set to zero. For example, recall the eigenstructure of the Earth-Moon \mathbb{E}_1 point for $a_{\text{lt}} = 0.07$, $\alpha = 180^\circ$ and $\beta = 0^\circ$, presented in Table 3.1. Two sets of complex conjugate eigenvalues, λ_{c1} and λ_{c2} , represent a 4D center mode. For simplicity, consider each mode individually and set the coefficients that correspond to the λ_{c2} eigenvalues to zero. To enable a general derivation of the center and mixed mode linearization, let

$$\lambda = \kappa + iw, \quad (3.75)$$

with the corresponding eigenvector, \vec{v} . The linearized dynamics are then described by

$$\delta\vec{X}(\tau) = c_1 \exp(\lambda\tau) \vec{v} + c_2 \exp(\bar{\lambda}\tau) \bar{\vec{v}}. \quad (3.76)$$

This complex equation may be expanded using Euler's formula,

$$\delta\vec{X}(\tau) = c_1 e^{\kappa\tau} \left[\vec{\varphi} \cos(w\tau) - \vec{\psi} \sin(w\tau) \right] + c_2 e^{\kappa\tau} \left[\vec{\psi} \cos(w\tau) + \vec{\varphi} \sin(w\tau) \right], \quad (3.77)$$

where $\vec{\varphi} = \text{Re}(\vec{v})$ and $\vec{\psi} = \text{Im}(\vec{v})$. Given an initial variation, $\delta\vec{X}(0)$, the c_1 and c_2 coefficients may be defined by solving this equation and its first time derivative at

$\tau = 0$. Alternatively, the two coefficients may be set to small, real values to initialize a center ($\kappa = 0$) or mixed ($\kappa \neq 0$) linear mode near the fixed point.

To illustrate the construction of the linear center solutions, the center modes associated with the Earth-Moon $E_1(0.07, 180^\circ, 0^\circ)$ and $E_1(0.07, 180^\circ, 60^\circ)$ are employed. Each of these equilibria possesses a 4D center subspace, i.e., two pairs of imaginary eigenvalues ($\kappa = 0, w \neq 0$). Thus, two distinct center solutions are available for each of the equilibrium points. For example, the center solutions associated with the planar point, $E_1(0.07, 180^\circ, 0^\circ)$, pictured in Figure 3.30(a), include a planar center mode (black) and an out-of-plane center mode (red). The planar solution is associ-

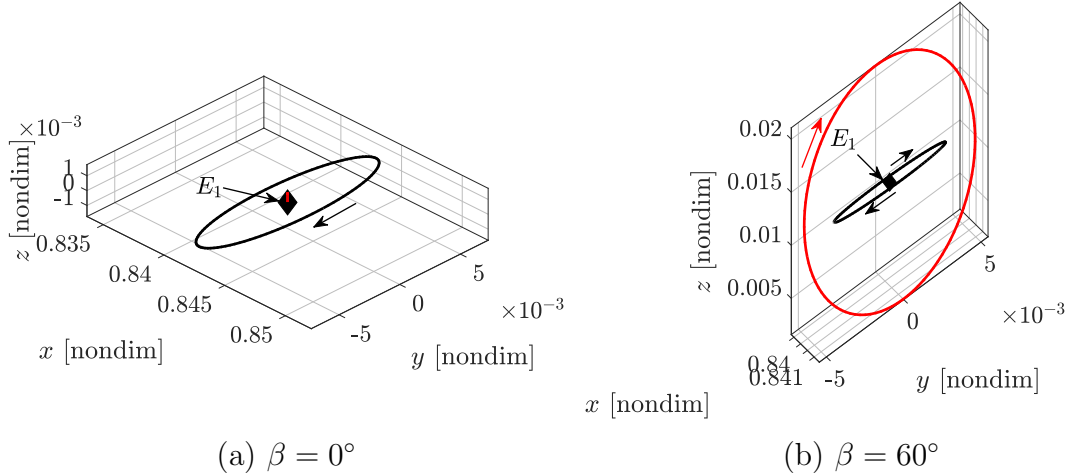


Figure 3.30.: Distinct center modes (black and red) from the linearized dynamics about the Earth-Moon E_1 point for $a_{1t} = 7e-2$ and $\alpha = 180^\circ$

ated with $\lambda_{c1} = \pm 2.4236i$ (from Table 3.1) while the out-of-plane mode corresponds to $\lambda_{c2} = \pm 2.3600i$. Accordingly, the frequencies of the two linear solutions, equal to the imaginary component of the related eigenvalue, w , are slightly different. The geometry of each center solution, i.e., each ellipse, is represented by the eigenvector; the real and imaginary components, $\vec{\varphi}$ and $\vec{\psi}$, are the principal axes of the ellipse. In contrast to the planar/spatial dichotomy observed in the center modes for $\beta = 0^\circ$, the linearized center modes for $E_1(0.07, 180^\circ, 60^\circ)$, displayed in Figure 3.30(b), are both spatial structures with nontrivial z components relative to the equilibrium point. In

either case, the two distinct center mode solutions form a “basis” of center solutions; any linear combination of the two distinct solutions is also a solution to the linearized dynamics expressed in Equation (3.67). Subsequently, a diverse set of center solutions are available.

Globalization to Nonlinear Dynamics

Similar to the hyperbolic manifolds, the linearized center motion is transitioned into the nonlinear dynamics by propagating a state (or multiple states) from the linear solution in the full, nonlinear model. However, in contrast to the hyperbolic manifold globalization, the center manifold is not directly available from this propagation. In other words, a periodic solution to the nonlinear dynamics does not intersect the periodic solution to the linear dynamics. However, the two solutions are similar; thus, by employing differential corrections, a periodic solution to the nonlinear dynamics is constructed.

While many strategies for differential corrections are available, a multi-dimensional Newton-Raphson algorithm is employed in this investigation because of its simplicity and adaptability to many different scenarios [55]. The simplicity and adaptability of the method stems from the formulation of the problem. Consider two vectors: a free variable vector, $\vec{\mathcal{X}}$, and a constraint vector, $\vec{\mathcal{F}}$. The elements within $\vec{\mathcal{X}}$ may represent states, times-of-flight, control parameters, or similar variables that are adjusted to obtain a desired solution. The elements of $\vec{\mathcal{F}}$ are constraints on the free variables and is equal to zero when satisfied. The goal of the Newton scheme is a set of design variables, $\vec{\mathcal{X}}^*$, that satisfies all constraints, i.e., $\vec{\mathcal{F}}(\vec{\mathcal{X}}^*) = \vec{0}$ [56]. A linear approximation of the relationship between $\vec{\mathcal{F}}$ and $\vec{\mathcal{X}}$ is employed to iteratively update an initial guess, $\vec{\mathcal{X}}^0$, until the constraints are satisfied,

$$\vec{\mathcal{X}}^{n+1} = \vec{\mathcal{X}}^n - \mathbf{G}^T(\mathbf{G}\mathbf{G}^T)^{-1}\vec{\mathcal{F}}(\vec{\mathcal{X}}^n), \quad (3.78)$$

where \mathbf{G} is the Jacobian of the constraint vector,

$$\mathbf{G} = \frac{\partial \vec{\mathcal{F}}(\vec{\mathcal{X}})}{\partial \vec{\mathcal{X}}}, \quad (3.79)$$

evaluated at $\vec{\mathcal{X}}^n$ (many sources supply this derivation; [57] is most consistent with this investigation). This update equation leverages a *minimum norm* solution to minimize the differences between the subsequent iterations of the free variable vector, ideally converging upon a set of variables that are similar to the initial guess, $\vec{\mathcal{X}}^0$.

To construct a nonlinear periodic orbit, the solution to the linearized dynamics is employed as an initial guess. A free variable vector is constructed,

$$\vec{\mathcal{X}} = \left\{ \vec{X}_1^T, \vec{X}_2^T, \dots, \vec{X}_n^T, \Delta\tau \right\}^T, \quad (3.80)$$

where $\vec{X}_i, i = 1, \dots, n$ are *patch points* along the linear solution and $\Delta\tau$ is the constant time-of-flight between the patch points. A set of constraints enforces continuity between propagated arcs, the periodicity of the solution, and fixes the orbit phasing,

$$\vec{\mathcal{F}} = \left\{ \begin{array}{c} \vec{\phi}(\Delta\tau, \vec{X}_1) - \vec{X}_2 \\ \vdots \\ \vec{\phi}(\Delta\tau, \vec{X}_{n-1}) - \vec{X}_n \\ \mathbf{M} \left(\vec{X}_n - \vec{X}_1 \right) \\ h(\vec{X}_1) \end{array} \right\}. \quad (3.81)$$

In this notation, $\vec{\phi}(\Delta\tau, \vec{X}_i)$ represents the *flow map* that results from numerically integrating \vec{X}_i for the time-of-flight equal to $\Delta\tau$. The periodicity of the nonlinear solution is enforced by equating the first and final patch points, as in the second to last row of $\vec{\mathcal{F}}$, where \mathbf{M} is a masking matrix. Finally, the orbit phasing is constrained by fixing one of the initial state values, as in the final row of $\vec{\mathcal{F}}$. Many other strategies for correcting periodic orbits exist, some more flexible and elegant than this method [58].

However, as differential corrections techniques are not the focus of this investigation, this simple set of constraints is deemed sufficient.

As an example of the differential corrections strategy to construct a nonlinear periodic orbit, consider the planar center solution for the Earth-Moon $\mathbb{E}_1(0.07, 180^\circ, 0^\circ)$ equilibrium point. The linear solution, displayed in black in Figures 3.30(a) and 3.31, is discretized by placing five patch points, equally spaced in time, along the linear solution with the final patch point collocated with the initial patch point. When the

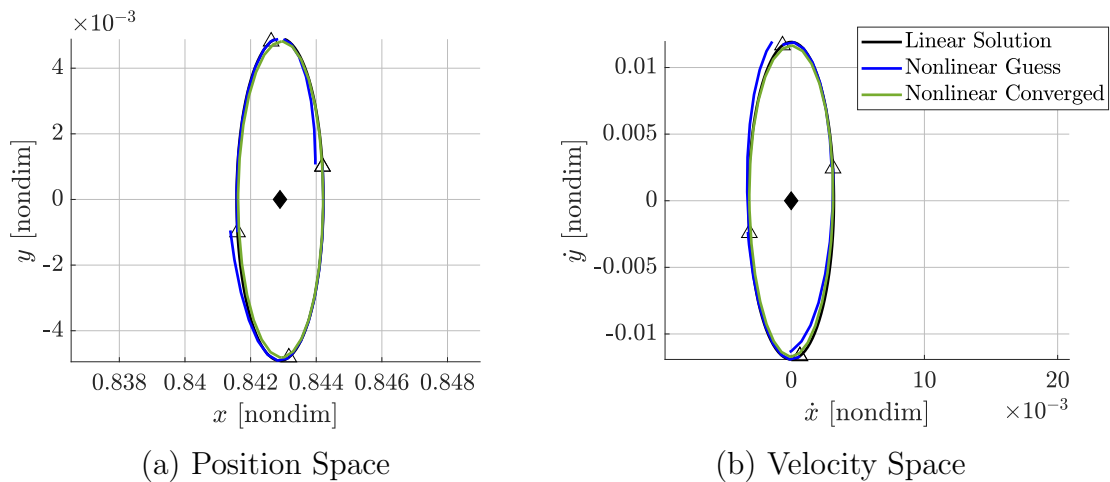


Figure 3.31.: A nonlinear periodic orbit is initialized from the linear solution and converged via differential corrections in the Earth-Moon system for $a_{lt} = 7e-2$, $\alpha = 180^\circ$, and $\beta = 0$

five points selected from the linear solution are propagated in the nonlinear dynamics, the resulting arcs, colored blue in Figure 3.31, are not continuous. The differential corrections process is then employed to adjust the patch points such that each arc connects smoothly (i.e., continuously) with the next and the nonlinear solution is periodic. Because the \vec{a}_{lt} vector is constant, the CR3BP+LT is a conservative system and an integral of the motion (i.e., H_{lt}) exists. Accordingly, only five of the six state variables need to be included in the periodicity constraint. To determine which of the state variables to leave unconstrained, it is prudent to consider the phase constraint. In general, non-symmetric periodic orbits always cross through $\dot{x} = 0$, $\dot{y} = 0$,

and $\dot{z} = 0$ at least twice, but are not guaranteed to pass through any specific hyperplane in position space (particularly when a continuation algorithm is utilized to compute multiple periodic orbits). Accordingly, a phase constraint on \dot{x} is employed, i.e., $h(\vec{X}_1) = \dot{x}_1 = 0$. A suitable periodicity constraint accounts for this phase constraint by identifying the largest of the other velocity coordinates at the point where the phase constraint is satisfied. For this planar periodic orbit, the \dot{y} component is large (i.e., far from zero) when $\dot{x} = 0$. Thus, the \mathbf{M} matrix is constructed such that the \dot{y} component of the periodicity constraint is not included in $\vec{\mathcal{F}}$. Because of this coordinated decision, the differential corrections algorithm is less likely to converge upon a solution that satisfies the constraints but is not periodic with $\dot{y}_1 = -\dot{y}_n$.

When the continuity and periodicity constraints are applied in the differential corrections process, the patch points are adjusted to achieve continuity and periodicity, resulting in the nonlinear periodic solution plotted in green in Figure 3.31. Let $\Gamma = \Gamma(a_{\text{lt}}, \alpha, \beta, H_{\text{lt}})$ represent a low-thrust periodic orbit (LTPO) with constant low-thrust control along the orbit specified by the magnitude, a_{lt} , and orientation angles, α and β ; the constant H_{lt} value associated with the orbit also distinguishes the orbit from others with the same control parameterization. Accordingly, the low-thrust periodic orbit in Figure 3.31 is denoted $\Gamma(0.07, 180^\circ, 0^\circ, -1.5352)$. While the low-thrust Hamiltonian is constant along the orbit, the natural Hamiltonian varies along an energy plane oriented by the low-thrust control parameters associated with the orbit. Because the control parameters are constant, the entire periodic orbit exists on the same energy plane and the H_{nat} value is periodic.

The same process may be applied to any of the solutions described by the linearized dynamics in (3.77) to generate a variety of low-thrust periodic orbits (LTPOs). Like the hyperbolic manifolds, these center manifold structures vary in geometry, location, and energy with the low-thrust equilibrium points. Periodic solutions with non-constant \vec{a}_{lt} vectors may also be computed. For example, when $\vec{a}_{\text{lt}} \perp \vec{v}$, Lyapunov-like low-thrust periodic solutions have been shown to exist [29] in families that evolve in H_{nat} (recall from Section 2.2.4 that H_{nat} is constant when $\vec{a}_{\text{lt}} \perp \vec{v}$) or in f . Accordingly,

a diverse set of periodic orbits are available for inclusion in itineraries that include low-thrust arcs.

Periodic Orbit Stability

Similar to an equilibrium solution, the linearized dynamics relative to a periodic orbit deliver the stability properties. Recall that the \mathbf{A} matrix, defined in Equation (3.64), that relates the derivative of a variational state, $\delta\dot{\vec{X}}$, to the variational state, $\delta\vec{X}$, is a constant matrix when evaluated at an equilibrium solution due to the time-invariance of the equilibria. However, the \mathbf{A} matrix is not constant when evaluated along a periodic orbit that evolves with time. Accordingly, integrating the variational Equation (3.61) (e.g., along an orbit) in the time-varying dynamics from τ_0 to τ yields

$$\delta\vec{X}(\tau) = \Phi(\tau, \tau_0)\delta\vec{X}(\tau_0), \quad (3.82)$$

where Φ is the *state transition matrix* (STM) and is defined as

$$\Phi(\tau, \tau_0) = \exp(\mathbf{A}(\tau - \tau_0)). \quad (3.83)$$

In this case $\mathbf{A}(\tau - \tau_0)$ is the \mathbf{A} matrix evaluated at time $\tau - \tau_0$, not the product of the two terms. The state transition matrix, Φ , represents a linear map between perturbations in an initial state, $\vec{X}(\tau_0)$, and a later state, $\vec{X}(\tau)$. In the ballistic CR3BP, Φ is symplectic with the properties,

$$\begin{aligned} \Phi(\tau_2, \tau_0) &= \Phi(\tau_2, \tau_1)\Phi(\tau_1, \tau_0), \\ \Phi(\tau_0, \tau) &= \Phi(\tau_1, \tau_0), \\ \det(\Phi) &= 1. \end{aligned}$$

Because the CR3BP+LT system with \vec{a}_{1t} held constant in the rotating frame is structurally equivalent to the ballistic CR3BP (the CR3BP+LT remains conserva-

tive, autonomous, and Hamiltonian), these properties also apply to the STM in the CR3BP+LT. A matrix differential equation is obtained by substituting Equation (3.82) into Equation (3.61),

$$\dot{\Phi}(\tau, \tau_0) = \mathbf{A}(\tau)\Phi(\tau, \tau_0). \quad (3.84)$$

This relationship is numerically integrated from the initial condition, $\Phi(\tau_0, \tau_0) = \mathbf{I}$, in parallel with the state vector equations of motion to yield a time history for the STM. In general, the STM associated with an arc predicts how variations in the initial state propagate to variations downstream. When evaluated along a periodic orbit, the STM is termed the *monodromy matrix*; it maps perturbations in the initial state to perturbations after one period of the orbit, T . By definition, a periodic orbit repeats after time T , i.e., $\vec{X}(\tau) = \vec{X}(\tau + T)$. Thus, the periodic solution is a *fixed point* on the stroboscopic map represented by the monodromy matrix and the linear approximation may be represented in discrete form,

$$\delta\vec{X}(\tau + kT) = \Phi(\tau + kT, \tau)\Delta\vec{X}(\tau) = \Phi(\tau + T, \tau)^k\delta\vec{X}(\tau). \quad (3.85)$$

The solution to this discrete-time differential equation is the superposition of the linear modes,

$$\delta\vec{X}(\tau + kT) = \sum_{j=1}^6 c_j \lambda_j^k \vec{v}_j, \quad (3.86)$$

where λ_j and \vec{v}_j are an eigenvalue-eigenvector pair of $\Phi(\tau + kT, \tau)$ and c_j is a scalar constant. Due to the symplectic properties of the STM, the eigenvalues occur in reciprocal pairs [59], i.e., λ and $1/\lambda$. Additionally, the eigenvalues of the monodromy matrix always include two unit eigenvalues [60].

Similar to the linearized dynamics relative to the equilibrium points, this discrete-time linearization supplies stability information about the reference solution, i.e., the periodic orbit. The hyperbolic, center, and mixed modes are identified by the relationship between the eigenvalues and the unit circle in the complex plane [61, 62]:

- $\text{Im}(\lambda) = 0$ and $|\lambda| \neq 1$ - the eigenvalue corresponds to a hyperbolic mode; the stable subspace is linked to the eigenvalue with a magnitude less than one and the unstable subspace is linked to the eigenvalue with a magnitude greater than one.
- $|\lambda| = 1$ - the eigenvalue is on the unit circle and corresponds to a center mode
- $\text{Im}(\lambda) \neq 0$ and $|\lambda| \neq 1$ - the complex eigenvalue is not on the unit circle and corresponds to a mixed mode

Note that if a mixed mode exists, it is four-dimensional; if λ and $1/\lambda$ are eigenvalues, then $\bar{\lambda}$ and $1/\bar{\lambda}$ are also eigenvalues because Φ is a real matrix. Since the periodic orbit is completely described by the fixed point on the stroboscopic map, the stability of the fixed point, as determined by the eigenvalues of the monodromy matrix, is synonymous to the stability of the periodic orbit [63]. The stability properties of an orbit are reduced to a two-parameter description by defining two stability indices,

$$s_j = \frac{1}{2} (\lambda_{2j-1} + \lambda_{2j}), \quad j = 1, 2, \quad (3.87)$$

where λ_j and λ_{j+1} are a reciprocal pair (i.e., $\lambda_j = 1/\lambda_{j+1}$). Since the unit eigenvalues, here denoted λ_5 and λ_6 , are consistent across the family, they are excluded from the stability analysis. The values of the s_1 and s_2 indices describe the type of linear mode associated with the eigenvalue pair:

- $\text{Im}(s_j) = 0, |s_j| > 1$ - the eigenvalues are a real, reciprocal pair associated with a hyperbolic mode
- $\text{Im}(s_j) = 0, -1 \leq s_j \leq 1$ - the eigenvalues are a pair of complex conjugates on the unit circle associated with a center mode
- $\text{Im}(s_j) \neq 0, |s_j| \neq 1$ - the eigenvalues are a complex reciprocal pair associated with a mixed mode

Again note that a mixed mode always occurs as a four-dimensional subspace relative to a periodic orbit.

A useful alternative to the stability indices are the parameters employed by Broucke [64]. These parameters, \tilde{a} and \tilde{b} , leverage the relationship between the eigenvalues of Φ and the trace of Φ to describe the stability properties without evaluating the eigenvalues (a process that can be computationally expensive and prone to error),

$$\tilde{a} = - \sum_{j=1}^4 \lambda_j = 2 - \text{tr} [\Phi(\tau + T, \tau)], \quad (3.88)$$

$$\tilde{b} = \frac{1}{2} \left(\tilde{a}^2 - \sum_{j=1}^4 \lambda_j^2 \right) = \frac{1}{2} \left(\tilde{a}^2 + 2 - \text{tr} [\Phi(\tau + T, \tau)^2] \right). \quad (3.89)$$

When plotted against each other, as in Figure 3.32, these parameters describe the stability properties of a periodic orbit. The space is separated into seven regions, labeled

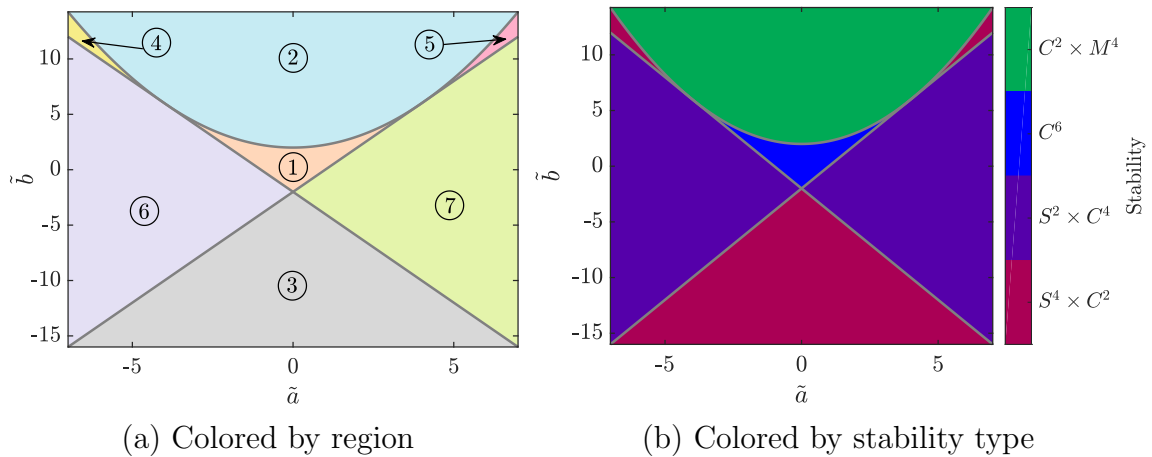


Figure 3.32.: Broucke stability diagram

in the figure with circled numbers, each corresponding to a specific eigenvalue configuration (see [64], Fig. 2). A periodic orbit is represented in this space by computing the \tilde{a} and \tilde{b} values from the monodromy matrix and plotting them on the stability diagram. The region the point is located within supplies stability information as in Figure 3.32(b), as well as detailed information about the structure of the eigenvalues. For example, regions 6 and 7 both correspond to the $S^2 \times C^4$ stability type but the locations of the hyperbolic manifold eigenvalues are different in the two regions; see

[64] for details. Observe that the center subspace always possesses a dimension of at least two as the two unit eigenvalues constitute a 2D center mode. The significance of the eigenvalues and their use in constructing additional dynamical structures are explored in the next section.

3.4 Periodic Orbit Manifolds

Similar to the analysis of the equilibrium points in Section 3.3, the linearized dynamics about a periodic orbit may be employed to initialize additional dynamical structures. While the methods to construct these structures are analogous to the equilibrium point analyses, the dimension of the resulting structures is increased by one. For instance, the equilibrium point is fixed in space and time, i.e., it is a zero-dimensional structure. The hyperbolic manifolds and center manifolds (i.e., periodic orbits) initialized from the linear dynamics near the equilibrium point are then 1D structures. Although the periodic orbit appears as a 0D point on the stroboscopic map, the orbit itself is a 1D structure. Thus, the hyperbolic and center manifolds associated with the orbit appear as 1D structures on the map but are 2D structures within the full 6D space. This pattern continues through the center manifold, e.g., a quasi-periodic orbit located within the center manifold of a periodic orbit may possess a hyperbolic and/or center subspace of its own, delivering even higher dimensional manifolds. For the purposes of this investigation, only the periodic orbit hyperbolic manifolds and the “trivial” center manifold (i.e., the center mode associated with the eigenvalues at $\lambda = +1$) are considered. The exploration of quasi-periodic low-thrust structures and their manifolds are reserved for a future investigation.

3.4.1 Hyperbolic Manifold

Similar to the hyperbolic manifolds associated with the equilibrium points, the hyperbolic manifolds associated with a periodic orbit describe paths that asymptotically approach and depart the orbit. Accordingly, these manifolds are frequently

employed as segments of spacecraft trajectories to supply a low-cost (in terms of Δv) path into or out of a periodic orbit [14]. Recall that the linearized dynamics relative to a periodic orbit fixed point are described by

$$\delta\vec{X}(\tau + kT) = \sum_{j=1}^6 c_j \lambda_j^k \vec{v}_j, \quad (3.86)$$

reprinted here for convenience. Consistent with the approach leveraged for the equilibrium point hyperbolic manifolds, the c_j coefficients may be selected such that the hyperbolic manifold directions are isolated. Accordingly, the linear representation of the stable or unstable LTPO manifold is given by,

$$\delta\vec{X} = c\lambda^k \vec{v}, \quad (3.90)$$

where $\delta\vec{X}$ is a state change relative to the periodic orbit fixed point, c is a “step size” scaling constant, λ is a hyperbolic eigenvalue, \vec{v} is the corresponding hyperbolic manifold eigenvector, and k is the map iteration. This discrete-time linearization locates the stable and unstable manifolds on the stroboscopic map relative to the periodic orbit, as plotted in Figure 3.33. In this representation, the fixed point at $y = 0$ and $\dot{y} < 0$ on the Earth-Moon \mathbb{E}_1 orbit, $\Gamma(0.07, 180^\circ, 0^\circ, -1.5342)$, is selected and plotted as a black “x”. The stable and unstable eigenvectors, \vec{v}_s and \vec{v}_u , indicate the direction of flow along the linearized manifolds, represented here on the stroboscopic map in the x vs \dot{x} projection. As the map iteration increases from $k = 1$, the linearized manifolds appear as points along the eigenvectors on the map; the first return (for $k = 1$) is plotted as a set of asterisks along the manifolds. Consistent with the hyperbolic manifolds for the equilibrium points, the LTPO stable manifold asymptotically approaches the LTPO fixed point and the LTPO unstable manifold asymptotically departs the fixed point.

The process to globalize the linearized manifold is similar to the method employed for the equilibrium point manifolds. First, an initial state on a manifold is obtained

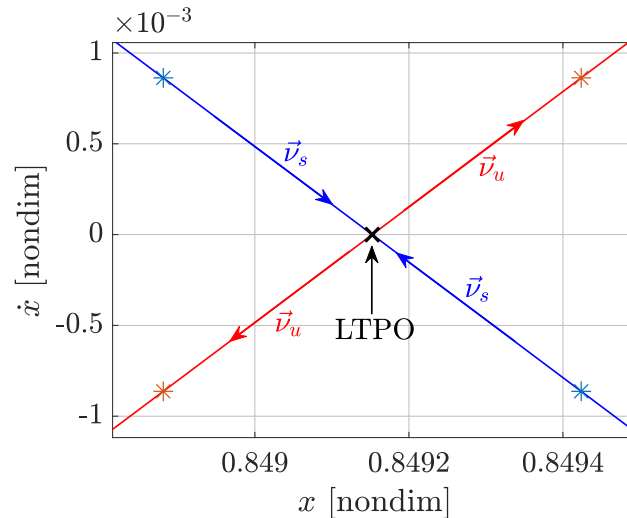


Figure 3.33.: The first return of the linearized manifolds, represented by asterisks, lie on the hyperbolic eigenvectors in the stroboscopic map for the the fixed point at $y = 0$ and $\dot{y} < 0$ along the Earth-Moon $\mathbb{E}_1 \Gamma(0.07, 180^\circ, 0^\circ, -1.5342)$ orbit

by setting $k = 0$ and selecting a small step size, c . The magnitude of c is selected to ensure that the manifolds asymptotically approach the periodic orbit while also avoiding unnecessary numerical error, as in the equilibrium point manifold computation. However, in contrast to the equilibrium point manifolds, a step along one of the hyperbolic subspace eigenvectors as described above only delivers a subset of the periodic orbit hyperbolic manifold. The fixed point representing the periodic orbit is not unique; any point along the orbit may be employed. Thus, the complete manifold is a *surface* that asymptotically approaches every point along the periodic orbit. A useful representation of this surface is formed by the following steps:

1. Discretize the periodic orbit into a set of points
2. Compute the monodromy matrix for each discretized point and identify the hyperbolic eigenvectors
3. Compute an initial state relative to each discretized point by perturbing the point by the scaled eigenvector, $\delta\vec{X}$, as defined in Equation (3.90). Ensure that $|\delta\vec{X}|$ is consistent for every point.

4. Numerically integrate all of the perturbed points (forward in time for an unstable manifold, backward in time for a stable manifold) to construct a mesh that represents the manifold surface.

To illustrate this process, the stable and unstable manifolds for the Earth-Moon \mathbb{E}_1 orbit described above, $\Gamma(0.07, 180^\circ, 0^\circ, -1.5342)$, are constructed. The initial conditions for the nonlinear manifolds are selected to be the first return of the linearized manifolds depicted as asterisks in Figure 3.33. When these states are propagated in the nonlinear dynamics back to the stroboscopic map, they do not return precisely to the linearized manifolds, as seen in Figure 3.34. This behavior is expected; the

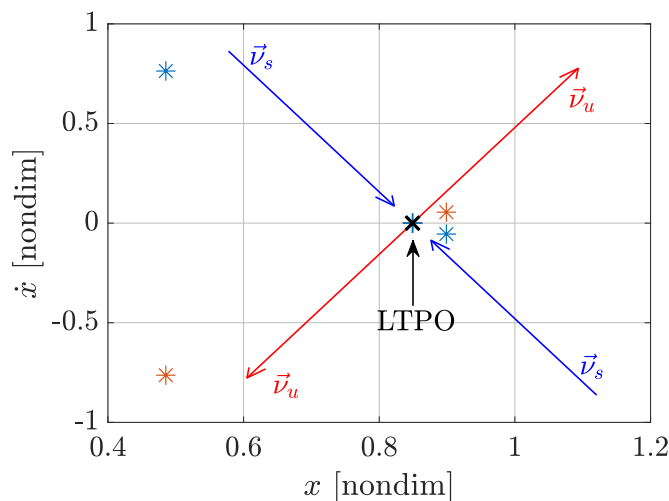


Figure 3.34.: The nonlinear hyperbolic manifold map returns, plotted as asterisks, stray from the linearized manifolds represented by the stable and unstable eigenvectors for the the fixed point at $y = 0$ and $\dot{y} < 0$ along the Earth-Moon \mathbb{E}_1 $\Gamma(0.07, 180^\circ, 0^\circ, -1.5342)$ orbit

nonlinear dynamics are only approximated by the linearization. When this process is repeated for 25 points distributed along the periodic orbit, a representation of the manifold surfaces is constructed and visualized in Figure 3.35. Similar to the equilibrium point manifold notation, the periodic orbit unstable manifolds are denoted \mathcal{W}^{u+} and \mathcal{W}^{u-} and the stable manifolds are denoted \mathcal{W}^{s+} and \mathcal{W}^{s-} .

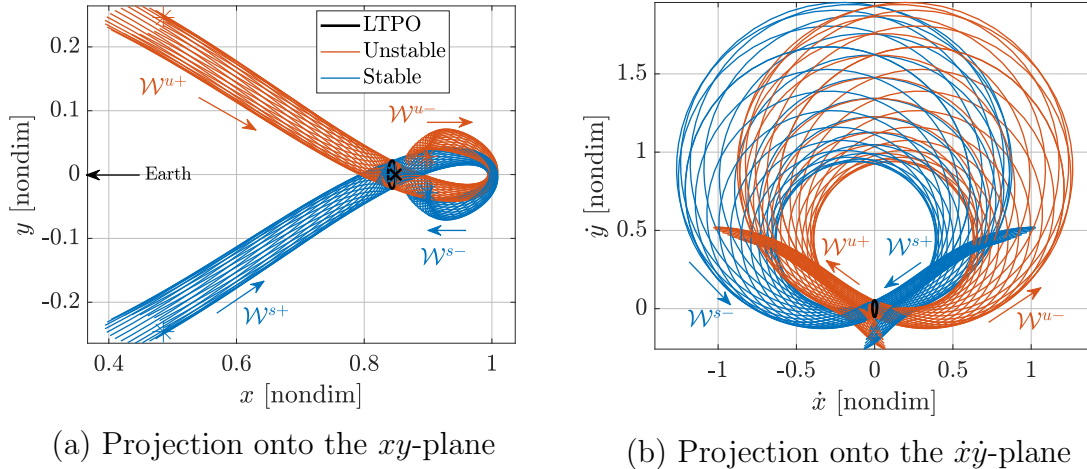


Figure 3.35.: The 2D manifold surfaces associated with the Earth-Moon \mathbb{E}_1 $\Gamma(0.07, 180^\circ, 0^\circ, -1.5342)$ orbit, propagated for one period of Γ . The first returns of the arcs associated with the fixed point at $y = 0$ and $\dot{y} < 0$ are marked by asterisks

In the ballistic model, i.e., the CR3BP, the stable and unstable manifolds associated with a planar periodic orbit are separatrices [65]. Because the dynamics in the simplified CR3BP+LT are structurally identical to the ballistic problem (a constant vector acceleration is included in the CR3BP+LT), the stable and unstable manifolds associated with planar LTPOs are also separatrices. When these planar orbits are within the center subspace of one of the equilibrium points, the associated manifolds separate “transit” motion from “non-transit” behavior. Recall that the forbidden regions bound all flow throughout the system for a specific H_{lt} value. A planar \mathbb{E}_1 (or \mathbb{E}_2) orbit is located within the gateway between the interior and P_2 (P_2 and exterior) regions but does not “fill” the gateway, as seen in Figure 3.36(a). In other words, the \mathbb{E}_1 orbit does not reach a velocity of zero and does not intersect with the zero velocity contours that bound the forbidden region, shaded gray in the plot. In contrast, the manifolds do fill the gateway; thus, these separatrices may be employed to distinguish between trajectories that transit through the gateway and arcs that do not transit. To clarify this description, the periodic orbit and the manifolds are projected into a *tube topology* [66]. This topology eliminates ambiguity inherent in the Cartesian

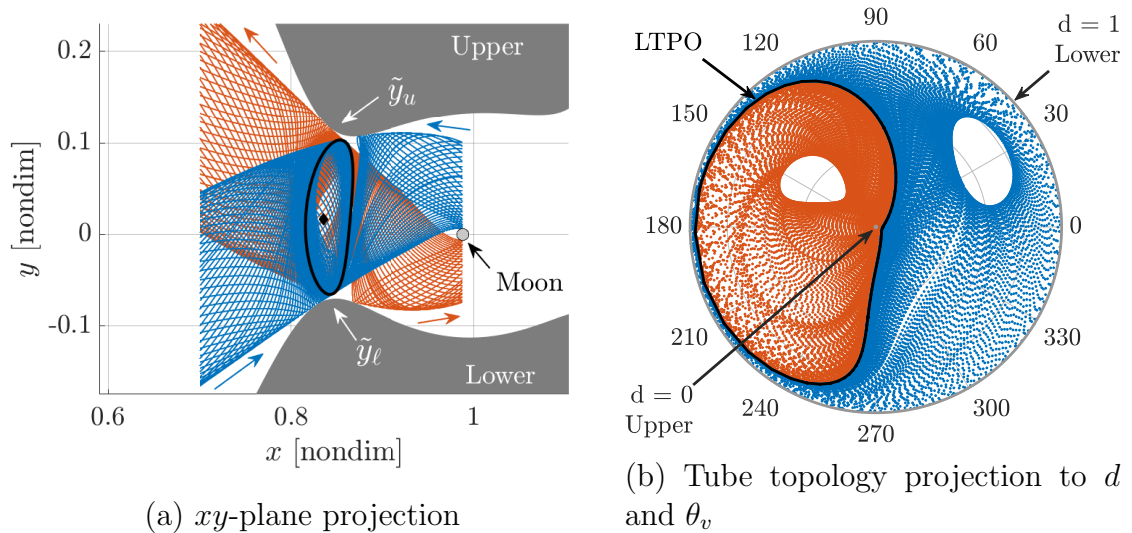


Figure 3.36.: Stable (blue) and unstable (orange/red) manifolds associated with the Earth-Moon $\mathbb{E}_1 \Gamma(0.07, 70^\circ, 0^\circ, -1.6)$ orbit bound transit through the $E_1(0.07, 70^\circ, 0^\circ)$ gateway for all motion with $H_{\text{t}} = -1.6$

projections of the trajectories by describing an arc within the 3D level set (i.e., the planar CR3BP+LT dynamics) via three variables rather than the usual four (x , y , \dot{x} , and \dot{y}). These variables are defined as,

$$\tilde{x} = x, \quad (3.91)$$

$$d = (\tilde{y}_u - y)/(\tilde{y}_u - \tilde{y}_\ell), \quad (3.92)$$

$$\theta_v = \arctan(\dot{y}/\dot{x}), \quad (3.93)$$

where \tilde{y}_u is minimum y value with $y > 0$ on the ZVC at the specified x value and \tilde{y}_ℓ is the maximum y value with $y < 0$ on the ZVC at the same x value. These coordinates are employed in a cylindrical space where d is the radius, θ_v is the angle around the cylinder, and \tilde{x} locates a point along the axis of the cylinder. When the periodic orbit, the hyperbolic manifolds, and the ZVCs are projected into this space, as in Figure 3.36(b), the relationships between these structures are clarified. The lower ($y < 0$) ZVC is a point at $d = 0$, the upper ($y > 0$) ZVC is a circle with radius $d = 1$; the space between the ZVCs is filled by the LTPO manifolds but not by the LTPO itself.

(Note that \tilde{y}_u and \tilde{y}_ℓ may be set arbitrarily but are most useful for a transit analysis when they are selected to locate the ZVCs.) Because these manifolds are separatrices, they serve as useful guides to distinguish between transit and non-transit motion [14].

In contrast to ballistic periodic orbit manifolds, the H_{nat} value along a LTPO manifold varies on the energy plane defined in Section 2.2.8. The manifolds and periodic orbit exist on the *same* energy plane (assuming the manifold step-off size is suitably small). The energy plane is straightforwardly visualized for the $\Gamma(0.07, 180^\circ, 0^\circ, -1.5342)$ orbit by plotting the x - and y -coordinates against the H_{nat} value, as in Figure 3.37, due to the symmetry of the α and β angles. Accordingly,

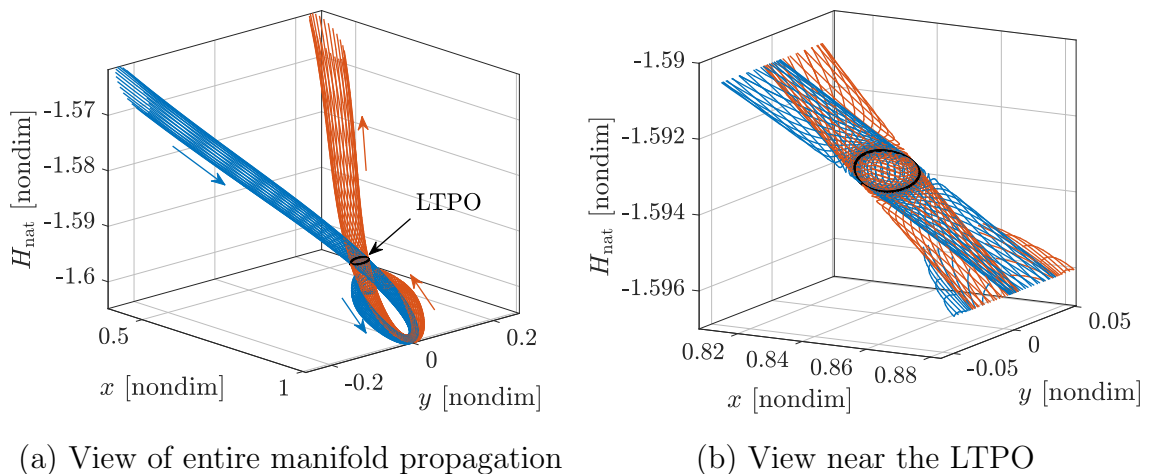


Figure 3.37.: The H_{nat} value along the 2D manifold surfaces associated with the Earth-Moon $\mathbb{E}_1 \Gamma(0.07, 180^\circ, 0^\circ, -1.5342)$ orbit evolves on a plane

the LTPO hyperbolic manifold may be employed in ways similar to the low-thrust equilibrium point hyperbolic manifold. The unique locations of some LTPOs and the corresponding forbidden region gateways offer novel transit options and the hyperbolic manifolds extend the bounds on such transit motion throughout the system. These structures may then be utilized to link a desirable transfer geometry or energy evolution to a set of control parameters in the preliminary design process. Additionally, because the LTPO manifolds are higher-dimensional structures than the equilibrium point manifolds, the LTPO manifolds characterize a larger portion of the

flow throughout the system. Applications of these manifolds for transit and capture are presented later in the document.

3.4.2 Center Manifold: Families

Every periodic orbit possesses a center manifold with a dimension of at least two because the monodromy matrix always includes two “trivial” unit eigenvalues [51]. As discussed at the beginning of this section, an exploration of the center manifold motion not associated with these unit eigenvalues (e.g., quasi-periodic orbits) is not included in this investigation. While the unit eigenvalues are located on the unit circle, they are also located on the real axis. Thus, the eigenvectors associated with these eigenvalues are real and the resulting motion is not oscillatory relative to the periodic orbit but does retain the oscillatory properties of the originating orbit. Two structures result from perturbing the periodic orbit along these center manifold directions: the phase-shifted periodic orbit, and a family of periodic orbits.

The eigenvectors associated with the unit eigenvalues are related to the Hamiltonian gradient, $\partial H_{\text{t}}/\partial \vec{X}$. Recall that variations relative to the periodic orbit are described by the relationship,

$$\delta \vec{X}(\tau) = \Phi(\tau, \tau_0) \delta \vec{X}(\tau_0), \quad (3.82)$$

reprinted here for convenience. Consider a small perturbation along the periodic orbit, i.e., along the derivative of the state vector, $\delta \vec{X}(\tau_0) = \epsilon \dot{\vec{X}}(\tau_0)$, where ϵ is a small scalar. When this perturbation is mapped for one full period, T , the initial perturbation is recovered,

$$\dot{\vec{X}}(\tau_0 + T) = \Phi(\tau_0 + T, \tau_0) \dot{\vec{X}}(\tau_0) = \dot{\vec{X}}(\tau_0). \quad (3.94)$$

Because the periodic orbit is not an equilibrium point, $\dot{\vec{X}}(\tau_0) \neq \vec{0}$ and the expression may be rearranged,

$$[\mathbf{I} - \Phi(\tau_0 + T, \tau_0)] \dot{\vec{X}}(\tau_0) = \vec{0}, \quad (3.95)$$

revealing that $\dot{\vec{X}}(\tau_0)$ is a *right eigenvector* associated with the unit eigenvalue, i.e.,

$$\vec{v}_r = \dot{\vec{X}} = \mathbf{T}_{-\tilde{\omega}} \mathbf{J} \mathbf{T}_{-\tilde{\omega}}^T \left(\frac{\partial H_{\text{lt}}}{\partial \vec{X}_{\mathcal{L}}} \right)^T, \quad (3.96)$$

where \vec{v}_r represents the right eigenvector. This result is unsurprising in the context of the periodic orbit. A perturbation along the orbit leads to a phase-shifted fixed point, i.e., a fixed point at another location along the periodic solution. As every state along the orbit is a fixed point under the stroboscopic mapping, the states are analogous to an oscillatory solution on the map.

Although the right eigenvector associated with the unit eigenvalue supplies some simple insight about the properties of additional, albeit trivial, periodic solutions, the unit eigenvalue is *defective*, i.e., the two eigenvectors corresponding to the unit eigenvalues are identical [51]. However, the *left eigenvector*, \vec{v}_l , associated with the unit eigenvalues provides additional insights that may be employed to construct additional periodic orbits. Due to the symplectic properties of the state transition matrix, the left eigenvector is straightforwardly available from the right eigenvector. The *Hamiltonian STM*, Φ_H , i.e., the STM that relates variations in the Hamiltonian state vector, \vec{X}_H , is symplectic and satisfies the condition

$$\Phi_H^T \mathbf{J} \Phi_H = \mathbf{J}, \quad (3.97)$$

where \mathbf{J} is defined in Equation (2.55) [51]. A similar relationship is available for the *Lagrangian STM*, $\Phi_{\mathcal{L}} = \Phi$. (Consistent with the coordinate definitions derived in Chapter 2, the Lagrangian basis is employed by default throughout this investigation.) First, relate the two STMs by substituting the relationship between the two bases in Equation (2.60) into the definition of the STM in Equation (3.82) to obtain

$$\delta \vec{X}_{\mathcal{L}}(\tau) = \mathbf{T}_{-\tilde{\omega}} \Phi_H(\tau, \tau_0) \mathbf{T}_{\tilde{\omega}} \delta \vec{X}_{\mathcal{L}}(\tau_0) = \Phi_{\mathcal{L}} \delta \vec{X}_{\mathcal{L}}(\tau_0) \quad (3.98)$$

Accordingly, the STM in the Lagrangian basis is related to the STM in the Hamiltonian basis via the $\mathbf{T}_{\tilde{\omega}}$ transformation matrix,

$$\Phi = \Phi_{\mathcal{L}} = \mathbf{T}_{-\tilde{\omega}} \Phi_H \mathbf{T}_{\tilde{\omega}}. \quad (3.99)$$

Solve this expression for the Hamiltonian STM and substitute it into Equation (3.97), yielding

$$(\mathbf{T}_{\tilde{\omega}} \Phi_{\mathcal{L}} \mathbf{T}_{-\tilde{\omega}})^T \mathbf{J} (\mathbf{T}_{\tilde{\omega}} \Phi_{\mathcal{L}} \mathbf{T}_{-\tilde{\omega}}) = \mathbf{J} \quad (3.100)$$

$$\mathbf{T}_{-\tilde{\omega}}^T \Phi_{\mathcal{L}}^T \mathbf{T}_{\tilde{\omega}}^T \mathbf{J} \mathbf{T}_{\tilde{\omega}} \Phi_{\mathcal{L}} \mathbf{T}_{-\tilde{\omega}} = \mathbf{J}. \quad (3.101)$$

Pre- and post-multiply by $\mathbf{T}_{\tilde{\omega}}^T$ and $\mathbf{T}_{\tilde{\omega}}$, respectively, to arrive at

$$\Phi_{\mathcal{L}}^T (\mathbf{T}_{\tilde{\omega}}^T \mathbf{J} \mathbf{T}_{\tilde{\omega}}) \Phi_{\mathcal{L}} = \mathbf{T}_{\tilde{\omega}}^T \mathbf{J} \mathbf{T}_{\tilde{\omega}}. \quad (3.102)$$

Thus, define

$$\mathbf{S} = \mathbf{T}_{\tilde{\omega}}^T \mathbf{J} \mathbf{T}_{\tilde{\omega}} \quad (3.103)$$

to simplify the equation to a form identical to the symplectic relationship in Equation (3.97). Accordingly, the right and left eigenvectors of the STM in the Lagrangian basis, Φ , are related by the \mathbf{S} matrix:

$$\vec{\nu}_\ell = (\mathbf{S} \vec{\nu}_r)^T. \quad (3.104)$$

(When expressed in the Hamiltonian basis, an equivalent expression, $\vec{\nu}_\ell = (\mathbf{J}\vec{\mu}_r)^T$, is available.) The left eigenvector corresponding to the unit eigenvalues is then

$$\vec{\nu}_\ell^T = \mathbf{S}\dot{\vec{X}} = \mathbf{S}\mathbf{T}_{-\tilde{\omega}}\mathbf{J}\mathbf{T}_{-\tilde{\omega}}^T \left(\frac{\partial H_{\text{lt}}}{\partial \vec{X}_\mathcal{L}} \right)^T \quad (3.105)$$

$$= \mathbf{T}_{\tilde{\omega}}^T \mathbf{J} \mathbf{T}_{\tilde{\omega}} \mathbf{T}_{-\tilde{\omega}} \mathbf{J} \mathbf{T}_{-\tilde{\omega}}^T \left(\frac{\partial H_{\text{lt}}}{\partial \vec{X}_\mathcal{L}} \right)^T \quad (3.106)$$

$$= -\mathbf{I} \left(\frac{\partial H_{\text{lt}}}{\partial \vec{X}_\mathcal{L}} \right)^T. \quad (3.107)$$

This result reveals that the left eigenvector associated with the unit eigenvalue points along the gradient of the Hamiltonian. Identical results are available in the Hamiltonian basis, i.e., the right eigenvector associated with the unit eigenvalue is $\dot{\vec{X}}_H$ and the left eigenvector is $\partial H_{\text{lt}}/\partial \vec{X}_H$. These results also apply to the ballistic CR3BP when the low-thrust Hamiltonian is replaced with the natural Hamiltonian.

Similar to the right eigenvector, the left eigenvector associated with the unit eigenvalue pair is physically significant. While $\vec{\nu}_r$ is tangent to the periodic orbit, $\vec{\nu}_\ell$ lies along the energy gradient direction, i.e., the direction in which the energy changes due to a change in the periodic orbit. Because periodic orbits in the simplified CR3BP+LT maintain a constant H_{lt} value, this direction cannot be parallel to the periodic orbit (additionally, $\mathbf{S} \neq \mathbf{I}$) and this direction leads to a new, distinct periodic orbit. Accordingly, the left eigenvector is said to be parallel to a *family* of periodic solutions. Because this direction is available for every periodic solution in the simplified CR3BP+LT, no periodic orbit is isolated, i.e., every periodic orbit exists in a family. In contrast to the center manifold corresponding to $\vec{\nu}_r$ that supplies “trivial” solutions (i.e., phase-shifted duplicates of the periodic orbit), the manifold corresponding to $\vec{\nu}_\ell$ leads to new, distinct periodic orbits with similar characteristics as the originating solution.

A family is defined as a set of solutions that evolves along a one-dimensional curve, i.e., a family member is located in the family by a single parameter [67, 68].

To distinguish between families of low-thrust periodic orbits, a family is denoted via set notation as \mathbb{Y} with a superscript identifying the family evolution parameter. The common periodic orbit families in the ballistic CR3BP (e.g., the Lyapunov, halo, vertical, axial, and resonant orbit families) all evolve with the natural Hamiltonian. Similar families of LTPOs that evolve in the low-thrust Hamiltonian may be constructed and are denoted

$$\mathbb{Y}^H(a_{\text{lt}}, \alpha, \beta) = \left\{ \Gamma(a'_{\text{lt}}, \alpha', \beta', H_{\text{lt}}) \mid a'_{\text{lt}} = a_{\text{lt}}, \alpha' = \alpha, \beta' = \beta \right\}. \quad (3.108)$$

Here, $\mathbb{Y}^H(a_{\text{lt}}, \alpha, \beta)$ is a set of periodic orbits that are all parameterized by the specified a_{lt} , α , and β control parameters while H_{lt} varies through the family. In contrast to the ballistic problem, LTPO families may also be continued in the control parameters. A family of periodic orbits that evolves in the α angle but fixes the Hamiltonian value (as well as the other parameters) is described by

$$\mathbb{Y}^\alpha(a_{\text{lt}}, \beta, H_{\text{lt}}) = \left\{ \Gamma(a'_{\text{lt}}, \alpha', \beta', H'_{\text{lt}}) \mid a'_{\text{lt}} = a_{\text{lt}}, \beta' = \beta, H'_{\text{lt}} = H_{\text{lt}} \right\}. \quad (3.109)$$

Observe that this notation does not entirely avoid ambiguity when comparing families. For instance, two families of LTPOs initialized from the distinct planar and spatial center modes associated with the $E_1(0.07, 180^\circ, 0^\circ)$ point (introduced in Section 3.3.2 and discussed in more detail below) may both be denoted $\mathbb{Y}^H(0.07, 180^\circ, 0^\circ)$. However, rather than further complicate the notation, specific indices or context clues will be appended, e.g., \mathbb{Y}_{2D}^H and \mathbb{Y}_{3D}^H may distinguish between the two families within the context of this discussion. Finally, the low-thrust acceleration magnitude will be omitted from the notation for brevity unless it is different than $a_{\text{lt}} = 7\text{e-}2$.

Given a single periodic orbit, such as a solution converged from the linear dynamics as in Section 3.3.2, a family of similar solutions may be constructed by applying a continuation algorithm. The left eigenvector associated with the monodromy matrix supplies a step direction between members of the family and may be leveraged in the continuation process; alternate methods are also available. Due to the diverse

geometries apparent among the LTPOs in this investigation, the pseudo-arclength continuation (PAC) algorithm is employed. This scheme offers a robust evolution of the family without requiring a priori knowledge of the family [69, 70]. Similar to a step along the left eigenvector, the PAC algorithm leverages information from the differential corrections Jacobian matrix to identify a change in the free variable vector that will yield a distinct periodic orbit that belongs to the same family as previously converged orbits. A more detailed explanation of the pseudo-arclength algorithm is included in [57] with notation very similar to that employed in this investigation.

As described in Section 3.3.2, one method to compute a periodic orbit is to apply differential corrections to an oscillatory solution from the center subspace associated with an equilibrium point. The dimension of the center subspace predicts the number of families of LTPOs that exist with properties (i.e., control parameters) matching the equilibrium point. For example, recall that the Earth-Moon $E_1(0.07, 180^\circ, 0^\circ)$ point possesses a 4D center mode; accordingly, two independent oscillatory solutions, pictured in Figure 3.30(a), may be employed to construct a periodic orbit within the linear dynamics. A family of planar LTPOs, $\mathbb{Y}_{2D}^H(180^\circ, 0^\circ)$, is initialized by globalizing the the planar linear solution, as pictured in Figure 3.31, and then applying the PAC algorithm. This family, plotted in Figure 3.38, evolves from the small periodic orbit converged from the linear solution to large orbits that approach the Earth and the Moon. Each orbit in this family is parameterized by the same low-thrust parameters as the originating equilibrium point and linear solution: $a_{lt} = 7e-2$, $\alpha = 180^\circ$, and $\beta = 0^\circ$. The low-thrust control is applied continuously with that magnitude and direction along each family member. Because the low-thrust acceleration vector is oriented in a “mirror configuration,” (i.e., $\sin(\alpha) = 0$), each family member is symmetric over the xz - and $y\dot{z}$ -planes. Additionally, because the control orientation is constant throughout the family, the entire family is symmetric about the same planes.

Similar to periodic orbit families in the ballistic CR3BP, the $\mathbb{Y}_{2D}^H(180^\circ, 0^\circ)$ family evolves in Hamiltonian. The linear solution that is located very close to the E_1

¹⁴https://engineering.purdue.edu/people/kathleen.howell.1/Publications/Dissertations/2020_Cox/#emE1Fam_plan_varHlt

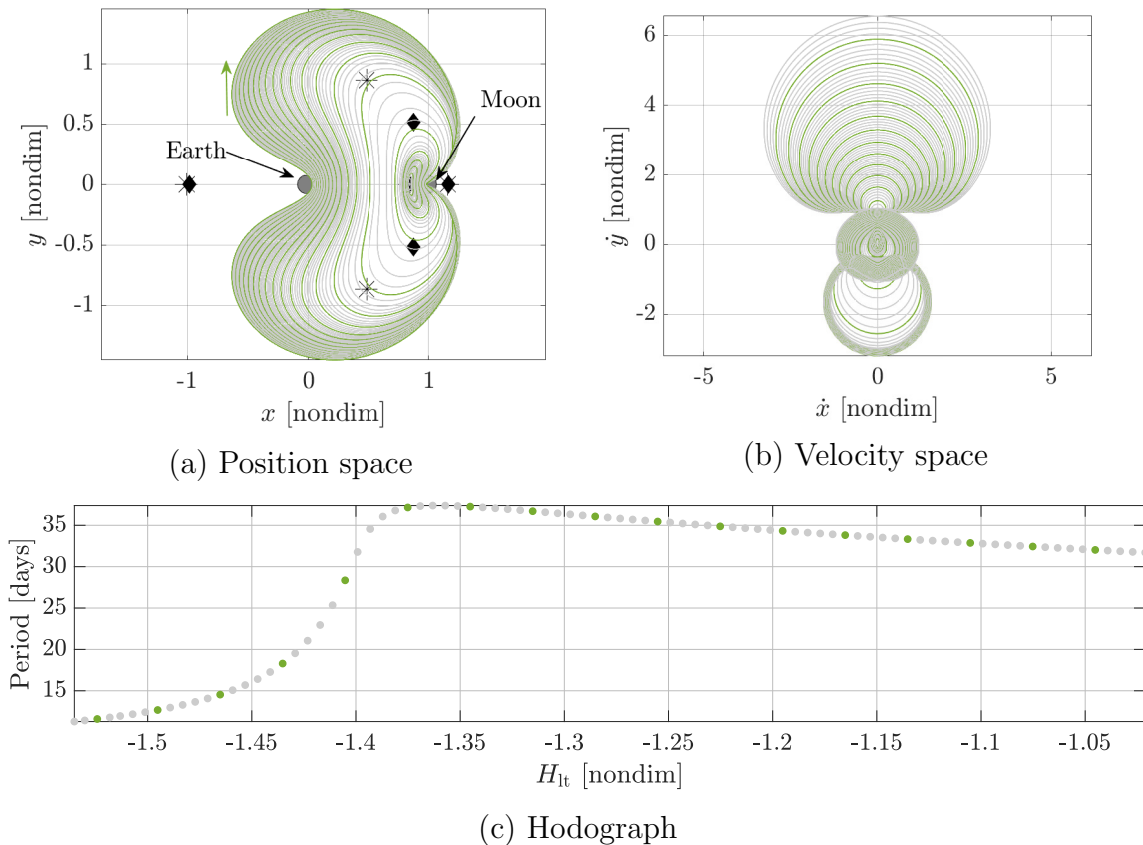


Figure 3.38.: Earth-Moon $\mathbb{Y}_{2D}^H(180^\circ, 0^\circ)$ family ([Animation](#))¹⁴

point, possesses a low-thrust Hamiltonian value approximately equal to the H_{1t} value associated with E_1 . As the orbits grow in size, the H_{1t} value (which is constant along each solution) also increases. This monotonic behavior is not characteristic of all families of LTPOs, but applies for this particular family. While the Hamiltonian along this family increases from the H_{1t} value of the E_1 point without an apparent limit, the family approaches an asymptote as the minimum distances between the LTPOs and the two primaries decrease. This evolution pattern is termed an *open family with one reflection*, one of four possible family evolution patterns [68]:

1. Closed family with no reflections; the hodograph is a closed curve
2. Closed family with two reflections; the hodograph is a finite curve segment
3. Open family with no reflections; hodograph extends to $\pm\infty$ in both directions

4. Open family with one reflection; hodograph extends to $\pm\infty$ in one direction and has a reflection point at the other end

In this case, the reflection point exists at $E_1(0.07, 180^\circ, 0^\circ)$; as H_{lt} decreases, the periodic orbits shrink to the equilibrium point and are analytically continued through the point with an arbitrary phase shift. As the H_{lt} value evolves in the opposite direction, i.e., grows, the hodograph approaches an asymptote, as depicted in Figure 3.39. Because the hodograph, i.e., the visualization of the *characteristic curve* associated

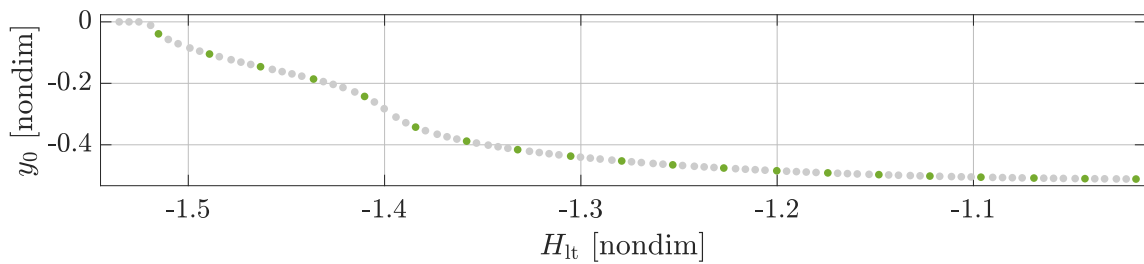


Figure 3.39.: Alternate hodograph for the $\mathbb{Y}_{2D}^H(180^\circ, 0^\circ)$ family

with the family, may be plotted in a variety of coordinates, each projection reveals slightly different properties. For example, the period vs. H_{lt} hodograph in Figure 3.38(c) does not represent the asymptotic evolution of the family as clearly as the y_0 vs. H_{lt} hodograph in Figure 3.39.

While the $\mathbb{Y}_{2D}^H(180^\circ, 0^\circ)$ family appears very similar to the ballistic L_1 Lyapunov family in position and velocity space, the low-thrust family differs in period and stability characteristics. These differences are minimal for very small acceleration magnitudes, as seen in the comparison between the $\mathbb{Y}_{2D}^H(0.001, 180^\circ, 0^\circ)$ family and the L_1 Lyapunov family depicted in Figure 3.40. The two families are compared in four metrics: the mean H_{nat} value along an orbit, the period of an orbit, and the \tilde{a} and \tilde{b} parameters from Broucke's stability diagram. The average H_{nat} value is employed to enable a straightforward comparison between the low-thrust and ballistic orbits. While H_{nat} is constant along the ballistic arcs, H_{nat} oscillates along an LTPO; thus, the mean H_{nat} value supplies a rough comparison of the ballistic energies associated with

the orbits. As seen by the practically identical hodograph and stability curve trends in Figure 3.40, the two families are very similar when the low-thrust magnitude is small. However, low-thrust periodic orbit families for larger a_{lt} values demonstrate more significant deviations from the Lyapunov family. A noticeable change in the period of the orbits as well as their stability properties is apparent in the $\mathbb{Y}(0.01, 180^\circ, 0^\circ)$ family in Figure 3.41. The differences between the low-thrust orbits and the ballistic orbits increase as the a_{lt} value increases, as seen in Figures 3.42 and 3.43. The final

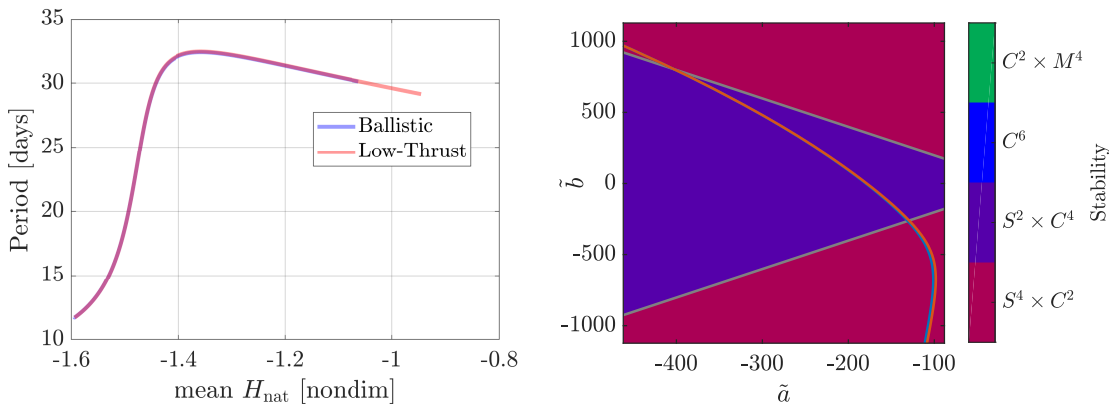


Figure 3.40.: $\mathbb{Y}_{2D}^H(0.001, 180^\circ, 0^\circ)$ vs. ballistic L_1 Lyapunov family

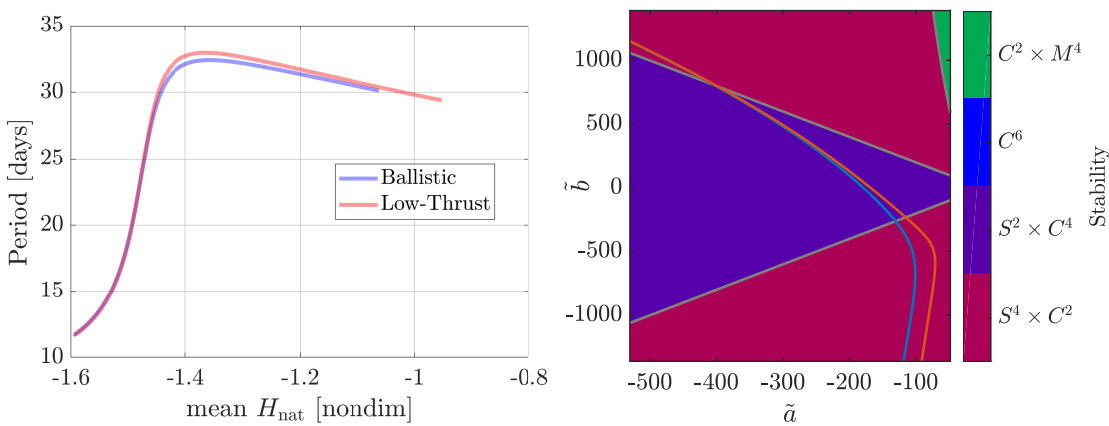


Figure 3.41.: $\mathbb{Y}_{2D}^H(0.01, 180^\circ, 0^\circ)$ vs. ballistic L_1 Lyapunov family

family parameterized by the familiar $a_{lt} = 7e-2$ value, i.e., the family plotted in Figure 3.38, displays the most significant deviations from the ballistic family. In addition to

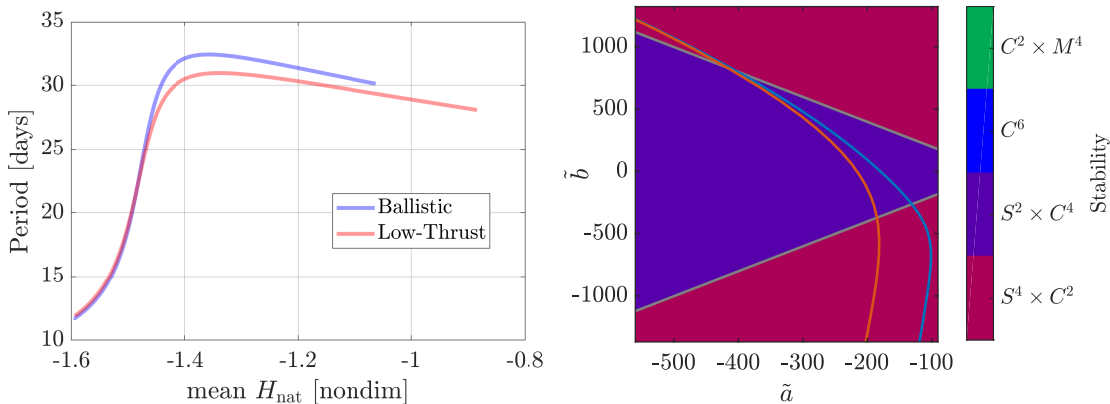


Figure 3.42.: $\mathbb{Y}_{2D}^H(0.03, 180^\circ, 0^\circ)$ vs. ballistic L_1 Lyapunov family

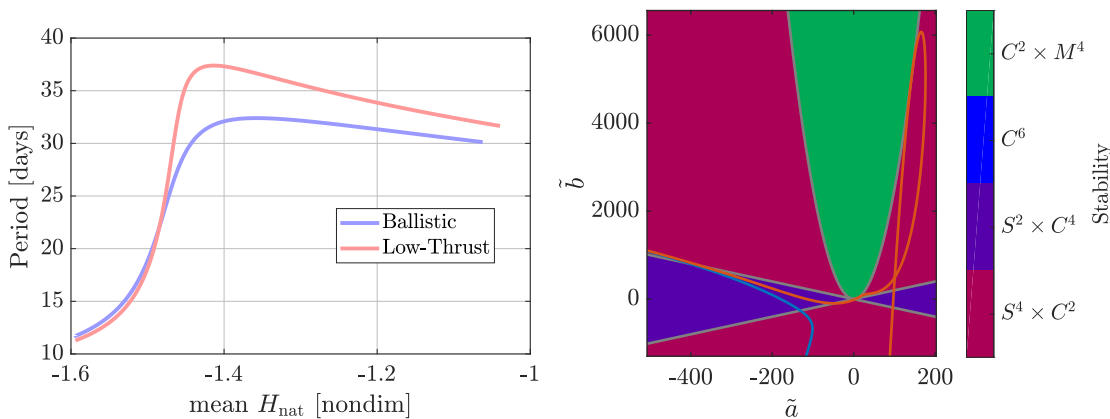


Figure 3.43.: $\mathbb{Y}_{2D}^H(0.07, 180^\circ, 0^\circ)$ vs. ballistic L_1 Lyapunov family

a large increase in orbital period, the stability characteristics of the low-thrust family deviate from the Lyapunov orbits more significantly than the low-thrust families parameterized by smaller a_{lt} values. Whereas the Lyapunov family curve maintains a negative \tilde{a} value, the low-thrust family crosses to the positive \tilde{a} values, passing through multiple bifurcations (i.e., the boundaries between colored regions). Although these bifurcations are not explored here, they suggest novel structures not apparent in the ballistic model and warrant future investigation.

In addition to planar families of low-thrust periodic orbits (LPTOs), spatial (i.e., 3D) families may also be constructed. The second center mode associated with the Earth-Moon $\mathbb{E}_1(0.07, 180^\circ, 0^\circ)$ point describes out-of-plane oscillations relative to the

equilibrium point. By applying the same globalization process that was used for the planar center mode, a spatial LTPO is converged near the equilibrium point. A family of “vertical” orbits, $\mathbb{Y}_{3D}^H(180^\circ, 0^\circ)$, pictured in Figure 3.44, is then constructed by leveraging the PAC method. Consistent with the planar $\mathbb{Y}_{2D}^H(180^\circ, 0^\circ)$ orbits, these

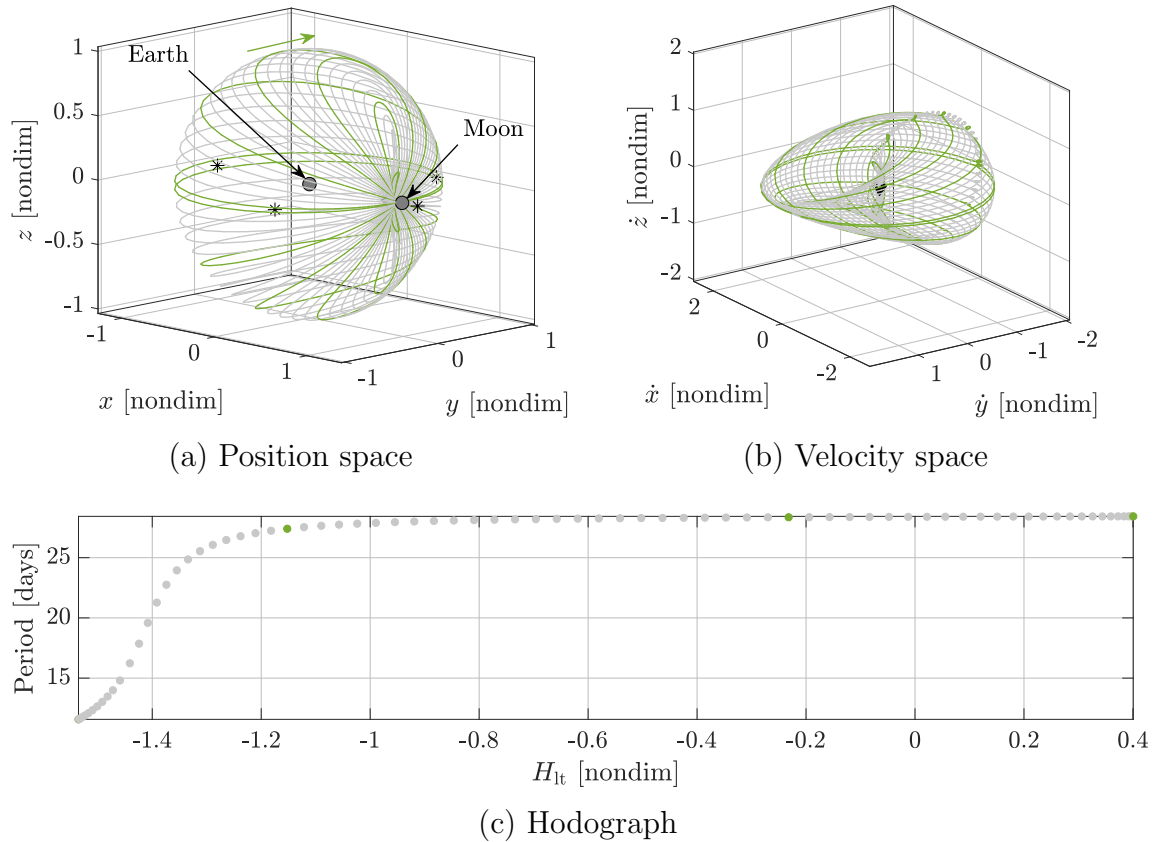


Figure 3.44.: Earth-Moon $\mathbb{Y}_{3D}^H(180^\circ, 0^\circ)$ family ([Animation](#))¹⁵

spatial LTPOs evolve from small solutions located near the E_1 point to large orbits that, in this case, encompass all five Lagrange points. These LTPOs are symmetric about the xz -plane because $\sin(\alpha) = 0$ and are also symmetric about the xy -plane because $\sin(\beta) = 0$; similar symmetries are apparent in velocity space. In contrast to the planar $\mathbb{Y}_{2D}^H(180^\circ, 0^\circ)$ family, the $\mathbb{Y}_{3D}^H(180^\circ, 0^\circ)$ is a closed family with two

¹⁵https://engineering.purdue.edu/people/kathleen.howell.1/Publications/Dissertations/2020_Cox/#emE1Fam_vert_varHIt

reflections: one at the E_1 point and another reflection at the large, planar LTPO that encircles the majority of the CR3BP.

As noted previously, while families of LTPOs may be constructed by evolving a converged periodic orbit in H_{lt} value, holding a_{lt} , α , and β constant, families may also be constructed by fixing the Hamiltonian and allowing one of the control parameters to evolve. To illustrate the various methods for family evolution, two E_1 LTPO families are constructed. The first family of planar E_1 LTPOs holds $\alpha = 0^\circ$ constant, displayed in Figure 3.45, and is denoted $\mathbb{Y}_H(0^\circ, 0^\circ)$. Although this family appears practically

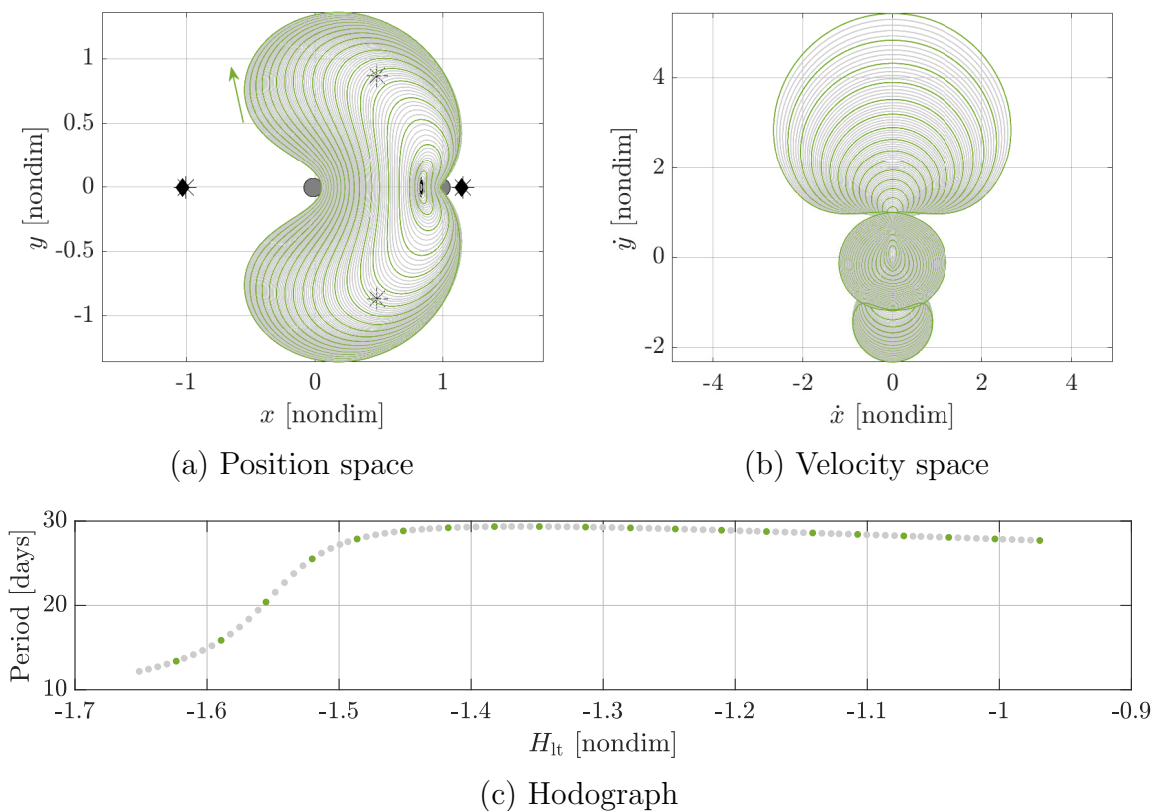


Figure 3.45.: Earth-Moon planar $\mathbb{Y}^H(0^\circ, 0^\circ)$ family near E_1 ([Animation](#))¹⁶

identical to the $\mathbb{Y}_{2D}^H(180^\circ, 0^\circ)$ family (i.e., the planar LTPOs with $\alpha = 180^\circ$), the two families are distinct. One key difference is the low-thrust Hamiltonian value associated with the orbits; the $\mathbb{Y}_{2D}^H(180^\circ, 0^\circ)$ orbits possess larger H_{lt} values than

¹⁶https://engineering.purdue.edu/people/kathleen.howell.1/Publications/Dissertations/2020_Cox/#emE1Fam_alpha0_varHlt

the $\mathbb{Y}_{2D}^H(0^\circ, 0^\circ)$ LTPOs; this difference is also apparent in the magnitudes of the velocities. To construct a family of LTPOs that evolves along a different parameter, the $\Gamma(0^\circ, 0^\circ, -1.544)$ orbit within the $\mathbb{Y}_{2D}^H(0^\circ, 0^\circ)$ family is selected as the initializing solution. When the $H_{\text{lt}} = -1.544$ value is fixed and the α angle is varied, a new family of low-thrust periodic orbits (LTPOs), $\mathbb{Y}^\alpha(0^\circ, -1.544)$, displayed in Figure 3.46, is constructed. Although the geometry of the entire family resembles the

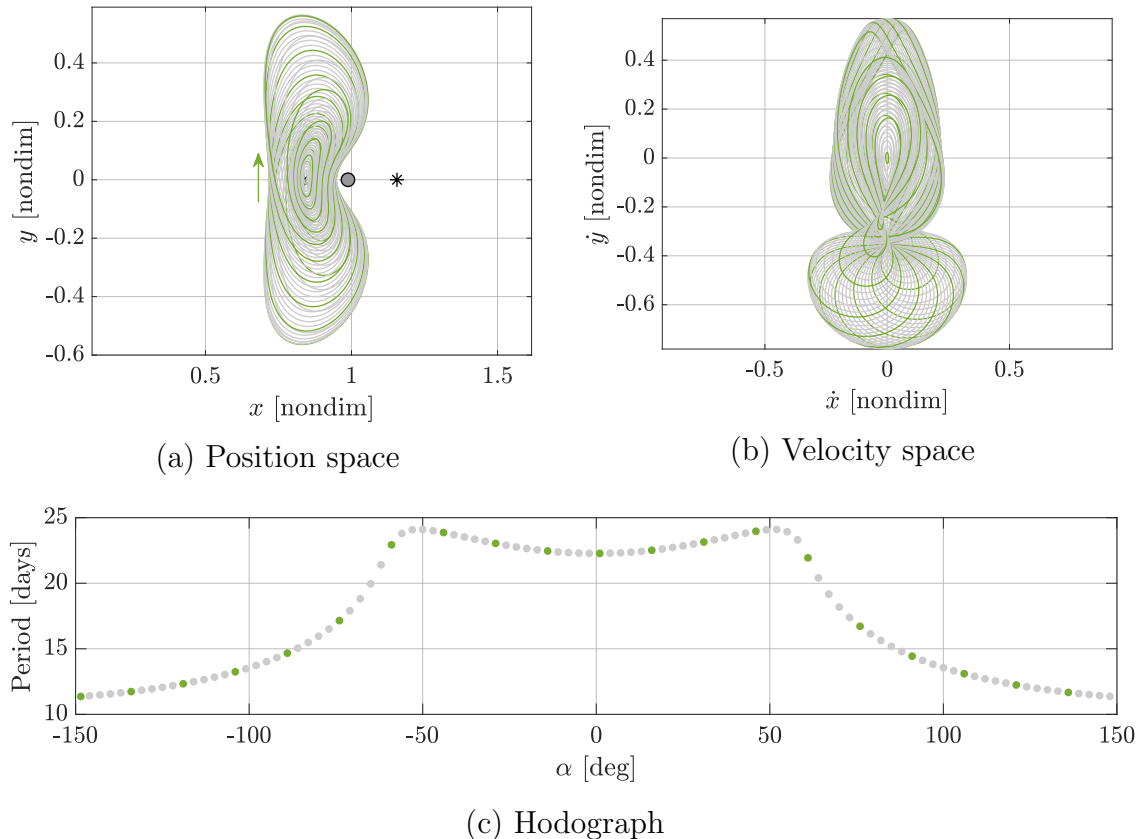


Figure 3.46.: Earth-Moon planar $\mathbb{Y}^\alpha(0^\circ, -1.544)$ family near E_1 ([Animation](#))¹⁷

$\mathbb{Y}^H(0^\circ, 0^\circ)$ family, the geometries of the individual family members differ. The most obvious difference is the lack of symmetry in the \mathbb{Y}_α family; as the α angle changes, the orientation, size, and location of the orbits shift (the animation clarifies these variations). These shifts correspond to the evolving $E_1(\alpha, 0^\circ)$ point. At the limits of

¹⁷https://engineering.purdue.edu/people/kathleen.howell.1/Publications/Dissertations/2020_Cox/#emE1Fam_varAlpha

the family, $\alpha \approx \pm 150^\circ$, the orbits are small and remain close to the E_1 point, which is located off of the \hat{x} -axis. As the magnitude of the α angle decreases (see the linked animation), the size of the orbits increases to a maximum at $\alpha = 0^\circ$. This evolution correlates to the geometry of the low-thrust forbidden regions and is straightforwardly visualized by comparing the family hodograph with the \mathbb{E}_1 ZAC, as in Figure 3.47. The limits of the \mathbb{Y}^α family are identified as the intersections of the ZAC with the

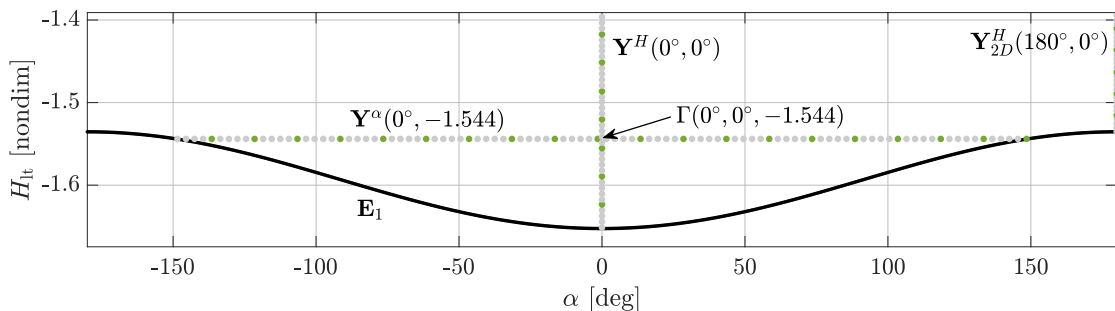


Figure 3.47.: The Earth-Moon LTPO families initialized from the linearized dynamics about \mathbb{E}_1 points are bounded by the \mathbb{E}_1 ZAC; $a_{lt} = 7e-2$ and $\beta = 0^\circ$

$H_{lt} = -1.544$ line. The $\mathbb{Y}^H(0^\circ, 0^\circ)$ and $\mathbb{Y}^H(180^\circ, 0^\circ)$ families are similarly bounded by the ZAC; the low-thrust Hamiltonian cannot decrease below the H_{lt} value associated with the $E_1(0^\circ, 0^\circ)$ or $E_1(180^\circ, 0^\circ)$ points, respectively. Finally, the intersection of the $\mathbb{Y}^H(0^\circ, 0^\circ)$ and $\mathbb{Y}^\alpha(-1.544, 0^\circ)$ families is the LTPO with characteristics that match both families, i.e., $\Gamma(0^\circ, 0^\circ, -1.544)$. Note that this intersection is not a *bifurcation*, at least not in usual dynamical systems context. There is no indication of a bifurcation – a change in stability, the formation of a new family of orbits, or the termination of the current family [71] – at the intersection orbit, $\Gamma(0^\circ, 0^\circ, -1.544)$. The stability index plots in Figure 3.48 demonstrate that no stability change occurs at $\alpha = 0^\circ$ in the \mathbb{Y}^α family or at $H_{lt} = -1.544$ in the \mathbb{Y}^H family. A bifurcation due to a stability change is located where one of the stability index curves intersects $s = \pm 1$; these intersections are marked with red arrows and $s = \pm 1$ are plotted as black dashed lines. Vertical black lines denote the intersection of the two families and do not correspond to a bifurcation. The lack of a period-multiplying bifurcation is confirmed by noting

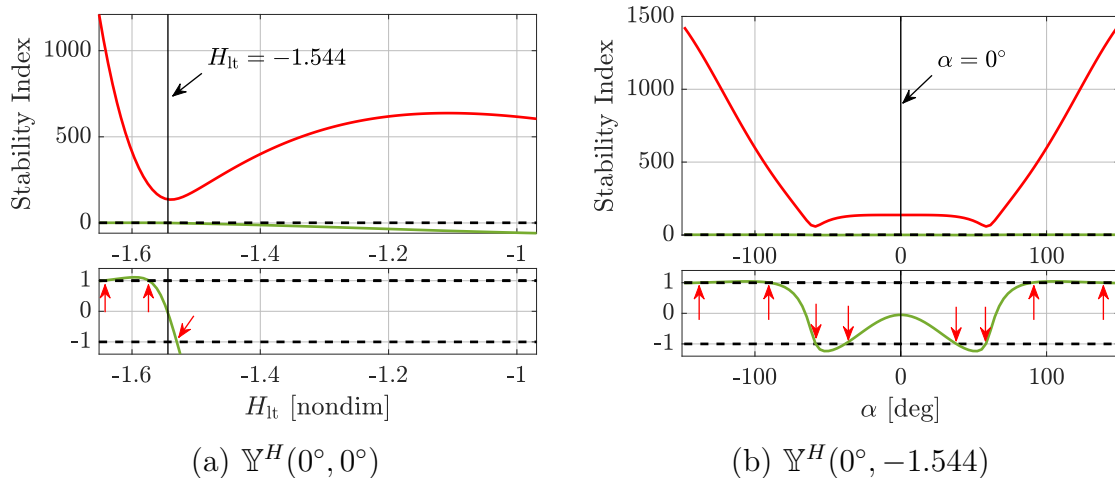


Figure 3.48.: Bifurcations at stability changes in the Earth-Moon $\mathbb{Y}^H(0^\circ, 0^\circ)$ family marked with red arrows; $a_{1t} = 7e-2$

that the period of $\Gamma(0^\circ, 0^\circ, -1.544)$, displayed in the hodographs of both families, is identical between the families. Although the intersection of the $\mathbb{Y}^H(0^\circ, 0^\circ)$ and $\mathbb{Y}^\alpha(0^\circ, -1.544)$ families at $\alpha = 0^\circ$ and $H_{1t} = -1.544$ does not represent a bifurcation, bifurcations to other families of low-thrust periodic orbits do occur, as observed in the Broucke stability diagrams in Figures 3.40 – 3.43. As noted previously, these bifurcations are not explored in this investigation but may lead to novel structures for preliminary low-thrust trajectory design.

While low-thrust periodic orbits in the vicinity of the \mathbb{E}_1 points have been discussed and displayed, periodic solutions also exist in the near the \mathbb{E}_2 and \mathbb{E}_3 points in the Earth-Moon system for $a_{1t} = 7e-2$. Recall from the stability discussion in Section 3.2.6, i.e., Figure 3.17, that the \mathbb{E}_1 and \mathbb{E}_2 points are characterized by $S^2 \times C^4$ motion for all α values when $\beta = 0^\circ$ and $a_{1t} = 7e-2$. The \mathbb{E}_3^1 points possess the same stability properties as \mathbb{E}_1 and \mathbb{E}_2 . The \mathbb{E}_3^2 and \mathbb{E}_3^3 points also possess a center mode due to their stability types of C^6 or $C^2 \times M^4$. Accordingly, periodic orbit families may be initialized from the linearized dynamics near any of the low-thrust equilibria for $\beta = 0^\circ$ and $a_{1t} = 7e-2$ in the Earth-Moon system. Many of the families initialized from the \mathbb{E}_3 points resemble the ballistic $L_{4/5}$ short- and long-period orbits. One such

family, $\mathbb{Y}^\alpha(0^\circ, -1.500)$, plotted in Figure 3.49, evolves with α at a constant H_{t} value of -1.500. For $\alpha = 180^\circ$, the E_3^1 point is located on the \hat{x} -axis near L_3 . As α changes,

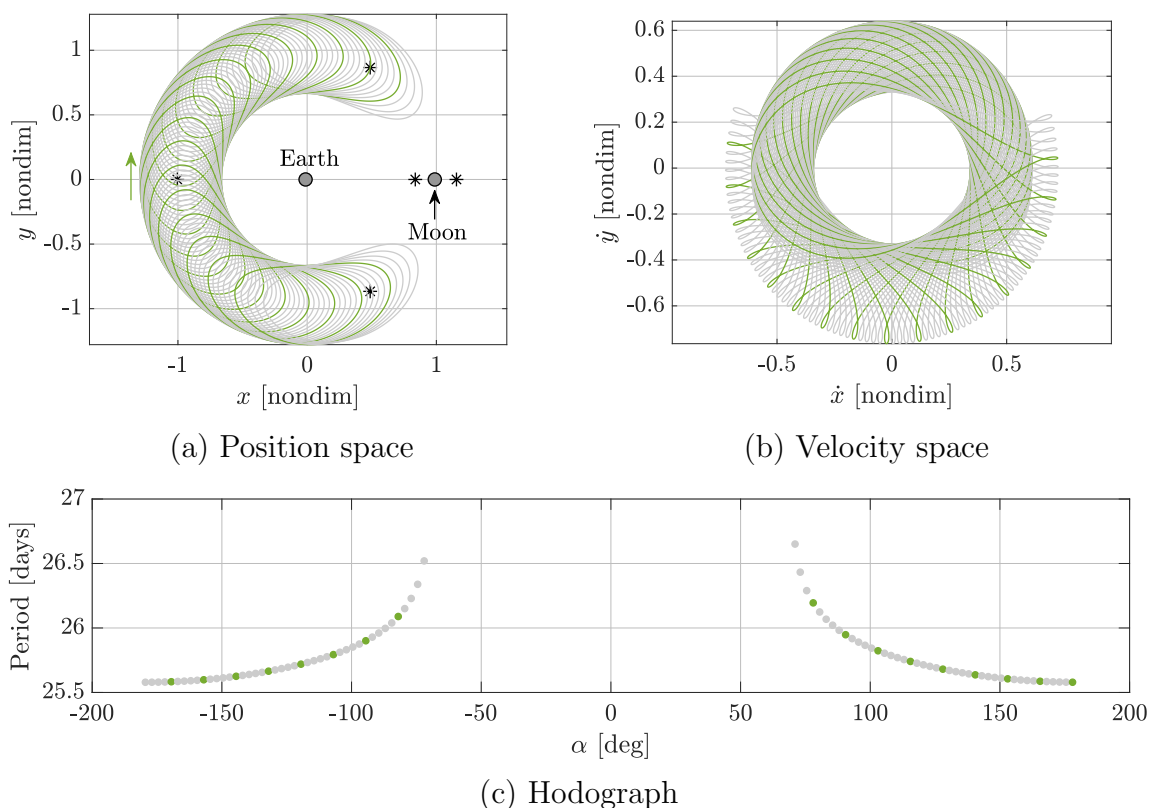


Figure 3.49.: Earth-Moon planar E_3 $\mathbb{Y}^\alpha(0^\circ, -1.500)$ family ([Animation](#))¹⁸

the E_3^1 point rotates about the system, approximately tracing a circle centered on the barycenter with a nondimensional radius of 1 (the linked animation depicts this rotation). The family evolution is limited by the range of α angles for which E_3^1 exists. Recall from Figure 3.17 (among others) that the E_3^1 and E_3^2 points merge at $|\alpha| \approx 54^\circ$; the period of the family members asymptotically increases as this limit is reached, as apparent in the hodograph in Figure 3.49(c). Accordingly, the $\mathbb{Y}^\alpha(0^\circ, -1.500)$ family is open with no reflections. Many similar E_3^1 families may be constructed at different H_{t} values; smaller Hamiltonian values yield smaller individual orbits (and vice versa), but the family remains bounded by the same α range.

¹⁸https://engineering.purdue.edu/people/kathleen.howell.1/Publications/Dissertations/2020_Cox/#emE3Fam_varAlpha

There exist many low-thrust periodic orbit families in addition to those discussed in this section. For example, families analogous to the ballistic distant retrograde orbits (DROs), distant prograde orbits (DPOs) and resonant orbits may be constructed in the CR3BP+LT by initializing differential corrections and continuation algorithms with the ballistic solutions or by directly identifying similar structures in the CR3BP+LT. In the next chapter, the stable and unstable manifolds associated with low-thrust periodic orbits are constructed and compared to similar ballistic structures. Trajectory design applications that leverage LTPOs and their manifolds are also detailed later in this document.

4. APPLICATIONS

A thorough understanding of the CR3BP+LT dynamics simplifies the preliminary design process by supplying links between the control parameters employed along a low-thrust arc and the resulting energy and geometry responses. This understanding mitigates the current difficulty in constructing an initial control strategy for low-thrust missions. This chapter presents several applications that illustrate the use of the structures and insights developed in this investigation. First, strategies to manipulate the forbidden region gateway locations and energies are developed. Next, a transfer between the Moon and Earth-Moon L_5 point is straightforwardly initialized from low-thrust equilibrium point hyperbolic manifolds, navigating the significant spatial and energy difference between the two locales. Finally, more general transit and capture scenarios are analyzed by leveraging the manifolds associated with planar LTPOs located in the forbidden region gateways.

4.1 Gateway Manipulation Using Energy Planes

One straightforward application of the theory developed in this investigation is a strategy to identify thrust durations and locations to open (or close) a gateway in the forbidden regions. Recall that the geometry of the ballistic forbidden regions is a function of the instantaneous (and time-varying) H_{nat} value along a low-thrust trajectory. Accordingly, the information provided by the energy plane associated with the low-thrust arc is useful to plan for desirable configurations of the forbidden regions. The H_{nat} values associated with the natural equilibrium solutions are significant as they represent critical H_{nat} values at which the forbidden regions shrink (or grow) to permit (or restrict) access to specific locations in the rotating frame. For example, for H_{nat} values slightly higher than the $H_{\text{nat}}(L_1)$ value, the forbidden regions include

a narrow neck near the L_1 point, i.e., the L_1 gateway through which trajectories may pass to transit between the P_1 and P_2 regions. Similar gateways form as H_{nat} increases past the L_2 and L_3 energy levels, as described in Section 3.1. Thus, to enable transit between regions of the rotating frame, the H_{nat} value along an arc is specified to achieve a desirable forbidden region configuration. As the energy along a low-thrust arc is described by an energy plane, the coupled geometry-energy challenge in navigating a gateway is mitigated by leveraging the energy plane.

To illustrate the manipulation of the forbidden regions via insights from an energy plane, consider a ballistic path that passes from the system interior (i.e., near P_1) through the L_1 and L_2 gateways to the exterior region, as plotted in black in Figure 4.1. Assume that the path must be modified to prohibit one or both gateway transits

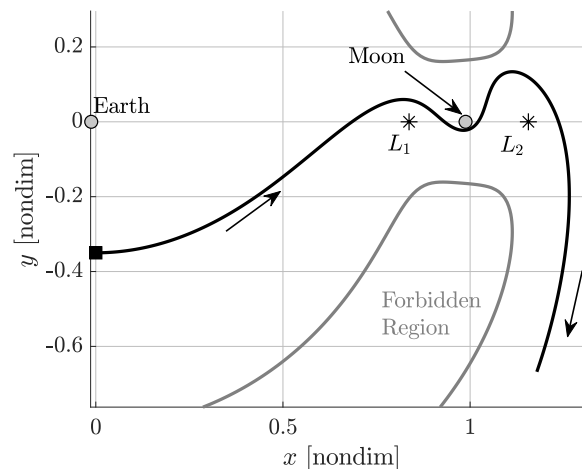


Figure 4.1.: Ballistic arc transiting the Earth-Moon L_1 and L_2 gateways at $H_{\text{nat}} = -1.55$

by applying a low-thrust acceleration with a magnitude of $a_{\text{lt}} = 7\text{e-}2$. Additionally, let the initial state, marked by a black square, be fixed. To avoid escape to the system exterior, it is sufficient to reduce the H_{nat} value along the low-thrust arc such that, at the location of the L_2 gateway transit, the spacecraft H_{nat} value is lower than $H_{\text{nat}}(L_2)$. Further energy reductions may restrict the spacecraft to the vicinity of P_2 , or prohibit transit into the P_2 region entirely by closing the L_1 gateway.

A strategy that leverages a low-thrust acceleration to reduce the H_{nat} value along an arc originating at the specified state is available from the insights derived from the energy plane. Recall that the energy plane is sloped toward increasing H_{nat} values in the direction of the low-thrust acceleration vector. Accordingly, to decrease the H_{nat} value as the spacecraft moves from the initial state (the black square in Figure 4.1) toward the Moon, the low-thrust acceleration vector should be oriented opposite the direction of travel to ensure that the H_{nat} value decreases. In this planar example, an α angle between 180° and 235° will deliver a suitably oriented acceleration vector.

Once the orientation of the \vec{a}_{lt} vector has been selected, the equation for the energy plane may be leveraged to identify limits on the low-thrust maneuver timing, i.e., the latest time (or, equivalently, the location) the maneuver may be initiated to prohibit transit through the L_2 and/or L_1 gateways. The energy plane equation,

$$\Delta H_{\text{nat}} = -a_{\text{lt}} [C_\alpha C_\beta \Delta x + S_\alpha C_\beta \Delta y + S_\beta \Delta z], \quad (2.130)$$

reprinted here for convenience, relates the energy change to the low-thrust acceleration magnitude, a_{lt} , the orientation angles, α and β , and the change in location between the initial and final points on a low-thrust arc. For simplicity, let $\alpha = 180^\circ$ to deliver a decreasing H_{nat} value as the spacecraft moves toward the Moon and let $\beta = 0^\circ$. The energy change is then a simple relationship with the change in the x -coordinate,

$$H_{\text{nat},f} - H_{\text{nat},0} = a_{\text{lt}}(x_f - x_0). \quad (4.1)$$

If the objective of the low-thrust maneuver is to prohibit transit through the L_2 gateway, the minimum H_{nat} change is $H_{\text{nat}}(L_2) - -1.55 \approx -0.0361$ and the final x -coordinate is the location of L_2 , i.e., $x_f = x_{L_2} \approx 1.1557$. The final x -coordinate where a maneuver may be initiated to close the L_2 gateway before the spacecraft transits through it is then available by solving Equation (4.1) for x_0 ,

$$x_0 = \max x_{\text{thrust}} = x_{L_2} - \frac{1}{a_{\text{lt}}} [H_{\text{nat},0} - H_{\text{nat}}(L_2)]. \quad (4.2)$$

A similar limit on the low-thrust maneuver is available by setting $x_f = x_{L_1}$ and $H_{\text{nat},f} = H_{\text{nat}}(L_1)$ and solving for x_0 ; the resulting position coordinate is the minimum x -value where a low-thrust maneuver may be initiated to close the L_1 gateway. These bounds, identified as black triangles in Figure 4.2(b), are employed to categorize a set of low-thrust arcs, all originating from the ballistic path at different x locations. Red

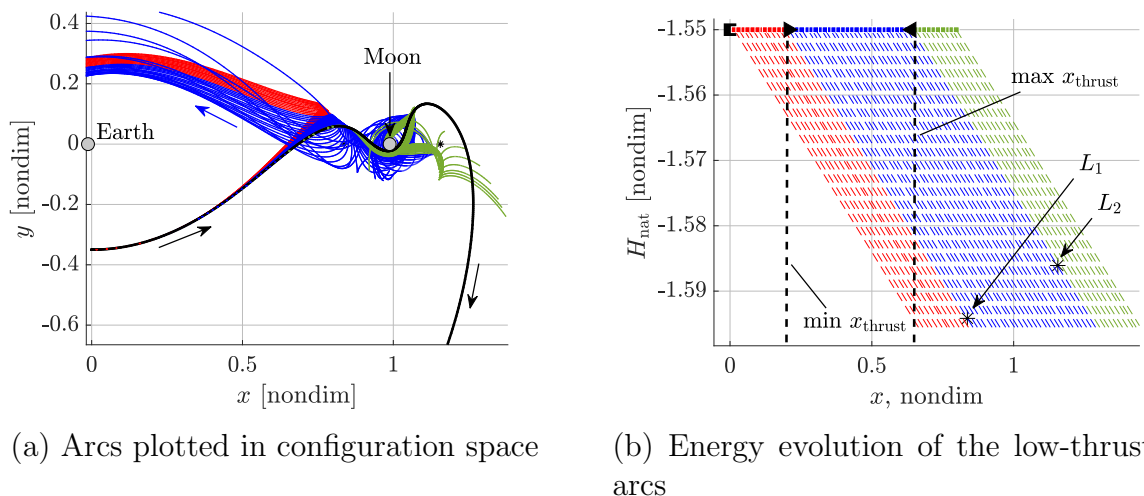


Figure 4.2.: The transit behaviors of low-thrust arcs (colored) in the Earth-Moon CR3BP-LT for $a_{lt} = 7e-2$, $\alpha = 180^\circ$, and $\beta = 0^\circ$ originating from different locations on a ballistic arc (black) are predicted by a simple trigonometric property of the energy plane geometry

arcs, plotted in the xy -plane in Figure 4.2(a), initiate thrusting at $x < \min x_{\text{thrust}}$. Similarly, green arcs depart the ballistic arc at locations such that $x > \max x_{\text{thrust}}$. Arcs that commence thrusting between these two bounds are plotted in blue. The energy plane analysis predicts that red arcs will fail to transit the L_1 gateway as the energy along these trajectories decreases below the L_1 gateway energy, i.e., the L_1 gateway is closed when the low-thrust arc arrives at the gateway. This prediction is supported by the results in Figure 4.2(a); all of the red arcs remain in the interior region. The energy planes associated with these arcs, plotted as dashed lines in Figure 4.2(b), visually demonstrate that the energy along each red arc decreases to $H_{\text{nat}}(L_1)$ before or at x_{L_1} . In contrast, as the blue arcs activate thrust forces sufficiently late

to avoid closing the L_1 gateway before passing through, they may transit into the P_2 region but will not pass through the L_2 gateway. This result is also supported by the plot, as many blue arcs enter the P_2 region and none transit the L_2 gateway. However, a subset of these trajectories do not pass through the L_1 gateway; while the energy on these paths at the L_1 gateway is sufficiently high to permit transit, transit is not guaranteed. Finally, the green arcs add thrust at locations where $x > \max x_{\text{thrust}}$, thus, the H_{nat} values on these arcs are sufficiently high to allow transit through the L_2 gateway; again this is a sufficient condition and does not guarantee transit, as evident from the configuration space representation in Figure 4.2(a).

This analysis demonstrates that the energy plane is a useful tool to design a low-thrust maneuver that modifies a ballistic path and the bounding forbidden regions. The geometry of the ballistic transit arc employed in this example (seen in black in Figure 4.2(a)) is only slightly modified by a low-thrust force during the approach to the P_2 vicinity, thus, the energy along the low-thrust arcs is straightforwardly controlled as the path moves predictably along the prescribed energy plane. However, as the arcs traverse the dynamic regions near L_1 , P_2 , and L_2 , the trajectory geometry is significantly affected by the addition of low-thrust and, thus, is more difficult to predict. Regardless of these sensitivities, the energy along each low-thrust arc is confined to the energy plane and transit (or capture) may be achieved by adjusting the control parameters via differential corrections. This strategy is also applicable to scenarios other than gateway transit behavior; any problem that requires a specific energy value at a specific location is facilitated by the CR3BP+LT energy planes.

4.2 Gateway Manipulation Using Control Curves

Building upon the simple method developed in the previous section, a more sophisticated strategy to manipulate the forbidden region gateways leverages the novel low-thrust forbidden region geometries and gateway energy orders. In the example from Section 4.1, low-thrust arcs are constructed with a single control parameteriza-

tion. However, maintaining a single set of low-thrust parameters may overly restrict the solution space; mid-course variations in α , β , and a_{lt} might also be leveraged to modify the dynamical landscape. To illustrate these energy design techniques, a simple example is employed throughout this section. Consider a spacecraft on a planar, ballistic path with $H_{nat} = -1.55$ that transits the P_2 region, passing from the exterior of the CR3BP+LT system to the interior as seen in Figure 4.3. Similar

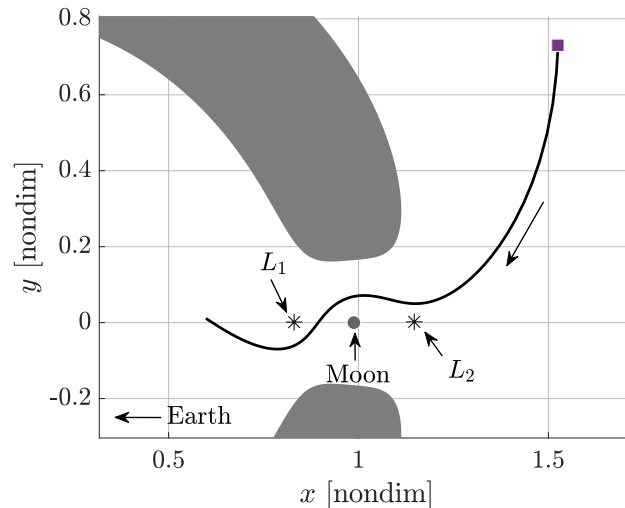


Figure 4.3.: Ballistic path (black curve) bounded by the natural Earth-Moon forbidden regions (gray) at $H_{nat} = -1.55$

to the scenario in the previous section, the spacecraft path must be adjusted via a low-thrust acceleration with magnitude $a_{lt} = 7e-2$ to achieve ballistic capture about P_2 , i.e., the final spacecraft state should yield a ballistic arc that is guaranteed to remain in the vicinity of P_2 . Let the spacecraft position and natural energy, given by \vec{r} and H_{nat} , respectively, be fixed at the initial time, $\tau = \tau_0$. Additionally, let $\beta = 0$ and $z = \dot{z} = 0$ to limit the analysis to the planar CR3BP+LT. The remaining variables (α , velocity orientation, and time-of-flight) are free to vary. Significant modifications to the ballistic path may be accomplished by leveraging insights from the CR3BP+LT to select values for these design variables.

4.2.1 Control Points and Control Curves

Similar to the example developed in Section 4.1, the goal of this gateway manipulation strategy is to adjust the energy along a low-thrust arc relative to the energy associated with the equilibrium points located in the gateways. While the natural energies (i.e., H_{nat} values) associated with the ballistic Lagrange points supply one metric for a transit analysis, the low-thrust Hamiltonian and low-thrust equilibria may also be employed. In contrast to the ballistic energy, the H_{lt} value along an arc is constant when the low-thrust acceleration vector is fixed in the rotating frame. Accordingly, the geometry of the low-thrust forbidden regions is also static, supplying a simpler bound on the spacecraft motion than the pulsating ballistic forbidden regions. Two entities – a *control point* and a *control curve* – are defined in this section to facilitate the selection of a suitable control parameterization that yields a suitable low-thrust forbidden region configuration.

Given a fixed low-thrust acceleration value, a_{lt} , the locations and number of the planar equilibria are a function only of α ; thus, while a spacecraft may use any thrust orientation to modify the equilibrium solution configuration (i.e., the geometry of the gateways), the H_{lt} value associated with the resulting low-thrust arc is not independent of α . Accordingly, the selection of an α value that yields an advantageous gateway geometry may simultaneously yield an energy level that undesirably closes (or opens) the gateway(s) of interest. In the context of the capture example, the locations of the E_1 and E_2 gateways corresponding to $a_{\text{lt}} = 7\text{e-}2$ remain near the natural CR3BP L_1 and L_2 solutions for all values of α . Subsequently, α may be selected to yield a desirable H_{lt} value somewhat independently of the E_1 and E_2 gateway geometry. However, this independence is not generally available, particularly if one of the \mathbb{E}_3 equilibria, which evolve with α along the large C-shaped ZAC in Figure 3.7(b), is the gateway of interest.

The range of H_{lt} energy values attainable from a specific position, $\vec{r}_i = \{x_i \ y_i \ z_i\}^T$, and natural Hamiltonian, $H_{\text{nat},i}$, is available from an analysis of the low-thrust Hamiltonian equation,

$$H_{\text{lt}} = H_{\text{nat},i} - a_{\text{lt}} \vec{r}_i \cdot \hat{a}_{\text{lt}}, \quad (2.107)$$

reprinted and expanded here for reference. Substitute the general definition of the low-thrust acceleration orientation vector from Equation (2.97) and expand the dot product to obtain

$$H_{\text{lt}} - H_{\text{nat},i} = -a_{\text{lt}} [x_i \cos(\alpha) \cos(\beta) + y_i \sin(\alpha) \cos(\beta) + z_i \sin(\beta)] \quad (4.3)$$

$$= -a_{\text{lt}} \|\vec{r}_i\| \cos \theta, \quad (4.4)$$

where θ is the angle between \vec{r}_i and \hat{a}_{lt} , and $H_{\text{nat},i}$ is a function only of the spacecraft position vector and velocity magnitude, v_i . Define a *control point* as the position and ballistic energy along a trajectory,

$$\vec{\rho}_i = \left\{ x_i \ y_i \ z_i \ H_{\text{nat},i} \right\}^T. \quad (4.5)$$

The H_{lt} values that may be achieved by implementing a low-thrust maneuver with the specified a_{lt} magnitude on an arc originating from $\vec{\rho}_i$ are described by the sinusoidal *control curve*,

$$\mathcal{U}_i(\vec{\rho}_i) : H_{\text{lt}} = H_{\text{nat},i} - a_{\text{lt}} \|\vec{r}_i\| \cos \theta, \quad (4.6)$$

with mean value $H_{\text{nat},i}$ and amplitude $a_{\text{lt}} \|\vec{r}_i\|$. Simplifying to the planar problem ($z_i = 0$, $\beta = 0$), additional insight is available by rewriting Equation (4.6) in amplitude-phase form,

$$H_{\text{lt}} = H_{\text{nat},i} + a_{\text{lt}} \|\vec{r}_i\| \sin(\alpha + \phi), \quad (4.7)$$

where $\phi = \arctan(-x_i / -y_i) = \pi + \arctan(x_i / y_i)$. This link between phase and the spacecraft position supplies information about the control curve geometry, including the locations of the $H_{\text{lt}} = H_{\text{nat}}$ points and the locations of the maximum

and minimum H_{lt} points. To illustrate these relationships, consider the control point at $\vec{\rho}_1 = \{1.53 \ 0.73 \ 0 \ -1.55\}^T$, as depicted by the purple square in Figure 4.3. Given the low-thrust acceleration magnitude $a_{\text{lt}} = 7\text{e-}2$, the resulting control curve, $\mathcal{U}_1(\vec{\rho}_1)$, also plotted in purple in Figure 4.4, is bounded by $-1.67 \leq H_{\text{lt}} \leq -1.43$ with a mean value at $H_{\text{nat}} = -1.55$. The phase shift of the curve, identical to the

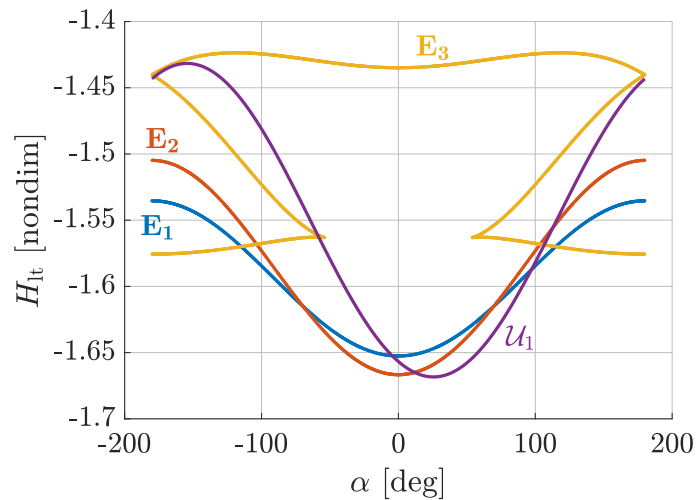


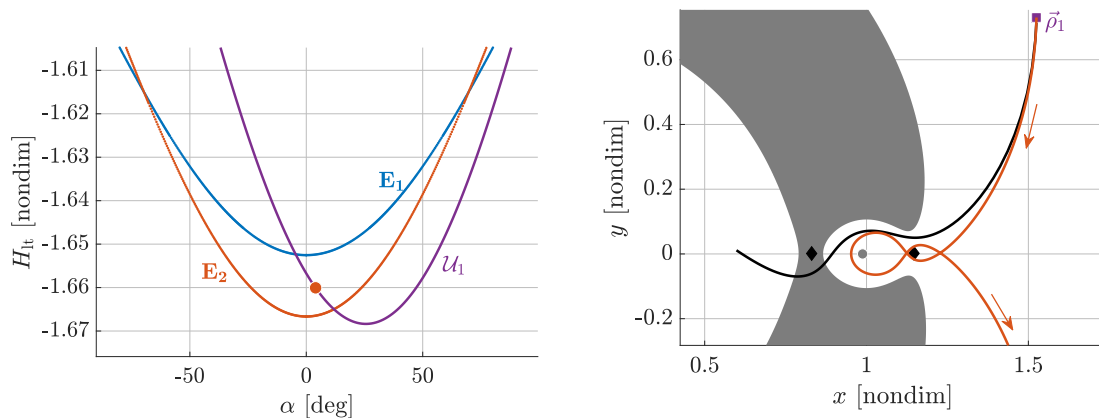
Figure 4.4.: Earth-Moon ZAC energy curves (blue, red, yellow) for $a_{\text{lt}} = 7\text{e-}2$ and $\beta = 0$ and the control curve, \mathcal{U}_1 (purple), associated with the $\vec{\rho}_1$ control point

angular separation between the $+\hat{y}$ -axis and $(-x_i, -y_i)$, is approximately 244.5° , or -115.5° . Together, these amplitude, mean value, and phase shift values define the control curve geometry. Thus, the range of H_{lt} values that may be achieved by implementing low-thrust with the specified a_{lt} magnitude on an arc originating from $\vec{\rho}_1$ are limited and follow the prescribed function of α , i.e., the control curve $\mathcal{U}_1(\vec{\rho}_1)$.

4.2.2 Low-Thrust Control for Partial Capture

When plotted with the ZAC energy curves, the control curve becomes a means to identify α values that deliver energies corresponding to desirable gateway configurations. For instance, to establish a captured orbit about P_2 , the ballistic path represented by the black curve in Figure 4.3 must be modified such that the spacecraft

does not transit the E_1 gateway to the interior of the Earth-Moon CR3BP+LT system. Thus, a forbidden region configuration with the E_1 gateway closed and with the E_2 gateway open (to allow transit *into* the P_2 region) is desired. Such a configuration is represented in energy curve space by a point that lies below (lower energy) the \mathbb{E}_1 energy curve and above (higher energy) the \mathbb{E}_2 energy curve. A set of suitable points are located in the range $-70^\circ < \alpha < 70^\circ$, as seen in the detailed view in Figure 4.5(a). While all of the points between the \mathbb{E}_1 and \mathbb{E}_2 energy curves for $-70^\circ < \alpha < 70^\circ$ yield



(a) Select $\alpha = 4^\circ$ (orange circle) with $a_{1t} = 7e-2$ to yield $H_{1t} = -1.6601$, sufficient to close the E_1 gateway while the E_2 gateway remains open

(b) A low-thrust arc (orange) propagated with the selected α value is bounded by the corresponding low-thrust forbidden regions (gray), and departs through the open E_2 gateway

Figure 4.5.: The selection of a suitable α value bounds the resulting CR3BP+LT Earth-Moon arc such that passage through the E_1 gateway is impossible, but the E_2 gateway remains open and the spacecraft escapes from the P_2 vicinity

a suitable forbidden region configuration to prohibit transit through the E_1 gateway, only the (α, H_{1t}) pairs that lie on the \mathcal{U}_1 control curve are attainable via a single low-thrust propagation from the initial state, i.e., from the control point $\vec{\rho}_1$. The control curve, \mathcal{U}_1 , passes through the set of suitable points for values angles in the range $\alpha_1 \in [-4.5^\circ, 11.5^\circ]$. For instance, the value $\alpha_1 = 4^\circ$, represented by an orange circle in Figure 4.5(a), is leveraged during a low-thrust propagation from $\vec{\rho}_1$ to yield the low-thrust forbidden regions depicted in gray in Figure 4.5(b). The spacecraft

path that employs this α_1 value, plotted in orange, is bounded by the forbidden regions and diverges from the ballistic path (plotted in black) to remain near P_2 for a short time. Other α_1 values on \mathcal{U}_1 that are located between the \mathbb{E}_1 and \mathbb{E}_2 energy curves are also sufficient to admit the desired forbidden region geometry and will yield low-thrust paths with slightly different geometries. Thus, insights from the simple analytical relationships between energy and low-thrust parameters inform the generation of preliminary low-thrust trajectory designs.

4.2.3 Control Curves Linking Two Control Points

While a single low-thrust propagation may be sufficient to achieve some mission design goals, as in the example in Section 4.1, multiple arcs are required in general. For instance, the addition of a mid-course thrust reorientation along the low-thrust arc (orange) in Figure 4.5(b) may further adjust the forbidden region to satisfy the mission goal, i.e., permanent capture about P_2 . In this scenario, the spacecraft is located on a low-thrust arc originating from an initial control point, $\vec{\rho}_1$, and the thrust vector is oriented by α_1 to yield the energy level $H_{lt,1}$ that admits the forbidden region geometry and low-thrust path depicted in Figure 4.5(b). By switching α to a different value after passing through the E_2 gateway, the energy of the subsequent low-thrust arc may be manipulated to close both gateways and bound the spacecraft motion to remain near P_2 . Mathematically, the problem is posed as such: the initial control point, i.e., $\vec{\rho}_1 = \{x_1 \ y_1 \ 0 \ H_{nat,1}\}^T$, as well as the initial low-thrust parameters, $(\alpha_1, H_{lt,1})$, and the desired final parameters, $(\alpha_2, H_{lt,2})$, are known. The goal is to identify a second control point, $\vec{\rho}_2 = \{x_2 \ y_2 \ 0 \ H_{nat,2}\}^T$, along or near the current low-thrust propagated path where α_1 may be instantaneously changed to α_2 while simultaneously yielding the desired energy, $H_{lt,2}$, and maintaining a consistent acceleration magnitude, $a_{lt} = 7e-2$. Such a control point yields the control curve,

$$\mathcal{U}_2(\vec{\rho}_2) : H_{lt} = H_{nat,2} - a_{lt} [x_2 \cos(\alpha) + y_2 \sin(\alpha)], \quad (4.8)$$

which must pass through both $(\alpha_1, H_{\text{lt},1})$ and $(\alpha_2, H_{\text{lt},2})$. Because \mathcal{U}_2 describes the range of H_{lt} values attainable from $\vec{\rho}_2$, both the prior and posterior (α, H_{lt}) pairs must lie on \mathcal{U}_2 to enable such an instantaneous change. Substituting the low-thrust Hamiltonian and thrust orientation values into Equation (4.8) yields two equations parameterized by the same control point,

$$H_{\text{lt},1} = H_{\text{nat},2} - a_{\text{lt}} [x_2 \cos(\alpha_1) + y_2 \sin(\alpha_1)], \quad (4.9)$$

$$H_{\text{lt},2} = H_{\text{nat},2} - a_{\text{lt}} [x_2 \cos(\alpha_2) + y_2 \sin(\alpha_2)]. \quad (4.10)$$

As this system includes two equations and three unknowns (x_2 , y_2 , and $H_{\text{nat},2}$), infinitely many solutions exist. However, by applying additional insights from the CR3BP+LT, the number of solutions is reduced.

As defined in Section 2.2.8 and demonstrated in Section 4.1, the H_{nat} value along a low-thrust arcs evolves on the energy plane. Subsequently, the variation in H_{nat} over a propagated arc is a function only of the constant thrust vector and the initial and final positions on the arc, i.e., ΔH_{nat} is path-independent. In the low-thrust capture scenario, the initial $H_{\text{nat}}(\tau_0) = H_{\text{nat},1}$ value is specified by $\vec{\rho}_1$, as are the initial position coordinates of the spacecraft, $\vec{r}(\tau_0) = \vec{r}_1$. Additionally, the low-thrust acceleration vector is defined by the selected a_{lt} magnitude and α_1 angle and the final (unknown) position and natural Hamiltonian associated with the low-thrust arc are denoted $\vec{r}(\tau_f) = \vec{r}_2$ and $H_{\text{nat}}(\tau_f) = H_{\text{nat},2}$, respectively. By substituting these values from the design problem into Equation (2.127), an additional relationship is available,

$$H_{\text{nat},2} = H_{\text{nat},1} + a_{\text{lt}} [(x_2 - x_1) \cos(\alpha_1) + (y_2 - y_1) \sin(\alpha_1)], \quad (4.11)$$

that may be substituted into Equations (4.9) and (4.10) to remove the $H_{nat,2}$ unknown. The resulting system of one equation and two unknowns (x_2 and y_2) describes a line, $\mathcal{P}_{1,2}$, written in slope-intercept form,

$$\mathcal{P}_{1,2} : y_2 = \frac{(H_{lt,2} - H_{nat,1})a_{lt}^{-1} + x_1 C_{\alpha_1} + y_1 S_{\alpha_1}}{S_{\alpha_1} - S_{\alpha_2}} + x_2 \tan(\bar{\alpha}), \quad (4.12)$$

where $\bar{\alpha} = 0.5(\alpha_1 + \alpha_2)$. Each point along this line represents a location where a change from α_1 to α_2 yields the desired change from $H_{lt,1}$ to $H_{lt,2}$. Therefore, intersections between the low-thrust arc propagated with $\alpha = \alpha_1$ and the $\mathcal{P}_{1,2}$ line serve as suitable control points at which to transition to α_2 and $H_{lt,2}$. If $\mathcal{P}_{1,2}$ and the low-thrust arc do not intersect, the initial velocity direction (an unconstrained variable) may be modified to target an intersection without changing $H_{lt,1}$. Alternatively, if some impulsive capability is available on the spacecraft, the y -intercept (the first term in Equation (4.12)) may be shifted by implementing a maneuver at the initial or final points on the arc. Because the velocity is only included in the $H_{lt,2}$ and $H_{nat,1}$ terms, the slope of $\mathcal{P}_{1,2}$ remains unchanged.

4.2.4 Feasible Regions

The set of suitable control points, i.e., $\mathcal{P}_{1,2}$, depends on the selection of a target (α , H_{lt}) pair, thus, scenarios with many suitable target pairs do not admit well-defined sets of control points. To reduce the number of (α , H_{lt}) options, the design problem is reversed by identifying bounds on the control point locations and leveraging Equation (4.12) to map the control point bounds to a set of (α , H_{lt}) pairs that may be achieved from the specified set of control points. A suitable (α , H_{lt}) target is then selected from the achievable set and a $\mathcal{P}_{1,2}$ line is defined to identify the control points that enable the specified energy change. Bounds on the location of a control point are informed by the geometry of the spacecraft path and by the unconstrained variables (e.g., in time-of-flight or velocity angle). In the capture scenario, the initial low-thrust parameter selection (α_1 , $H_{lt,1}$) is sufficient to deliver the spacecraft to the P_2 region

without escaping through the E_1 gateway, as seen in Figure 4.5(b), but an additional control point is desired in the P_2 vicinity where a thrust reorientation may be located to reconfigure the forbidden regions to bound the spacecraft near P_2 . This goal – a forbidden region geometry that closes the E_1 and E_2 gateways – is satisfied by any $(\alpha_2, H_{lt,2})$ pair located below both the \mathbb{E}_1 and \mathbb{E}_2 energy curves in Figure 4.4. Thus, the definition of a set of suitable control point locations and the corresponding set of attainable (α, H_{lt}) pairs, collectively termed *feasible regions*, are required to reduce the number of design options. In the capture scenario, the second control point must be located between the E_1 and E_2 gateways. A set of bounds on the x and y control point locations, i.e., $x \in [x_{\min}, x_{\max}]$ and $y \in [y_{\min}, y_{\max}]$, are implemented to approximate the P_2 vicinity within the forbidden regions, as depicted by the orange rectangle in Figure 4.6(a). As a simple estimate, a line of control points, i.e., $\mathcal{P}_{1,2}$ from

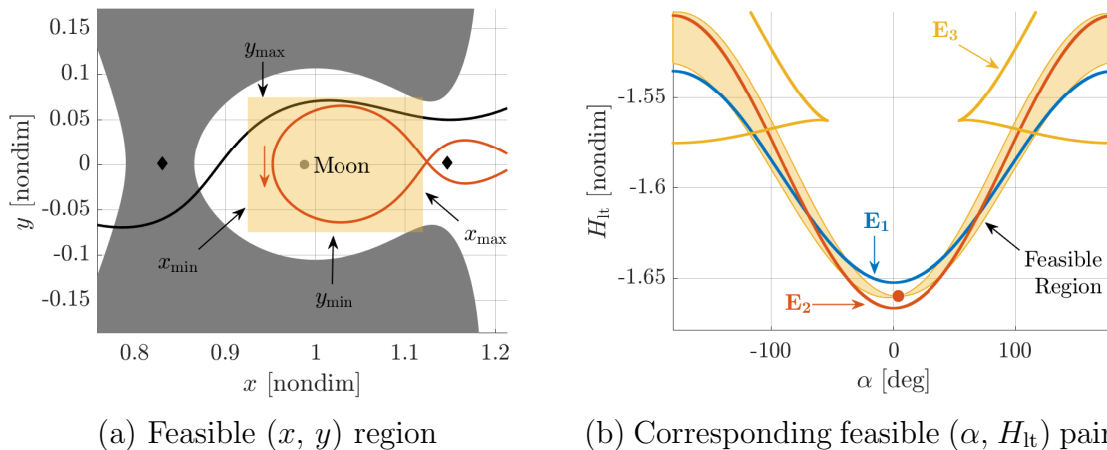


Figure 4.6.: By defining a region of feasible positions, $x \in [x_{\min}, x_{\max}]$ and $y \in [y_{\min}, y_{\max}]$, a corresponding set of feasible (α, H_{lt}) pairs are identified in parameter space for the Earth-Moon CR3BP+LT with $a_{lt} = 7e-2$

Equation (4.12), intersects this feasible region if $y_2 = y_{\max}$ within the $[x_{\min}, x_{\max}]$ bounds or if $y_2 = y_{\min}$ within the same bounds. Accordingly, the intercepts of $\mathcal{P}_{1,2}$ are constrained and Equation (4.12) may be rearranged to identify bounds on α_2 and $H_{lt,2}$ associated with lines that intersect the feasible region. Write Equation (4.12) in

slope-intercept form, $y_2 = b + \sigma x_2$, with $y_2 = y_{\min}$ or y_{\max} , and solve for x , which is bounded,

$$x_{\min} \leq \frac{1}{\sigma} (y_{\max} - b) \leq x_{\max}. \quad (4.13)$$

As σ and b are functions of α_2 and $H_{lt,2}$, this set of inequalities represents the (α, H_{lt}) pairs that produce $\mathcal{P}_{1,2}$ lines intersecting y_{\max} within the bounds on x . A similar equation is also written to identify pairs that produce $\mathcal{P}_{1,2}$ solutions intersecting y_{\min} . Together, the inequalities then yield all (α, H_{lt}) values that correspond to lines of control points passing through the rectangular feasible region. The inequality (4.13) delivers $H_{lt,2}$ as a function of α_2 , such that

$$\left. \begin{array}{l} h(\alpha_2, x_{\max}, y_i) \quad s \geq 0 \\ h(\alpha_2, x_{\min}, y_i) \quad s < 0 \end{array} \right\} \leq H_{lt,2} \leq \left\{ \begin{array}{l} h(\alpha_2, x_{\min}, y_i) \quad s \geq 0 \\ h(\alpha_2, x_{\max}, y_i) \quad s < 0 \end{array} \right., \quad (4.14)$$

where

$$h(\alpha_2, x_j, y_i) = H_{lt,1} - a_{lt} [S_{\alpha_1} - S_{\alpha_2}] (\tan(\bar{\alpha})x_j - y_i), \quad (4.15)$$

$$s = \text{sgn} [(S_{\alpha_1} - S_{\alpha_2}) \cot(\bar{\alpha})], \quad (4.16)$$

and $y_i = y_{\max}$ or y_{\min} . Accordingly, the feasible energy region bounded by these inequalities, depicted in Figure 4.6(b), includes only $(\alpha_2, H_{lt,2})$ pairs attainable from control points within the rectangular (x_2, y_2) feasible region given the initial control point, $\vec{\rho}_1$ and natural Hamiltonian, $H_{nat,1}$. Finally, other constraints on $\mathcal{P}_{1,2}$ may be employed to construct feasible regions, such as the set of bounding x -intercepts, or a desired slope for the $\mathcal{P}_{1,2}$ line. Regardless of the specific definition of “feasibility,” the set of acceptable (x_2, y_2) locations maps to a set of corresponding feasible $(\alpha_2, H_{lt,2})$ energy pairs.

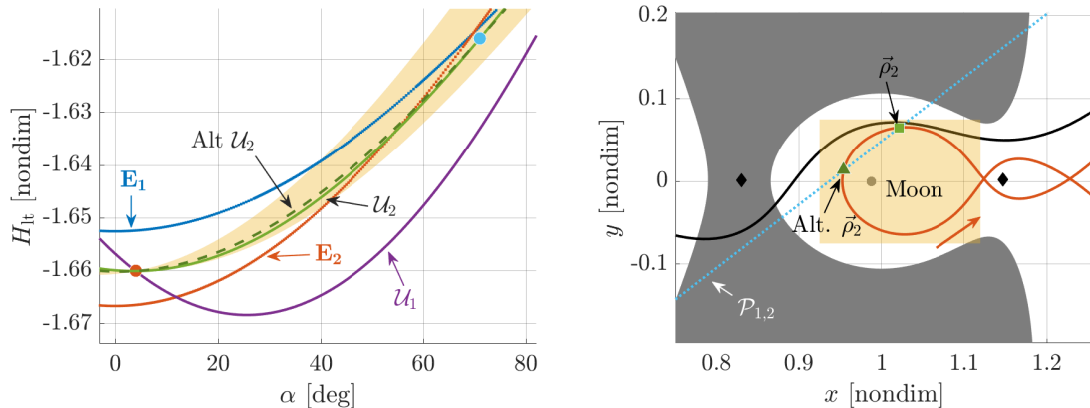
The feasible energy pairs follow patterns that are qualitatively predicted by the analytical equations. First, as observed by the lack of feasible region above and below the $(\alpha_1, H_{lt,1})$ point in Figure 4.6(b), no energy change is possible if $\alpha_2 = \alpha_1$. This

result follows directly from Equation (4.14) (substituting $\alpha_2 = \alpha_1$ yields $H_{\text{lt},2} = H_{\text{lt},1}$) but also follows intuitively from the dynamics; without a change in α , it is impossible to change H_{lt} with a fixed a_{lt} value. Second, the phase and amplitudes of the sinusoids bounding the feasible energy region are related to the bounds of the (x, y) feasible region; the points furthest from and closest to the system barycenter (i.e., the origin) define the amplitude range, while the angular separation of the corners in the rectangle from the $+\hat{y}$ -axis bound the phase of the sinusoids. In this example, the region is roughly centered on $(x = 1, y = 0)$; thus, the amplitudes of the available control curves are approximately $a_{\text{lt}}\sqrt{1^2 + 0^2} = 7\text{e-}2$. Similarly, the phases of the curves are $\phi \approx \arctan(-1/0) = -\pi/2$. Subsequently, an approximation of the feasible energy region is available from the properties of the control point bounds, supplying some insight before further computational effort is expended.

4.2.5 Low-Thrust Control for Full Capture

By leveraging the insights from the control curve equations and feasible regions, an $(\alpha_2, H_{\text{lt},2})$ pair is straightforwardly identified and targeted. Recall that the goal of the mid-course thrust reorientation is to close both the E_1 and E_2 gateways; thus, an $(\alpha_2, H_{\text{lt},2})$ pair located below the \mathbb{E}_1 and \mathbb{E}_2 ZAC energy curves is desired. The rectangular bounds on the control point location, depicted in Figure 4.6(a), yield a corresponding set of bounds in energy curve space, as in Figure 4.6(b). Accordingly, the selection of an $(\alpha_2, H_{\text{lt},2})$ pair within the feasible energy region that satisfies the mission objective (to close the gateways) yields a $\mathcal{P}_{1,2}$ line that intersects the set of feasible control points, likely intersecting the initial low-thrust path as well. Only two small sections of the feasible energy region satisfy the mission objective: one near the “feasible region” arrow in Figure 4.6(b), and another approximately mirrored across $\alpha = 0^\circ$. One candidate pair in this region, $(71^\circ, -1.616)$, marked by a cyan circle in Figure 4.7(a), yields a set of control points, $\mathcal{P}_{1,2}$, which intersect the initial low-thrust propagation in two locations, as depicted by the dotted cyan line in Figure

4.7(b). These intersections define two control point options, labeled $\vec{\rho}_2$ and Alt. $\vec{\rho}_2$

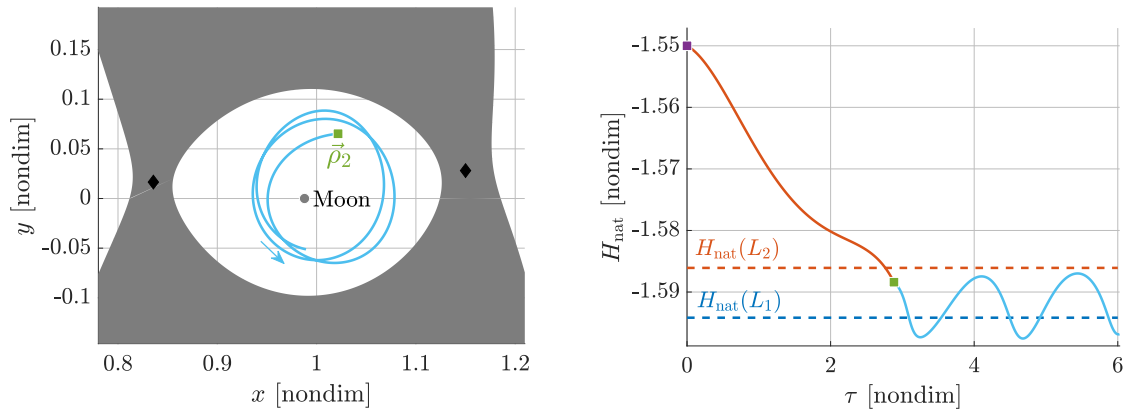


(a) An $(\alpha_2 = 71^\circ, H_{lt,2} = -1.616)$ pair (cyan circle) is attainable via the control curves \mathcal{U}_2 (solid) or Alt. \mathcal{U}_2 (dashed) from the initial $(\alpha_1, H_{lt,1})$ pair (orange circle)

(b) The $\mathcal{P}_{1,2}$ set (dotted cyan) identifies (x,y) locations where a change from α_1 to α_2 yields the desired $H_{lt,2}$ value. Two control points are located at the intersection of $\mathcal{P}_{1,2}$ and the low-thrust arc

Figure 4.7.: An $(\alpha_2, H_{lt,2})$ pair is attainable by changing low-thrust parameters at intersections of $\mathcal{P}_{1,2}$ and the low-thrust arc

and marked by a green square and triangle, respectively, that subsequently define two control curves, \mathcal{U}_2 and Alt. \mathcal{U}_2 , plotted in green in Figure 4.7(a), that link the $(\alpha_2, H_{lt,2})$ target to the $(\alpha_1, H_{lt,1})$ pair implemented on the orange low-thrust arc. Thus, a control change from α_1 to α_2 at either $\vec{\rho}_2$ or Alt. $\vec{\rho}_2$ yields the desired $H_{lt,2}$ value and the resulting propagation with $a_{lt} = 7e-2$ and $\alpha = 71^\circ$ is constrained to remain near P_2 by the low-thrust forbidden regions, as depicted in Figure 4.8(a). If this low-thrust vector is maintained, the spacecraft will never depart the P_2 vicinity. However, continuous thrusting is not required to ensure the spacecraft remains captured. When the natural energy of the trajectory sufficiently low such that the L_1 and L_2 gateways of the natural CR3BP forbidden regions are closed, the low-thrust force may be switched off. Following engine shutdown, the spacecraft follows a ballistic path, the natural energy remains constant, and the spacecraft remains bounded by the natural forbidden regions. Such a strategy is possible with the captured arc in this example. The trajectory H_{nat} value, plotted in Figure 4.8(b), dips below the minimum capture



(a) Propagating from $\vec{\rho}_2$ with $\alpha_2 = 71^\circ$ yields a captured arc (cyan), bounded by the low-thrust forbidden region (gray) at the corresponding energy, $H_{lt,2} = -1.616$

(b) The H_{nat} energy of the low-thrust trajectory decreases below the CR3BP L_2 and L_1 energies, at which point a coast arc will maintain the captured geometry

Figure 4.8.: The low-thrust capture in the Earth-Moon CR3BP+LT for $a_{\text{lt}} = 7\text{e-}2$

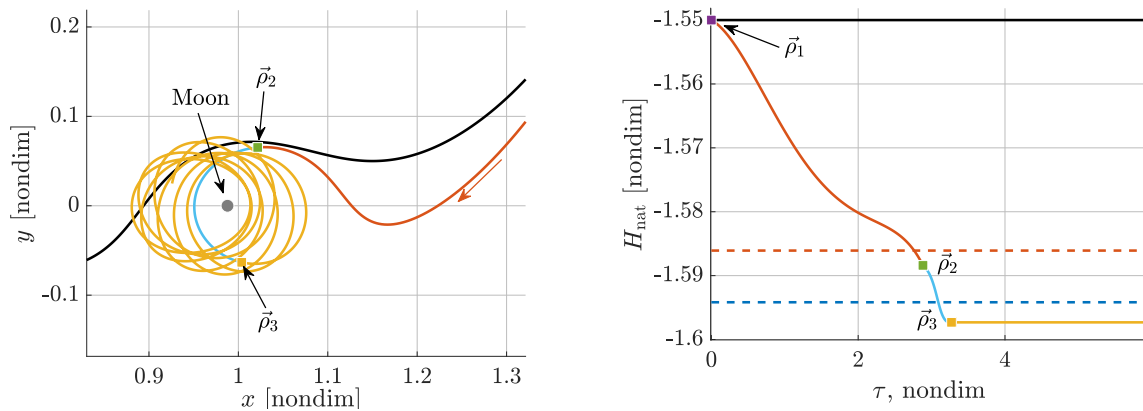


Figure 4.9.: Low-thrust capture trajectory ending in a ballistic coast (yellow) constrained to remain near the Moon

energy, $H_{\text{nat}}(L_1)$ shortly after control point $\vec{\rho}_2$ (green square). Thus, at any point on the cyan H_{nat} history below the $H_{\text{nat}}(L_1)$ boundary, the low-thrust propulsion may be switched off while maintaining captured behavior. For example, a third control point, $\vec{\rho}_3$, is placed near the first H_{nat} minimum on the cyan arc, as depicted in Figure 4.9. The resulting ballistic arc, plotted in yellow, is constrained to remain near P_2 by the ballistic forbidden regions, concluding the low-thrust capture mission.

4.3 P_2 to L_5 Transfer Leveraging Equilibria Manifolds

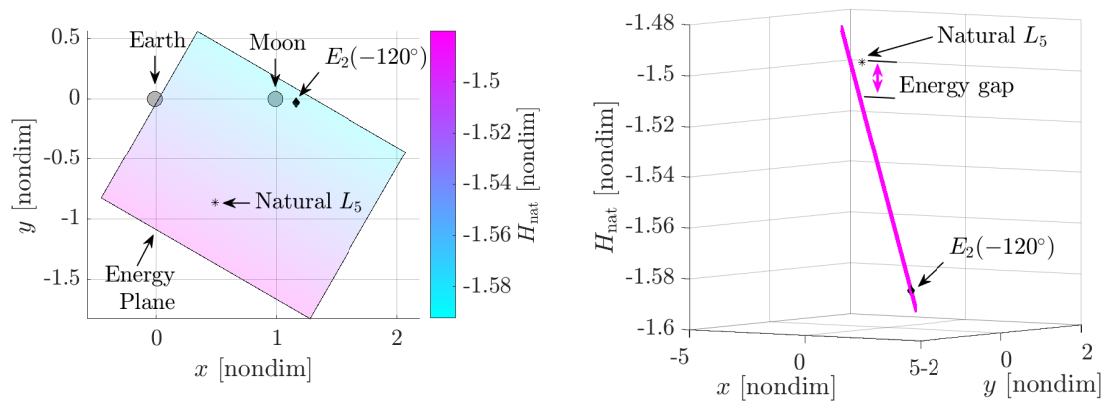
In addition to the insights available from the energy plane, the hyperbolic equilibrium point manifolds may be employed to guide a spacecraft from the vicinity of P_2 to other locations in the system. To illustrate such a methodology, a transfer from the lunar vicinity to a stable L_5 short-period orbit (SPO) is constructed in the Earth-Moon system. While the L_1 and L_2 manifolds offer flow patterns that depart the lunar region, these trajectories, plotted in Figure 3.25, do not approach L_5 , even when propagated for longer time intervals than depicted in the plot. Furthermore, these natural manifold paths maintain a fixed H_{nat} value consistent with the originating equilibrium point and, thus, do not approach the much higher $H_{\text{nat}}(L_5)$ value. An additional complication arises from the fact that L_5 is characterized by C^6 motion; thus, L_5 possesses no manifolds to further attract the flow. Farrés [72] mitigates this problem when designing similar transfers in the Sun-Earth system that employ an additional force generated by a solar sail by using a “brute force search” to identify sail orientations and states near the triangular point that, when propagated in reverse time, may be linked to the $E_1(0)$ or $E_2(0)$ unstable manifolds in both position and energy to construct an end-to-end transfer design. By leveraging insights from energy planes and employing equilibrium solutions in the CR3BP+LT located near L_5 with nontrivial saddle modes, a transfer is straightforwardly designed without a grid search.

4.3.1 Preliminary Design Generation

A transfer design that incorporates both the energetic and geometric differences between the L_5 and lunar regions is facilitated by leveraging manifolds associated with the low-thrust planar equilibria. A similar strategy may be employed for spatial equilibria and their manifolds. Motion near the Moon is available from the manifolds associated with points on the \mathbb{E}_1 and \mathbb{E}_2 sets. Because the \mathbb{E}_1 and \mathbb{E}_2 structures for $a_{\text{lt}} = 7\text{e-}2$ and $\beta = 0$ are characterized by $S^2 \times C^4$ motion regardless of α (see Section

3.2.6), many manifolds that depart the region are available. A survey of these manifolds over the full range of α values indicates that, while small differences are apparent as α varies, as in Figure 3.25, the general flow geometry remains consistent. Thus, the energy on these manifold trajectories may be designed relatively independently of the geometry by selecting an α value to supply an appropriate energy plane, i.e., an energy plane sloped in the desirable orientation.

To develop an initial guess for a transfer between the Moon and L_5 , the manifolds corresponding to a planar ($\beta = 0$) Earth-Moon CR3BP+LT \mathbb{E}_2 solution are explored (alternatively, manifolds corresponding to an \mathbb{E}_1 point may be leveraged). As illustrated in Figure 4.10(b), the H_{nat} value associated with L_5 is significantly larger than the H_{nat} values at the \mathbb{E}_2 (or \mathbb{E}_1) sets. To maximize the H_{nat} value available at L_5 along a single low-thrust arc originating from one of these low-thrust equilibria, the energy plane is aligned with the Moon- L_5 line, e.g., $\alpha = -120^\circ$, as plotted in Figure 4.10. However, even with the plane oriented to maximize the energy at the L_5 loca-



(a) Planar projection of the energy plane with $\alpha = -120^\circ$

(b) Edge-on view of the energy plane; the natural L_5 point possesses an H_{nat} value higher than those attainable on the energy plane at the location of the L_5 point

Figure 4.10.: The energy plane associated with the Earth-Moon CR3BP+LT $E_2(-120^\circ)$ point for $a_{lt} = 7e-2$ ($\gamma \approx 4^\circ$) is too shallow to reach $H_{\text{nat}}(L_5)$ at the L_5 location

tion, the slope of the energy plane is too shallow to reach $H_{\text{nat}}(L_5)$ at the L_5 position, visualized as an “energy gap” between the energy plane and the L_5 point in Figure 4.10(b). The slope of the plane is a function of the low-thrust acceleration magnitude, a_{lt} , and is limited by the capabilities of the propulsion system. Accordingly, given the limitation of $a_{\text{lt}} = 7\text{e-}2$, a single manifold arc originating from an \mathbb{E}_2 point cannot reach the natural L_5 point with the desired energy. Additional energy manipulations are required to construct a set of multiple “energy switchbacks” that reach both the L_5 position and energy level.

To facilitate an energy increase from $H_{\text{nat}}(L_2)$ to $H_{\text{nat}}(L_5)$, low-thrust flow originating near the natural L_5 point is linked to low-thrust flow near the Moon. In contrast to the natural CR3BP, the CR3BP+LT possesses equilibrium points near L_5 on the \mathbb{E}_3 structure with a hyperbolic manifold. In the Earth-Moon CR3BP+LT with $a_{\text{lt}} = 7\text{e-}2$ and $\beta = 0$, these equilibria, plotted as purple points in Figure 4.11, are located near L_5 when $\alpha \approx -60^\circ$. While the locations and energies of the equi-

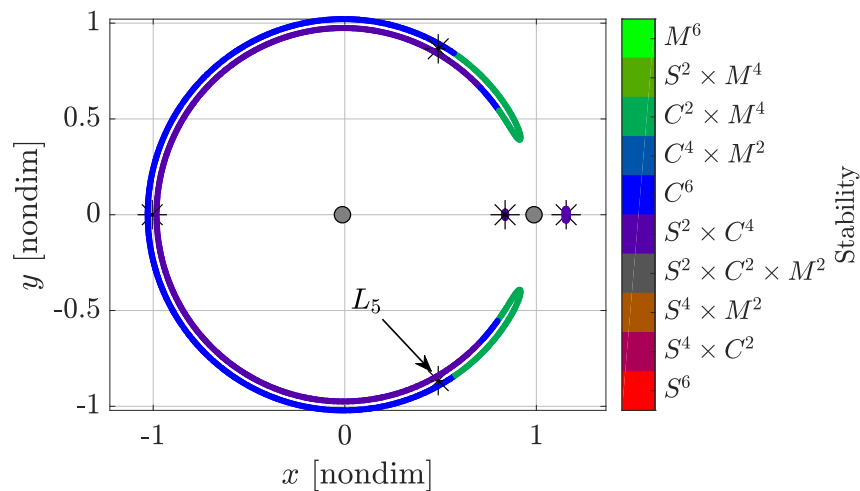


Figure 4.11.: Earth-Moon ZACs colored by stability for $a_{\text{lt}} = 7\text{e-}2$ and $\beta = 0$; Lagrange points marked by asterisks

libria on \mathbb{E}_1 and \mathbb{E}_2 vary only a small amount with α , the \mathbb{E}_3 equilibrium points shift over large distances throughout the xy -plane as α varies. Accordingly, only the $E_3^1(-60^\circ)$ solution near L_5 supplies manifolds that evolve sufficiently to attract flow.

The energy along these manifold trajectories evolves on the energy plane oriented by $\alpha = -60^\circ$, as depicted in Figure 4.12. A transfer from $E_2(-120^\circ)$ to $E_3^1(-60^\circ)$ may

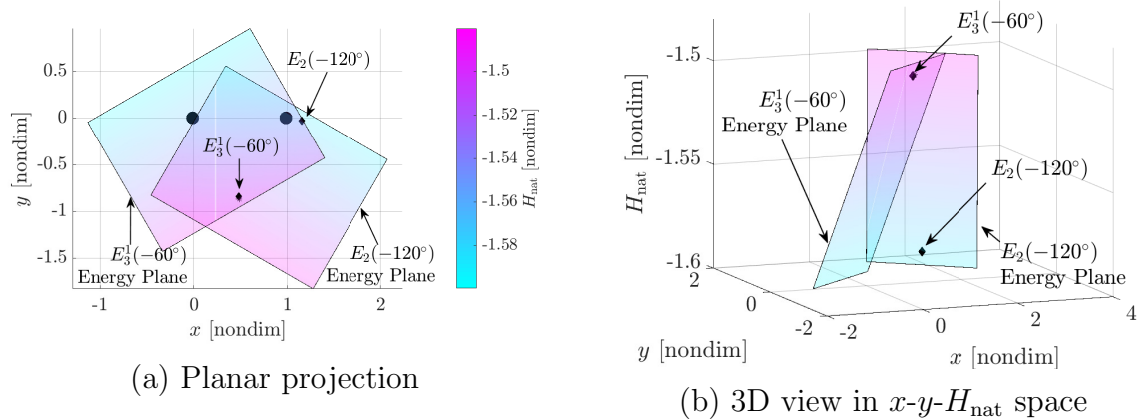


Figure 4.12.: The energy planes corresponding to the low-thrust equilibrium points $E_3^1(-60^\circ)$ near L_5 and $E_2(-120^\circ)$ contain all trajectories originating from the two equilibria; control adjustments at the intersection of the two planes facilitates transfers between the two points

leverage flow along both energy planes. Such a transfer originates at the $E_2(-120^\circ)$ point and subsequently flows along the corresponding energy plane. Then, at an intersection between the $E_2(-120^\circ)$ energy plane and the $E_3^1(-60^\circ)$ energy plane, the low-thrust parameters may be switched to match those associated with the $E_3^1(-60^\circ)$ point, i.e., α is switched from -120° to -60° . The resulting propagation then flows along the $E_3^1(-60^\circ)$ energy plane, which includes the $E_3^1(-60^\circ)$ equilibrium solution very near the location and energy of the natural L_5 point, facilitating the required energy change.

4.3.2 Poincaré Mapping at Energy Plane Intersections

The locations where the equilibrium point manifolds reach the energy plane intersection are available by employing a *Poincaré* mapping. A Poincaré map includes three key components: a set of initial conditions,

$\{\vec{X}_{i,0}, i = 1, 2, \dots, n\}$, a hyperplane, Σ , and a visualization strategy. The initial condi-

tions are numerically integrated to the hyperplane for p returns, yielding the mapping, $\mathbb{M}_{\Sigma}^p(\vec{X}_{i,0})$. In many applications the hyperplane is a geometric plane, e.g., a plane at some x , y , or z value, but Σ may also be a non-geometric plane. For this energy-plane traversal example, a physical plane located at the intersection of the energy planes is employed. In the planar problem ($z = \dot{z} = 0$, $\beta = 0$), the intersection of two energy planes defines a line, $\mathcal{H}_{1,2}$, in x - y - H_{nat} space. The orientation of this line is described by the cross product of the two plane normal vectors,

$$\hat{n}_1 \times \hat{n}_2 = \left\{ \begin{array}{c} S_{\alpha_1} S_{\gamma_1} C_{\gamma_2} - S_{\alpha_2} S_{\gamma_2} C_{\gamma_1} \\ C_{\alpha_2} S_{\gamma_2} C_{\gamma_1} - C_{\alpha_1} S_{\gamma_1} C_{\gamma_2} \\ C_{\alpha_1} S_{\gamma_1} S_{\alpha_2} S_{\gamma_2} - C_{\alpha_2} S_{\gamma_2} S_{\alpha_1} S_{\gamma_1} \end{array} \right\}, \quad (4.17)$$

where

$$\hat{n}_i = \hat{H}_i''' = C_{\alpha_i} S_{\gamma_i} \hat{x} + S_{\alpha_i} S_{\gamma_i} \hat{y} + C_{\gamma_i} \hat{H}. \quad (4.18)$$

A point on the intersection line is located by evaluating Equation (2.130) on each energy plane,

$$C_{\alpha_1} S_{\gamma_1} (\tilde{x} - x_1) + S_{\alpha_1} S_{\gamma_1} + C_{\gamma_1} (\tilde{H}_{\text{nat}} - H_{\text{nat},1}) = 0, \quad (4.19)$$

$$C_{\alpha_2} S_{\gamma_2} (\tilde{x} - x_1) + S_{\alpha_2} S_{\gamma_2} + C_{\gamma_2} (\tilde{H}_{\text{nat}} - H_{\text{nat},2}) = 0, \quad (4.20)$$

where $\vec{\rho}_1 = \{x_1 \ y_1 \ 0 \ H_{\text{nat},1}\}^T$ is a control point anywhere on the first energy plane, $\vec{\rho}_2 = \{x_2 \ y_2 \ 0 \ H_{\text{nat},2}\}^T$ is a control point anywhere on the second energy plane, and $\vec{\rho}_{\text{ref}} = \{\tilde{x} \ \tilde{y} \ 0 \ \tilde{H}_{\text{nat}}\}^T$ is a control point on the intersection of the two planes. As this system includes three unknowns (\tilde{x} , \tilde{y} , and \tilde{H}_{nat}) but only two equations, one of the $\vec{\rho}_{\text{ref}}$ components may be selected arbitrarily; the choice of a convenient geometric location or Hamiltonian value can offer useful insight later in the analysis.

Once the $\vec{\rho}_{\text{ref}}$ point has been located, the energy plane intersection line is projected into the xy -plane to be used as a hyperplane for the low-thrust trajectories. Assuming

the magnitude of the low-thrust acceleration is identical for both planes, $\gamma_1 = \gamma_2$ and the orientation of the intersection line simplifies to

$$\hat{n}_1 \times \hat{n}_2 = \left\{ S_\gamma C_\gamma (S_{\alpha_1} - S_{\alpha_2}) \quad S_\gamma C_\gamma (C_{\alpha_1} - C_{\alpha_2}) \quad S_\gamma^2 (C_{\alpha_1} S_{\alpha_2} - C_{\alpha_2} S_{\alpha_1}) \right\}^T. \quad (4.21)$$

The planar projection of this vector, $\Sigma_{\mathcal{H}_{1,2}}$, is spanned by the \hat{x} and \hat{y} components of $\hat{n}_1 \times \hat{n}_2$. The projection may be simplified by applying a trigonometric identity,

$$\Sigma_{\mathcal{H}_{1,2}} : \left\{ \begin{array}{c} 2S_\gamma C_\gamma \cos([\alpha_1 + \alpha_2]/2) \sin([\alpha_1 - \alpha_2]/2) \\ 2S_\gamma C_\gamma \sin([\alpha_1 + \alpha_2]/2) \sin([\alpha_1 - \alpha_2]/2) \\ 0 \end{array} \right\} \quad (4.22)$$

For all technologically feasible propulsion systems, $0 < \gamma < \pi/2$, thus $S_\gamma C_\gamma \neq 0$ and can be divided out of the vector without affecting the orientation. Similarly, $\sin([\alpha_1 - \alpha_2]/2) = 0$ if and only if α_1 and α_2 yield identical orientations; if the angles are identical and the thrust magnitude for both planes is also the same, the two planes do not intersect. Accordingly, the sine function is nonzero may also be divided out of the projection to obtain

$$\Sigma_{\mathcal{H}_{1,2}} : \left\{ \cos([\alpha_1 + \alpha_2]/2) \quad \sin([\alpha_1 + \alpha_2]/2) \quad 0 \right\}^T \quad (4.23)$$

The out-of-plane component of $\mathcal{H}_{1,2}$ is available from the definition of the tangent function. Let ψ measure the angle between the intersection line and the planar projection in x - y - H_{nat} space, as depicted in Figure 4.13. The out-of-plane and in-plane components of $\mathcal{H}_{1,2}$ are then related via the expression,

$$\tan(\psi) = \frac{S_\gamma^2 (C_{\alpha_1} S_{\alpha_2} - C_{\alpha_2} S_{\alpha_1})}{2S_\gamma C_\gamma \sin\left(\frac{\alpha_1 - \alpha_2}{2}\right) \sqrt{\cos^2\left(\frac{\alpha_1 + \alpha_2}{2}\right) + \sin^2\left(\frac{\alpha_1 + \alpha_2}{2}\right)}}. \quad (4.24)$$

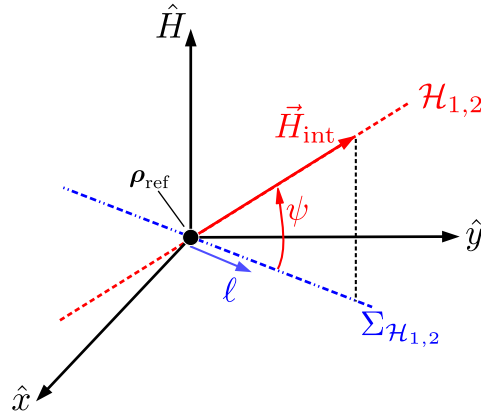


Figure 4.13.: The intersection of two energy planes, $\mathcal{H}_{1,2}$ is decomposed into the \vec{H}_{int} vector and the ℓ coordinate, measured along the projection of the intersection line, $\Sigma_{\mathcal{H}_{1,2}}$; the base point, $\vec{\rho}_{\text{ref}}$, locates the line in x - y - H_{nat} space

By applying an additional trigonometric identities and reducing common terms, this expression simplifies to

$$\tan(\psi) = -\tan(\gamma) \cos\left(\frac{\alpha_2 - \alpha_1}{2}\right) = a_{\text{lt}} \cos\left(\frac{\alpha_2 - \alpha_1}{2}\right). \quad (4.25)$$

Finally, combine the in-plane and out-of-plane components to locate any point on the intersection line,

$$\mathcal{H}_{1,2} : \vec{\rho}_{\text{int}} = \vec{\rho}_{\text{ref}} + \ell \vec{H}_{\text{int}}, \quad (4.26)$$

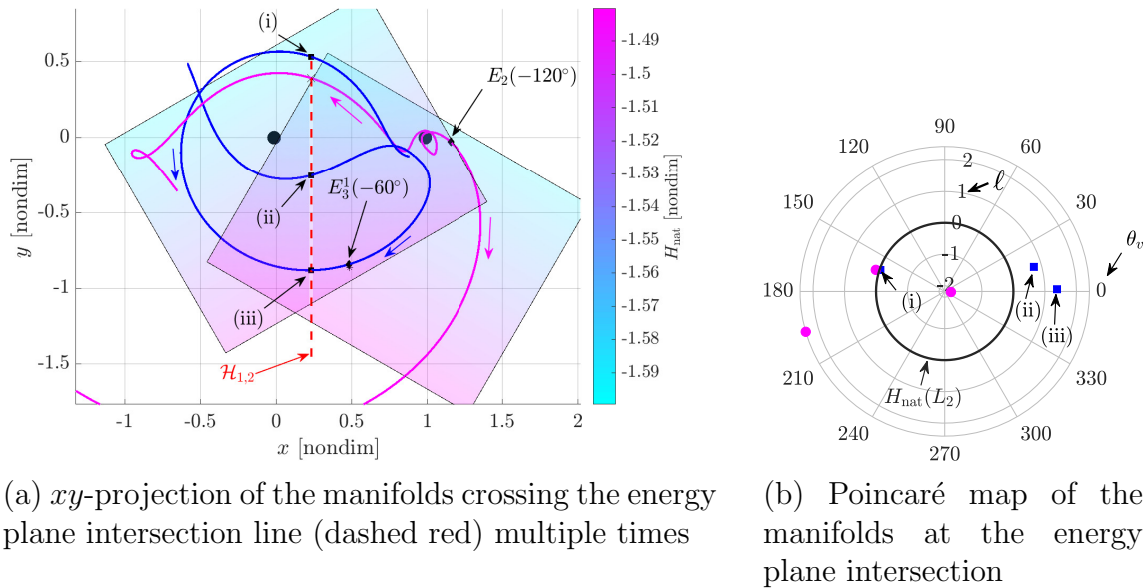
where

$$\vec{H}_{\text{int}} = \left\{ \cos([\alpha_1 + \alpha_2]/2) \quad \sin([\alpha_1 + \alpha_2]/2) \quad a_{\text{lt}} \cos([\alpha_2 - \alpha_1]/2) \right\}^T \quad (4.27)$$

where ℓ is a distance from $\vec{\rho}_{\text{ref}}$ measured along the *planar projection* of $\mathcal{H}_{1,2}$, not along the intersection line itself, as depicted in Figure 4.13. This distance is defined such that $\ell > 0$ maps to points on $\mathcal{H}_{1,2}$ with H_{nat} values greater than the Hamiltonian at $\vec{\rho}_{\text{ref}}$.

To identify links between trajectories on these energy planes, the $\Sigma_{\mathcal{H}_{1,2}}$ hyperplane is employed as a stopping condition for planar trajectories. Because $\mathcal{H}_{1,2}$ defines points that lie on both energy planes, proximity between two points (i.e., similar ℓ values) on the projection, $\Sigma_{\mathcal{H}_{1,2}}$, indicates not only similar positions in the xy -plane, but also similar H_{nat} values. Furthermore, a switch from α_1 to α_2 at a point on $\Sigma_{\mathcal{H}_{1,2}}$ ensures that the trajectory transitions from the first energy plane to the second.

While the displacement along $\Sigma_{\mathcal{H}_{1,2}}$ relative to $\vec{\rho}_{\text{ref}}$, represented by ℓ , supplies position and energy information, an additional coordinate is required to represent the full spacecraft state. Given ℓ , the spacecraft position and H_{nat} value are computed via Equation (4.26). Additionally, the velocity magnitude at this point is available by solving the H_{nat} expression in Equation (2.58) for the spacecraft speed in the rotating frame, v . Only the velocity direction is undefined; thus, a Poincaré map leveraging the coordinates ℓ and $\theta_v = \arctan(\dot{y}/\dot{x})$ supplies the complete spacecraft state; intersections on this map guarantee full state continuity between planar trajectories. In contrast to traditional Poincaré maps in the CR3BP that include only trajectories at one energy level, this representation incorporates arcs with various H_{nat} values. Additionally, as the full state of each map crossing is available from the 2D representation, multiple low-thrust paths may be linked together, or low-thrust and natural arcs may be connected. Such a map is leveraged to identify a transfer between the unstable manifold of $E_2(-120^\circ)$, plotted in magenta in Figure 4.14(a), and the stable manifold of $E_3^1(-60^\circ)$, plotted in blue. Each manifold trajectory crosses the $\Sigma_{\mathcal{H}_{1,2}}$ hyperplane (or, equivalently, $\mathcal{H}_{1,2}$ in x - y - H_{nat} space), plotted as a dashed red line in Figure 4.14(a), at least once. The hyperplane crossing points are transformed to ℓ and θ_v coordinates and plotted in polar form on the Poincaré map in Figure 4.14(b). Each $\Sigma_{\mathcal{H}_{1,2}}$ crossing on the $E_3^1(-60^\circ)$ stable manifold is marked by a blue square and labeled with a lowercase roman numeral to link the points between configuration space and the map. The $E_2(-120^\circ)$ unstable manifold crossings are left unlabeled as several occur far from the primaries and are not depicted in Figure 4.14(a). In this example, $\vec{\rho}_{\text{ref}}$ is selected such that the reference H_{nat} value is identical to the



(a) xy -projection of the manifolds crossing the energy plane intersection line (dashed red) multiple times

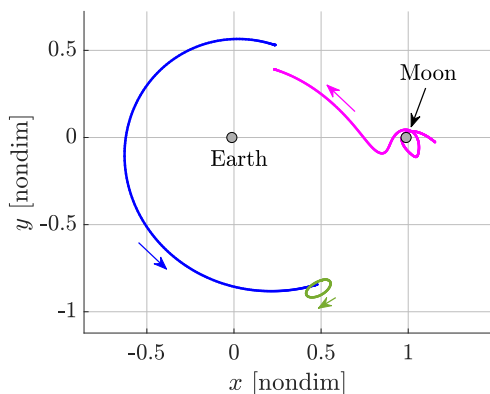
(b) Poincaré map of the manifolds at the energy plane intersection

Figure 4.14.: The stable manifolds (blue) of the $E_3^1(-60^\circ)$ point and the unstable manifolds (magenta) of the $E_2(-120^\circ)$ point are propagated in the Earth-Moon CR3BP+LT for $a_{lt} = 7e-2$; crossings of the energy plane intersection line are marked and included in a Poincaré map to identify a transfer with minimal discontinuities

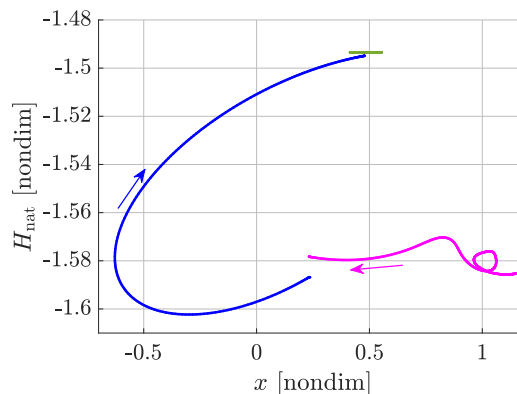
natural L_2 energy, $H_{\text{nat}}(L_2)$. Accordingly, $\ell > 0$ corresponds to energies greater than $H_{\text{nat}}(L_2)$ and $\ell < 0$ indicates lower energy values; the boundary at $\ell = 0$ is plotted as a black circle in Figure 4.14(b) for reference.

4.3.3 Transfer Construction and Corrections

By leveraging the information available from the Poincaré map, a transfer from the lunar vicinity to L_5 is constructed. Two points near $\ell = 0$ and $\theta_v = 160^\circ$, one from a stable manifold and another from an unstable manifold, are selected due to their close proximity to one another on the map. The corresponding trajectories, plotted in blue and magenta in Figure 4.15, are discontinuous in position, velocity, and natural Hamiltonian value. Thus, some corrections are required. To preserve the lunar flybys, the initial state on the $E_2(-120^\circ)$ unstable manifold trajectory is constrained in position and energy (H_{nat}). Additionally, near the destination, a



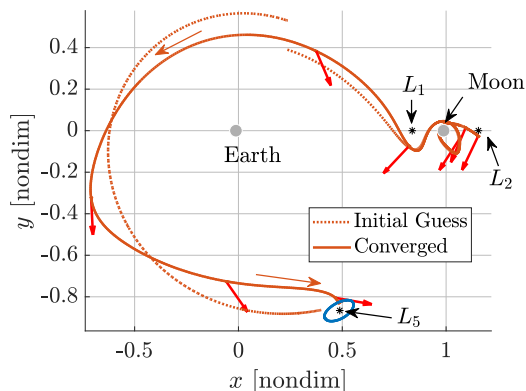
(a) The arcs are discontinuous in position



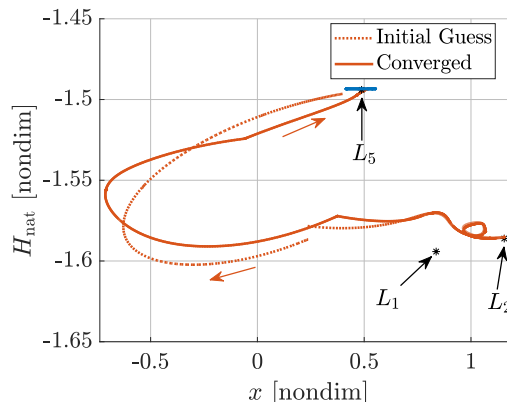
(b) An additional energy discontinuity is apparent

Figure 4.15.: The unstable $E_2(-120^\circ)$ manifold (magenta), stable $E_3^1(-60^\circ)$ manifold (blue), and natural L_5 short period orbit (green) are linked together as an initial design for a Moon to L_5 transfer

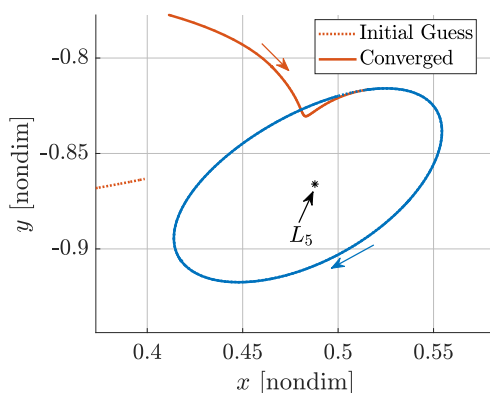
single revolution of a small, natural L_5 short period orbit is included to ensure the spacecraft remains near L_5 after arrival; this orbit is fully constrained to preserve its geometry and energy. Each manifold arc is subdivided into smaller segments, each of which maintains a fixed α value, independent of the other segments, and a thrust magnitude of $a_{lt} = 7e-2$ as in a turn-and-hold strategy. A multiple shooting differential corrections algorithm, consistent with the algorithm described in Section 3.3.2, is then applied to eliminate the position and velocity discontinuities between the arcs. The position and velocity vectors and the spacecraft mass at the beginning of each segment are allowed to vary, as is the epoch associated with the beginning of each segment. The only control variable included in the corrections is the α angle; both $\beta = 0$ and $a_{lt} = 7e-2$ are held constant. As a result of the corrections, a continuous transfer is constructed and plotted as a solid arc in Figure 4.16, with low-thrust segments in orange and ballistic segments in blue. To achieve this result, the initial design is first corrected in the simplified CR3BP+LT with constant a_{lt} on all low-thrust arcs. Following convergence in the simplified model, the transfer is transitioned to the unrestrained CR3BP+LT with variable mass (i.e., variable



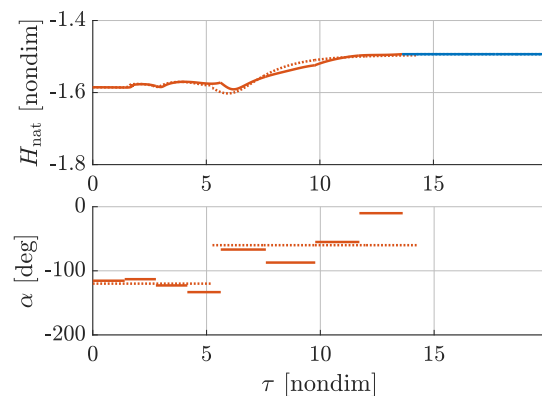
(a) Red arrows indicate the thrust orientation on each segment



(b) Energy (H_{nat}) varies continuously along the transfer



(c) Detailed view of arrival at L_5 SPO



(d) Time histories of H_{nat} and α remain similar to the initial guess

Figure 4.16.: Following corrections, the transfer is continuous in position and velocity and energy; the majority of the transfer leverages low-thrust (orange segments) to reach the natural L_5 SPO (blue)

$a_{lt} = f/m$) where the thrust magnitude is fixed at $f = 7e-2$ and the engine efficiency is parameterized by $I_{sp} = 3000$ seconds. Although the initial design is constructed by leveraging insights from the simplified model with a constant a_{lt} value, convergence in the unrestrained model is achieved rapidly, i.e., in fewer than 20 iterations. The final spacecraft mass along the converged trajectory in Figure 4.16 is 0.9668; thus, the spacecraft requires propellant equivalent to approximately 3.32% of the spacecraft wet mass to complete the transfer. This mass fraction may be reduced further by

applying optimization techniques, but represents a feasible scenario even without optimization. For comparison, Deep Space 1, with low-thrust capabilities consistent with this example, was equipped with 82 kg of Xenon propellant for maneuvers, i.e., about 17% of the spacecraft wet mass.¹

As the initial design, represented by dashed arcs, includes minimal discontinuities due to the Poincaré map analysis, the converged solution consequently maintains the geometry of the initial guess in x - y - H_{nat} space. Additionally, the control history, plotted in Figure 4.16(d), remains similar to the preliminary solution with $\alpha \approx -120^\circ$ for the first 5.5 time units and reaches $\alpha \approx -60^\circ$ over the duration of the final thrusting segments. The variations in α between the preliminary design and the converged solution (most notably the final segment with $\alpha \approx -10^\circ$) are the control response adjusting the preliminary solution to meet the constraints imposed as part of the corrections process. These similarities between the initial and final solutions are not surprising as the differential corrections algorithm employs an update that minimizes the variations from the initial design (i.e., the “minimum-norm” update defined in Section 3.3.2). While the convergence properties of the algorithm depend on many variables, including the numerical implementation strategy, convergence in any corrections scheme is generally more rapid and more consistent with the initial design when the discontinuities (i.e., constraint violations) are initially small; a very discontinuous initial guess forces the differential corrections algorithm to make more significant changes to the design to meet the specified constraints. Thus, by leveraging insights from the CR3BP+LT, an initial design is straightforwardly constructed with minimal discontinuities in both configuration space and in energy that may be rapidly corrected. In contrast to a transfer construction procedure that employs only arcs from the natural CR3BP, these low-thrust dynamical insights supply a preliminary control profile (i.e., α , β , and a_{lt} for the low-thrust segments) that subsequently delivers a suitable transfer geometry and a suitable energy profile.

¹See the Deep Space 1 Asteroid Flyby press kit, https://www.jpl.nasa.gov/news/press_kits/ds1asteroid.pdf

4.4 Low-Thrust Transfer from GTO to P_2

The gateway transit analyses in Sections 4.1 and 4.2 are generalized by leveraging the hyperbolic manifold that is tangent to the center manifold of a gateway equilibrium point. Recall from Section 3.4 that the hyperbolic manifolds associated with *planar* low-thrust periodic orbits (LTPOs) act as separatrices. Accordingly, the hyperbolic manifolds associated with a planar LTPO located within the center manifold of a planar equilibrium point bound all low-thrust-enabled trajectories that transit through the gateway, consistent with the behavior of the ballistic Lyapunov orbit manifolds [73, 74]. Because the low-thrust manifolds exist within a 3D level set, the bounds span a larger set of states than the results obtained by leveraging only the energy plane, as in Section 4.1. The control curve strategy explored in Section 4.2 and energy plane intersection mappings discussed in Section 4.3 are useful tools that may be combined with the geometric and energetic bounds supplied by the LTPO manifolds to construct preliminary designs for transit trajectories.

4.4.1 \mathbb{E}_1 and \mathbb{E}_2 Planar LTPO Stability Properties

As LTPOs exist for a range of α and H_{lt} values, a first step in identifying transit options is an exploration of the stability properties of the LTPOs. Additionally, since the focus of this section is transit through the P_2 region, only LTPOs within the center manifold of the \mathbb{E}_1 and \mathbb{E}_2 equilibrium points are considered. The set of available orbits is further restricted to planar paths with planar low-thrust acceleration vectors to simplify the visualization of the results. These planar orbits, plotted in the familiar α vs. H_{lt} parameter space in Figure 4.17, are bounded by the ZAC energy curves, plotted in gray. Each point, i.e., each (α, H_{lt}) pair, represents a single LTPO with the specified α angle and H_{lt} value. Accordingly, each horizontal and vertical line of colored points represents a family of LTPOs that evolve in α or H_{lt} , respectively, as discussed in Section 3.4.2. This parameter space representation straightforwardly displays the bounds on the LTPOs as the ZACs; each ZAC identifies the H_{lt} value at

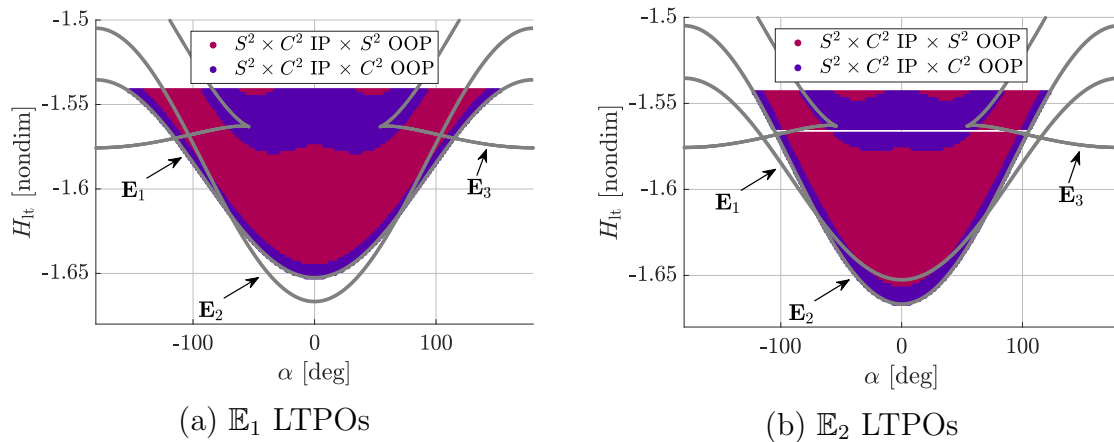


Figure 4.17.: LTPO families within the \mathbb{E}_1 and \mathbb{E}_2 center manifolds in the Earth-Moon CR3BP+LT for $a_{1t} = 7e-2$ and $\beta = 0$ over a variety of α and H_{1t} values; each orbit is colored by its in-plane (IP) and out-of-plane (OOP) stability properties

which the gateway closes for each α angle; at H_{1t} values below a ZAC contour, the gateway is closed and motion is forbidden at or nearby that equilibrium point. Thus, the E_1 and E_2 LTPOs only exist above the \mathbb{E}_1 and \mathbb{E}_2 energy curves. The color of each point in Figure 4.17 denotes the linear stability properties of the corresponding periodic orbit. Similar to the \mathbb{E}_1 and \mathbb{E}_2 structures (in the Earth-Moon system for $\beta = 0$ and $a_{1t} = 7e-2$), the in-plane stability properties (abbreviated as “IP” in the figure legends) of each LTPO are described by the superposition of a 2D saddle (S^2 , i.e., a 2D hyperbolic mode) and a 2D center (C^2). This in-plane C^2 subspace describes the LTPO and the LTPO family (i.e., the center motion associated with the two unit eigenvalues), while the in-plane S^2 subspace contains the planar stable and unstable manifolds. Because this S^2 subspace is common to all of the LTPOs, planar manifolds to guide flow through the $E_1(\alpha)$ and $E_2(\alpha)$ gateways are available for *every* combination of α and H_{1t} values depicted in Figure 4.17. Finally, note that a significant number of the LTPOs include an out-of-plane S^2 subspace, depicted by the red points, but the associated 3D motion is not leveraged in this application.

4.4.2 Transit Through E_1

To illustrate the use of the LTPO hyperbolic manifolds for a low-thrust transit trajectory design, consider a lunar mission with a spacecraft path that originates near the Earth (P_1 in the Earth-Moon CR3BP+LT) with a very low H_{lt} value along a geostationary transit orbit (GTO). The first challenge is increasing the H_{lt} value such that transit through the E_1 gateway is possible. This challenge has been well studied by others [19, 75, 76, 77] and is not explored in detail here. To construct a reasonable set of initial conditions for the transit analysis, a set of trajectories are initialized at apogee on a GTO orbit with a variety of arguments of perigee. For simplicity, the GTO is assumed to be coplanar with the Earth-Moon orbital plane, i.e., the GTO is planar in the CR3BP+LT. Each initial state is propagated in the CR3BP+LT with a thrust magnitude of $f = 7e-2$, an initial mass of $m = 1$, and a specific impulse of $I_{sp} = 3000$ seconds. The low-thrust acceleration vector is aligned with the velocity vector to maximize $dH_{\text{nat}}/d\tau$, resulting in an energy-optimal spiral departing the GTO state. Many other departure options are available (and, perhaps, even more mass-optimal), but this formulation proves sufficient to demonstrate a process that leverages low-thrust to achieve transit through the E_1 gateway to P_2 .

To initiate the transit analysis, states along the spiral with $\dot{x} > 0$ are captured on a hyperplane, Σ_1 , parallel to the yz -plane at $x = -\mu$. Although the spiral arcs are propagated with velocity-pointing thrust vectors, the control strategy may be adjusted at any time to achieve a goal other than escaping Earth's gravity well. A useful alternative is the control strategy that fixes \vec{a}_{lt} in the rotating frame, yielding the autonomous, Hamiltonian system in which H_{lt} is an integral of the motion.

The first requirement for transit through $E_1(\alpha)$ is that the low-thrust arc possesses a low-thrust Hamiltonian value greater than the gateway energy, i.e., $H_{\text{lt}} > H_{\text{lt}}(E_1(\alpha))$. Since H_{lt} remains constant along low-thrust arcs using this fixed- \vec{a}_{lt} strategy, manipulating H_{lt} to an appropriately large value at the Σ_1 map guarantees that the E_1 gateway remains open as long as \vec{a}_{lt} is not modified en route to E_1 . Re-

call that H_{lt} , described in Equation (2.107), is a function of H_{nat} , \vec{r} , and \vec{a}_{lt} . The H_{nat} value cannot be instantaneously changed without an impulsive $\Delta\vec{v}$, and \vec{r} cannot be manipulated. However, the α angle that orients \vec{a}_{lt} may be adjusted to achieve a different H_{lt} value. Accordingly, a control curve (first defined in Section 4.2) is formulated to describe the range of attainable H_{lt} values as a function of α ,

$$\mathcal{U}_i(\alpha) : H_{\text{lt}} = H_{\text{nat},i} - a_{\text{lt}}(x_i \cos \alpha + y_i \sin \alpha), \quad (4.28)$$

where $H_{\text{nat},i}$ is the natural Hamiltonian value at the map crossing,

$$\vec{X}_i = \left\{ x_i \quad y_i \quad 0 \quad \dot{x}_i \quad \dot{y}_i \quad 0 \right\}^T. \quad (4.29)$$

The \vec{X}_i points are filtered by H_{nat} to include only crossings with $-1.6 \leq H_{\text{nat},i} \leq -1.45$, as plotted in Figure 4.18(a). This range generally yields curves that pass

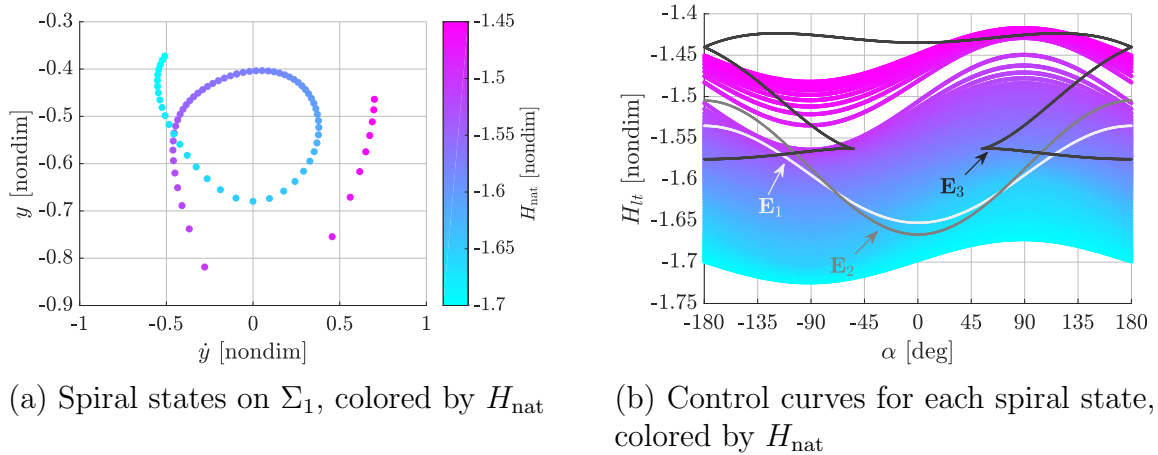


Figure 4.18.: States on energy-optimal spirals from GTO apogee states with various arguments of perigee are captured on the Σ_1 Poincaré map; each point on the map is also represented as a control curve to identify LTPOs that facilitate transit through the E_1 gateway

above the E_1 energy curve depicted in Figure 4.18(b). Some of these control curves, colored cyan to indicate low H_{nat} values, only pass above the E_1 energy curve for a small range of α values. Higher-energy curves, such as those with $H_{\text{nat}} \approx -1.5$,

colored magenta, lie entirely above the \mathbb{E}_1 energy curve, indicating that any α value is available to orient \vec{a}_{lt} while maintaining an open E_1 gateway.

While the control curves in Figure 4.18(b) provide energy information to guide the transit design, additional geometric information is required; an H_{lt} value above the E_1 gateway energy is a necessary condition for transit, but is not sufficient. Recall that the manifolds associated with an LTPO, one located in a gateway, bound transit motion through the gateway. Thus, to transit the E_1 gateway, a \vec{X}_i point must lie *inside* a stable manifold associated with an E_1 LTPO, $\Gamma_1(\alpha, H_{\text{lt}})$. (The β parameter is omitted from the notation here as this analysis is restricted to planar motion.) Such a stable manifold, \mathcal{W}_1^{s-} , plotted in Figure 4.19, asymptotically approaches the E_1 LTPO, $\Gamma_1(76.36^\circ, -1.604)$, from the negative \hat{x} -direction. All arcs that pass through

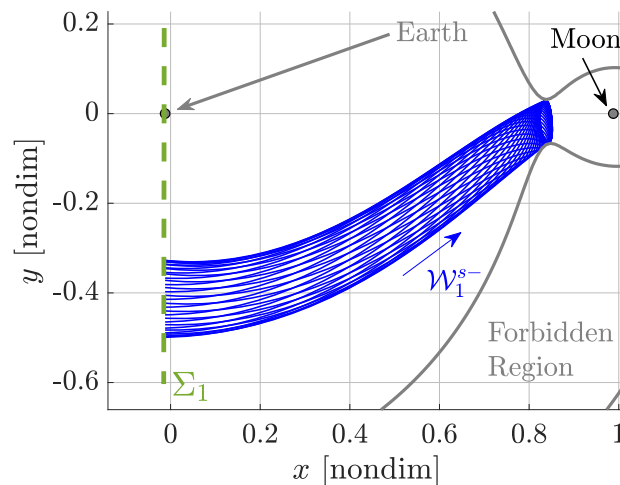


Figure 4.19.: Stable manifold approaching the Earth-Moon $\Gamma_1(76.36^\circ, -1.604)$ orbit

the E_1 gateway with $a_{\text{lt}} = 7\text{e-}2$, $\alpha = 76.36^\circ$ and $H_{\text{lt}} = -1.604$ are bounded by \mathcal{W}_1^{s-} . Thus, the next step is to determine the spiral trajectory map states that lie within \mathcal{W}_1^{s-} .

To identify an intersection between a spiral trajectory map crossing, \vec{X}_i , and \mathcal{W}_1^{s-} , the points on the \mathcal{U}_i control curve are employed. For α values that yield $\mathcal{U}_i(\alpha) \geq H_{\text{lt}}(E_1(\alpha))$, the $\Gamma_1(\alpha, \mathcal{U}_i(\alpha))$ orbit is constructed and the associated \mathcal{W}_1^{s-} manifold is propagated to the Σ_1 hyperplane for comparison with \vec{X}_i . The hyperplane

fixes the x -coordinate, with three variables (y_i , \dot{x}_i , and \dot{y}_i) remaining for representation on the map. Because the H_{lt} value associated with the spiral trajectory state, \vec{X}_i , may be manipulated by changing α at the Σ hyperplane (as represented by \mathcal{U}_i), the Hamiltonian is leveraged to further reduce the number of free variables to two. The velocity magnitude is extracted from H_{lt} by solving Equation (2.104). Thus, the remaining free variables, y_i and $\theta_{v,i} = \arctan(\dot{y}_i/\dot{x}_i)$, are visualized via the tube topology transformation defined in Section 3.4.1. Polar coordinates are employed to avoid discrete jumps of 360° in θ_v , and the y -coordinate is scaled by the geometry of the low-thrust forbidden region to yield a radius,

$$\tilde{d} = \frac{y - \tilde{y}_\ell}{\tilde{y}_u - \tilde{y}_\ell}, \quad (4.30)$$

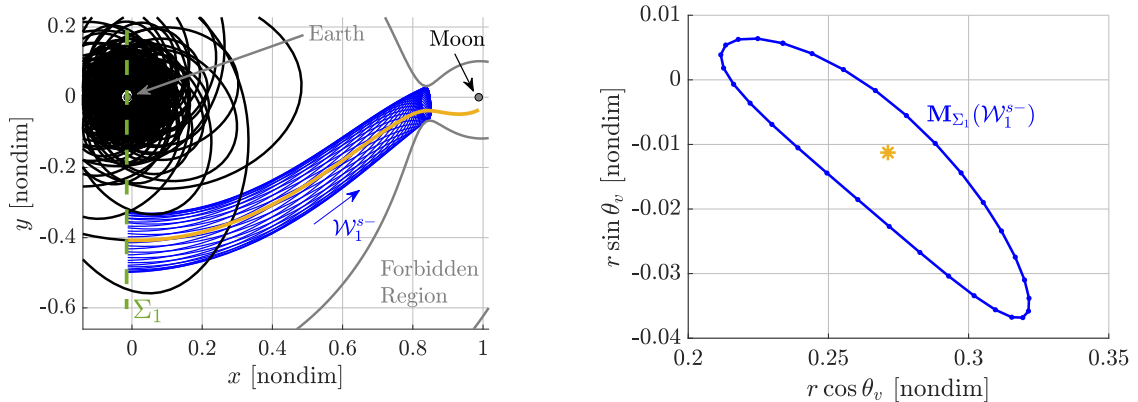
where \tilde{y}_u and \tilde{y}_ℓ are the y -values of the forbidden region boundaries closest to the \hat{x} -axis at Σ_1 , as illustrated in Figure 4.23(a). Note that this radial coordinate is modified slightly from d defined in Equation (3.92); this \tilde{d} is measured relative to \tilde{y}_ℓ while d is measured from \tilde{y}_u . The topological transformation is qualitatively similar, but the upper and lower ZVC bounds are represented differently; in this \tilde{d} definition, the upper ZVC bound is located at $\tilde{d} = 1$ and the lower ZVC bound corresponds to $\tilde{d} = 0$. Combine the tube topology representation with the Poincaré mapping via the operator,

$$\mathbb{M}_{\Sigma_1}^p(\mathcal{W}) := \mathcal{W} \xrightarrow[\tilde{d}, \theta_v]{\tilde{r}, \tilde{v}} \mathbb{M}_{\Sigma_1}^p(\mathcal{W}), \quad (4.31)$$

where \mathcal{W} is a manifold (this mapping also applies to single states like \vec{X}_i), and p represents the p^{th} map iteration. (If the p superscript is omitted, $p = 1$ is implied.) Equivalently, $\mathbb{M}_{\Sigma}^p(\mathcal{W})$ captures the p^{th} return of \mathcal{W} to Σ and incorporates a two-dimensional representation of \mathcal{W} in the tube topology.

Once the spiral trajectory map crossing, \vec{X}_i , and the manifold, \mathcal{W}_1^{s-} , are represented in the tube topology on Σ_1 , identifying a transit arc is straightforward. If $\mathbb{M}_{\Sigma_1}(\vec{X}_i)$ is encircled by $\mathbb{M}_{\Sigma_1}(\mathcal{W}_1^{s-})$, the low-thrust trajectory propagated from \vec{X}_i with the selected α angle remains bounded by \mathcal{W}_1^{s-} and the trajectory passes through

the E_1 gateway. An example of this behavior is illustrated in Figure 4.20, with the spiral trajectory plotted in black, \mathcal{W}_1^{s-} plotted in blue, and the transit arc plotted in yellow. Note that this example represents one possible α and H_{lt} combination on \mathcal{U}_i ;



(a) The spiral trajectory (black) and manifold (blue) interface at the Σ_1 hyperplane

(b) Tube topology representation of the manifold (blue) and transit arc (yellow asterisk)

Figure 4.20.: A transit arc (yellow) is identified within \mathcal{W}_1^{s-} at the Σ_1 map in the Earth-Moon CR3BP+LT for $a_{\text{lt}} = 7\text{e-}2$, $\alpha = -76.36^\circ$, and $H_{\text{lt}} = -1.604$

additional points along \mathcal{U}_i must be compared to LTPOs characterized by consistent α and H_{lt} values. Accordingly, to evaluate the transit possibilities for the entire set of spiral trajectories represented in Figure 4.18(a), a control curve is constructed for each \vec{X}_i , and points along that curve are compared to a matching \mathcal{W}_1^{s-} manifold. The result of this search, visualized in Figure 4.21, identifies α values for each \vec{X}_i that will deliver the spacecraft through the $E_1(\alpha)$ gateway. In this energy-space representation, each sinusoidal curve is a control curve, \mathcal{U}_i , linked to a distinct four-dimensional map state, \vec{X}_i . Many of these curves are colored black for all α values, indicating that the associated \vec{X}_i point cannot be adjusted to be within a stable manifold that delivers the spacecraft to the P_2 region. However, a subset of the control curves do include feasible transit options, plotted in green. Each of these points represents an arc that originates from the associated \vec{X}_i state and, when propagated with the specified α value, transits the E_1 gateway. A comparison of the feasible transfer options between

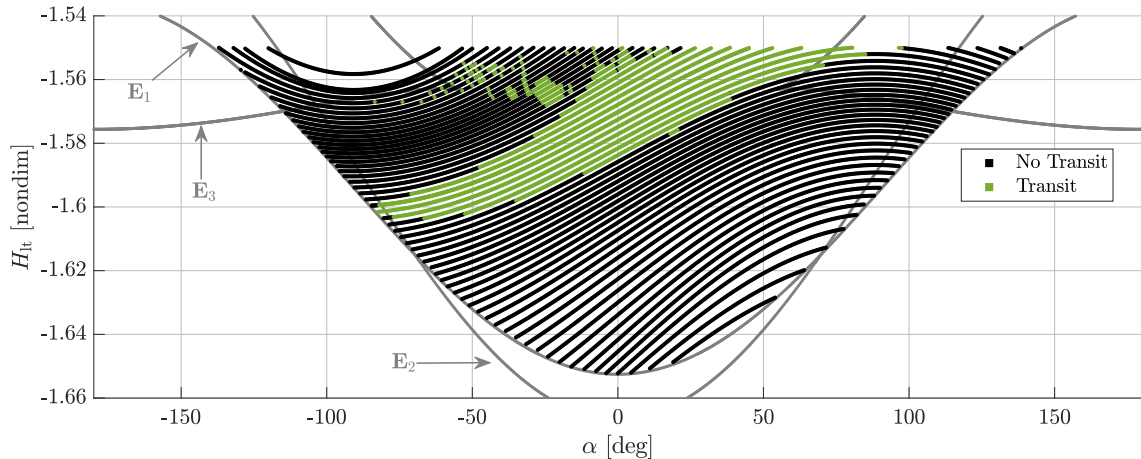


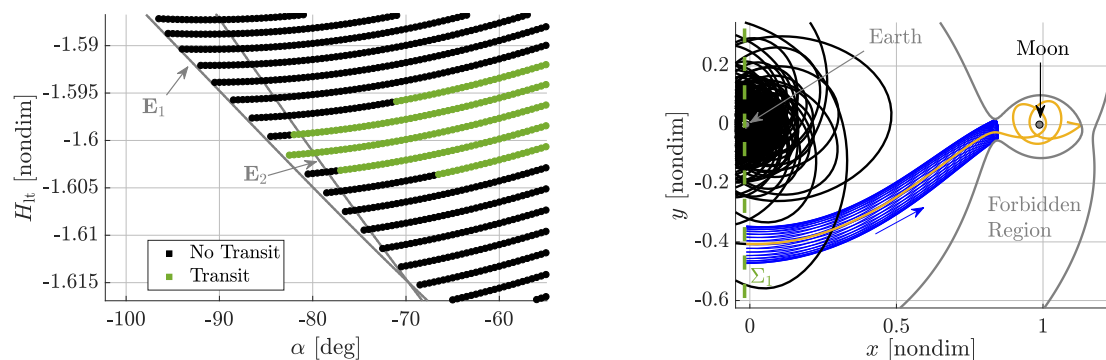
Figure 4.21.: Sinusoidal control curves colored by their ability to transit the E_1 gateway; only a subset of the curves, and a subset of the α values on those curves, successfully deliver a transit arc.

Figures 4.18(b) and 4.21 demonstrates that the number of transit options is greatly reduced when geometry is considered in addition to energy. However, recall that this analysis leverages only one set of initial conditions: energy-optimal spirals that originate at apogee on a GTO. Many other options exist to deliver a spacecraft from a low-energy state near the Earth to higher-energy states capable of reaching the Moon; this analysis can be applied to any such scheme. Additionally, these strategies may be reversed to identify regions to be used as targets for Earth-departing trajectories that enable transit.

4.4.3 Capture: Avoiding Transit Through E_2

For many space missions, capture near P_2 , e.g., the Moon in the Earth-Moon system, is desirable. Originating from the system interior, one strategy to capture near P_2 and avoid transit through the E_2 gateway is to select an α and H_{lt} configuration that lies below the E_2 energy curve. As a result, the E_2 gateway remains closed as the spacecraft moves along the low-thrust arc into the P_2 region. Consider the configurations plotted in green in Figure 4.21 (reproduced in Figure 4.22(a)) that adjust

the CR3BP+LT dynamics to allow a spacecraft to transition from the energy-optimal spiral to an arc that transits the E_1 gateway: the majority of these configurations are located above the \mathbb{E}_2 energy curve, but a small number near $\alpha = -90^\circ$ and $H_{lt} = -1.6$ are located below the \mathbb{E}_2 energy curve. Selecting one of these configurations yields a transfer that cannot continue through the E_2 gateway. For example, selecting $\alpha = -80.86^\circ$ at Σ_1 results in a trajectory with $H_{lt} = -1.602$, plotted in yellow in Figure 4.22(b), that cannot escape through E_2 as the gateway is closed. Alternatively, the control curve strategy detailed in Section 4.2 may be employed to



(a) A detailed view of transit options below the \mathbb{E}_2 energy curve

(b) Selecting $\alpha = -80.86^\circ$ at Σ_1 yields an arc with $H_{lt} = -1.602$ that transits E_1 but not E_2

Figure 4.22.: A trajectory that captures near the Moon in the Earth-Moon CR3BP+LT for $a_{lt} = 7e-2$

identify a suitable location near P_2 where the α angle can be adjusted to close one or both of the gateways. Another strategy, discussed in the next section, leverages the hyperbolic manifolds associated with an E_2 LTPO to further differentiate between trajectories that transit through or remain within the P_2 region.

4.5 P_2 Region Transit Through Intersecting LTPO Manifolds

Similar to the exploration of low-thrust trajectories that transit through the E_1 gateway in the previous section, this section investigates flow throughout the P_2

region by leveraging the E_1 and E_2 low-thrust periodic orbit (LTPO) hyperbolic manifold separatrices. Once a spacecraft has passed through the E_1 gateway, a new challenge emerges: navigating the nonlinear dynamics of the P_2 region. An additional passage through the E_2 gateway constitutes a transit of the P_2 region, while arcs that remain near P_2 are denoted as “captured,” at least for some finite time. As captured trajectories are merely those that do not transit, both possibilities are explored via the same analyses. The strategies employed to navigate the P_2 region are similar to those previously discussed, but include additional algorithmic complexity to compensate for the nonlinearities near P_2 .

4.5.1 A Strategy for Transit Detection

Just as all arcs that originate in the system interior and pass through the E_1 gateway are bounded by \mathcal{W}_1^{s-} , arcs that continue through the gateway into the P_2 region are bounded by unstable manifold, \mathcal{W}_1^{u+} . Similarly, trajectories that reach the system exterior via the E_2 gateway are bounded by \mathcal{W}_2^{s-} . Recall that Γ_1 and Γ_2 orbits possess these manifolds for all α and H_{lt} values of interest, as illustrated by the existence of a saddle mode for every orbit in Figure 4.17. Accordingly, every combination of α and H_{lt} that lies above the \mathbb{E}_1 and \mathbb{E}_2 energy curves may permit transit through the P_2 region as the necessary manifolds exist and the H_{lt} value guarantees that both gateways are open. However, similar to the E_1 transit scenario described in the previous section, geometry must also be considered. A trajectory that passes through both gateways must be bounded by \mathcal{W}_1^{u+} and by \mathcal{W}_2^{s-} . To illustrate the process of locating transit arcs, consider a scenario in the Earth-Moon CR3BP+LT with $a_{\text{lt}} = 7\text{e-}2$, an α value of -76.5° , and $H_{\text{lt}} = -1.604$. Consistent with the previous section, the planar dynamics ($z = \dot{z} = 0, \beta = 0$) are considered; thus, β is omitted from the notation for brevity. The E_1 LTPO, $\Gamma_1(-76.5^\circ, -1.604)$ (plotted in purple in Figure 4.23(a)), and the associated stable manifold, \mathcal{W}_1^{s-} (plotted in red) bound motion that flows through E_1 toward the Moon. Similarly, $\Gamma_2(-76.5^\circ, -1.604)$

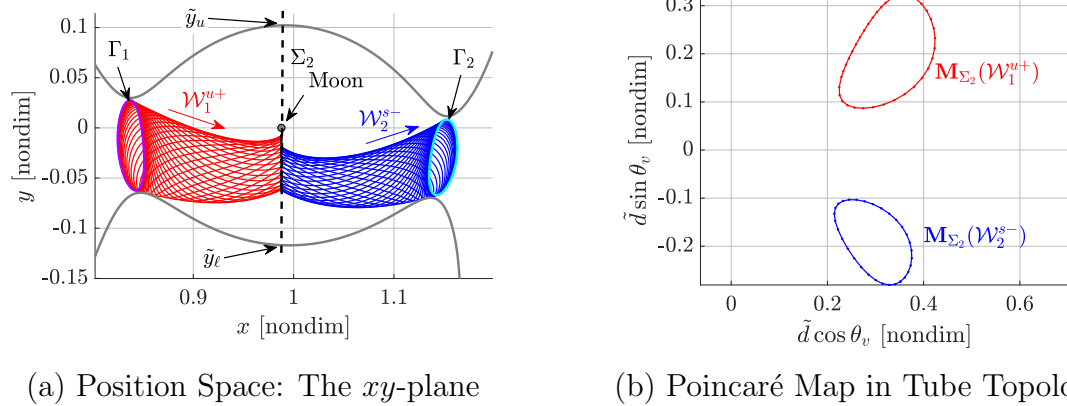


Figure 4.23.: Unstable (red) and stable (blue) manifolds are propagated from $\Gamma_1(-76.5^\circ, -1.604)$ and $\Gamma_2(-76.5^\circ, -1.604)$ LTPOs in the Earth-Moon CR3BP+LT with $a_{1t} = 7e-2$ to the Σ_2 hyperplane at $x = 1 - \mu$.

(plotted in cyan in Figure 4.23(a)) and the associated \mathcal{W}_2^{s-} manifold (plotted in blue), bound arcs that flow through the E_2 gateway to the system exterior. A new hyperplane, Σ_2 , located at $x = 1 - \mu$ and plotted as a black, dashed line, is employed to compare the manifolds. Because both manifolds are characterized by the same α and H_{1t} values, the manifolds are reduced to two dimensions and represented in the tube topology via the same process outlined in the previous section. The usefulness of this mapping, represented by the \mathbb{M}_{Σ_2} operator, is clear when comparing the two manifold representations. While the \mathcal{W}_1^{u+} and \mathcal{W}_2^{s-} manifolds may seem to intersect in position space at Σ_2 in Figure 4.23(a), this xy -projection of the manifolds does not include velocity information. The separation between the two structures is obvious when the mapping is applied, as plotted in Figure 4.23(b): the $\mathbb{M}_{\Sigma_2}(\mathcal{W}_1^{u+})$ and $\mathbb{M}_{\Sigma_2}(\mathcal{W}_2^{s-})$ curves do not intersect.

While there is no intersection at the first map iteration of the two manifolds, propagating for additional returns may yield intersections. For example, when the map is iterated twice more, as plotted in Figure 4.24, an intersection occurs between $\mathbb{M}_{\Sigma_2}^3(\mathcal{W}_1^{u+})$ and $\mathbb{M}_{\Sigma_2}^3(\mathcal{W}_2^{s-})$. This change underscores an important caveat to the intersection analyses: a lack of intersections between manifolds does not support a

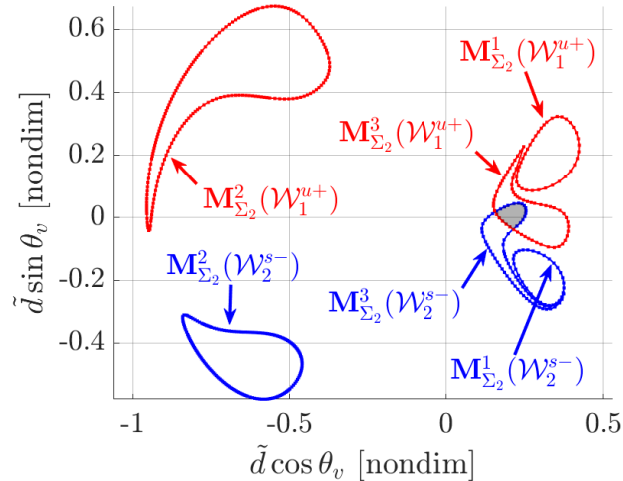
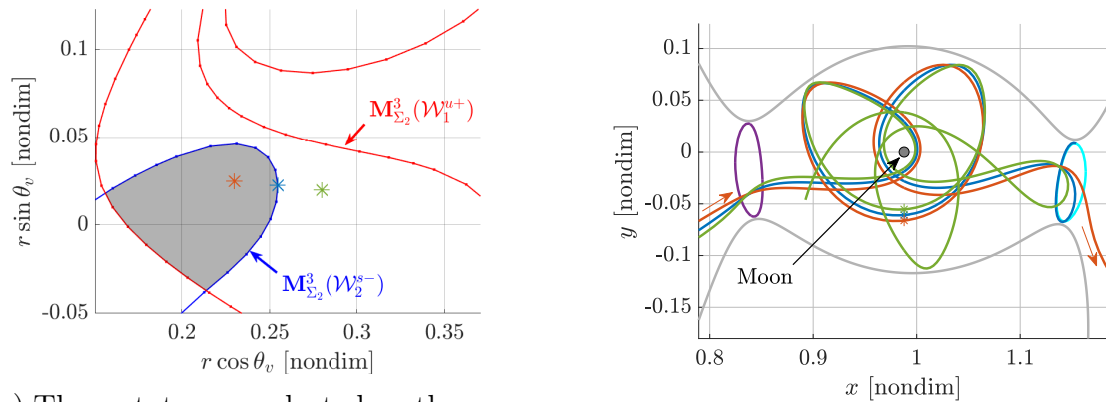


Figure 4.24.: Three iterations of the map, represented in tube topology, capture unstable (red) and stable (blue) manifolds in the Earth-Moon CR3BP+LT with $a_{\text{lt}} = 7e-2$, $\alpha = -76.5^\circ$, and $H_{\text{lt}} = -1.604$

conclusion that no transit motion exists. While the results plotted in Figure 4.23(b) may lead to a claim that transit is not possible with the given a_{lt} , α , and H_{lt} combination, it is clear an intersection does exist when additional map iterations are included. Only a few specific insights are available from the maps in Figures 4.23(b) and 4.24. First, arcs within the intersection regions, such as the point marked by an orange asterisk in Figure 4.25(a), are guaranteed to transit the P_2 region in the time prescribed by the manifolds bounding the arc. Since this arc is bounded by the third map iteration of each manifold, the trajectory, plotted in orange in Figure 4.25(b), includes five crossings through the Σ_2 hyperplane: three crossings for each manifold, with one shared between the manifolds. A second guarantee is that arcs along a manifold, such as the blue asterisk on $\mathbb{M}_{\Sigma_2}^3(\mathcal{W}_2^{s-})$ in Figure 4.25(a), will remain on the manifold and will asymptotically approach the associated periodic orbit. Because a portion of $\mathbb{M}_{\Sigma_2}^3(\mathcal{W}_2^{s-})$ lies within $\mathbb{M}_{\Sigma_2}^3(\mathcal{W}_1^{u+})$, arcs from the system interior (e.g., the blue trajectory plotted in Figure 4.25(b) that is associated with the blue asterisk map state) may transit the E_1 gateway within \mathcal{W}_1^{u+} and also reach Γ_2 . In essence, this scenario represents a capture as the spacecraft remains on Γ_2 , near P_2 , as long as the α angle is maintained. Finally, some insights regarding non-transit motion is



(a) Three states are selected on the map within the third map iterations of one or both of the manifolds (zoomed-in view of Figure 4.24)

(b) The trajectories that result from the selected map states; the map states are again located by asterisks

Figure 4.25.: A transit trajectory (orange), a trajectory to Γ_2 (blue), and a captured trajectory (green) in the Earth-Moon CR3BP+LT with $a_{lt} = 7e-2$, $\alpha = -76.5^\circ$ and $H_{lt} = -1.604$

also available from the map. Consider a state within \mathcal{W}_1^{u+} (capable of transit into the P_2 region via the E_1 gateway) but not within \mathcal{W}_2^{s-} , such as the state located by the green asterisk in Figure 4.25(a). The corresponding trajectory cannot pass through the E_2 gateway before crossing Σ_2 at least twice, i.e., the trajectory may pass through the E_2 gateway after crossing Σ_2 three or more times. Additionally, the trajectory may return to the system interior via the E_1 gateway if the green asterisk lies within any mappings of \mathcal{W}_1^{s+} (not included in the plots). This non-transit path, plotted in green in Figure 4.25(b), crosses Σ_2 five times after passing through $M_{\Sigma_2}^3(\mathcal{W}_2^{s-})$ and additional crossings of Σ_2 may occur if propagated for a longer interval.

While the overall behavior of the three arcs depicted in Figure 4.25 are very different, the initial conditions that are selected from the map are located very close to one another. Each arc originates on Σ_2 with a similar θ_v angle and slightly different \tilde{d} values (that translate to different y values). When propagated in reverse time, these states yield arcs that remain near one another and pass through the E_1 gateway. When propagated in forward time, the arcs maintain similar geometries until they

reach Γ_2 , plotted in cyan in Figure 4.25(b). At this point, the red arc passes through the gateway, the blue arc asymptotically approaches Γ_2 , and the green arc returns toward P_2 . Without the manifolds to differentiate these chaotic behaviors, the path of each arc is difficult to predict. Additionally, the same techniques may be leveraged in other applications, such as the identification heteroclinic connections between the two LTPOs [78], or the determination of arcs that do not transit either gateway. Clearly, the manifolds associated with the gateway LTPOs serve as useful structures to differentiate many types of motion.

4.5.2 Global Transit Search

To determine the combinations of α and H_{lt} that permit transit, as well as the details of each transit opportunity, the process of identifying intersections between manifolds is automated to evaluate the criteria over the grid of α and H_{lt} values that satisfy the gateway energy constraints. For each combination:

1. Compute the low-thrust periodic orbits, $\Gamma_1(\alpha, H_{\text{lt}})$ and $\Gamma_2(\alpha, H_{\text{lt}})$.
2. Construct an initial representation of \mathcal{W}_1^{u+} and \mathcal{W}_2^{s-} with a small number of arcs (31 are used per orbit to minimize the computation time) and iterate the map n times, yielding the mappings $\mathbb{M}_{\Sigma_2}^p(\mathcal{W}_1^{u+})$ and $\mathbb{M}_{\Sigma_2}^p(\mathcal{W}_2^{s-})$ for $p = 1, 2, \dots, n$. Note that, at some combinations of α and H_{lt} , a subset of the arcs along a manifold may not reach a map return; some escape through one of the gateways, while others reach the P_2 singularity, defined here as a state with $r_{23} < 5\text{e-}3$ nondimensional units, or approximately 192 km in the Earth-Moon system. These arcs are excluded from the map iterations following the escape or impact “event” to avoid excessively long propagation times.
3. Fill “gaps” in each mapping, $\mathbb{M}_{\Sigma_2}^p(\mathcal{W})$. Gaps may occur when arcs on the manifold fail to reach the map, as described in the previous step. Gaps also occur due to the nonlinear dynamics in the CR3BP+LT. For example, while all of the arcs representing \mathcal{W} may reach the map, they may not be uniformly

distributed across the range of \tilde{d} and θ_v values. Large inter-arc differences in \tilde{d} or θ_v (θ_v almost always reflects the most uneven coverage) at Σ_2 can result in large distances between points on $\mathbb{M}_{\Sigma_2}^p(\mathcal{W})$. Gaps are filled via two techniques:

- a. *Discrete Fourier Series.* The y , \dot{x} , and \dot{y} states that are used to construct $\mathbb{M}_{\Sigma_2}^p(\mathcal{W})$ are approximated via discrete Fourier series. (This choice of variables produces a more accurate approximation of $\mathbb{M}_{\Sigma_2}^p(\mathcal{W})$ than fitting the series directly to \tilde{d} and θ_v .) This Fourier scheme is only applied when $\mathbb{M}_{\Sigma_2}^p(\mathcal{W})$ is uniformly sampled in τ (the time-of-flight along Γ from $\tau = 0$ to the manifold arc “step-off” point), i.e., when all the arcs representing \mathcal{W} reach the map. The Fourier representations of y , \dot{x} , and \dot{y} states are transformed into the tube topology and compared to the data points on $\mathbb{M}_{\Sigma_2}^p(\mathcal{W})$. If the error between the Fourier representation and the true manifold states exceeds a certain threshold, the Fourier representation is abandoned in favor of the second strategy. If the error in the approximation remains within the desired limits, points are selected from the Fourier approximations to minimize the maximum inter-point distance along $\mathbb{M}_{\Sigma_2}^p(\mathcal{W})$.
- b. *Interpolation and Propagation.* When $\mathbb{M}_{\Sigma_2}^p(\mathcal{W})$ is not uniformly sampled in τ , or when the Fourier series fail to accurately approximate $\mathbb{M}_{\Sigma_2}^p(\mathcal{W})$, additional points on $\mathbb{M}_{\Sigma_2}^p(\mathcal{W})$ are computed by propagating arcs from the originating periodic orbit, Γ , to the p^{th} map iteration. Points along Γ are selected between the τ values associated with the manifold arcs that bound large gaps on $\mathbb{M}_{\Sigma_2}^p(\mathcal{W})$. These initial conditions are then propagated and included in $\mathbb{M}_{\Sigma_2}^p(\mathcal{W})$ (assuming the arcs do not escape or impact P_2 before reaching the map). Gaps in $\mathbb{M}_{\Sigma_2}^p(\mathcal{W})$ are iteratively filled until all gaps are smaller than some tolerance, or until a maximum number of iterations occurs.

If the gaps in $\mathbb{M}_{\Sigma_2}^p(\mathcal{W})$ cannot be filled, the p^{th} map iteration is abandoned and not incorporated in subsequent steps. This failure occurs most frequently at higher H_{lt} values where manifold arcs are more likely to escape or impact.

4. Compute intersecting regions between two manifold mappings, $\mathbb{M}_{\Sigma_2}^p(\mathcal{W}_1^{u+})$ and $\mathbb{M}_{\Sigma_2}^k(\mathcal{W}_2^{s-})$. If intersections exist, the bounds of the region, denoted $\mathbb{A}^{p,k}$, are extracted for further analysis.

Following the completion of these steps for the gridded α and H_{lt} values, several properties of the data are investigated.

As a first exploration of the transit options between E_1 and E_2 in the Earth-Moon CR3BP+LT with $a_{\text{lt}} = 7\text{e-}2$, consider a binary measure of “transitability.” The p^{th} iteration of $\mathbb{M}_{\Sigma_2}(\mathcal{W}_1^{u+})$ is compared with $\mathbb{M}_{\Sigma_2}^k(\mathcal{W}_2^{s-})$ for $k = 1, \dots, n$. The smallest k for which an intersection between manifolds occurs is captured and plotted for $p = 1, 2$, and 3 in Figure 4.26. Accordingly, each plot in the figure depicts the most

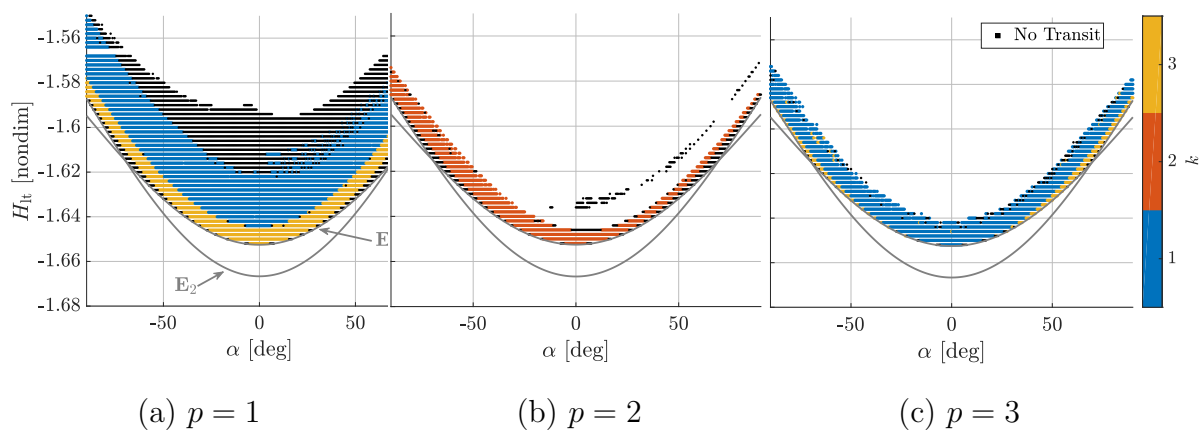


Figure 4.26.: Earliest intersections of $\mathbb{M}_{\Sigma_2}^p(\mathcal{W}_1^{u+})$ by $\mathbb{M}_{\Sigma_2}^k(\mathcal{W}_2^{s-})$

rapid (in terms of map iterations) transit opportunities for arcs within \mathcal{W}_1^{u+} at each of the three map iterations. Black points indicate that no intersections exist between $\mathbb{M}_{\Sigma_2}^p(\mathcal{W}_1^{u+})$ and $\mathbb{M}_{\Sigma_2}^k(\mathcal{W}_2^{s-})$ for $k = 1, 2$, or 3. Empty space in each plot represents combinations of α and H_{lt} that cannot be analyzed, including areas above and below the \mathbb{E}_1 and \mathbb{E}_2 energy curves. Points below the energy curves do not possess H_{lt}

values that are sufficiently high to open both gateways and are discarded from the search. However, the automated search considers all points above the curves, and the remaining empty regions are discarded due to failures to fill gaps in the mappings during step 3 of the algorithm outlined above. The forbidden region geometries associated with these difficult combinations of α and H_{lt} frequently include wide gateways, thus, the arcs on the two manifolds are more likely to escape, particularly after the first map iteration. Additionally, many arcs along these manifolds pass near the P_2 singularity and, subsequently, are discarded. The combinations of α and H_{lt} most straightforwardly analyzed are those located near the \mathbb{E}_1 and \mathbb{E}_2 energy curves. These combinations are linked to geometries defined by the forbidden region boundaries with relatively narrow gateways; these dynamics yield manifolds that cross Σ_2 several times.

To understand the results in Figure 4.26, consider the transit example identified by the red arc in Figure 4.25(a) with $\alpha = -76.5^\circ$ and $H_{\text{lt}} = -1.604$. In energy space, this trajectory is located very near the \mathbb{E}_2 energy curve, above and to the left of the intersection between the \mathbb{E}_1 and \mathbb{E}_2 curves. The mappings in Figure 4.24 demonstrate that the only manifold intersection for this configuration (for $p, k \leq 3$) occurs at $p = k = 3$. Thus, the α and H_{lt} combination is located in a black, no-transit, region in Figures 4.26(a) and 4.26(b) as neither $\mathbb{M}_{\Sigma_2}^1(\mathcal{W}_1^{u+})$ nor $\mathbb{M}_{\Sigma_2}^2(\mathcal{W}_1^{u+})$ intersects any of the \mathcal{W}_2^{s-} map iterations. However, the corresponding region in Figure 4.26(c) is colored yellow to indicate that $\mathbb{M}_{\Sigma_2}^3(\mathcal{W}_1^{u+})$ includes an intersection with $\mathbb{M}_{\Sigma_2}^k(\mathcal{W}_2^{s-})$ for $k = 3$. Many of the points near the bounding \mathbb{E}_1 and \mathbb{E}_2 energy curves are characterized by similar trends: the first transit opportunity for these α and H_{lt} configurations occurs only after three map iterations of each manifold. However, for configurations slightly further from the two energy curves, intersections occur earlier, yielding a smaller number of map iterations for those transits. For example, the yellow band in Figure 4.26(a) identifies α and H_{lt} configurations for which the first transit opportunity at $\mathbb{M}_{\Sigma_2}^1(\mathcal{W}_1^{u+})$ occurs with $\mathbb{M}_{\Sigma_2}^3(\mathcal{W}_2^{s-})$. As this sequence links the $p = 1$ map iteration and the $k = 3$ iteration, the total number of map iterations to

complete the transit is $p + k - 1 = 3$, whereas the red trajectory from Figure 4.25(b) crosses Σ_2 five times.

The number of map iterations required to complete a transit is directly linked to the minimum time-of-flight (TOF) for the transit. A TOF metric for an intersection area, $\mathbb{A}^{p,q}$ is computed by averaging the TOF for the arcs on $\mathbb{M}_{\Sigma_2}^p(\mathcal{W}_1^{u+})$ and $\mathbb{M}_{\Sigma_2}^k(\mathcal{W}_2^{s-})$ that bound $\mathbb{A}^{p,k}$ and then summing the two averages. Although these minimum TOFs for each intersection, plotted in Figure 4.27, do not necessarily supply an accurate measure of the true TOF along any arc in $\mathbb{A}^{p,q}$, this approximation does facilitate comparisons between various α and H_{lt} combinations. For instance,

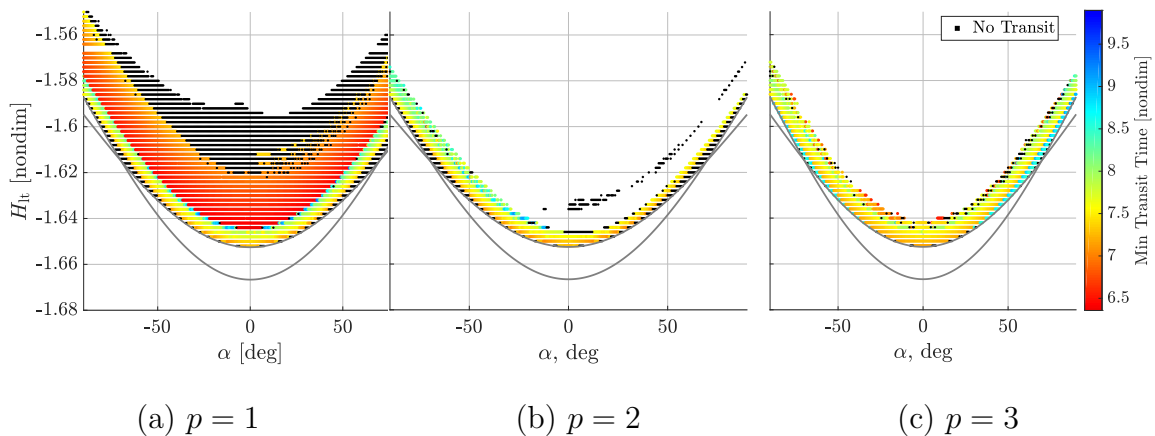


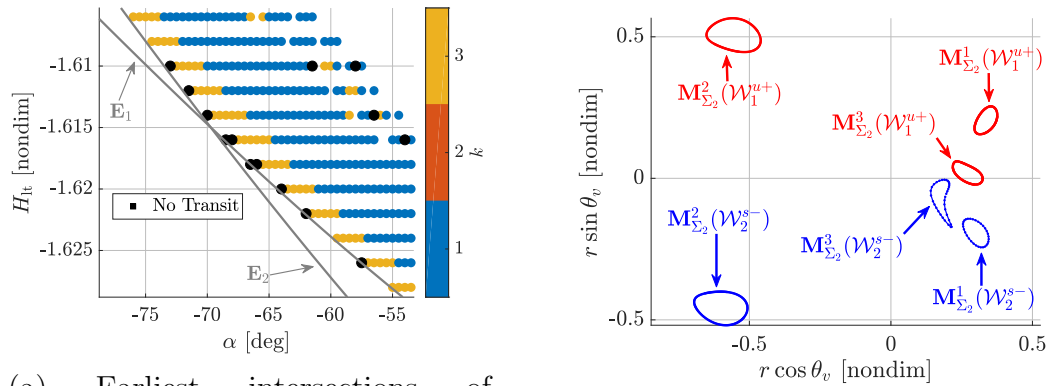
Figure 4.27.: Minimum times-of-flight for intersections between $\mathbb{M}_{\Sigma_2}^p(\mathcal{W}_1^{u+})$ and $\mathbb{M}_{\Sigma_2}^k(\mathcal{W}_2^{s-})$ for $k = 1, 2$, and 3

the yellow ($p = 1, k = 3$) region in Figure 4.26(a), when mapped to the same α and H_{lt} values in Figure 4.27(a), corresponds to TOFs between 7.0 and 8.0 nondimensional time units (about 30-35 days in the Earth-Moon system). Similarly, the yellow ($p = 3, k = 3$) region in Figure 4.26(c) corresponds to TOFs in Figure 4.27(c) between 8.5 and 9.0 (about 37-40 days). These TOFs are consistent with the TOFs for the red ($p = 2, k = 2$) region in Figure 4.26(b) as well as with the TOFs for the blue ($p = 3, q = 1$) region in Figure 4.26(c). This result is expected given that the total number of map iterations during the transit, $p + q - 1$, is identical for all three of these regions. Thus, it is consistent that the shortest times-of-flight are associated

with the $(p = 1, k = 1)$ region in Figure 4.26(a); the minimum TOF for this region is below 6.5 nondimensional time units, or less than 28 days. In summary, a diverse selection of transit options are available by locating intersections between the hyperbolic manifolds of E_1 and E_2 orbits. Transit arcs are most frequently available for H_{lt} values close to the bounding \mathbb{E}_1 and \mathbb{E}_2 energy curves.

4.5.3 Capture Within Non-Intersecting Manifolds

Recall that one strategy to prohibit transit, presented in Section 4.4.3, employs an (α, H_{lt}) pair located below the \mathbb{E}_2 energy curve; a more general configuration with both the E_1 and E_2 gateways open is available by inspecting the manifold intersections (or lack thereof). For instance, the results in Figure 4.26 include regions of black, non-transit options located very near the \mathbb{E}_1 energy curve where the \mathbb{E}_1 and \mathbb{E}_2 energy curves intersect. These regions are large and visible at the scale depicted in Figures 4.26(a) and 4.26(b), but are very small in Figure 4.26(c). These latter results for $p = 3$, reproduced at a larger scale in Figure 4.28(a), also include a set of non-transit options, colored black, near the intersection of the two energy curves. Selecting one of these configurations yields a map with no intersections between manifold mappings, as depicted in Figure 4.28(b) for $\alpha = 70^\circ$ and $H_{\text{lt}} = -1.614$. Thus, an arc that passes through the E_1 gateway, i.e., through the red \mathcal{W}_1^{u+} mappings, will not exit through the E_2 gateway for the given number of map iterations (in this case, three). Although both of these strategies supply only a limited number of options to avoid transiting E_2 , this limitation may benefit the design process by narrowing the number of control parameters. Another strategy to avoid transit through the E_2 gateway is to select states from within the $\mathbb{M}_{\Sigma_2}^p(\mathcal{W}_1^{u+})$ for the maximum value of p that are not located within one of the $\mathbb{M}_{\Sigma_2}^k(\mathcal{W}_2^{s-})$ contours, such as the green arc plotted in Figure 4.25. Finally, the control curve method described in Section 4.2 offers yet another option to manipulate the gateway geometry and capture a trajectory in the P_2 region.



(a) Earliest intersections of $M_{\Sigma_2}^3(\mathcal{W}_1^{u+})$ by $M_{\Sigma_2}^k(\mathcal{W}_2^{s-})$; Some configurations, marked by black dots, do not include transit options for $k = 1, 2, \text{ or } 3$

(b) The $M_{\Sigma_2}^p(\mathcal{W}_1^{u+})$ (red) and $M_{\Sigma_2}^p(\mathcal{W}_2^{s-})$ (blue) manifolds do not intersect for $p = 1, 2, \text{ or } 3$ with $\alpha = 70^\circ$ and $H_{\text{lt}} = -1.614$

Figure 4.28.: Although both the E_1 and E_2 gateways are open, some α and H_{lt} configurations do not include transit options in the Earth-Moon CR3BP+LT for $a_{\text{lt}} = 7e-2$

While the E_1 and E_2 hyperbolic manifolds reveal a plethora of transit options through the P_2 region, manifold intersections are most readily available for only a small range of H_{lt} values. As visualized in Figure 4.26, the algorithm employed in this section struggles to locate manifold intersections with the H_{lt} value corresponding to a particular α angle is significantly larger than the $H_{\text{lt}}(E_1(\alpha))$ and $H_{\text{lt}}(E_2(\alpha))$ values due to the more chaotic manifold geometries apparent at such energies. Accordingly, additional strategies, discussed in the next section, are employed to identify “high-energy” arcs that capture in the P_2 region by leveraging a low-thrust force.

4.6 Strategies for High-Energy Capture

When the properties of periodic orbits and their manifolds are unavailable (either because they are difficult to compute, unknown, or because the system is non-autonomous), Poincaré maps may be employed to explore the system. As noted in the previous section, low-thrust periodic orbit (LTPO) manifolds are most readily

available to guide transit trajectories when the H_{lt} value along a trajectory is near the E_1 and E_2 gateway energies. In other words, the LTPO manifolds are most useful to design low-energy transit and capture itineraries. In this section, two strategies to design *high*-energy, low-thrust lunar capture trajectories are explored. The first scheme leverages a low-thrust apsis map to identify points in the lunar region at a high H_{nat} value that result in captured motion. The second technique augments an L_2 Lyapunov manifold with low-thrust to decrease the H_{nat} value along the trajectory before arriving in the lunar region, where a similar (but lower energy) low-thrust apsis map is employed to identify capture options. In both strategies, the low-thrust force is aligned with the anti-velocity direction to supply the maximum H_{nat} rate of change and the mass is modeled as a linear function of time, consistent with the constant specific impulse model defined in Equation (2.92). Accordingly, the low-thrust acceleration magnitude is parameterized by the thrust magnitude, f , and the time-varying spacecraft mass, m , as in Equation (2.79). The resulting CR3BP+LT model is non-autonomous and non-conservative, yet dynamical structures persist and are captured in the Poincaré maps.

4.6.1 Apsis Maps

Poincaré maps that capture trajectory apsides, i.e., *apsis maps*, are employed in this analysis to visualize flow patterns near the Moon. An apsis is a point where the relative velocity between the spacecraft and a primary body is zero, i.e., a point such that

$$\dot{r}_{j3} = (\vec{r} - \vec{r}_j) \cdot (\vec{v} - \vec{v}_j) = 0, \quad (4.32)$$

where \vec{r}_j and \vec{v}_j are the position and velocity of the j^{th} primary body in the rotating frame relative to the system barycenter. For lunar capture applications, apsides relative to the Moon (i.e., P_2 in the Earth-Moon system) are of particular interest. Accordingly, the set of initial states $\{\vec{X}_{i,0}\}$, are selected near the Moon, where each initial state is a planar apsis (periapsis *or* apoapsis) with respect to the Moon at a

specific H_{nat} value. The mapping hyperplane is the periapsis condition, $\dot{r}_{23} = 0$ and $\ddot{r}_{23} > 0$. Because the initial states all satisfy Equation (4.32) for $j = 2$ and are all characterized by the same H_{nat} value, the four-dimensional planar problem is fully represented on a two-dimensional map, enabling straightforward visualization of the complete dynamics.

To construct the apsis map for this analysis, each initial state, $\vec{X}_{i,0}$, is propagated until one of the following stopping conditions occurs:

1. Impact: $r_{23} \leq r_{\text{moon}}$. The initial states of arcs that reach this condition are colored orange.
2. Escape: $r_{23} > 115,000$ km. The initial states of arcs that escape are colored by the location of the spacecraft when r_{23} reaches the escape radius; a location with $x > x_{\text{moon}}$ is an “ L_1 escape” and is colored purple while a location with $x < x_{\text{moon}}$ is an “ L_2 escape” and is colored green.
3. Hover: $\|\vec{v}\| = 0$. The initial states of arcs that reach this condition are colored blue.
4. Capture: the p^{th} periapsis is reached. The initial states of arcs that remain near the Moon without reaching the other stopping conditions are colored yellow.

The map is visualized by coloring the initial apsis states by the behavior of the resulting arc, i.e., the final “fate” of the trajectory as described by the stopping conditions above. For example, a map of ballistic motion in the Earth-Moon CR3BP for $H_{\text{nat}} = -1.584$, displayed in Figure 4.29, includes distinct regions of impact, capture, and escape motion. For this map, the initial states are propagated for a maximum of $p = 2$ perilunes. Gradients of the colors are included to indicate the number of apses that occur along an arc between the initial state and the stopping condition. Although captured arcs always reach the p^{th} perilune, arcs that reach one of the other stopping conditions never reach the p^{th} perilune. Thus, the color gradients for the impact, escape, and hover fates distinguish regions of the map by the number of apses reached. For example, the dark orange propeller-shaped contour that includes the Moon’s profile at (0,0) represents the initial states of arcs that impact

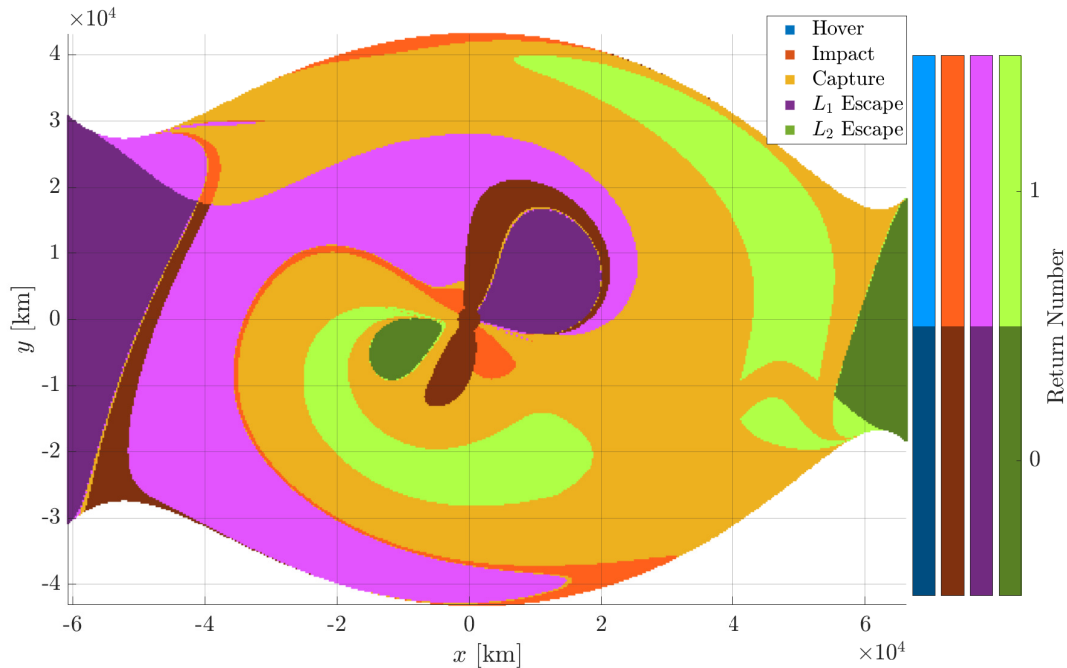


Figure 4.29.: A ballistic lunar apsis map for $H_{\text{nat}} = -1.584$ and $p = 2$ map returns in Moon-centered rotating coordinates.

the Moon before reaching the first perilune; the return number for these arcs is zero. In contrast, the lighter orange regions reach one perilune before impacting the Moon. Gradients in escape colors reveal similar differences. Finally, note that no hover arcs are identified in this ballistic map but are apparent in low-thrust apsis maps that are discussed later in this section.

Distinct structures, i.e., colored lobes, are visible in the map and are linked to other known structures in the CR3BP. For example, the invariant manifolds associated with the L_1 and L_2 Lyapunov orbits at the same H_{nat} value bound the L_1 and L_2 escape regions [79, 80, 81]. This relationship is consistent with the separatrix properties of the planar periodic orbit hyperbolic manifolds; all states within the manifold remain bounded and transit through one of the forbidden region gateways, as discussed in Section 4.5. Accordingly, an apsis map with this visualization scheme supplies useful information for capture applications. A spacecraft entering the lunar region may target an apsis in one of the capture regions to remain near the Moon for at least p

map iterations; if an apsis along the incoming trajectory is located in one of the escape regions, the spacecraft will depart within p map iterations. Similarly, a trajectory that targets a point within the impact regions will reach the lunar surface.

If only discrete data is required from the map, e.g., a discrete trajectory fate metric, the time required to compute a map is significantly reduced by employing a mesh refinement strategy. Rather than propagating a fine grid of initial states to identify the trajectory fates throughout the lunar region, a course grid (i.e., a grid with more distance between initial states) is employed. The course grid is refined to accurately locate boundaries between the distinct structures while avoiding unnecessary computations in locations where there is no change in the trajectory fate. The algorithm used to accomplish this mesh refinement strategy is detailed further in Section E.2.

4.6.2 Low-Thrust Apsis Maps

Apsis maps may also be employed in the CR3BP+LT with anti-velocity-pointing thrust to explore options for lunar capture by leveraging a low-thrust force. The low-thrust map is constructed in the same way as the ballistic map: a set of apsides near the Moon, all at a consistent initial H_{nat} value, $H_{\text{nat},0}$, are propagated with anti-velocity-pointing thrust for p returns to the periapsis hyperplane and colored by the fate of the resulting trajectory. When the thrust magnitude is very small, as in Figure 4.30(a), the low-thrust apsis maps appear very similar to the ballistic maps. However, as the thrust magnitude increases, the structures on the map change, as illustrated in Figure 4.30(b). For example, the low-thrust apsis map for $f = 3\text{e-}2$ (consistent with the capabilities of Lunar IceCube) retains a teardrop-shaped lobe of L_1 escape motion near the center of the map, as well as some L_1 and L_2 escape regions on the left and right sides of the plot. However, there is significantly less escape motion in the center of the plot; instead, many more options for capture exist. Because the propagation is implemented with anti-velocity-pointing thrust, a strategy to decrease

²https://engineering.purdue.edu/people/kathleen.howell.1/Publications/Dissertations/2020_Cox/#periapsisMap_varThrustMag

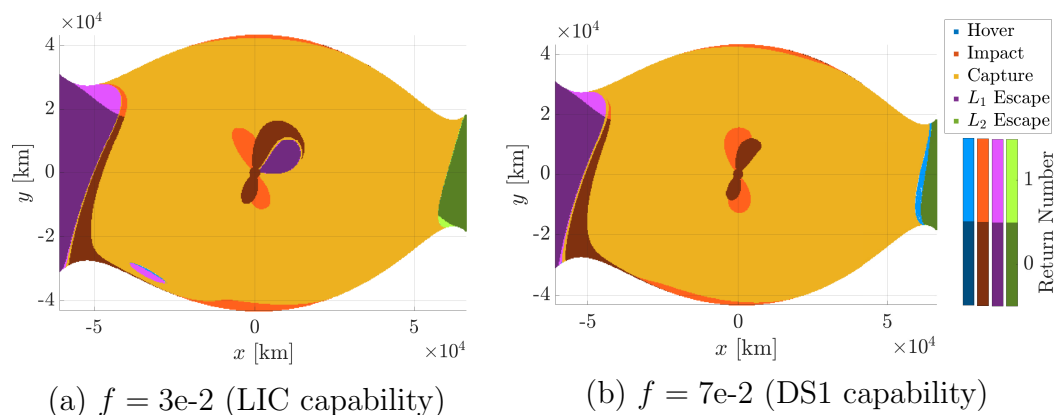


Figure 4.30.: Low-thrust lunar periapsis maps for $H_{\text{nat},0} = -1.584$ and $p = 2$ in Moon-centered rotating coordinates. The initial states are propagated with anti-velocity-pointing thrust with $I_{\text{sp}} = 2500$ seconds ([Animation](#)²)

H_{nat} , it is not surprising that fewer arcs escape during the two map returns. As the energy decreases, the L_1 and L_2 gateways close, prohibiting transit from the lunar region. At a larger thrust magnitude of $f = 7e-2$ (a Deep Space 1 capability), the apsis map, plotted in Figure 4.30(b) includes even more opportunities for capture.

When a greater number of map iterations are permitted, the number of arcs that impact the Moon increases, as seen for $f = 3e-2$ and $p = 75$ in Figure 4.31. In fact, the only change between the $p = 2$ (i.e., Figure 4.30(a)) and the $p = 75$ maps is that a large portion of the arcs that are captured for $p = 2$ impact the moon by $p = 75$. This simple transition is not guaranteed in general; an arc that is initially captured may escape the region given additional time, as observed in the ballistic apse map in Figure 4.29, particularly when the initial H_{nat} value is increased. However, it is useful to note that arcs propagated with an anti-velocity low-thrust force tend to remain captured at “sufficiently low” Hamiltonian values.

Finally, for capture applications it is useful to explore the instantaneous Keplerian elements associated with the final states on the low-thrust arcs represented by the periapsis map. The eccentricity of the captured arcs is of particular interest as it sup-

³https://engineering.purdue.edu/people/kathleen.howell.1/Publications/Dissertations/2020-Cox/#periapsisMap_varNumReturns

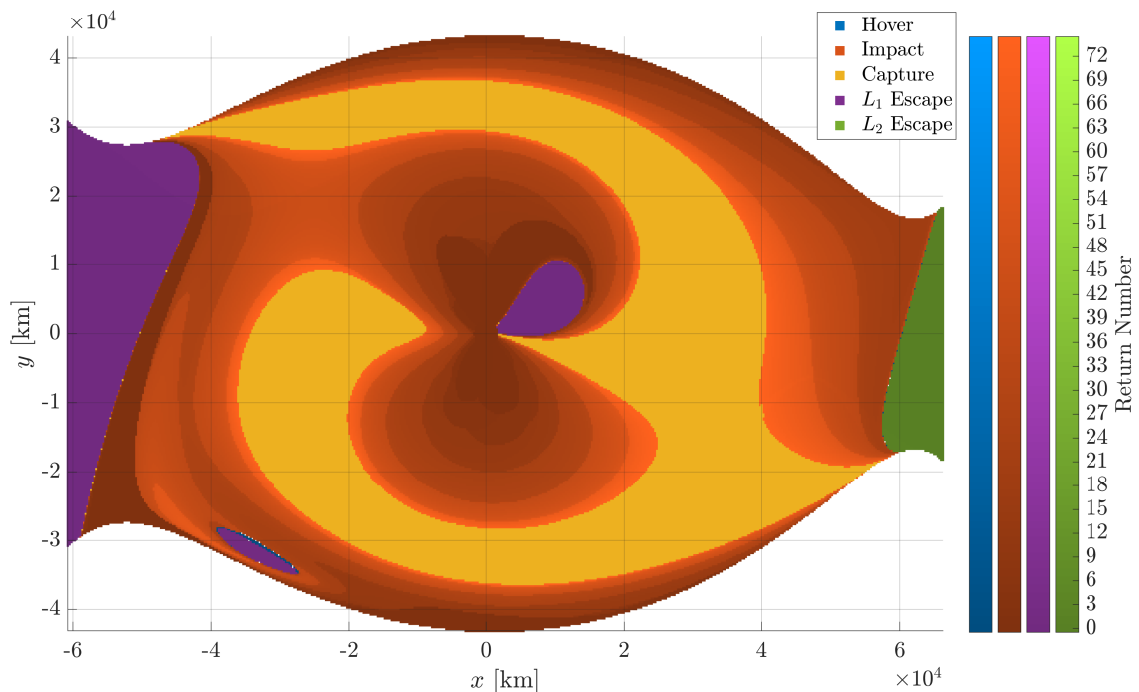


Figure 4.31.: Low-thrust lunar periapsis map for $H_{\text{nat},0} = -1.584$ and $p = 75$ in Moon-centered rotating coordinates ([Animation](#)³)

plies some information about the “stability” of a captured arc in that trajectory with an eccentricity near unity is energetically close to a hyperbolic path that may depart the lunar region while a captured arc with an eccentricity near zero is energetically far from an escaping path. The eccentricity of the captured arcs, displayed in Figure 4.32, is closest to unity at the boundaries of the capture and impact regions and is closest to zero in the center of the capture regions. Accordingly, an initial condition in the dark blue regions of the eccentricity map yields a nearly circular lunar orbit after 75 map iterations. These initial conditions also avoid lunar impact for the greatest number of map returns. In contrast, an initial condition near the boundary of the capture and impact regions depicted in Figure 4.31 is characterized by a much higher eccentricity (near 0.7 in this case) and is likely to impact the Moon if propagated for additional map returns. This insight may be incorporated into the design process to

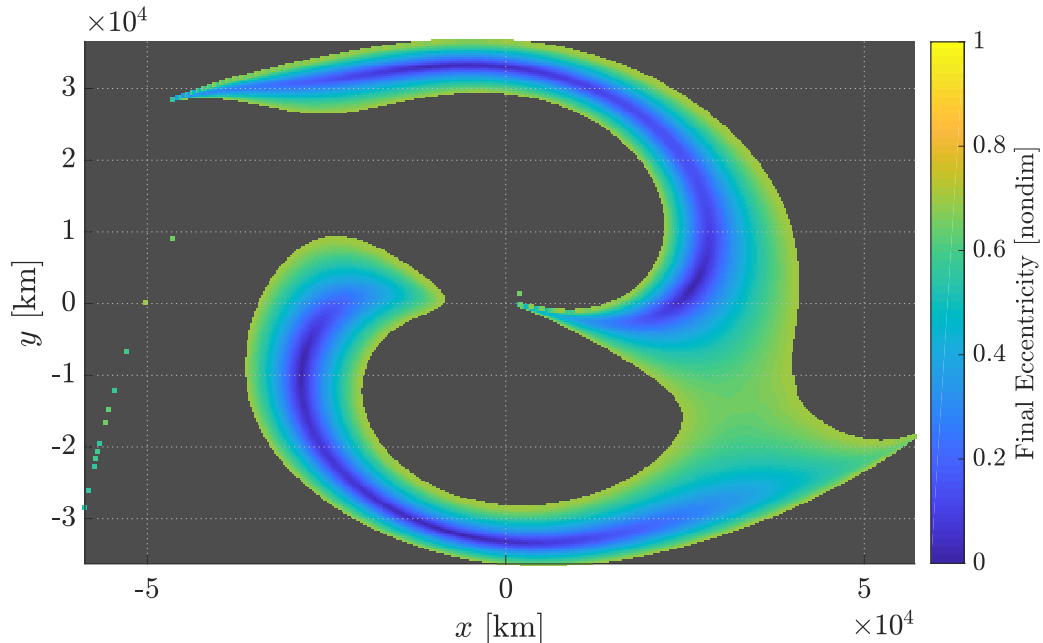


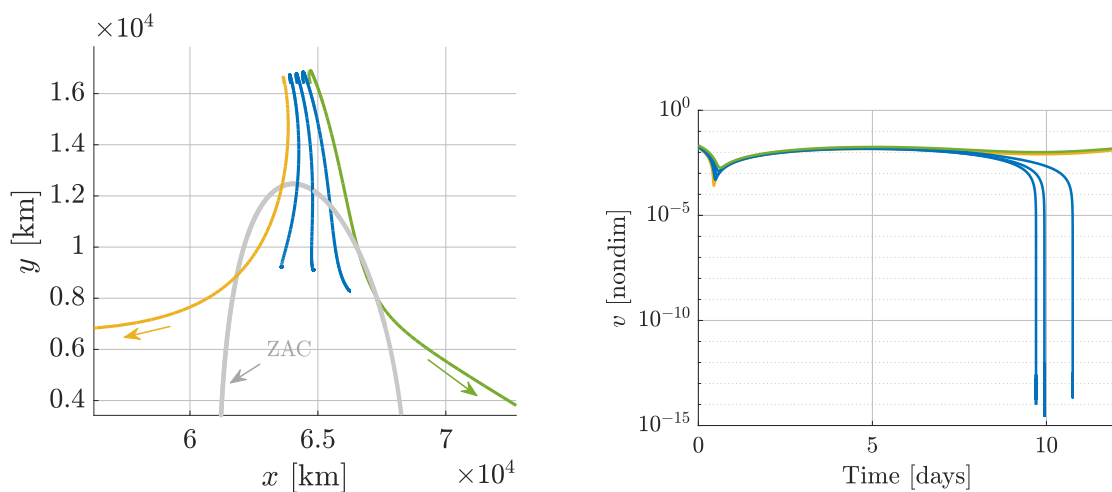
Figure 4.32.: Eccentricity of captured arcs for $H_{\text{nat},0} = -1.584$ and $p = 75$

deliver a final, captured trajectory with a particular eccentricity or to identify the initial conditions that can deliver the lowest-energy captured arcs.

While the boundaries of the colored regions in the planar, ballistic apsis maps (e.g., Figure 4.29) are defined by the L_1 and L_2 Lyapunov manifolds, no such structures are known to bound the regions on the low-thrust apsis maps. As noted above, because the thrust orientation, \hat{a}_{lt} , is aligned with the evolving anti-velocity vector, the CR3BP+LT is nonautonomous, does not admit an integral of the motion, and includes no periodic solutions. Accordingly, hyperbolic low-thrust manifolds analogous to the Lyapunov manifolds are not available to bound the transit and capture trajectories. Despite the lack of dynamical structures that may be employed to predict transit or capture, it is clear that some form of structure persists in this nonautonomous model. Flow-based concepts, such as Lagrangian Coherent Structures observed in a finite-time Lyapunov exponent field, reveal order in many nonautonomous systems that do not admit periodic orbits, invariant manifolds, or other dynamical structures [82]. This line of study is not pursued in this investigation and is left for future work.

4.6.3 Hovering with Low-Thrust

The low-thrust maps include a new type of behavior, colored blue and termed “hover” motion, that is not present in the ballistic map. These initial states yield trajectories that, when propagated with anti-velocity-pointing thrust, eventually reach a velocity magnitude of zero. Due to the implementation of the control law, as the velocity magnitude approaches zero (numerically equivalent to 2^{-52} nondimensional units, or about $2.27\text{e-}16$ km/s in the Earth-Moon system), as in Figure 4.33(b), the orientation of the velocity vector is poorly defined, oscillating with numerical noise as well as the with spacecraft motion. Accordingly, the hover is accomplished by



(a) Moon-centered Earth-Moon rotating frame with the low-thrust zero acceleration contours (ZACs) for reference

(b) The hover arcs reach a velocity magnitude of zero

Figure 4.33.: Sample arcs from the low-thrust apsis map in Figure 4.30(b); the “hover” arcs (blue) reach a zero velocity magnitude in the vicinity of the ZAC

rapidly reorienting the low-thrust acceleration vector, an impractical control method in practice.

Despite the practical difficulty of accomplishing a hover maneuver, the associated map regions supply insights for trajectory design. In the maps depicted in Figure 4.30, the initial states that yield hover motion are located on several of the boundaries be-

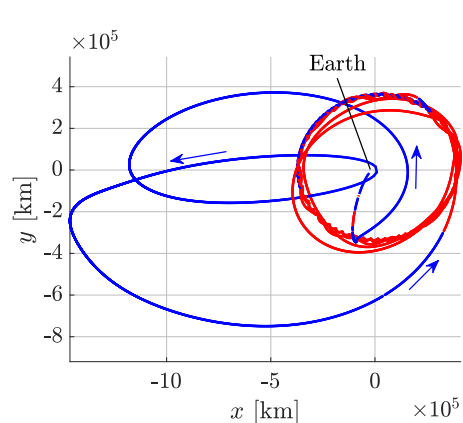
tween states linked to captured motion and states associated with L_1 or L_2 escape. A sample of the trajectories initiated from these states, plotted in Figure 4.33, illustrate the differences between the regions. The initial states for the five sample arcs are selected in a horizontal line at $y = 16,384.6$ km spanning the blue hover region near $x = 6 \times 10^4$ km in Figure 4.30(b). (A similar band of hover motion is included in the map for $f = 3e-2$ at the boundary between capture and L_2 escape motion in the L_2 gateway.) The arcs, plotted in position space in Figure 4.33(a), initially flow along the $-\hat{y}$ direction toward L_2 and toward the \mathbb{E}_2 ZAC, plotted in gray. One intuitive hypothesis to explain the hover motion is that the arcs reach one of these equilibria states. However, because \hat{a}_{lt} changes continuously with the orientation of \vec{v} when the velocity-pointing control law is employed, no single point on the ZAC is associated with a trajectory; during the hover maneuvers (located at the ends of the blue arcs), the location of the instantaneous low-thrust equilibrium solution changes as rapidly as the orientation of \hat{a}_{lt} . Accordingly, the hover arcs do not intersect an equilibrium point. In fact, the locations where the arcs reach $v = 0$ appear unrelated to the ZAC. Instead, the hover locations are the points where the forbidden regions “catch up” with the low-thrust trajectory. Recall that H_{nat} decreases monotonically when the anti-velocity-pointing control law is applied; thus, as the trajectories evolve from the initial states on the apsis map, the forbidden regions grow, increasingly restricting the motion of the spacecraft. At the hover locations, the boundary of a forbidden region, the ZVC, intersects with the trajectory, leaving the space “in front” of the hover location (i.e., in the direction of the trajectory evolution prior to the hover) accessible but the area “behind” the hover location inaccessible. Having reached a lower H_{nat} value, an alternative control technique (a velocity-aligned direction is undefined) may be employed to further influence the trajectory evolution. Indeed, the low-thrust acceleration is particularly influential on the spacecraft path due to the low velocity magnitude at these points. Thus, the map states associated with hover motion are candidates for further study.

4.6.4 Lunar IceCube Reference Trajectory

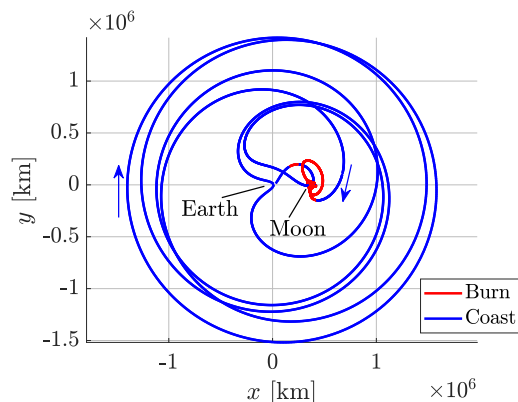
The Lunar IceCube trajectory is referenced as a source of realistic parameters to illustrate the proposed design strategies. Lunar IceCube (LIC), a 14 kilogram, 6U “cubesat”, is equipped with a low-thrust propulsion system that can deliver up to 1.15 millinewtons ($f \approx 3e-2$ in the Earth-Moon CR3BP+LT) of force with a specific impulse, or I_{sp} , of 2500 seconds.[6] About 5 days after deployment from EM-1, LIC flies past the Moon, as illustrated in Figure 4.34, and the subsequent trajectory extends far from the Earth and Moon. A little less than six months later, the spacecraft returns to the Moon and employs the low-thrust propulsion system to decrease the orbital energy and capture into a polar lunar orbit. For the current analysis, only the final approach to the Moon and the subsequent energy decrease and capture are considered. During this final phase, the H_{nat} value in the Earth-Moon rotating frame remains between -1.53 and -1.4; the Hamiltonian fluctuates because the trajectory is propagated in an ephemeris model in which H_{nat} is not an integral of the motion. Accordingly, H_{nat} values in this range are employed as reasonable values to illustrate the proposed capture strategies. Additionally, while the trajectory does include several small thrusting arcs prior to the long, final burn, the mass change is negligible (0.011 kg of the 14 kg wet mass); thus, the initial mass for all capture strategies is set to 100%.

4.6.5 Capture Initiated Near the Moon

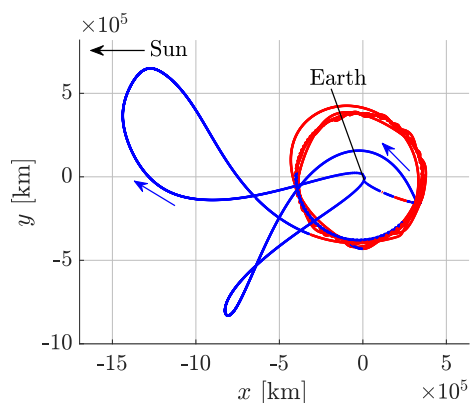
One strategy for high-energy capture initiates thrusting in the anti-velocity direction when the spacecraft arrives in the vicinity of the Moon, as illustrated by the Lunar IceCube (LIC) trajectory in Figure 4.34. Clearly, capture near the Moon is accomplished in this specific scenario, but the single LIC trajectory does not supply information about other nearby solutions. For a more general view of capture opportunities in the lunar region, an apsis map is constructed. Consistent with the LIC trajectory, the set of initial states is characterized by an H_{nat} value of -1.425, and the



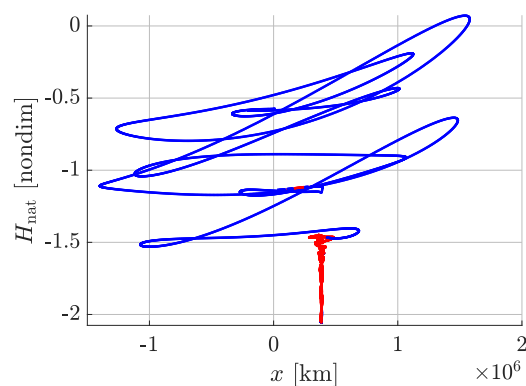
(a) Earth-Centered J2000 frame



(b) Earth-Centered Earth-Moon rotating frame



(c) Earth-Centered Sun-Earth rotating frame



(d) Earth-Centered Earth-Moon rotating frame

Figure 4.34.: Planar projections of a LIC trajectory option in a variety of reference frames; blue arcs represent ballistic (coasting) motion, while red arcs indicate that the low-thrust engine is active (burning). This baseline solution begins at a deployment epoch of June 27, 2020 at 21:08:03 UTC, and ends in a low-lunar orbit on May 22, 2021.

propagation is modeled with an I_{sp} value of 2500 seconds. Two thrust magnitudes are employed: the LIC thrust capability of $f = 3e-2$, and a larger thrust magnitude of $f = 7e-2$, consistent with a Deep Space 1 (DS1) capability. To explore capture options, each point on the map is propagated for up to 20 map returns (i.e., apsides), and the initial conditions are colored by the fate of the associated trajectory, consistent with the scheme in Figure 4.29. The resulting maps, plotted in Figure 4.35,

are dominated by escaping trajectories. The lack of other types of motion is not

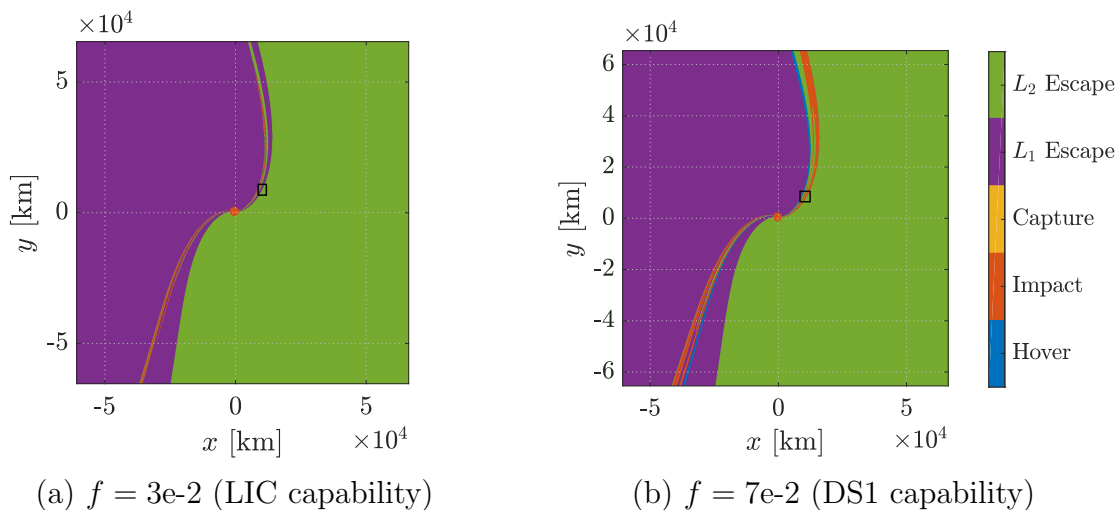


Figure 4.35.: Apsis maps in the Moon-centered Earth-Moon rotating frame for $H_{\text{nat}} = -1.425$, $I_{\text{sp}} = 2500$ seconds, and $p = 20$ map returns.

surprising given the high energy and small thrust force; at energies this high, the low-thrust propulsion is generally not sufficient to prevent the spacecraft from departing the lunar region. (For these high energy maps, departure is defined by the radius $r_{23} > 385,000$ km.) However, thin bands of more nuanced behavior appear in the maps between the large regions of L_1 and L_2 escapes. Zooming in on the structures within the black boxes in Figure 4.35, as depicted in Figure 4.36, reveals even thinner bands of initial conditions with different fates. At the resolution available in these maps, no capture options are revealed for the LIC thrust capability. This result does not necessarily preclude capture at this energy and thrust capability; a modified thrust strategy may adjust some of the collision arcs to achieve capture. When a larger thrust magnitude is employed, as in Figure 4.36(b), capture opportunities become available. These apses, colored yellow on the map, correspond to arcs that pass through 20 apses without colliding with the Moon or departing the lunar region. Although capture opportunities are apparent at the higher thrust capability, they are generally isolated and located on the boundaries between bands of other behaviors, in contrast with the dense bands of L_1 escape, L_2 escape, and impact motion. In-

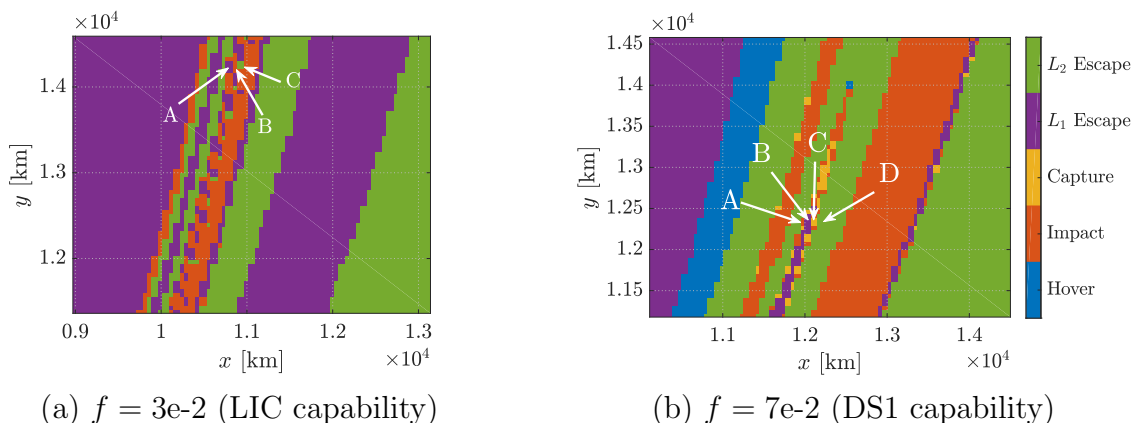


Figure 4.36.: Close-up views of the apsis map regions marked by black squares in Figure 4.35 reveal chaotic motion; Moon-centered Earth-Moon rotating frame

deed, one of the defining characteristics of the high-energy apsis maps in Figures 4.35 and 4.36 is *chaos*: initial states at apses located close together frequently yield very different arcs, particularly in the thin bands viewed in Figure 4.36. Selecting several points in this regions with impact and capture motion, as labeled in Figure 4.36, and plotting the associated trajectories, visualized in Figure 4.37, illustrates the chaotic nature of the dynamics. For each set of arcs, the initial conditions are located at a

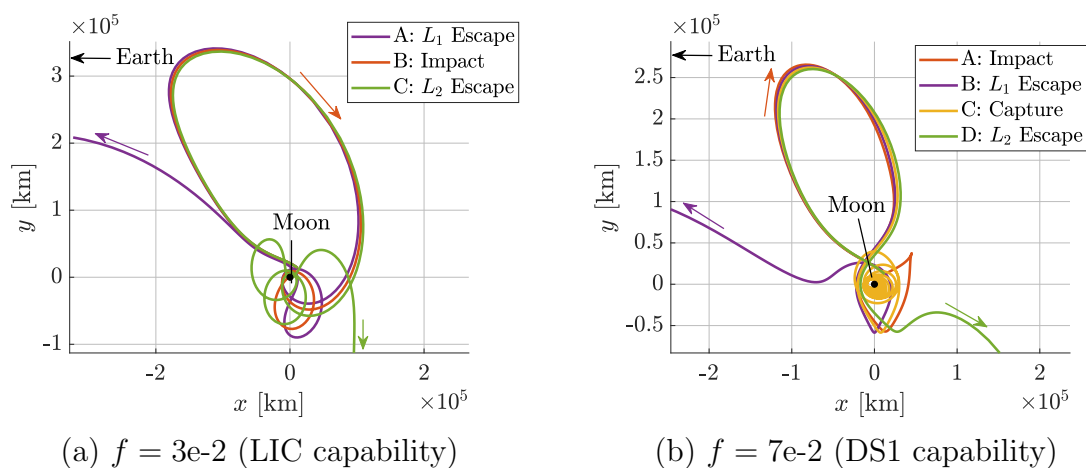


Figure 4.37.: The arcs associated with the points labeled in Figure 4.36 illustrate the chaotic nature of the dynamics; Moon-centered Earth-Moon rotating frame

consistent y -coordinate, and are separated by an x distance of less than 39 kilometers. (The velocity magnitude is a function of the H_{nat} value and the velocity direction is orthogonal to the \vec{r}_{23} vector.) Despite the similar initial states, the evolution of each trajectory varies significantly.

Although no capture opportunities are apparent for the LIC thrust magnitude of $f = 3\text{e-}2$, the geometries of the arcs represented by the map are similar to the LIC ephemeris solution. For example, the large lobe common to the arcs in Figure 4.37(a) is very similar to the LIC trajectory at the beginning of the thrust arc that delivers the spacecraft to lunar orbit, plotted in Figure 4.34(b). These similarities, as well as first-hand knowledge of the difficulties associated with designing the LIC trajectory, suggest that the chaos observed in the this planar apsis map is also a significant factor within the spatial ephemeris model.

For either of the thrust levels, opportunities for capture exist only in the thin, chaotic bands. Accordingly, a design strategy that initiates the capture burn near the Moon is likely to be sensitive, diverging from the desired behavior when small perturbations are encountered. This sensitivity affects not only the design process, but has implications for operations as well. Any failure in the propulsion or navigation systems are likely to effect large changes on the trajectory and may place the spacecraft on a path that does not capture near the Moon, effectively ending a cubesat mission like Lunar IceCube.

4.6.6 Capture Initiated Far from the Moon

As an alternative to a strategy that initiates the capture sequence at a location near the Moon, consider a strategy that employs low thrust to decrease the H_{nat} value prior to arrival at the Moon. As illustrated in the apsis maps for $H_{\text{nat}} = -1.584$, depicted in Figure 4.29, opportunities for capture are more abundant and less chaotic at lower energies than the high-energy results illustrated in Figure 4.35. In fact, a majority of the points on the low-energy map represent capture opportunities with

far less sensitivity than the options at $H_{\text{nat}} = -1.425$. Accordingly, a spacecraft that enters the lunar region with a lower H_{nat} energy value is afforded more flexibility in achieving lunar capture; even if the baseline trajectory is perturbed from a specific target, the spacecraft is unlikely to rapidly depart the region.

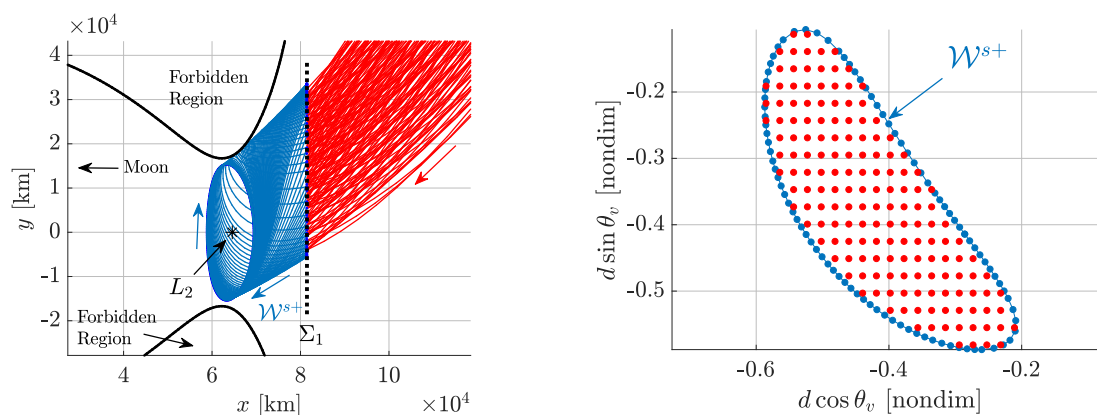
To isolate low-thrust arcs that reach the lunar vicinity at a low energy, the invariant manifolds associated with a ballistic L_2 Lyapunov orbit are employed. In previous studies, such arrival arcs have been produced by propagating a trajectory in reverse time from a low lunar orbit to some energetic or physical hyperplane [6]. While this method reveals capture paths, it restricts the exploration to a specific destination orbit. By utilizing the separatrix property of the L_2 Lyapunov manifolds, a more general set of capture options may be constructed. The proposed capture strategy is comprised of several steps:

1. Propagate the *stable* manifold, \mathcal{W}^{s+} , associated with an Earth-Moon L_2 Lyapunov orbit in reverse time to a hyperplane, Σ_1 , that is located exterior to the L_2 gateway.
2. Propagate the stable manifold states with anti-velocity-pointing low-thrust in reverse time from Σ_1 to another hyperplane, Σ_2 that serves as an interface between a high-energy trajectory incoming to the Moon and a low-thrust arc that decreases the H_{nat} energy. These low-thrust arcs are collectively notated $\tilde{\mathcal{W}}_{\text{lt}}$ as a “pseudo-manifold.”
3. Construct a low-thrust apsis map (anti-velocity-pointing thrust, forward time) at the same H_{nat} energy value as the L_2 Lyapunov orbit
4. Overlay the ballistic *unstable* manifold, \mathcal{W}^{u-} , associated with the L_2 Lyapunov orbit on the low-thrust apsis map and identify intersections with capture opportunities.

From a mission sequence (i.e., forward time) perspective, a spacecraft approaching the Moon first targets a state at Σ_2 “inside” $\tilde{\mathcal{W}}_{\text{lt}}$. At Σ_2 , the low-thrust propulsion is enabled with an anti-velocity-pointing orientation and the spacecraft proceeds to Σ_1 . During this propagation, the H_{nat} value along the trajectory decreases to match

the energy associated with the L_2 orbit. At Σ_1 , the low-thrust force is disabled and the trajectory is allowed to evolve ballistically, bounded by the L_2 Lyapunov manifold separatrices, \mathcal{W}^{s+} and then \mathcal{W}^{u-} . Apses on the trajectory during this ballistic evolution are plotted on the apsis map and compared with the low-thrust behavior available at each apsis; assuming one or more of the apses correspond to a low-thrust trajectory that captures about the Moon, the low-thrust propulsion is re-enabled at the appropriate apsis to begin a low-thrust spiral into a low-energy lunar orbit.

To illustrate this sequence, parameters consistent with the LIC trajectory are again employed. Select an L_2 Lyapunov orbit with an H_{nat} value of -1.584 , a low energy level that still permits transit through the L_2 gateway. The stable manifold that arrives at the orbit from the right side, \mathcal{W}^{s+} , is propagated in reverse time to the Σ_1 hyperplane, located exterior to the system at $x = 81,422.6$ km in the Moon-centered Earth-Moon rotating frame, as depicted in Figure 4.38(a). At this hyperplane, a



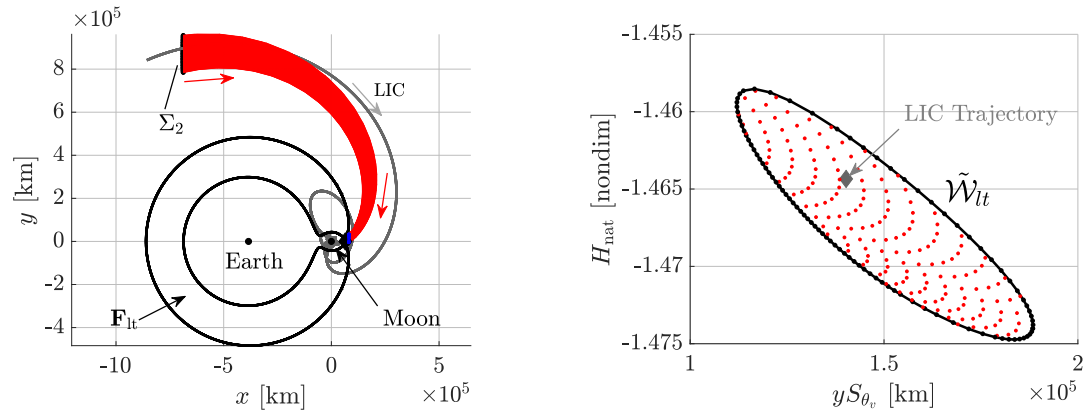
(a) The low-thrust arcs (red) flow directly into and onto the ballistic L_2 Lyapunov manifold (blue); Moon-centered Earth-Moon rotating frame. The ballistic motion is bounded by the forbidden region at $H_{\text{nat}} = -1.584$

(b) Initial conditions for the low-thrust arcs are selected at Σ_1 from the interior (red points) of the ballistic manifold, and from the manifold itself (blue); tube topology at $x = 81,422.6$ km

Figure 4.38.: At the Σ_1 hyperplane, low-thrust arcs flow into and onto the ballistic L_2 Lyapunov manifold

tube-topology representation of the manifold is constructed, consisting of a radial coordinate, $d = (\tilde{y}_u - y)/(2\tilde{y}_u)$, and an angular coordinate $\theta_v = \arctan(\dot{y}/\dot{x})$, consistent with the definitions in Section 3.4. When plotted in polar form, as in Figure 4.38(b), this topology supplies a full representation of the planar states (i.e., all four Cartesian components of the state vector are available from the 2D representation). Because the full state is represented on the map, determining whether a planar trajectory exists within the manifold separatrix is straightforward - simply consider if the trajectory is encircled by the manifold contour on the map. Leveraging this technique, a set of states inside the manifold are selected (plotted as red dots in Figure 4.38(b)). These states are then employed as initial conditions for low-thrust arcs that are propagated in reverse time with anti-velocity-pointing thrust to the second hyperplane, Σ_2 . Additionally, the manifold states (plotted in blue) are also propagated to Σ_2 with the same thrust strategy, yielding the $\tilde{\mathcal{W}}_{lt}$ set; although these arcs appear similar to a manifold structure, they are not mathematically related to the originating periodic orbit, nor are they manifold arcs associated with a low-thrust periodic orbit.

The Σ_2 hyperplane serves as an interface between an incoming high-energy trajectory and a low-thrust arc that decreases the H_{nat} energy. To facilitate high-energy capture, Σ_2 should be sufficiently far from the low-energy \mathcal{W}^{s+} manifold such that the energy change along the low-thrust arcs between Σ_2 and Σ_1 is large. Placing the Σ_2 hyperplane at $x = -687,871.5$ km (again in the Moon-centered Earth-Moon rotating frame), as illustrated in Figure 4.39(a), supplies an energy change consistent with the LIC trajectory. At this interface, a mapping strategy similar to the tube topology employed at Σ_1 is applied; the y -coordinate of the arcs replaces the scaled y -coordinate, but the velocity angle, θ_v , is identical to the previous definition. However, in contrast to the map at Σ_1 , this mapping cannot represent the full state in a 2-dimensional plot due to the variations in the H_{nat} values associated with the low-thrust arcs at Σ_2 . Accordingly, H_{nat} is included in the mapping, yielding a 3-dimensional surface, a projection of which appears in Figure 4.39(b). This mapping illustrates a similar structure: The low-thrust arcs propagated from within the ballistic manifold, plotted



(a) The low-thrust arcs (red) originate at the Σ_2 hyperplane, and have a similar geometry to the Lunar IceCube (LIC) approach path; Moon-centered Earth-Moon rotating frame

(b) A projection of the low-thrust states at Σ_2 . Low-thrust arcs propagated from the stable manifold (black) completely enclose low-thrust arcs propagated from the interior of the manifold

Figure 4.39.: Low-thrust trajectories that flow into a ballistic manifold decrease the H_{nat} value while simultaneously delivering the spacecraft to the lunar vicinity; Moon-centered Earth-Moon rotating frame

in red, remain within low-thrust arcs propagated from the manifold itself, $\tilde{\mathcal{W}}_{lt}$, plotted in black. In contrast to the ballistic CR3BP, this apparent low-thrust separatrix behavior is not predicted by the dynamics, but it does persist across a variety of Σ_2 locations and a variety of H_{nat} energy values. Increasing the density of the low-thrust arcs propagated from within the ballistic manifold confirms this separatrix behavior: all of the points within $\tilde{\mathcal{W}}_{lt}$ flow into \mathcal{W}^{s+} .

While this analysis is conducted in the Earth-Moon CR3BP+LT, solar gravity is a non-negligible force far from the system barycenter, i.e., along the arcs that approach Σ_2 . The geometry of the LIC trajectory, propagated in an Earth-Moon-Sun ephemeris model, is different than the Earth-Moon arcs despite the similarities in the states at Σ_2 , as illustrated in Figure 4.39(b). Indeed, previous investigations note the importance of solar gravity during this approach to the Earth-Moon system [6]. However, including the Sun in the model eliminates the autonomous nature of the gravitational dynamics, complicating the analysis by adding an epoch-dependency.

Thus, to develop the proposed capture strategy, solar gravity is omitted from the model. For mission-specific applications, a relevant epoch (or range of epochs) limits the scope of the design problem, and the low-thrust arcs may be propagated between Σ_1 and Σ_2 in the appropriate dynamical environment. Regardless of the specific model employed for the approach to Σ_1 , the method remains unchanged.

Once a spacecraft has navigated through the low-thrust pseudo-manifold, $\tilde{\mathcal{W}}_{lt}$, and, subsequently, the ballistic \mathcal{W}^{s+} manifold, the trajectory remains bounded by the L_2 Lyapunov unstable manifold that departs the orbit to the left, \mathcal{W}^{u-} . However, the H_{nat} energy associated with the trajectory and the bounding manifold are not sufficiently low to prevent escape from the lunar region. Accordingly, additional thrusting must be incorporated to reduce the H_{nat} value, i.e., to capture about the Moon. The low-thrust apsis map constructed at the same energy level as the ballistic manifold with anti-velocity-pointing thrust, plotted in Figure 4.40, identifies locations in the lunar region where the thruster may be re-activated to capture in a low-energy orbit about the Moon. Note that this map is constructed with the same parameters as

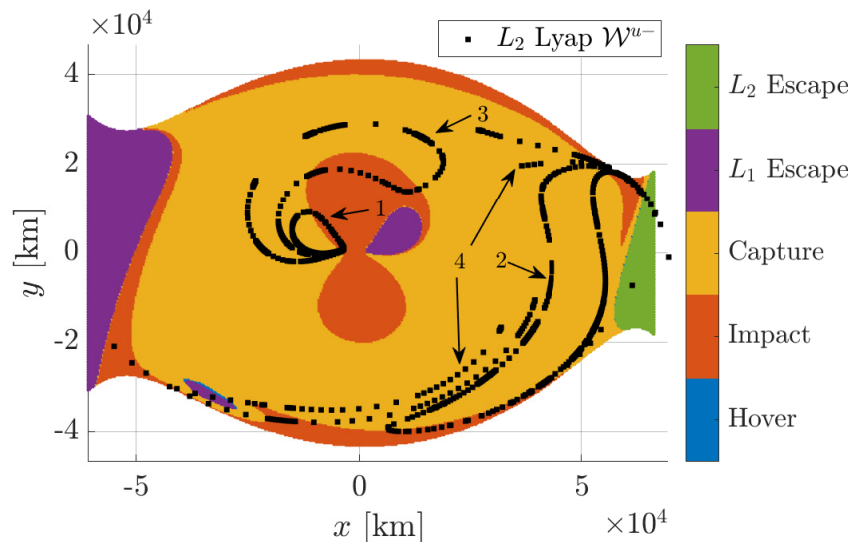


Figure 4.40.: Ballistic L_2 Lyapunov unstable manifolds (black) overlaid on a low-thrust apsis map (anti-velocity-pointing, $f = 3\text{e-}2$, $I_{\text{sp}} = 2500$ sec) for $H_{\text{nat}} = -1.584$ and $p = 20$; Moon-centered Earth-Moon rotating frame

the map in Figure 4.30(a), but this latter map is propagated to 20 apses (a sufficient amount of time for the low-thrust force to decrease the H_{nat} value such that both gateways are closed) whereas the map in Figure 4.30(a) is propagated to only two apses. Accordingly, the 20-return map includes all of the information available in the 2-return map; every escape and impact condition from the 2-return map is captured by the 20-return map. However, some of the initial conditions that yield capture motion for two map returns escape or impact the Moon when propagated for 20 returns. Overlaying the \mathcal{W}^{u-} ballistic manifold apses on the map (plotted as black dots and labeled with map return number), reveals a specific subset of the capture opportunities that are accessible from within the manifold separatrix. The first and second manifold apsis regions overlap almost entirely with capture opportunities; thus, nearly every arc within the L_2 Lyapunov manifold can be linked to a low-thrust path that delivers a capture trajectory. Consequently, the majority of the arcs within $\tilde{\mathcal{W}}_{lt}$ at Σ_2 (Figure 4.39(b)) may be linked to a low-energy lunar orbit.

Several sample arcs are constructed to illustrate the capture process. The initial states for the arcs are located within the $\tilde{\mathcal{W}}_{lt}$ contour at Σ_2 , as depicted by the colored symbols in Figure 4.41(a). Each arc is propagated with anti-velocity-pointing low-thrust to Σ_1 , where the thrust is disabled and the arcs are allowed to evolve ballistically. The arcs coast for different time intervals: arcs 1 and 2 coast to the first apsis, arcs 3 and 4 coast to the second apsis, and arcs 5 and 6 coast to the third apsis. As expected, these apses, plotted as colored symbols in Figure 4.41(c), remain within the \mathcal{W}^{u-} separatrix. Additionally, each of these apses is located in the yellow-colored capture region on the low-thrust apsis map. In contrast to the capture initiated near the Moon, the coast periods between Σ_1 and the subsequent apses provide opportunities for orbit determination and navigation updates before the second low-thrust maneuver is initiated to capture near the Moon. Additional coasting time can be incorporated into the trajectory by directly targeting insertion onto the L_2 Lyapunov orbit, i.e., by following an arc on $\tilde{\mathcal{W}}_{lt}$ and, equivalently, on \mathcal{W}^{s+} , as illustrated by arc 1 in Figures 4.41(a) and 4.41(b). The initial state for arc

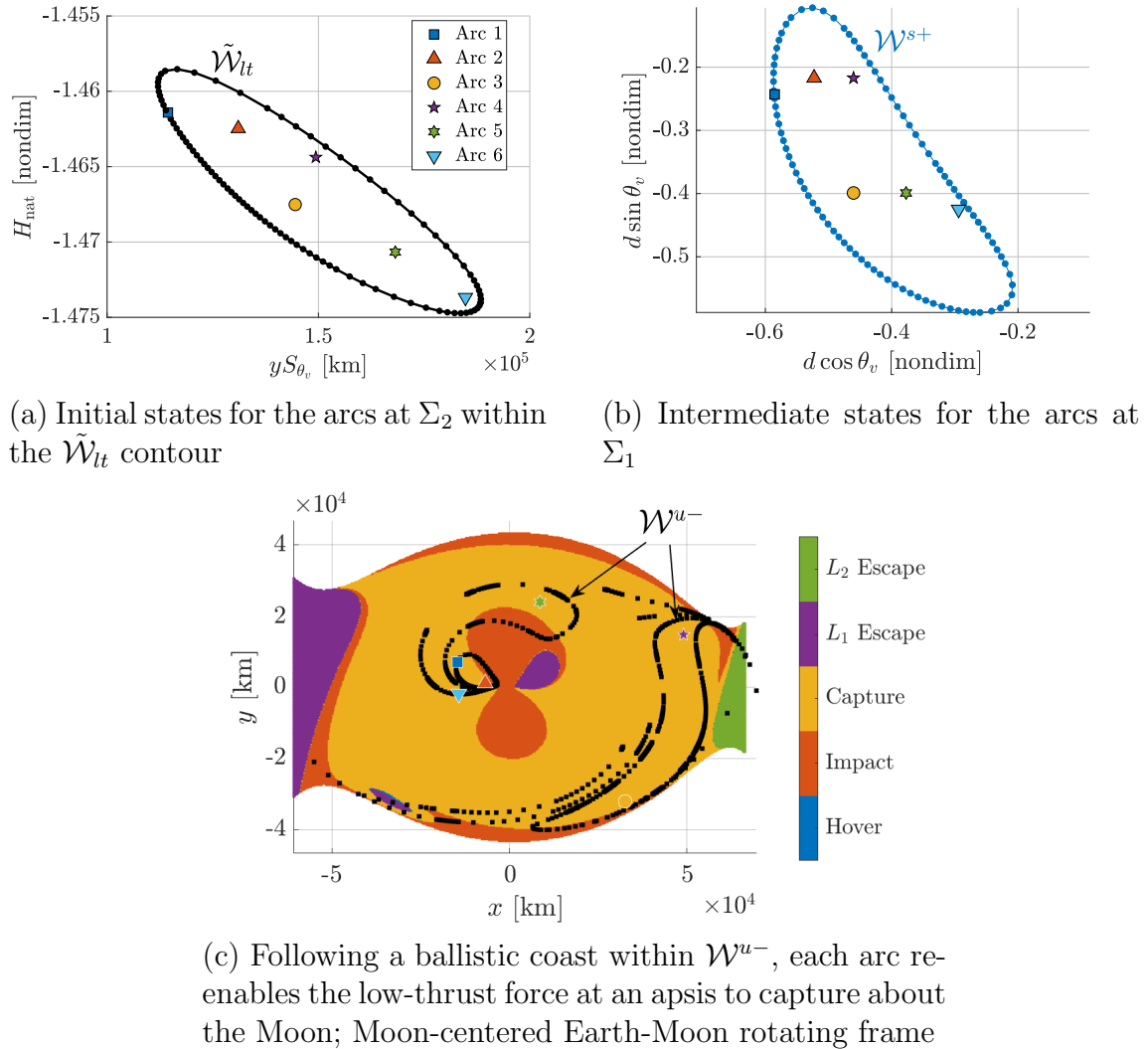
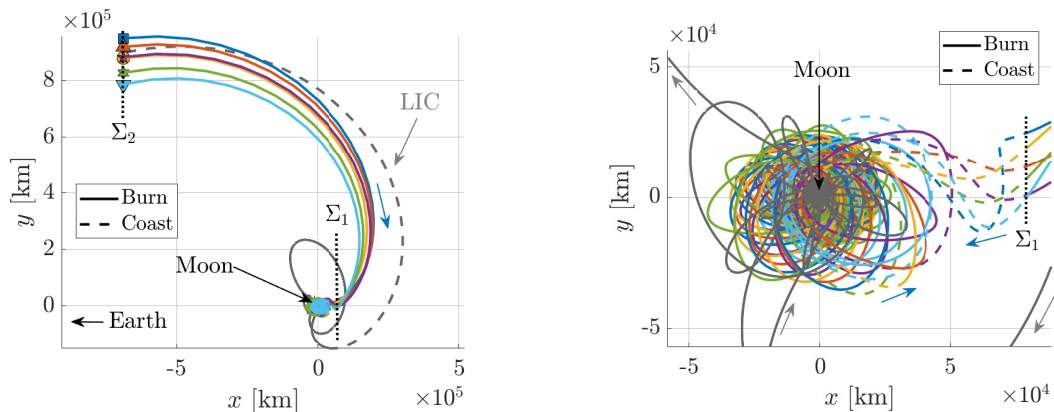


Figure 4.41.: Arcs that reach a low-energy lunar orbit are designed by identifying appropriate states on the Σ_2 , Σ_1 , and apsis maps

1, represented by a blue square, is located very near the $\tilde{\mathcal{W}}_{lt}$ boundary at Σ_2 and remains near the \mathcal{W}^{s+} contour at Σ_1 . From the Σ_1 hyperplane, a ballistic coast along \mathcal{W}^{s+} delivers the spacecraft to the Lyapunov orbit where an arbitrarily long coast may be included. At some later time (e.g., when a phasing constraint is satisfied), a small maneuver is sufficient to perturb the spacecraft from the periodic orbit and place it on the unstable manifold, \mathcal{W}^{U+} , such that the spacecraft reaches the apses in Figure 4.41(c).

Although the six sample arcs are clearly separated on the Σ_2 , Σ_1 , and apsis maps, the arcs follow similar paths through configuration space. The physical trajectories, plotted in Figure 4.42, are particularly dense as the arcs approach the Moon. The Lu-



(a) Configuration space representation in the Moon-centered Earth-Moon rotating frame

(b) A zoomed view of the lunar region

Figure 4.42.: Sample capture trajectories in configuration space; Moon-centered Earth-Moon rotating frame

nar IceCube (LIC) trajectory, plotted in gray, follows a similar path as the the sample arcs, but differs considerably near the Moon. Although many of these differences are a result of the different models employed to propagate the arcs (recall that the LIC trajectory is propagated in a full, spatial ephemeris model whereas the sample arcs are propagated in the planar, Earth-Moon CR3BP+LT), some of the differences are certainly due to the thrust strategy. The sample arcs employ low-thrust to decrease the H_{nat} value, constraining the approach geometry to flow through the L_2 gateway. In contrast to these sample arcs, the LIC trajectory, characterized by a much higher H_{nat} value and an initial ballistic coast, is not similarly constrained.

Another useful illustration of the capture trajectories is the H_{nat} energy evolution through time and space. The LIC trajectory, plotted in gray in Figure 4.43, coasts to the lunar vicinity before initiating a low-thrust maneuver to decrease energy and capture near the Moon. (Because the LIC trajectory is propagated in an ephemeris

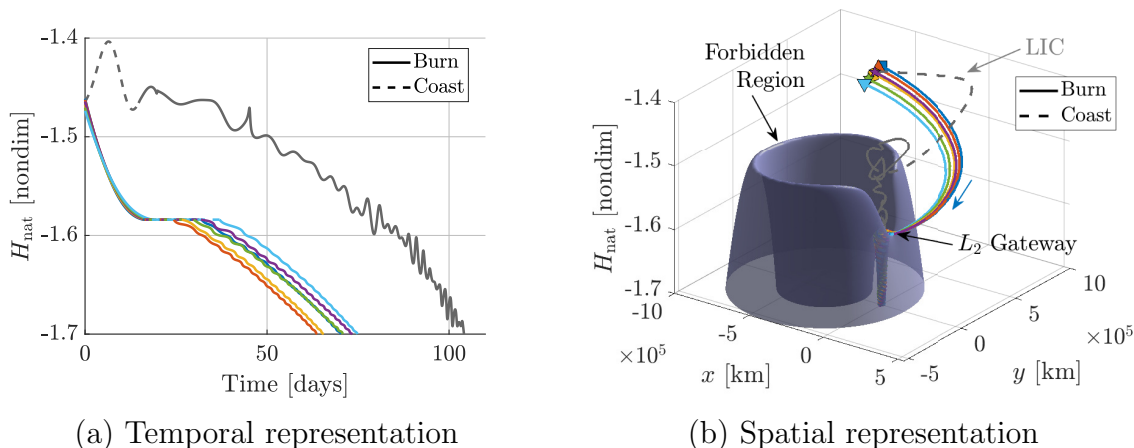


Figure 4.43.: The H_{nat} energy along the sample arcs and the LIC trajectory decreases to a low-energy lunar orbit

model with forces not included in the CR3BP+LT, such as solar gravity, the H_{nat} value is not constant during the coast.) In contrast, the capture arcs designed via the strategy detailed in this investigation initiate a low-thrust maneuver to decrease the H_{nat} value immediately, as is evident in the time-history plotted in Figure 4.43(a). A spatial representation of these planar trajectories in Figure 4.43(b) further illustrates the relationship between the H_{nat} value along the arcs and geometry of the forbidden region. In this representation, each horizontal “slice” of the forbidden region surface is the zero velocity contour at the corresponding H_{nat} value. The planar projection of the LIC trajectory maintains a high H_{nat} value, remaining unconstrained by the forbidden region. Rather than offering flexibility, this lack of an energy constraint results in sensitivities that create design difficulties, as illustrated in the chaotic apsis maps depicted in Figures 4.35 and 4.36. In contrast, the colored trajectories that employ thrusting to reduce the H_{nat} energy before arriving at the Moon pass just above the L_2 gateway and are relatively bounded near the Moon. As a result, the ballistic coast arcs that begin at Σ_1 remain captured for several returns to the apsis map, bounded by \mathcal{W}^{u-} . Thrusting may resume at any of the apses that overlap with low-thrust capture motion to further decrease the H_{nat} value along the trajectory

such that escape from the lunar region is not possible, i.e., delivering the spacecraft to a low-energy lunar orbit.

Trajectory designs that reduce the H_{nat} energy prior to arriving near the Moon benefit from reduced chaos compared to trajectories that begin energy-reducing maneuvers near the Moon. These differences between the high-energy, high-chaos dynamics and the low-energy, low-chaos dynamics are apparent when comparing energy-optimal low-thrust spirals on apsis maps. Additionally, a trajectory that reaches the lunar vicinity with a relatively low H_{nat} energy may incorporate coasting segments prior to the final low-thrust maneuver, facilitating orbit determination and navigation updates. While this analysis has focused on the lunar region, the capture strategies may be generalized for capture about any secondary body in a CR3BP system. Additionally, capture via the L_1 gateway may be accomplished via similar processes. Finally, this investigation considers only the planar dynamics but may be applicable to the spatial realm. The separatrix properties of spatial manifolds are less well-established than the separatrix nature of planar manifolds, but appear to behave similarly.

5. INTERACTIVE TRAJECTORY DESIGN SOFTWARE

The delivery of new information to an individual, regardless of their expertise, is often aided by a visual, interactive environment. Many of the most popular trajectory design tools, e.g., the General Mission Analysis Tool (GMAT) [83], Systems Tool Kit [84], Copernicus [85], and FreeFlyer [86], are designed to operate primarily as graphical user interfaces (GUIs), allowing mission designers to interact with visual representations of trajectory data. While most of these software tools support analyses only in an ephemeris model, mission design efforts in lower-fidelity models such as the CR3BP or CR3BP+LT also benefit from a visual and interactive environment. Several tools developed in the early 2000's, namely Generator [87] and LTool [88], leveraged dynamical systems theory for mission design applications and laid the groundwork for future interactive software. One derivative of these early tools is the Adaptive Trajectory Design (ATD) software developed at Purdue University and NASA Goddard; it supplies an interactive GUI for multi-body trajectory design in the Earth-Moon and Sun-Earth CR3BP systems [89, 90, 91]. A catalog of periodic and quasi-periodic structures in the Earth-Moon and Sun-Earth system, developed to complement ATD, supplies a GUI that allows a user to explore a diverse range of dynamical structures to be included in a trajectory design [92, 93]. Similar tools, including an ATD "module" that supports mission analysis for the Wide Field InfraRed Survey Telescope (WFIRST) [94] and a module for locating and correcting transfers between libration point orbits [95], have also been developed. In this investigation, a new version of the ATD software is developed to address shortcomings in the original design while also incorporating its strengths. Within this new ATD architecture, tools that enable an intuitive exploration of the CR3BP+LT and facilitate future research are developed.

5.1 A New Adaptive Trajectory Design Architecture

Before discussing the dedicated low-thrust trajectory design tools developed to support this investigation, the new architecture for the ATD software is detailed. This new architecture, denoted version 2 or “v2” seeks to maintain and enhance the strengths of the original ATD software, i.e., version 1 or “v1”. These strengths include:

- The ability to assemble arcs from multiple dynamical structures (e.g., conic arcs, CR3BP periodic orbits, periodic orbit manifolds, or quasi-periodic orbits) to construct an itinerary
- A catalog of pre-computed dynamical structures
- The ability to compute new dynamical structures as needed
- An interactive environment to apply constraints to an itinerary and perform differential corrections

While ATD v1 supplies many useful capabilities, it is also limited by several shortcomings; the v2 architecture is designed to address these shortcomings and anticipate future requirements, as summarized in Table 5.1. When combined, these shortcomings make ATD v1 difficult to extend to new applications. For example, the common

Table 5.1.: Solutions implemented in ATD v2 to address shortcomings in ATD v1

Shortcoming (v1)	Solution (v2)
Supports only the Earth-Moon and Sun-Earth CR3BP	Object-oriented MATLAB and Java code enables analyses agnostic to model and system
Compiled C++ scripts lack error handling and are difficult to compile on some OS	A Java library interfaces with MATLAB with intuitive error handling, compiles easily on every OS
Analysis tools are entangled with the visualization tools	Stand-alone plug-ins supply analysis tools to a core visualization framework
Many critical parameters are hard-coded and are inconsistent between scripts	System parameters and software settings are saved in JSON files

(and relatively simple) need to enable analyses in addition CR3BP systems (e.g., Sun-Mars, or Saturn-Titan) in ATD v1 requires the modification of a large portion of the source code. Rather than modify the existing code, the decision was made to begin from scratch. The new architecture is separated into three main components: a Java library that enables rapid and model-agnostic analyses (i.e., analyses in the CR3BP, CR3BP+LT, ephemeris, and other models), an interactive MATLAB GUI, and a suite of plug-ins that supply analysis tools, additional GUIs, or additional Java libraries. The development of this software has been a collaborative effort with other members of the Multi-Body Dynamics Research Group at Purdue University; please see the [Acknowledgments](#) section for a list of contributors.

5.1.1 Java Library: `atd-core`

The most common analysis required in multi-body dynamics research is the numerical integration of a state. This process can be computationally expensive and slow in an interpreted language (i.e., code that is compiled in real time as it is run) like MATLAB. In the ATD v1 software, rapid numerical integration is performed by compiled C++ scripts that employ the GNU Science Library (GSL) [96]. While this method is fast and accurate, the GSL library must be compiled separately for each operating system (and for different versions of the same operating system, e.g., Windows 10 vs Windows 7), a process that can be incredibly tedious, particularly on Microsoft Windows. Additionally, the interfaces between MATLAB and the C++ scripts must be explicitly coded to convert arrays of memory “pointers” into more useful objects; such conversions are prone to low-level errors that crash the MATLAB software and are tedious to develop, particularly when a large number of C++ functions are to be accessed from MATLAB.

To mitigate the difficulties associated with the ATD v1 C++ back-end code, a new Java library, named “`atd-core`”, is developed. The Java language was selected for several reasons. First, in contrast to C++ code, Java is straightforwardly

compiled once, then distributed and run on any operating system. Second, because MATLAB is written in Java, the custom `atd-core` library functions are easily called from MATLAB scripts without the need for interface functions to translate between the two languages. As MATLAB is the tool of choice for many astrodynamists throughout academia and industry, this simple interface enables ATD to be incorporated into existing work flows. For example, a few lines of code suffice to load the Java library in a MATLAB script; the propagation, corrections, and continuation methods within the `atd-core` may then be called directly from the MATLAB script. Next, Java provides powerful object-oriented programming constructs that are employed to write analysis tools that are model- and system-agnostic. For example, a `Propagation` class includes a `propagate()` function that accepts a generic `AbstractDynamicsModel` object as an input. The `AbstractDynamicsModel` defines key functions, such as `getEquationsOfMotion()`, that are common to all types of dynamics models. Accordingly, this single `propagate()` function (with event detection and other useful features) is applied to any dynamical model that incorporates the `AbstractDynamicsModel` functionality. This design pattern is applied to many other aspects of multi-body analyses in the `atd-core` library: linearization, differential corrections, and continuation routines are all model- and system-agnostic. Finally, as a compiled language, Java code runs much more quickly than MATLAB scripts, though not quite as quickly as C, C++, or Fortran code. Accordingly, numerical integration of trajectories is completed rapidly in the Java library; the small speed decrease from a similar C++ integration is deemed acceptable given the straightforward interface between Java and MATLAB.

To ensure that this core library maintains the highest possible quality, a rigorous set of unit tests are included with the source code. These unit tests include checks on all of the classes and methods, including comparisons with results from the industry-standard GMAT software. The tests cover practically every instruction in the library, as revealed by the code coverage report in Figure 5.1. Every addition to the library

¹<https://www.jacoco.org>

atd-core

Element	Missed Instructions	Cov.	Missed Branches	Cov.	Missed	Cxty	Missed	Lines
edu.purdue.mbd.atd.bcfbp		99%		93%	4	75	2	362
edu.purdue.mbd.atd.ephemeris		99%		99%	1	135	3	421
edu.purdue.mbd.atd.dynamics		99%		98%	3	168	2	469
edu.purdue.mbd.atd.crtbp		100%		96%	2	67	0	181
edu.purdue.mbd.atd.propagation.events		100%		100%	0	123	0	264
edu.purdue.mbd.atd.propagation		100%		100%	0	101	0	225
edu.purdue.mbd.atd.util		100%		100%	0	28	0	55
edu.purdue.mbd.atd.ephemeris.events		100%		90%	1	11	0	34
edu.purdue.mbd.atd.corrections		100%		n/a	0	4	0	8
edu.purdue.mbd.atd		100%		n/a	0	1	0	1
Total	62 of 16,919	99%	11 of 723	98%	11	713	7	2,020

Figure 5.1.: Code coverage report for `atd-core`; generated with JaCoCo 0.8.4¹

is tested against the existing unit tests and a strict set of code coverage limits certifies that the software remains accurate and predictable. Finally, a thorough set of documentation aids in the validation effort; the process of describing the functionality of a method or class is frequently sufficient to identify design flaws. A math specification document outlines the mathematics employed in each method, and a thorough set of “Javadocs” describes the inputs and outputs of every function. As a result of the unit tests, code coverage, and documentation, the `atd-core` library supplies a high-quality suite of analysis tools for use in scripts and graphical user interfaces.

5.1.2 MATLAB Interface: `atd-matlab`

While the `atd-core` library supplies powerful tools to be employed in custom scripts, a graphical user interface (GUI) is a useful addition to the ATD software that enables interactivity and exploration. Due to the prevalence of MATLAB in astrodynamics work flows and the powerful plotting capabilities it supplies, the main ATD graphical user interface is coded in MATLAB. Similar to the `atd-core` library, MATLAB runs on all major operating systems; thus, the interface is available to practically all users. Object-oriented programming is again employed to define basic objects that facilitate analyses in multiple dynamics models; this strategy also minimizes redundant code and duplicated (possibly inconsistent) parameters. The primary function

of this MATLAB interface, named “atd-matlab”, is to supply a visual, interactive environment, pictured in Figure 5.2. The atd-matlab software stores trajectory arcs

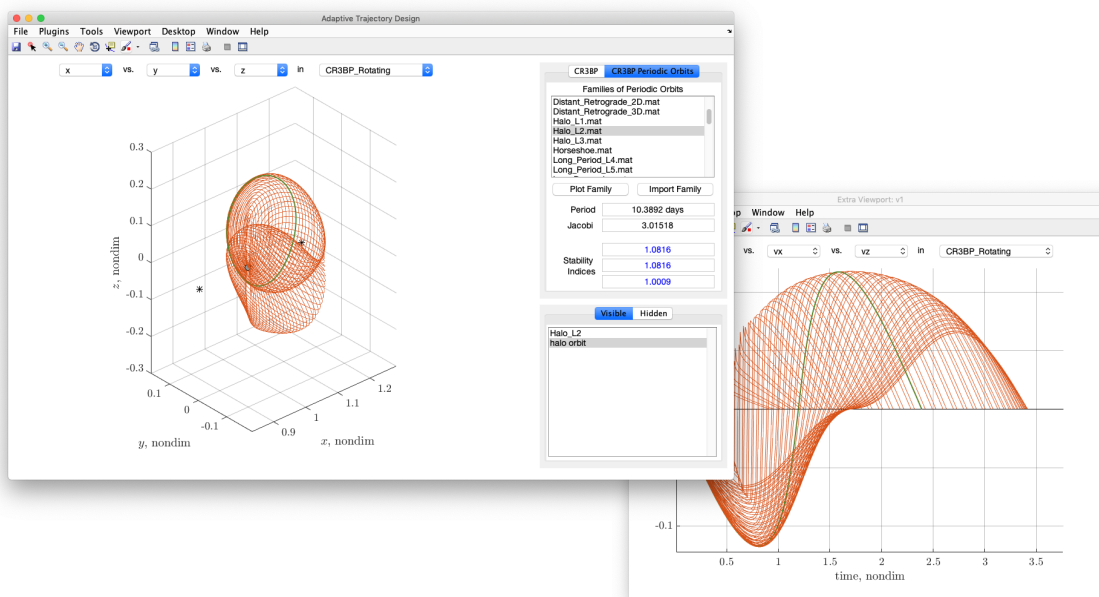


Figure 5.2.: The Earth-Moon L_2 halo family depicted in position space (left) and as a time series (right)

and other dynamically relevant data sets as a collection of “plot objects,” i.e., data than can be visualized in 3D and interacted with via the cursor, inspired by existing interactive design software [97, 98, 99, 100]. Accordingly, atd-matlab supplies functions to plot data in a variety of reference frames across many different coordinates (e.g., Cartesian position and velocity coordinates, Hamiltonian values, time, etc.) as well as functions to interact with the data in a 3D environment. Brushing and linking, a powerful visualization tool that correlates data across visualizations [101], is another key component of atd-matlab. In essence, when a trajectory (or any other data structure) is selected (i.e., “brushed”) in one view, the software selects the same structure in all other available views (i.e., the views are “linked”). Figure 5.2 demonstrates this multi-view linking: A single halo orbit, colored green, is selected by the user from the family of halo orbits in one view but is highlighted in both views.

In contrast to the original ATD version, v1, the new GUI supplies only the most basic analysis tools; more advanced methods are available from dedicated plug-ins. By separating the visualization and interactivity routines from the analysis tools, `atd-matlab` is capable of supporting numerous use cases without any modifications to the base code; a specific set of plug-ins may be loaded for each analysis task. Additionally, by supplying only the most basic tools by default and allowing the user to load more complex plug-ins as the need arises, `atd-matlab` follows the “progressive data disclosure” paradigm [102], facilitating a gradual learning curve.

5.1.3 Plug-ins

The plug-in architecture developed for `atd-matlab` ensures that the software is flexible and extensible. As described above, the main `atd-matlab` software supplies only the most basic visualization and interactivity tools; individual plug-ins can leverage these tools and provide analysis capabilities. For example, a “CR3BP Dynamics” plug-in is enabled by default and supplies the interface to select a CR3BP system. This plug-in computes the locations of the equilibrium points, plots forbidden region boundaries, and offers GUIs to numerically integrate states within the CR3BP, including the hyperbolic manifolds associated with the equilibria. Similarly, a “CR3BP Periodic Orbit” plug-in provides an interface to load and plot families of periodic orbits. Individual orbits may be extracted from their families, and the hyperbolic manifolds associated with an orbit may be computed. With the exception of the CR3BP Dynamics plug-in, all plug-ins are stand-alone packages that can be loaded and unloaded as needed. Accordingly, an alternative plug-in to analyze and compute CR3BP orbits may be developed and straightforwardly enabled; this independence between plug-ins is the primary mechanism that enables the flexibility and extensibility of `atd-matlab`. Because plug-ins are packaged individually, the `atd-matlab` software does not need to be modified to support new analyses. Additionally, researchers may modify a plug-in to suit their own needs without affecting the functionality of other

plug-ins or the main `atd-matlab` software; these modified plug-ins can be distributed between researchers as easily as sharing a `.zip` file, enabling rapid prototyping and collaboration.

In addition to the CR3BP Dynamics and CR3BP Periodic Orbit plug-ins, several other plug-ins are available. At the time of writing, these additional plug-ins include:

- **BCR4BP Dynamics Plug-in:** similar to the CR3BP Dynamics plug-in, an interface to construct a bicircular restricted 4-body problem (BCR4BP) model is available; once constructed, this model can be employed in numerical integration. The zero-acceleration contours may also be visualized.
- **Ephemeris Dynamics Plug-in:** provides an interface to load and unload SPICE ephemeris data kernels, and a GUI to construct an N -body ephemeris model. These ephemeris models are added to the list of available dynamics models for use in numerical integration.
- **Map Explorer Plug-in:** defines a format for Poincaré map data and supplies an interface to load data from the local file system. Once loaded, the map data can be visualized in a dedicated GUI in a number of reference frames and coordinates; data points may also be colored by a scalar coordinate value. Individual points on the map may be selected to reveal the underlying structures, i.e., the trajectory associated with the point.
- **Differential Corrections Plug-in** (*In development*): allows the user to assemble arcs into an itinerary, select patch-point locations, apply constraints, and perform differential corrections via a multi-dimensional Newton-Raphson scheme

Additional plug-ins exist to support analyses in the CR3BP+LT and are the focus of the rest of this chapter.

The ATD software (v1 and v2) is available on an internal Purdue University website; please direct all inquiries to Kathleen Howell (howell@purdue.edu).

5.2 Low-Thrust Analyses in ATD V2

Analyses within the CR3BP+LT are enabled by the development of several software products. First, a Java library, `atd-core-low-thrust`, augments the capabilities of the `atd-core` library with the CR3BP+LT dynamics model as well as dedicated classes to locate equilibrium solutions. The `atd-core-low-thrust` library also supports the addition of a low-thrust force to any other dynamics model, including the CR3BP, BCR4BP, or an ephemeris model. Second, two plug-ins to `atd-matlab` provide GUIs to generate and interact with the CR3BP+LT equilibria, to propagate with any separable control law, and to explore LTPOs and their associated manifolds. The descriptions included in this section are meant as a brief overview of these tools; more detailed documentation for users is included with each software product.

5.2.1 Java Library: `atd-core-low-thrust`

Similar to the `atd-core`, analysis tools for low-thrust trajectory design are included in a Java library entitled `atd-core-low-thrust`. This library primarily provides tools for analysis in the CR3BP+LT but is designed for use in any dynamical model. For example, a package of control policy objects compute a low-thrust acceleration vector that can be applied to any dynamical model. Although the control policies are currently limited to those described in Section 2.2.4, additional policies may be straightforwardly implemented in the library by extending well-defined interfaces to support variable specific impulse thrust models, feedback control laws, or any other control parameterization. The `atd-core-low-thrust` library also supplies event functions to be employed during numerical integration of low-thrust trajectories and constraints for use in differential corrections processes.

5.2.2 General Low-Thrust Propagation

Two plug-ins to `atd-matlab` supply visual, interactive interfaces for the `atd-core-low-thrust` library. The first plug-in, simply named “Low-Thrust Dynamics” visualizes the low-thrust equilibrium points, the forbidden regions, and provides a GUI to propagate an arbitrary state in the CR3BP+LT with a low-thrust control law. The second plug-in offers the means to select pre-computed families of low-thrust periodic orbits, compute new families, and view family hodographs, similar to the CR3BP Periodic Orbit plug-in described above.

Recall that the CR3BP+LT augments the ballistic CR3BP dynamics with an arbitrary low-thrust acceleration, \vec{a}_{lt} , a vector that is separated into the thrust magnitude, f , the spacecraft mass, m , and the orientation, \hat{a}_{lt} , as defined in Equation (2.79). Each of these quantities is computed by a control policy; by selecting one policy for each component, a variety of low-thrust control parameterizations are available (see Section 2.2.4). The low-thrust dynamics plug-in supplies a GUI to select the various control policies and set the relevant parameters, as seen in Figure 5.3. Consistent with the discussion in Section 2.2.4, only one thrust magnitude policy is available: the constant thrust magnitude parameterization. Next, two orientation policies are possible: the policy that fixes the \hat{a}_{lt} vector in the rotating frame (as displayed in the figure), and the policy that aligns \hat{a}_{lt} with $\pm\vec{v}$. Finally, the mass policy may be selected to vary the mass with a constant specific impulse (CSI, pictured in the figure), or to fix the mass at a constant value. The initial state for the propagation, displayed in the fields at the top of the GUI in Figure 5.3, is populated when the GUI is opened. For example, the user may select a point on an existing structure by right-clicking; a subsequent click on the “Propagate” context-menu item opens the propagation GUI and auto-fills the initial state with the point the user has selected. Finally, the time-of-flight (TOF) along the arc is specified and a set of propagation events may be included to stop the propagation or mark useful points along the path.

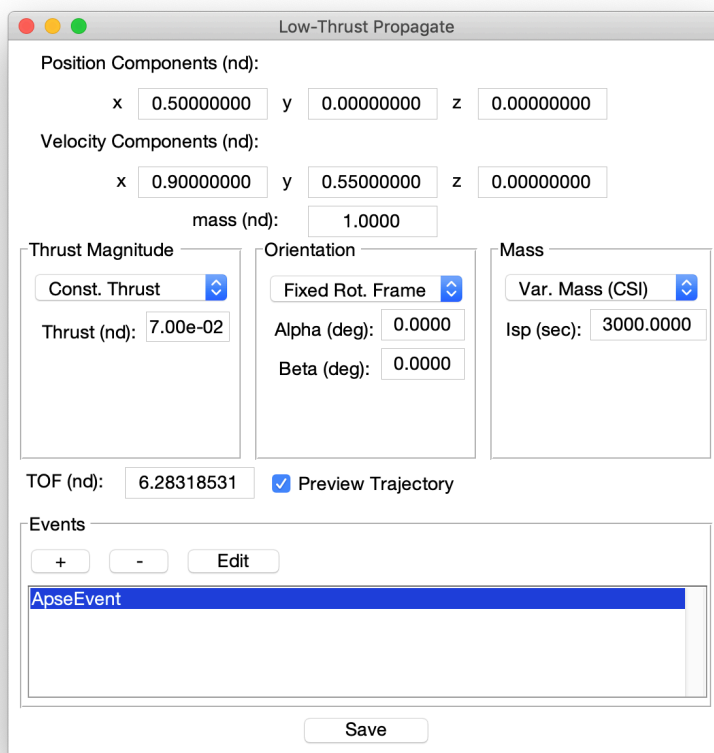


Figure 5.3.: GUI to propagate a trajectory with low-thrust

5.2.3 Equilibrium Point Analyses

In addition to supplying a propagation GUI, the Low-Thrust Dynamics plugin allows the user to set the magnitude and orientation of a low-thrust vector and visualize the corresponding equilibrium points and forbidden regions (i.e., the ZVCs). The interface consists of a series of fields for the a_{lt} , α , β , and H_{lt} values, as seen in Figure 5.4. Changes to the a_{lt} or β values affect the entire set of zero acceleration contours (ZACs), while changes to the α angle move the markers for the distinct equilibria (diamonds). When the forbidden regions are visualized (not shown in this depiction), modifications to any of the four fields are reflected in changes to the forbidden region boundaries. In this example, the Earth-Moon system was selected

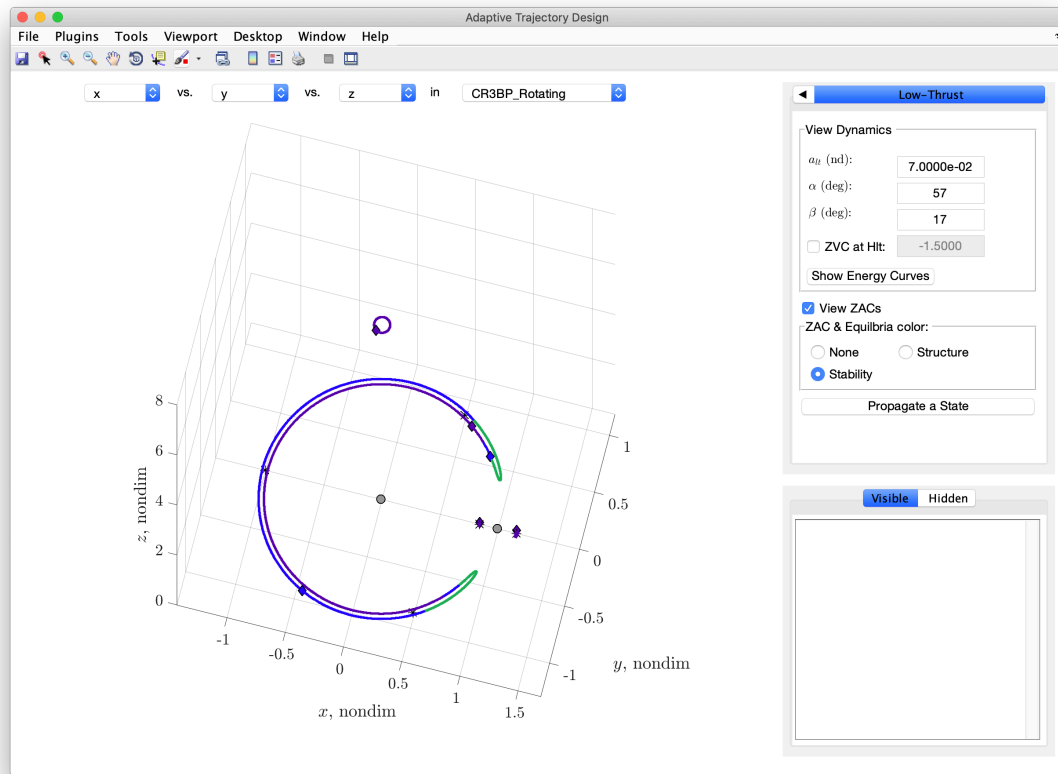


Figure 5.4.: The low-thrust dynamics plug-in visualizing the stability of the Earth-Moon ZACs for $a_{lt} = 7e-2$

to initialize the analysis. The Low-Thrust Dynamics plug-in was then loaded. The a_{lt} value is set to $7e-2$, a value that represents the thrust capability delivered by Deep Space 1. The α angle is 57° and the β angle is 17° . Accordingly, four ZACs exist and are colored by stability, as selected in the plug-in interface.

A parameter space view of the ZACs is also available and is linked to the configuration seen in Figure 5.4. Clicking the "Show Energy Curves" button from the plug-in interface opens a window that plots the ZACs in α vs. H_{lt} space, as seen in Figure 5.5. By selecting a point in this space, the α and H_{lt} values are adjusted to match the selected point. This link between the visualizations in the main interface and the parameter space view facilitates rapid exploration of the equilibrium points

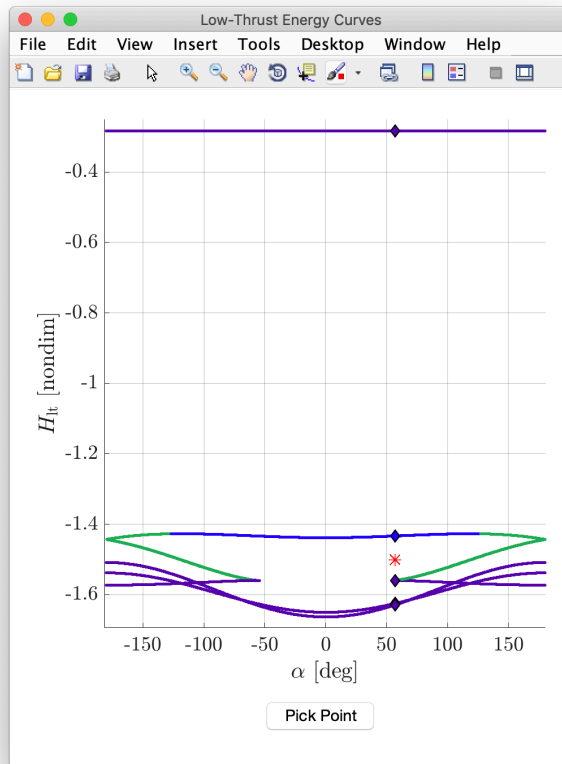


Figure 5.5.: Parameter-space view of the Earth-Moon ZACs for $a_{1t} = 7e-2$ and $\beta = 17^\circ$. The distinct solutions at $\alpha = 57^\circ$ are marked by diamonds and the Hamiltonian value is represented by the red asterisk

and the forbidden region geometries associated with various control orientations and H_{1t} values. For example, the diverse forbidden region gateway configurations near the cusps in the \mathbb{E}_3 ZAC are straightforwardly explored by selected nearby points.

Finally, the hyperbolic manifolds associated with any of the distinct equilibrium solutions may be propagated. A simple interface, displayed in Figure 5.6, allows the user to select a mode as well as the specific manifold branches to propagate. In this example, the stable (blue) and unstable (red/orange) manifolds associated with the Earth-Moon $E_3^1(0.07, 57^\circ, 17^\circ)$ point are propagated. Similar to the state propaga-

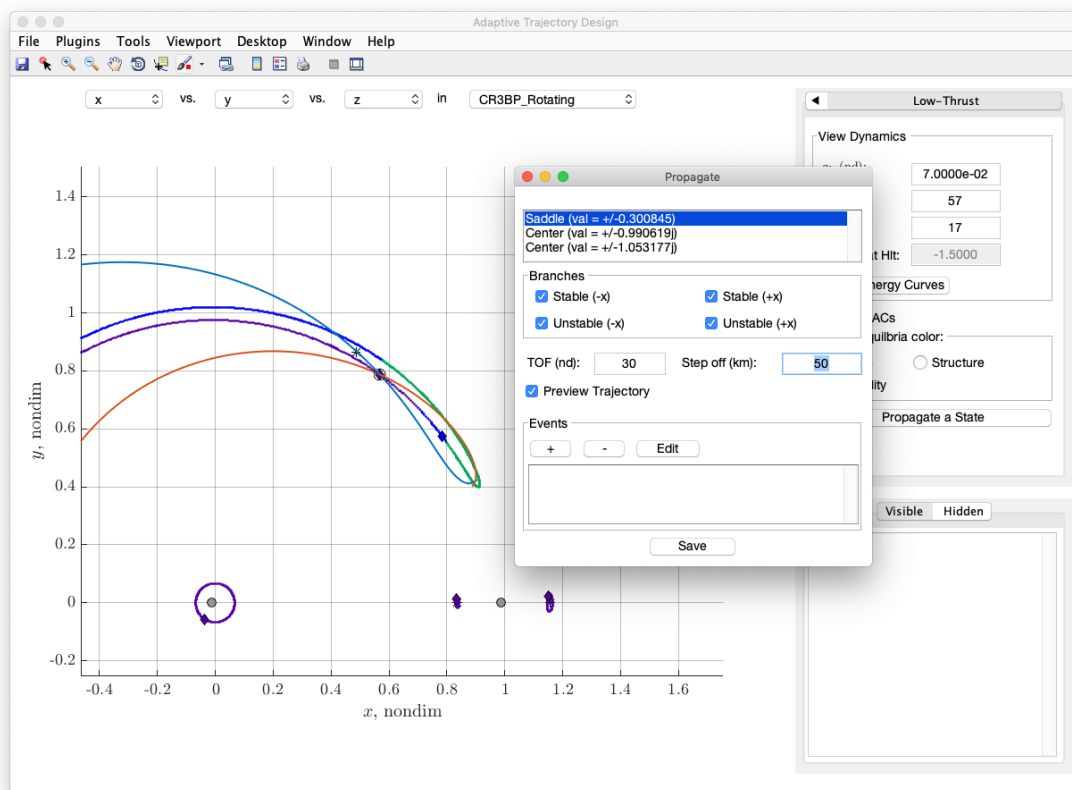


Figure 5.6.: The Earth-Moon $E_3^1(0.07, 57^\circ, 17^\circ)$ hyperbolic manifolds are propagated via a simple GUI

tion interface, the time-of-flight is straightforwardly modified, and events along the propagation may be implemented.

The interfaces supplied by the Low-Thrust Dynamics plug-in are meant to supply a catalog of dynamical structures that communicate the results of this investigation to other researchers. While a more conventional catalog (i.e., a reference document with quantitative data and visual representations) may be constructed, the diversity of the low-thrust structures makes such an undertaking difficult. For instance, the locations of the CR3BP+LT equilibrium points vary with μ , a_{lt} , α , and β ; a thorough documentation of these points requires many pages of reference material. On the other hand, the few hundred lines of code contained within the plug-in are sufficient to explore the equilibria across the full range of parameters.

5.2.4 Low-Thrust Periodic Orbit Analyses

Distinct from the Low-Thrust Dynamics plug-in, the low-thrust periodic orbit plug-in supplies tools to analyze families of low-thrust periodic orbits (LTPOs). Pre-computed families located on the local file system may be loaded and plotted, as in Figure 5.7. Multiple views of the family are available by selection coordinates in the

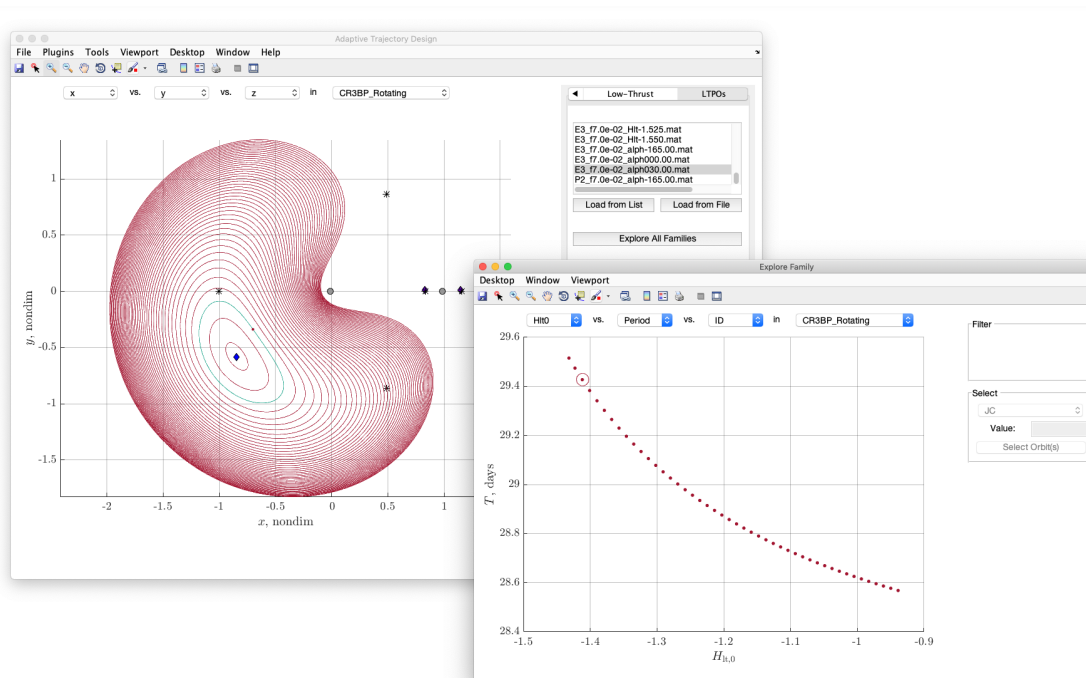


Figure 5.7.: A family of low-thrust periodic orbits is displayed in position space and as a hodograph; brushing and linking ensures that orbits selected in one view are also selected in the other

main interface or by selecting the "Explore Family" option from the LTPO family context menu. The resulting GUI, displayed on the right in Figure 5.7, shows the family hodograph; the coordinates here are also adjustable. Consistent with the rest of the `atd-matlab` suite, selections made in one view are reflected in all other views. This brushing and linking enables comparisons across coordinates and reference frames for a quick exploration of the LTPO family. Consistent with the CR3BP Periodic Orbit

plug-in, individual family members may be extracted for further analysis, including the propagation of the stable and unstable manifolds.

An additional interface displays all available LTPO families that match the a_{lt} and β values specified in the low-thrust dynamics plug-in GUI. By default, the families are plotted in the α vs. H_{lt} parameter space, as displayed in Figure 5.8, but can also be displayed via other coordinates. The user toggles between the ZACs to view the

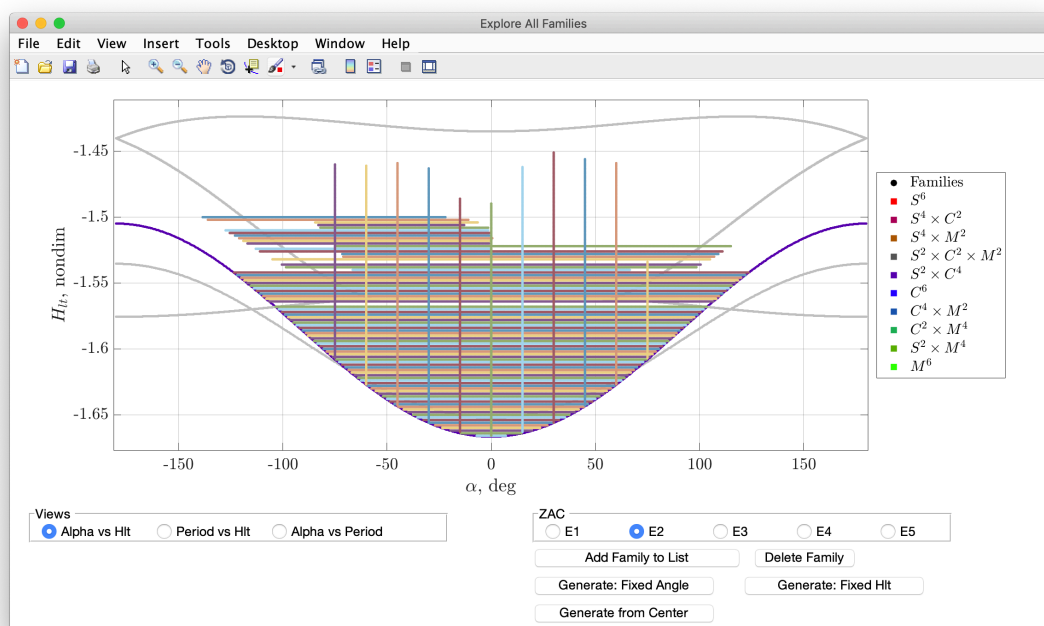


Figure 5.8.: An interface to view families in the context of the ZAC energy curves

families that exist within the center subspaces of the various equilibrium solutions. In the figure, the \mathbb{E}_2 ZAC is selected; the ZAC curve itself is colored by its stability properties while the orbit families are assigned arbitrary colors to distinguish between families. Horizontal lines represent families with a fixed H_{lt} value that evolve in the α angle, as discussed in Section 3.4.2. Similarly, the vertical lines represent H_{lt} families with a fixed α angle that evolve in the H_{lt} . New families of LTPOs may be constructed by selecting an existing orbit from one of the families or an equilibrium solution with a center manifold. Similar to the Low-Thrust Dynamics plug-in, this tool supplies a

catalog of dynamical structures within the CR3BP+LT and the real-time computation of new families enables the exploration of systems that have not been documented.

6. CONCLUDING REMARKS

As the number of low-thrust enabled space missions grows, strategies to design trajectories that incorporate a low-thrust force are increasingly important. This investigation facilitates the preliminary design of such trajectories by identifying relationships between useful metrics such as energy or geometry and the low-thrust control parameters, namely the magnitude and orientation of the low-thrust acceleration vector relative to the rotating frame. In contrast to many other studies, this work does not leverage optimization or other numerical algorithms to “guess and check” or “grid search” for control parameters that meet a specific goal. Instead, a dynamical systems perspective is adopted. When reasonable simplifications are incorporated into a combined multi-body, low-thrust model, useful insights become apparent and dynamical structures are straightforwardly computed. These results are summarized below.

6.1 Insights from Dynamical Systems Theory

To construct a suitable dynamical model, the circular restricted 3-body problem (CR3BP) is augmented with a low-thrust force to form the CR3BP+LT. As the addition of low thrust to the model only increases the complexity and the number of independent variables, simplifying assumptions are explored. Most notably, the magnitude of the low-thrust acceleration is held constant, a strategy equivalent to assuming a constant spacecraft mass; Monte Carlo analyses verify that this assumption is reasonable in planet-moon systems. When the orientation of the low-thrust acceleration vector is also held constant in the rotating frame, the CR3BP+LT reduces to a conservative, autonomous system with an integral of the motion, H_{lt} . Within this model, the ballistic CR3BP integral, H_{nat} , is revealed to vary independently of

the spacecraft path, enabling straightforward relationships between the orientation of the low-thrust force and the evolution of H_{nat} . Additionally, symmetry properties within this simplified model facilitate the prediction of flow patterns without requiring additional computation. Finally, when the low-thrust acceleration vector varies in magnitude or in orientation, the time-derivative of H_{nat} still reveals useful insights. Control strategies to extremize \dot{H}_{nat} or to maintain a constant H_{nat} value along a low-thrust arc are straightforwardly derived.

6.2 Novel Dynamical Structures

When the low-thrust acceleration vector is held constant in the rotating frame, a plethora of dynamical structures are available to guide low-thrust trajectories. The first structure considered in this investigation is the set of equilibrium points associated with a CR3BP+LT system and a particular low-thrust acceleration vector. The number, locations, and stability properties of these equilibria vary with the orientation angles, α and β , and with the acceleration magnitude, a_{lt} . The equilibrium points also vary from system to system as the μ value changes. For very small a_{lt} magnitudes, the low-thrust equilibria remain near the ballistic Lagrange points and are characterized by similar stability properties. However, as a_{lt} increases to the magnitudes associated with spacecraft such as Deep Space 1, the low-thrust equilibrium solutions can vary significantly from the ballistic solutions. Novel locations and energy values associated with the low-thrust points yield new forbidden region geometries that can be leveraged for transit and capture applications.

Once the low-thrust equilibrium points are located and analyzed, dynamical structures predicted by the local, linearized dynamics are constructed. The hyperbolic manifolds, i.e., the stable and unstable manifolds, associated with the equilibrium solutions supply novel flow patterns throughout the CR3BP+LT, particularly on the rings of solutions that encircle L_3 , L_4 , and L_5 . Additionally, many of the low-thrust equilibria include a 2D or 4D center manifold that includes periodic orbits. The ge-

ometries of these orbits range from ballistic-like motion to entirely new orbit paths. Both the hyperbolic and center manifolds yield variations in H_{nat} that may be employed to navigate between ballistic structures.

The final set of dynamical structures included in this investigation are the manifolds associated with low-thrust periodic orbits (LTPOs). Consistent with ballistic (i.e., CR3BP) periodic orbits, most LTPOs possess a hyperbolic subspace that includes stable and unstable manifolds. In the planar dynamics, these manifolds appear to act as separatrices between transit and non-transit flow, analogous to the ballistic periodic orbit manifold separatrices. By leveraging these separatrices, transit and capture trajectories that rely on a low-thrust force are straightforwardly identified. Additionally, every LTPO exists as part of a family; thus, a single LTPO initialized from the center manifold of an equilibrium point yields infinitely many additional LTPOs. In contrast to the ballistic periodic orbit families, these low-thrust sets may evolve in several parameters, including the H_{lt} value and the low-thrust control parameters, a_{lt} , α , and β .

6.3 Interactive Trajectory Design Software

Due to the increased dimension of the design space as compared to the ballistic CR3BP, an interactive suite of trajectory design software is developed to enable exploration of the CR3BP+LT. These tools iterate upon the existing Adaptive Trajectory Design (ATD) software developed at Purdue University and NASA Goddard to address shortcomings in the original code and implement new data visualization techniques. Two plug-ins dedicated to the CR3BP+LT allow the user to investigate the low-thrust equilibrium solutions, the associated hyperbolic and center manifolds, and the low-thrust periodic orbits and their hyperbolic manifolds. Any of these dynamical structures may be selected, adjusted, and included in an itinerary to construct a preliminary trajectory design for a low-thrust spacecraft.

6.4 Recommendations for Future Work

As low-thrust spacecraft continue to visit destinations throughout the solar system, an understanding of the dynamics that govern the low-thrust trajectory segments is increasingly necessary. Many avenues for future work in this area are apparent and are listed below:

1. **Explore other systems** —The bulk of this investigation has focused on the Earth-Moon CR3BP+LT with occasional comparisons to the Sun-EMB system. It is clear from the analyses discussed in Section 2.2.6 that the influence of the low-thrust acceleration on the ballistic structures varies dramatically with the system mass ratio and the characteristic quantities. For example, the Deep Space 1 a_{lt} value affects the Sun-EMB dynamics more strongly than the Earth-Moon dynamics. Accordingly, a more detailed investigation of structures within the Sun-EMB system, as well as other systems of interest (e.g., Mars-Phobos, Saturn-Titan, Jupiter-Io, Pluto-Charon), are of interest.
2. **Applications for mixed mode** —The hyperbolic and center modes associated with the low-thrust equilibrium points are explored in detail in this work. The “mixed” modes, on the other hand, are left for future work. These modes include a stable/unstable component that attracts/repels flow as well as an oscillatory component; the resulting linear motion resembles a spiral that asymptotically approaches or departs the equilibrium point. The $L_{4/5}$ points in the Pluto-Charon system are characterized by a similar spiral-type linearization. The properties of and applications for these “spiral manifolds” remain to be investigated.
3. **Energy plane intersections** —Strategies to leverage the intersection of two energy planes parameterized by the same low-thrust acceleration magnitude, a_{lt} , and a β angle of zero are presented in Section 4.3. Extending these tools to incorporate different a_{lt} magnitudes, including one ballistic plane ($a_{lt} = 0$) and one low-thrust plane ($a_{lt} \neq 0$), as well as non-zero β angles will greatly

increase the capability of this tool. Due to the complexity of the mathematics, it would be particularly useful to build a software tool to display the intersection geometry and the corresponding maps at the intersection hyperplane.

4. **Control curve extensions** —The design algorithms that leverage control points and control curves, described in Section 4.2, may be extended to incorporate nonzero β angles for applications to spatial trajectories. Additionally, feasible region geometries that are non-rectangular may be of interest to enable more targeted analysis.
5. **Quasi-periodic low-thrust orbits** —Many of the low-thrust periodic orbits (LTPOs) explored in this work possess a nontrivial center subspace, i.e., quasi-periodic orbits exist near the LTPOs. The computation of these structures and an exploration of their properties, particularly in regimes where no ballistic quasi-periodic structures are apparent, may facilitate novel trajectory options.
6. **LTPO family bifurcations** —Bifurcations in LTPO families are apparent in Section 3.4.2; the families that result from these bifurcations remain to be computed and may offer even more exotic geometries than already available from the LTPOs that are initialized directly from the equilibrium point center manifold.
7. **Structure in velocity-aligned model** —Clear distinctions between flow patterns are apparent in the periapsis maps constructed for velocity-aligned low-thrust arcs in Section 4.6. However, the CR3BP+LT with this orientation policy is nonautonomous and does not include dynamical structures such as periodic orbits or invariant manifolds to bound the various flow patterns. Nevertheless, order persists amidst the chaos; a flow-based investigation (e.g., the computation of Lagrangian Coherent Structures and/or finite-time Lyapunov exponent fields) may supply additional insight.

These recommendations offer several potential areas for future research to further support the construction of preliminary low-thrust trajectory designs.

REFERENCES

- [1] M. D. Rayman, P. A. Chadbourne, J. S. Culwell, and S. N. Williams. Mission design for Deep Space 1: A low-thrust technology validation mission. *Acta Astronaut.*, 45(4):381–388, 1999.
- [2] M. Rayman, T. Fraschetti, C. Raymond, and C. Russel. Dawn: A mission in development for exploration of main belt asteroids Vesta and Ceres. *Acta Astronaut.*, 58:605–616, 2006.
- [3] J. Kawaguchi, A. Fujiwara, and T. Uesugi. Hayabusa - its technology and science accomplishment summary and Hayabusa-2. *Acta Astronaut.*, 62(10-11): 639–647, May-June 2008.
- [4] Y. Tsuda, M. Yoshikawa, M. Abe, H. Minamino, and S. Nakazawa. System design of the Hayabusa 2 - asteroid sample return mission to 1999 JU3. *Acta Astronaut.*, 91:356–362, October-November 2013.
- [5] D. Y. Oh, S. Collins, D. Goebel, B. Hart, G. Lantoine, S. Snyder, G. Whiffen, L. Elkins-Tanton, P. Lord, Z. Pirkl, and L. Rotlisburger. Development of the psyche mission for NASA’s discovery program. In *35th International Electric Propulsion Conference*, Atlanta, Georgia, 2017.
- [6] N. Bosanac, A. D. Cox, K. C. Howell, and D. C. Folta. Trajectory design for a cislunar cubesat leveraging dynamical systems techniques: The Lunar IceCube mission. *Acta Astronaut.*, 144:283–296, March 2018.
- [7] M. L. McGuire, L. M. Burke, S. L. McCarty, K. J. Hack, R. J. Whitley, D. C. Davis, and C. Ocampo. Low-thrust cis-lunar transfers using a 40 kw-class solar electric propulsion spacecraft. In *AAS/AIAA Astrodynamics Specialist Conference*, Columbia River Gorge, Stevenson, Washington, August 2017.
- [8] R. W. Farquhar and A. Kamel. Quasi-periodic orbits around the transular libration point. *Celest. Mech. Dyn. Astron.*, 7(4):458–473, June 1973.
- [9] J. V. Breakwell, A. A. Kamel, and M. J. Ratner. Station-keeping for a translunar communication station. *Celest. Mech.*, 10:358–373, 1974.
- [10] R. W. Farquhar, D. P. Muhonen, and D. L. Richardson. Mission design for a halo orbiter of the Earth. *J. Spacecr. Rockets*, 14:170–177, January 1977.
- [11] V. Domingo, B. Fleck, and A. I. Poland. The SOHO mission: An overview. In B. Fleck, V. Domingo, and A. Poland, editors, *The SOHO Mission*. Springer, Dordrecht, 1995.
- [12] M. W. Lo, B. G. Williams, W. E. Bollman, D. Han, Y. Hahn, J. L. Bell, E. A. Hirst, R. A. Corwin, P. E. Hong, K. C. Howell, B. T. Barden, and R. S. Wilson. GENESIS mission design. *J. Astronaut. Sci.*, 49(1):169–184, 2001.

- [13] D. Folta, M. Woodard, K. C. Howell, C. Patterson, and W. Schlei. Application of multi-body dynamical environments: The ARTEMIS transfer trajectory design. *Acta Astronaut.*, 73:237–249, 2012.
- [14] W. S. Koon, M. W. Lo, J. E. Marsden, and S. D. Ross. *Dynamical Systems, the Three-Body Problem and Space Mission Design*. Springer, New York, 2011.
- [15] M. Belló, G. Gómez, and J. J. Masdemont. Invariant manifolds, Lagrangian trajectories and space mission design. In *Space Manifold Dynamics*, pages 1–96. Springer New York, November 2009.
- [16] R. L. Anderson. *Low-Thrust Trajectory Design for Resonant Flybys and Captures Using Invariant Manifolds*. Ph.D. dissertation, University of Colorado at Boulder, Boulder, Colorado, 2005.
- [17] G. Mingotti, F. Topputo, and F. Bernelli-Zazzera. Combined optimal low-thrust and stable-manifold trajectories to the Earth-Moon halo orbits. In *AIP Conference Proceedings*. AIP, 2007.
- [18] J. Stuart. *A Hybrid Systems Strategy for Automated Spacecraft Tour Design and Optimization*. Ph.D. dissertation, Purdue University, West Lafayette, Indiana, May 2014.
- [19] F. Topputo. *Low-Thrust Non-Keplerian Orbits: Analysis, Design, and Control*. Ph.D. dissertation, Politecnico di Milano, 2005.
- [20] D. Grebow, M. Ozimek, and K. Howell. Design of optimal low-thrust lunar pole-sitter missions. *J. Astronaut. Sci.*, 58(1):55–79, January 2011.
- [21] R. Pritchett, E. Zimovan, and K. C. Howell. Impulsive and low-thrust transfer design between stable and nearly stable periodic orbits in the restricted problem. In *AIAA SciTech Forum*, Kissimmee, Florida, January 2018.
- [22] G. Mingotti, F. Topputo, and F. Bernelli-Zazzera. Low-energy, low-thrust transfers to the Moon. *Celest. Mech. Dyn. Astron.*, 105:61–74, 2009.
- [23] R. L. Anderson and M. W. Lo. Role of invariant manifolds in low-thrust trajectory design. *J. Guid. Control Dyn.*, 32(6):1921–1930, November 2009.
- [24] G. Mingotti, F. Topputo, and F. Bernelli-Zazzera. Optimal low-thrust invariant manifold trajectories via attainable sets. *J. Guid. Control Dyn.*, 34(6):1644–1656, November 2011.
- [25] A. Das-Stuart, K. C. Howell, and D. C. Folta. A rapid trajectory design strategy for complex environments leveraging attainable regions and low-thrust capabilities. In *68th International Astronautical Congress*, Adelaide, Australia, September 2017.
- [26] J. F. L. Simmons, A. J. C. McDonald, and J. C. Brown. The restricted 3-body problem with radiation pressure. *Celest. Mech.*, 35:145–187, February 1985.
- [27] C. R. McInnes, A. J. C. McDonald, J. F. L. Simmons, and E. W. MacDonald. Solar sail parking in restricted three-body systems. *J. Guid. Control Dyn.*, 17(2), March 1994.

- [28] A. McInnes. Strategies for solar sail mission design in the circular restricted three-body problem. Master's thesis, Purdue University, August 2000.
- [29] A. D. Cox, K. C. Howell, and D. C. Folta. Dynamical structures in a combined low-thrust multi-body environment. In *AAS/AIAA Astrodynamics Specialist Conference*, Columbia River Gorge, Stevenson, Washington, August 2017.
- [30] M. Y. Morimoto, H. Yamakawa, and K. Uesugi. Artificial equilibrium points in the low-thrust restricted three-body problem. *J. Guid. Control Dyn.*, 30(5), September 2007.
- [31] S. Baig and C. R. McInnes. Artificial three-body equilibria for hybrid low-thrust propulsion. *J. Guid. Control Dyn.*, 31(6):1644–1655, November 2008.
- [32] S. B. Broschart and D. J. Scheeres. Control of hovering spacecraft near small bodies: Application to asteroid 25143 Itokawa. *J. Guid. Control Dyn.*, 28(2): 343–354, March - April 2005.
- [33] A. Farrés and À. Jorba. Solar sail surfing along families of equilibrium points. *Acta Astronaut.*, 63:249–257, July 2008.
- [34] A. Farrés and N. Miguel. Solar sailing at the 14/15 libration points. In *AAS/AIAA Astrodynamics Specialist Conference*, Columbia River Gorge, Stevenson, Washington, August 2017.
- [35] A. D. Cox, K. C. Howell, and D. C. Folta. Trajectory design leveraging low-thrust, multi-body equilibria and their manifolds. *J. Astronaut. Sci.*, 2020. Available online April 14, 2020.
- [36] A. Mittal and K. Pal. Artificial equilibrium points in the low-thrust restricted three-body problem when both primaries are oblate spheroids. *Int. J. Astron. Astrophys.*, 8(4):406–424, January 2018.
- [37] A. D. Cox, K. C. Howell, and D. C. Folta. Transit and capture in the planar three-body problem leveraging low-thrust dynamical structures. In *29th AAS/AIAA Space Flight Mechanics Meeting*, Ka'anapali, Maui, Hawai'i, January 2019.
- [38] A. D. Cox, K. C. Howell, and D. C. Folta. Dynamical structures in a low-thrust, multi-body model with applications to trajectory design. *Celest. Mech. Dyn. Astron.*, 131(12), 2019. Available Online.
- [39] A. D. Cox, K. C. Howell, and D. C. Folta. High-energy lunar capture via low-thrust dynamical structures. In *AAS/AIAA Astrodynamics Specialist Conference*, Portland, Maine, August 2019.
- [40] M. Corless. AAE 203 notes, Purdue University. Online, December 2009.
- [41] D. T. Greenwood. *Principles of Dynamics*. Prentice-Hall, 2nd edition, 1988.
- [42] E. D. Gustafson and D. J. Scheeres. Dynamically relevant local coordinates for halo orbits. In *AIAA/AAS Astrodynamics Specialist Conference and Exhibit*, Honolulu, Hawaii, August 2008.

- [43] M. Rayman, P. Varghese, D. Lehman, and L. Livesay. Results from the Deep Space 1 technology validation mission. In *International Astronautical Congress, Session IAA.11.2: Small Planetary Missions*, Amsterdam, The Netherlands, 1999.
- [44] K. Nishiyama, S. Hosoda, K. Ueno, R. Tsukizaki, and H. Kuninaka. Development and testing of the Hayabusa2 ion engine system. *Trans. JSASS Aerospace Tech. Japan*, 14(ists30):131–140, 2016.
- [45] C. Russel and C. Raymond. *The Dawn Mission to Minor Planets 4 Vesta and 1 Ceres*. Springer, Berlin, 2012. ISBN 978-1-4614-4902-7.
- [46] J. Bekenstein and J. Magueijo. Modified newtonian dynamics habitats within the solar system. *Phys Rev D*, 2006.
- [47] A. Farres, D. C. Folta, and C. Webster. Using spherical harmonics to model solar radiation pressure accelerations. In *AAS/AIAA Astrodynamics Specialist Conference*, Columbia River Gorge, Stevenson, Washington, August 2017.
- [48] H. Oberth. Ways to spaceflight. techreport NASA Technical Translation F-622, NASA, Washington, D.C., 1972.
- [49] G. G. Wawrzyniak and K. C. Howell. Look-ahead flight path control for solar sail spacecraft. *Proceedings of the Institution of Mechanical Engineers, Part G: Journal of Aerospace Engineering*, 227(12):1938–1952, November 2012.
- [50] V. Szebehely. *Theory of Orbits: The Restricted Problem of Three Bodies*. Academic Press, New York, 1967.
- [51] K. R. Meyer and D. C. Offin. *Introduction to Hamiltonian Dynamical Systems and the N-Body Problem*. Springer Nature, 3rd edition, 2017.
- [52] R. Thom and D. H. Fowler. *Structural Stability and Morphogenesis: An Outline of a General Theory of Models*. The Advanced Book Program, 1975.
- [53] V. I. Arnold. *Catastrophe Theory*. Springer, Berlin, Heidelberg, 1992.
- [54] J. E. Guckenheimer, L. Sirovich, and F. John. *Nonlinear Oscillations, Dynamical Systems, and Bifurcations of Vector Fields*. Springer, New York, 1983.
- [55] H. Keller. *Numerical Solution of Two Point Boundary Value Problems*. Society for Industrial and Applied Mathematics, Philadelphia, 1976.
- [56] K. E. Atkinson. *An Introduction to Numerical Analysis*. John Wiley and Sons, New York, second edition edition, 1989.
- [57] A. D. Cox. Transfers to a Sun-Earth saddle point: An extended mission design for LISA Pathfinder. M.S. thesis, Purdue University, West Lafayette, Indiana, May 2016.
- [58] D. J. Grebow. *Trajectory Design in the Earth-Moon System and Lunar South Pole Coverage*. Ph.D. dissertation, Purdue University, May 2010.
- [59] V. A. Yakubovich and V. M. Starzhinskii. *Linear Differential Equations with Periodic Coefficients*, volume 1. John Wiley and Sons, New York, 1975.

- [60] B. A. Steves, A. J. Maciejewski, and M. Hendry. *Chaotic Worlds: From Order to Disorder in Gravitational N-Body Dynamical Systems*, volume 227 of *Mathematics, Physics and Chemistry*. Springer, Dordrecht, Netherlands, 2006.
- [61] T. S. Parker and L. O. Chua. *Practical Numerical Algorithms for Chaotic Systems*. Springer-Verlag, Berlin, 1989.
- [62] L. Perko. *Differential Equations and Dynamical Systems*. Springer, New York, 2001.
- [63] M. Hénon. Numerical exploration of the restricted three-body problem. In G. Kontopoulos, editor, *The Theory of Orbits in the Solar System and in Stellar Systems*, volume 25, pages 157–169. IAU Symposium, 1966.
- [64] R. Broucke. Stability of periodic orbits in the elliptic, restricted, three-body problem. *AIAA Journal*, 7(6):1003–1009, 1969.
- [65] C. Conley. Low energy transit orbits in the restricted three-body problem. *SIAM Rev. Soc. ind. Appl. Math*, 16:732–746, 1968.
- [66] T. Swenson, M. W. Lo, B. Anderson, and T. Gordordo. The topology of transport through planar Lyapunov orbits. In *AIAA SciTech Forum*, Kissimmee, Florida, January 2018.
- [67] A. Wintner. Grundlagen einer Genealogie der periodischen Bahnen im restringierten Dreikörperproblem. *Math. Zeitsch.*, 34(1):321–349, 1932.
- [68] M. Hénon. *Generating Families in the Restricted Three-Body Problem*, volume 52 of *Lecture Notes in Physics Monographs*. Springer-Verlag Berlin Heidelberg, 1 edition, 1997.
- [69] E. Doedel and V. Romanov. Elemental periodic orbits associated with the libration points in the circular restricted 3-body problem. *International Journal of Bifurcation and Chaos*, 17(8), 2007.
- [70] H. Keller. Numerical solutions of bifurcations and nonlinear eigenvalue problems. In P. Rabinowitz, editor, *Applications of Bifurcation Theory*, pages 359–384. Academic Press, 1977.
- [71] R. Seydel. *Practical Bifurcation and Stability Analysis: From Equilibrium to Chaos*. New York: Springer-Verlag, 1994.
- [72] A. Farrés. Transfer orbits to l4 with a solar sail in the Earth-Sun system. *Acta Astronaut.*, 137:78–90, 2017.
- [73] W. S. Koon, M. W. Lo, J. E. Marsden, and S. D. Ross. Low energy transfer to the Moon. *Celest. Mech. Dyn. Astron.*, 81:63–73, 2001.
- [74] G. Gómez, W. Koon, M. Lo, J. Marsden, J. Masdemont, and S. Ross. Connecting orbits and invariant manifolds in the spatial restricted three-body problem. *Nonlinearity*, 17(5):1571–1606, 2004.
- [75] A. Petropoulos and J. Sims. A review of some exact solutions to the planar equations of motion of a thrusting spacecraft. In *2nd International Symposium on Low Thrust Trajectories*, Toulouse, France, June 2002.

- [76] A. Moore, S. Ober-Blöbaum, and J. Marsden. Trajectory design combining invariant manifolds with discrete mechanics and optimal control. *J. Guid. Control Dyn.*, 35(5):1507–1525, September 2012.
- [77] S. Hernandez and M. Akella. Lyapunov-based guidance for orbit transfers and rendezvous in Levi-Civita coordinates. *J. Guid. Control Dyn.*, 37(4), July 2014.
- [78] A. F. Haapala and K. C. Howell. A framework for construction of transfers linking periodic libration point orbits in the Earth-Moon spatial circular restricted three-body problem. *Int. J. Bifurcat. Chaos*, 26(5), May 2016.
- [79] M. E. Paskowitz and D. J. Scheeres. Robust capture and transfer trajectories for planetary satellite orbiters. *J. Guid. Control Dyn.*, 29(2):342–353, 2006.
- [80] D. C. Davis and K. C. Howell. Characterization of trajectories near the smaller primary in the restricted problem for applications. *J. Guid. Control Dyn.*, 35(1):116–128, January 2012.
- [81] K. Howell, D. Davis, and A. Haapala. Application of periapse maps for the design of trajectories near the smaller primary in multi-body regimes. *Mathematical Probl. Eng.*, 2012:1–22, 2012.
- [82] C. Short, D. Blazevski, K. Howell, and G. Haller. Stretching in phase space and applications in general nonautonomous multi-body problems. *Celest. Mech. Dyn. Astron.*, 122(3):213–238, June 2015.
- [83] General Mission Analysis Tool, available from gmatcentral.org. Software package, 2020.
- [84] Satellite Toolkit, Analytical Graphics Inc., Exton, PA. Software package, 2016.
- [85] J. Williams. A new architecture for extending the capabilities of the Copernicus trajectory optimization program. *Advances in the Astronautical Sciences*, 156, 2015.
- [86] FreeFlyer, a.i. solutions, Lanham, Maryland. Software package, 2016.
- [87] K. C. Howell and J. J. Guzmán. Generator. IOM AAE-0140-010, 2001.
- [88] M. Lo. LTool version 1.0G delivery. JPL, IOM 00-2147, September 2000.
- [89] A. Haapala, M. Vaquero, T. Pavlak, K. Howell, and D. Folta. Trajectory selection strategy for tours in the earth-moon system. In *AAS/AIAA Astrodynamics Specialist Conference*, Hilton Head, South Carolina, August 2013.
- [90] A. D. Cox, N. Bosanac, D. Guzzetti, K. C. Howell, D. C. Folta, and C. M. Webster. An interactive trajectory design environment leveraging dynamical structures in multi-body regimes. In *6th International Conference on Astrodynamics Tools and Techniques*, Darmstadt, Germany, March 2016.
- [91] D. C. Folta, C. M. Webster, N. Bosanac, A. D. Cox, D. Guzzetti, and K. C. Howell. Trajectory design tools for libration and cislunar environments. In *6th International Conference on Astrodynamics Tools and Techniques*, Darmstadt, Germany, March 2016.

- [92] D. C. Folta, N. Bosanac, D. Guzzetti, and K. C. Howell. An Earth-Moon system trajectory design reference catalog. *Acta Astronaut.*, 110:341–353, May-June 2015.
- [93] D. Guzzetti, N. Bosanac, A. Haapala, K. C. Howell, and D. C. Folta. Rapid trajectory design in the Earth-Moon ephemeris system via an interactive catalog of periodic and quasi-periodic orbits. *Acta Astronaut.*, 126:439–455, September-October 2016.
- [94] N. Bosanac, C. M. Webster, K. C. Howell, and D. C. Folta. Trajectory design and station-keeping analysis for the wide field infrared survey telescope mission. In *AAS/AIAA Astrodynamics Specialist Conference*, Columbia River Gorge, Stevenson, Washington, August 2017.
- [95] A. Haapala. *Trajectory Design in the Spatial Circular Restricted Three-Body Problem Exploiting Higher-Dimensional Poincaré Maps*. Ph.D. dissertation, Purdue University, West Lafayette, Indiana, December 2014.
- [96] M. Galassi, J. Davies, J. Theiler, B. Gough, G. Jungman, P. Alken, M. Booth, and F. Rossi. *GNU Scientific Library Reference Manual*, 3rd edition, 2009.
- [97] W. Schlei, K. C. Howell, X. Tricoche, and C. Garth. Enhanced visualization and autonomous extraction of Poincaré map topology. *J. Astronaut. Sci.*, 61: 170–197, 2014.
- [98] D. C. Davis, S. M. Phillips, and B. McCarthy. Multi-body mission design using the Deep Space Trajectory Explorer. In *26th AAS/AIAA Space Flight Mechanics Meeting*, Napa, California, February 2016.
- [99] A. D. Cox, X. S. Trofimov, A. Mysore, P. Polack, J. Stuart, S. Lombeyda, H. Mushkin, M. Hendrick, and S. Davidoff. Data visualization for astrodynamics, mission design, and navigation. JPL internal report, July 2016.
- [100] W. Schlei. *Interactive Spacecraft Trajectory Design Strategies Featuring Poincaré Map Topology*. Ph.D. dissertation, Purdue University, May 2017.
- [101] R. Becker and W. Cleveland. Brushing scatterplots. *Technometrics*, 29(2): 127–142, 1987.
- [102] J. Carroll and C. Carrithers. Blocking learner error states in a training-wheels system. *Hum. Factors*, 26(4):377–389, August 1984.
- [103] E. Hairer, S. P. Norsett, and G. Wanner. *Solving Ordinary Differential Equations*, volume I - Nonstiff Problems of *Springer Series in Computational Mathematics*. Springer, 2nd edition, November 2011.
- [104] J. Kawaguchi, A. Fujiwara, and T. K. Uesugi. The ion engines cruise operation and the Earth swingby of 'Hayabusa' (MUSES-C). In *55th International Astronautical Congress*, Vancouver, Canada, 2004.
- [105] Y. Tsuda, M. Yoshikawa, M. Abe, H. Minamino, and S. Nakazawa. System design of the Hayabusa 2–Asteroid sample return mission to 1999 JU3. *Acta Astronaut.*, 91:356–362, 2013.
- [106] H. Ji, F.-S. Lien, and E. Yee. A new adaptive mesh refinement data structure with an application to detonation. *J. Comput. Phys.*, 229(23):8981–8993, November 2010.

A. NUMERICAL INTEGRATION

Throughout this document, trajectories are propagated using version 3.6 of the [Apache Commons Math Java library](#)¹. Specifically, an embedded 8(5,3) Dormand-Prince integrator is employed for the numerical integration. The details of the method are available from the [documentation](#)²:

“This integrator is an embedded Runge-Kutta integrator of order 8(5,3) used in local extrapolation mode (i.e. the solution is computed using the high order formula) with stepsize control (and automatic step initialization) and continuous output. This method uses 12 functions evaluations per step for integration and 4 evaluations for interpolation.”

...

“This method is based on an 8(6) method by Dormand and Prince (i.e. order 8 for the integration and order 6 for error estimation) modified by Hairer and Wanner to use a 5th order error estimator with 3rd order correction.”

[103]

In general, a relative tolerance of 1e-12 and an absolute tolerance of 1e-14 are employed to minimize numerical error in the integration scheme.

¹<https://commons.apache.org/proper/commons-math/>

²<https://commons.apache.org/proper/commons-math/javadocs/api-3.6/org/apache/commons/math3/ode/nonstiff/DormandPrince853Integrator.html>

B. SYSTEM AND SPACECRAFT PARAMETERS

This appendix chapter lists detailed parameters for systems and spacecraft used throughout this document to enable others to reproduce the results as closely as possible.

Table B.1 lists system parameters for CR3BP systems used in this document

Table B.2 lists the low-thrust propulsion system parameters for a variety of spacecraft that are relevant to this analysis

Table B.1.: CR3BP System Parameters

P_1	P_2	μ [nondim]	L_* [km]	T_* [sec]
Earth	Moon	0.0121505842699404	384747.991979046	375699.859037759
Sun	Earth Barycenter	3.04042340382006e-06	149597894.005107	5022636.42910374
Sun	Mars Barycenter	3.22715499610173e-07	227940471.963575	9446616.3421449
Pluto	Charon	0.108539888353507	19596.2113365379	87830.6129323748

Table B.2.: Low-Thrust Spacecraft Parameters¹

Spacecraft	Engine Type	Propellant Type	Wet Mass [kg]	Propellant Mass [kg]	Max Spacecraft Thrust [mN]	Isp [sec]	Sources
Deep Space 1	NSTAR ²	Xenon	486.3	81.5	92	1900–3200	[43]
Hayabusa	IES ³	Xenon	510.0	66.2	22.8	2760–3000	[104, 44]
Hayabusa 2	IES ³	Xenon	608.6	66.5	27.0	2740–2890	[105, 44]
Dawn	NSTAR ²	Xenon	1217.8	425	91.0	1814–3127	[45]
Lunar IceCube	BIT-3 ⁴	Iodine	14	1.5	1.15	2500	[6]

¹ Many thanks to Robert Pritchett for locating references for many of these data

² NASA Solar electric propulsion Technology Application Readiness (NSTAR)

³ Ion Engines System (IES); includes four thrusters but operates only three at a time

⁴ Busek Ion Thruster (BIT)

C. MONTE CARLO ANALYSES

This chapter details the parameters and distributions employed in Monte Carlo analyses in this investigation. Many of these details are included in the text where an analysis is described, but the specifics of the implementation are not generally within the scope of the discussion and are relegated to this appendix.

C.1. Low-Thrust Hamiltonian Rate Validation

The goal of this Monte Carlo analysis is to measure the change in the H_{lt} value due to the time-varying spacecraft mass in a variety of CR3BP+LT systems. To obtain a result that represents the system as a whole, a large number of arcs are propagated. The initial conditions are uniformly distributed in the following ranges:

$$\{x, y, z\} \in [-1.2, 1.2]; \quad \{\dot{x}, \dot{y}, \dot{z}\} \in [-0.875, 0.875]; \quad m = 1.$$

These ranges capture the majority of the motion typically studied, including families of periodic orbits in the vicinity of the Lagrange points, both in and out of the plane. The low-thrust acceleration vector is assigned a constant thrust magnitude consistent with the Deep Space 1 parameters, $F = 9.2\text{e-}5$ kN, $M_{3,0} = 486$ kg, and the mass flow rate is modeled as a CSI process via Equation (2.92) with $I_{\text{sp}} = 1900$ sec. Although Deep Space 1 is capable of an I_{sp} of up to 3200 seconds (see Table B.2), the minimum I_{sp} value is employed to maximize the mass flow rate. Like the initial state, the orientation of the acceleration vector is randomly chosen from a uniform distribution of the two angles,

$$\alpha \in [-\pi, \pi], \quad \beta \in [-\pi/2, \pi/2],$$

that span the entire unit sphere; the orientation is fixed for each propagation. Accordingly, the magnitude of \vec{a}_{lt} changes only as the spacecraft mass evolves. Each arc is propagated until one of the following conditions is met:

1. $\tau \geq \pi$ – a maximum time-of-flight (TOF) is reached
2. $r_{13} \geq 2$ – a maximum distance from P_1 is reached
3. $r_{13} \leq 10^{-4}$ – a minimum distance from P_1 is reached
4. $r_{23} \leq 10^{-4}$ – a minimum distance from P_2 is reached
5. $m \leq 0.83$ – a minimum spacecraft mass is reached

As the goal is to compare results between systems, a consistent nondimensional maximum time-of-flight of π , or half of the system period, is employed in condition 1. Similar structures tend to have similar sizes in nondimensional units, e.g., a portion of the halo orbits in the Earth-Moon and Sun-Earth systems have periods of approximately π , corresponding to about 2 weeks in the Earth-Moon system and to about 6 months in the Sun-Earth system. On the other hand, the mass flow rate is a constant of the *dimensional* terms; the \dot{m} value for Deep Space 1 is approximately $4.94\text{e-}6$ kg/s². At this rate, the available propellant (17% of the spacecraft wet mass) is spent in 193.67 days. Accordingly, for CR3BP+LT systems with a rotation period greater than $2 \times 193.67 = 387.34$ days, the propellant will run out before the maximum time-of-flight is reached. The 5th condition ensures that the propagation ends when the available propellant has been depleted. The 2nd condition ends the propagation of trajectories departing the system. As this investigation is primarily interested in motion *near* the two primaries, arcs that depart before the time or propellant run out are not relevant. Finally, the 3rd and 4th conditions end the propagation of trajectories passing very close to the centers of the primary bodies. These distances are not identical to the physical radii of the bodies but are instead meant to avoid numerical difficulties at the singularities, i.e., at the center of the primaries.

Once a trajectory has been propagated, the H_{lt} values along the trajectory are computed. The metric of interest is the maximum deviation of H_{lt} from the initial value,

$$\max|\Delta H_{\text{lt}}| = \max_{\tau} |H_{\text{lt}}(\tau) - H_{\text{lt}}(0)|. \quad (2.123)$$

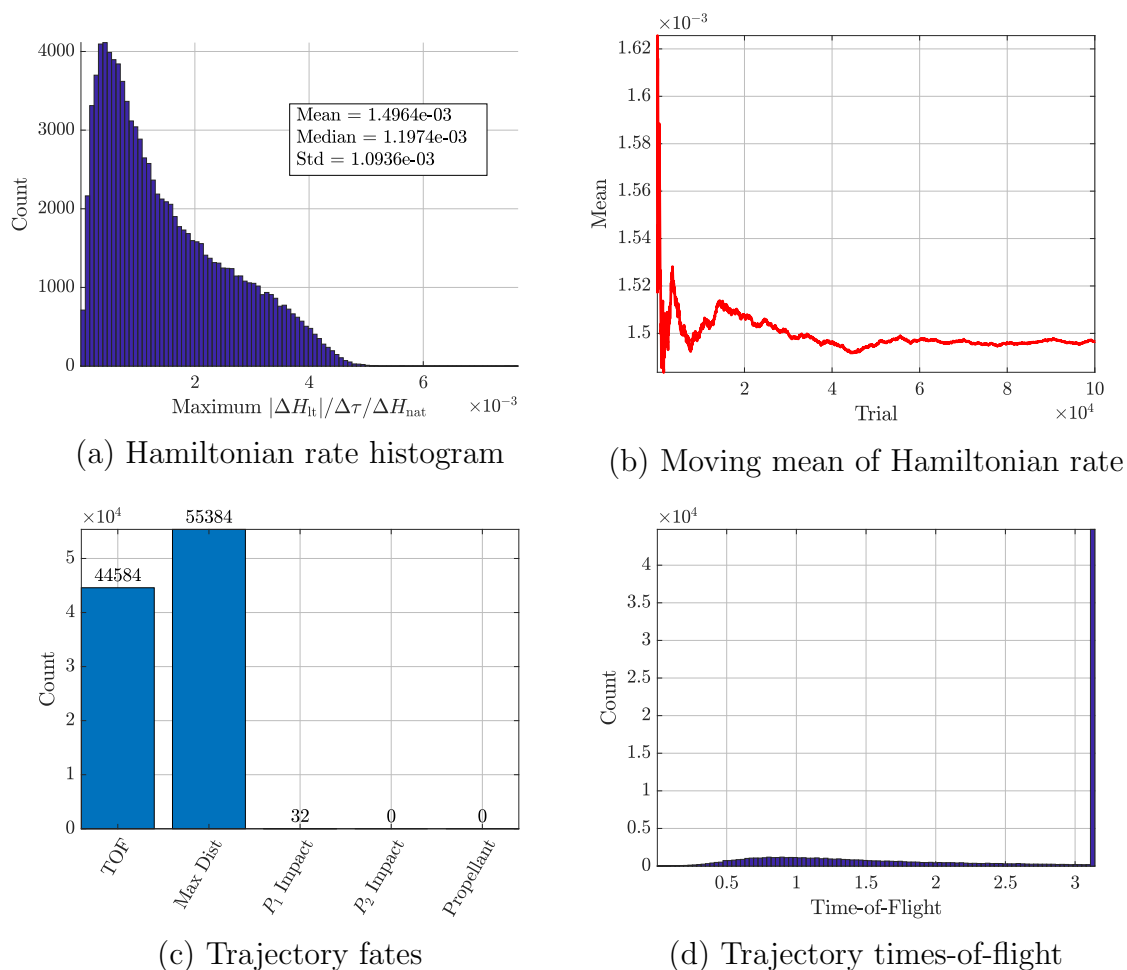
To account for the various arc times-of-flight, this energy change is scaled by the total time-of-flight on the arc,

$$\Delta\tau = \tau_f - 0, \quad (C.1)$$

where τ_f is not necessarily equal to the τ value associated with the maximum energy change as expressed in Equation (2.123). Finally, the maximum energy change is scaled by the natural Hamiltonian difference between the L_1 and L_5 points,

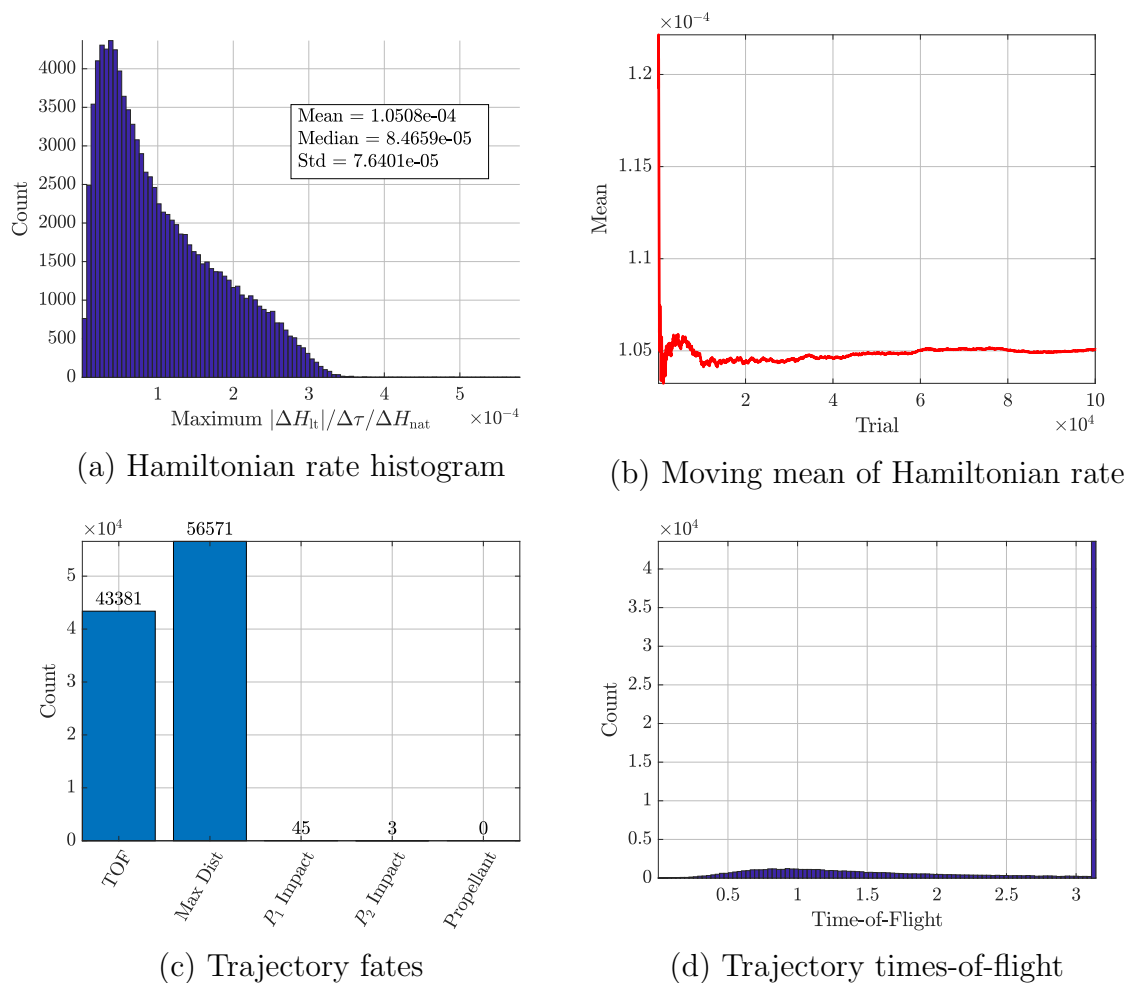
$$\Delta H_{\text{nat}} = H_{\text{nat}}(L_5) - H_{\text{nat}}(L_1), \quad (2.122)$$

as discussed in Section 2.2.6. To evaluate the energy rate, $\max|\Delta H_{\text{lt}}|/\Delta\tau/\Delta H_{\text{nat}}$, for a CR3BP+LT system, a large number of arcs are propagated and the energy rate is computed for each arc. The results of the Monte Carlo, plotted in Figure C.1 for the Earth-Moon system, may be evaluated in several ways. First, a histogram of the energy rates, as seen in Figure C.1(a), displays the distribution of the energy rate over the full Monte Carlo. The mean, median, and standard deviation of this distribution are included in the plot for reference. To validate that these statistics represent the behavior of the system, the mean value is plotted against the number of trials (i.e., the number of propagated arcs) in Figure C.1(b). The mean stabilizes after the first 60,000 trials; the median and standard deviation also stabilize in the same number of trials, though their evolutions are not plotted. To further validate the analysis, the “fates” of the propagated arcs are evaluated. Nearly half of the arcs remain within the maximum r_{13} distance, as seen by the in Figure C.1(c), until the maximum TOF is reached. The vast majority of the remaining arcs reach the maximum distance before the maximum TOF; only a small number of the arcs impact P_1 , as defined by

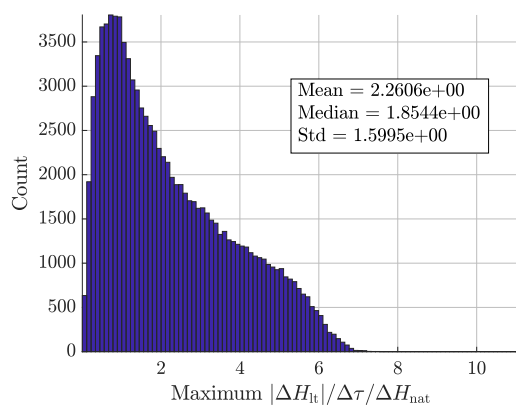
Figure C.1.: Earth-Moon ΔH_{t} Monte Carlo Results

the 3rd condition. Finally, because the maximum TOF is less than the time required to exhaust the propellant supplies, none of the propagations are ended to the mass constraint.

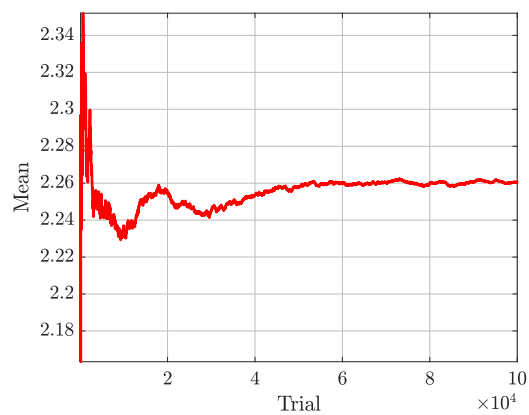
The analysis is repeated for the Pluto-Charon system and the results are collected in Figure C.2. Like the Earth-Moon system, the statistics describing the Hamiltonian rate stabilize within about 60,000 trials and the propagated arcs either reach the maximum TOF or the maximum r_{13} distance. Propagations in the Sun-EMB system, visualized in Figure C.3, follow a similar trend. Finally, results in the Sun-Mars system differ slightly from the others in the fate of the propagated arcs. The half-

Figure C.2.: Pluto-Charon ΔH_{t} Monte Carlo Results

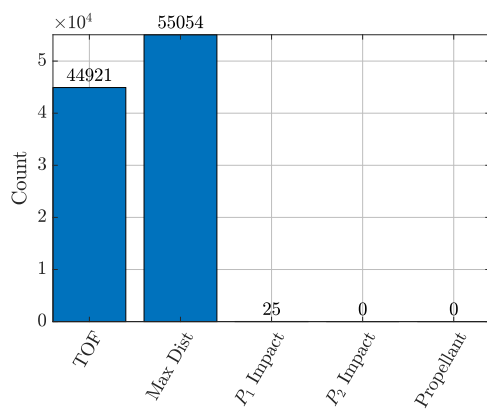
period of the Sun-Mars rotation is 343.5 days, much longer than the time required to exhaust the propellant. Thus, the majority of the propagations end due to the propellant constraint and no arcs reach the maximum TOF. The arcs that do not reach the propellant constraint escape the system, i.e., reach the maximum r_{13} distance. These results are discussed further in Section 2.2.6.



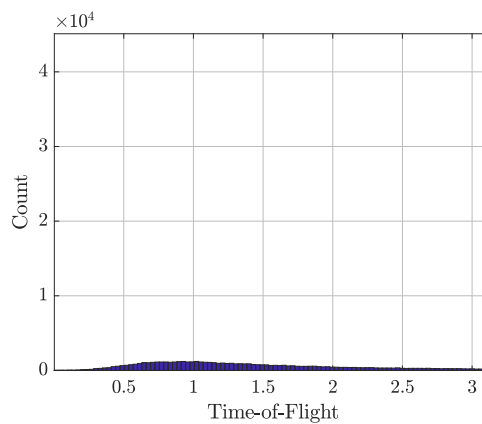
(a) Hamiltonian rate histogram



(b) Moving mean of Hamiltonian rate

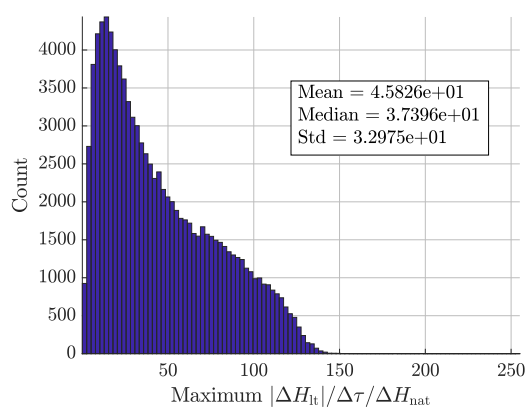


(c) Trajectory fates

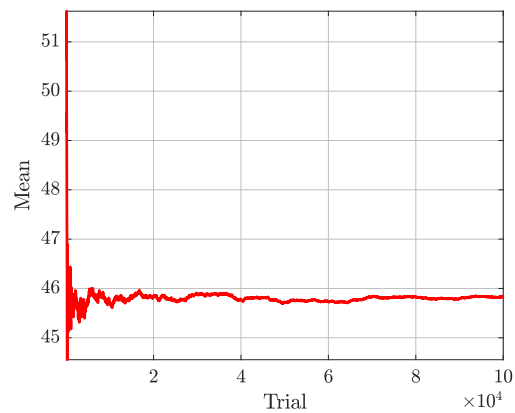


(d) Trajectory times-of-flight

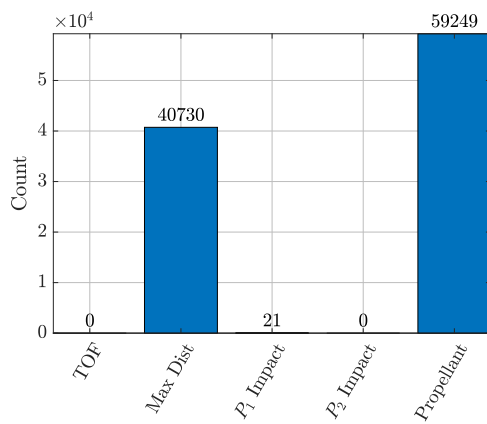
Figure C.3.: Sun-EMB ΔH_{lt} Monte Carlo Results



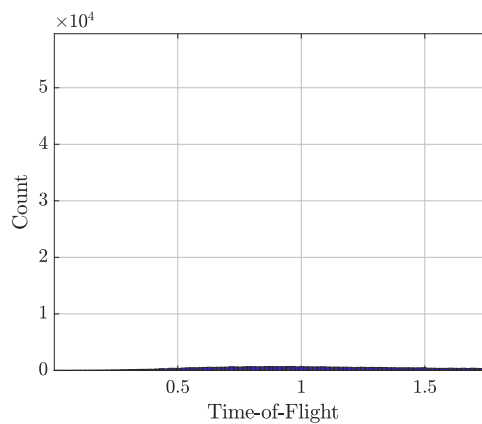
(a) Hamiltonian rate histogram



(b) Moving mean of Hamiltonian rate



(c) Trajectory fates



(d) Trajectory times-of-flight

Figure C.4.: Sun-Mars ΔH_{lt} Monte Carlo Barycenter Results

C.2. Validate acceleration magnitude decrease

A Monte Carlo analysis identical to the analysis described in Section C.1 is employed to explore the effect of changes in F on the low-thrust Hamiltonian evolution. In this case, the thrust magnitude is decreased from the Deep Space 1 capability of $9.2e-5$ kN to $1e-5$ kN. As postulated in Section 2.2.6, this thrust magnitude reduction should yield a $\dot{H}_{lt}/\Delta H_{nat}$ ratio of about $1e-2$. The results for the Sun-EMB system, plotted in Figure C.5, confirm this prediction. Compared to the results for $F = 9.2e-5$

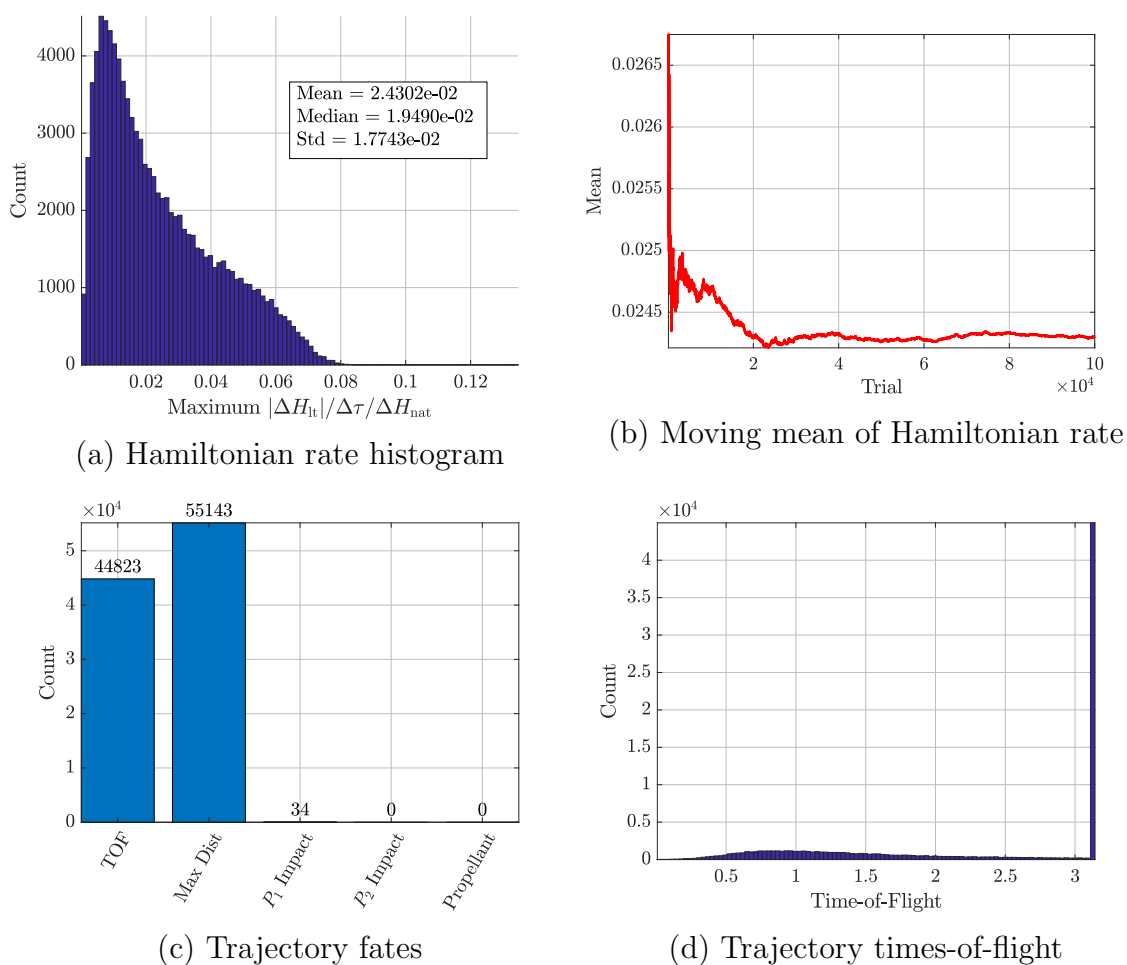


Figure C.5.: Sun-EMB ΔH_{lt} Monte Carlo results for $F = 9.2e-7$ kN

kN, the mean Hamiltonian rate has decreased by two orders of magnitude ($2.26e+00$ decreases to $2.43e-2$).

D. EQUILIBRIUM POINT SEARCH

The low-thrust equilibrium solutions solve Equations (3.15) – (3.17), reprinted below for convenience.

$$x_{eq} \left[1 - \frac{1-\mu}{r_{13}^3} - \frac{\mu}{r_{23}^3} \right] + \mu \left[-\frac{1-\mu}{r_{13}^3} - \frac{\mu}{r_{23}^3} \right] + \frac{\mu}{r_{23}^3} + a_{lt} \cos(\alpha) \cos(\beta) = 0, \quad (3.15)$$

$$y_{eq} \left[1 - \frac{1-\mu}{r_{13}^3} - \frac{\mu}{r_{23}^3} \right] + a_{lt} \sin(\alpha) \cos(\beta) = 0, \quad (3.16)$$

$$z_{eq} \left[-\frac{1-\mu}{r_{13}^3} - \frac{\mu}{r_{23}^3} \right] + a_{lt} \sin(\beta) = 0. \quad (3.17)$$

This system of three equations is a function of five variables, x , y , z , α , and β . Accordingly, infinitely many solutions exist. By selecting convenient values of specific variables (i.e., selecting values that remove terms from the equations, simplifying them to permit analytical solutions), insights about the structure of the solutions and several analytical solutions are available. The following list outlines the search for solutions.

1. Set $\alpha = 0$ or $\alpha = \pi$, i.e., set $\sin(\alpha) = 0$

As a result of this constraint, Equation (3.16) simplifies to

$$y_{eq} \left[1 - \frac{1-\mu}{r_{13}^3} - \frac{\mu}{r_{23}^3} \right] = 0. \quad (D.1)$$

The number of variables is reduced by one, but there are still infinitely many solutions (3 equations, 4 variables). Thus, additional constraints are required.

- (a) Set $y_{eq} \neq 0$

An analytical solution is available. See Section 3.2.3 for details.

- (b) Set $y_{eq} = 0$

Equation (3.16), i.e., Equation (D.1), is solved, and the number of variables

is reduced by one. The system (2 equations, 3 variables) still possesses infinitely many solutions. Additional constraints are required.

- i. Set $z_{eq} = 0$; (requires $\beta = 0$)

Equation (3.17) is solved and the number of variables is reduced by two. Under these conditions, Equation (3.15) is only a function of x but is transcendental. A one-dimensional line search yields three distinct solutions for the planar collinear points. See Section 3.2.1 for details.

- ii. Set $z_{eq} \neq 0$; (implies $\beta \neq 0$)

The system of 2 equations is a function of 3 variables (x, z, β); additional constraints are required.

- A. Set $\beta = \pm\pi/2$, i.e., set $\cos(\beta) = 0$

While the $\cos(\beta)$ term disappears from Equation (3.15), the system of 2 equations and 2 variables (x, z) is transcendental and no analytical solution or straightforward iterative solution is apparent.

- B. Set $x_{eq} = 0$

Similar to the solutions for $\beta = \pm\pi/2$, the equations appear transcendental and no solution is apparent. However, by exploring the limits of the low-thrust pseudo-potential gradient expressions, an approximate expression for the location of a point on the highly out-of-plane equilibria is derived. See Section 3.2.2 for the details.

- 2. Set $\beta = \pm\pi/2$; (implies $z_{eq} \neq 0$)

When the out-of-plane angle, β , is oriented orthogonal to the xy -plane, α is undefined. Accordingly, α is removed from the system, yielding a set of three equations and three variables (x, y, z). Equation (3.16) once again simplifies to the form expressed in Equation (D.1); additional constraints are implemented to gain further insight.

- (a) Set $y_{eq} \neq 0$

An analytical solution is available. See Section 3.2.3 for details.

(b) Set $y_{eq} = 0$

Equation (3.16), i.e., Equation (D.1), is solved, reducing the system to two equations with two variables (x, z) . With the implicit constraint that $z \neq 0$, this case is identical to 1.b.ii.A.

3. Set $\beta = 0$; (implies $z = 0$)

The number of variables is reduced by one; the system of two equations is a function of three variables (x, y, α) . Further constraints are necessary to obtain a distinct solution.

(a) Set $y_{eq} \neq 0$

Because the $a_{lt} \sin(\alpha) \cos(\beta)$ term in Equation (3.16) is not zero, terms within the square brackets are not necessarily zero and the familiar strategy of substituting those terms into Equation (3.15) does not apply. The system of two equations remains parameterized by three variables.

i. Set $\alpha = 0$

Identical to 1.a

ii. Set $\alpha = \pm\pi/2$

This constraint removes the low-thrust terms from Equation (3.15), but the remaining system of two equations, parameterized by x and y , is transcendental and cannot be solved analytically.

iii. Set $x_{eq} = 0$

Similar to the $\alpha = \pm\pi/2$ constraint, the system (now parameterized by y and α) is transcendental and no analytical solution is available.

(b) Set $y_{eq} = 0$

As a result of this constraint, Equation (3.16) reduces to

$$a_{lt} \sin(\alpha) \cos(\beta) = a_{lt} \sin(\alpha) = 0. \quad (\text{D.2})$$

This equation is satisfied if and only if $\alpha = 0$ or π ; thus, this case is identical to 1.b.i.

4. Set $\alpha = \pm\pi/2$

With the selection of α , the number of free variables is reduced by one, yielding a system of three equations and four variables (x, y, z, β). Additional constraints are required.

(a) Set $y_{eq} \neq 0$

Because the $a_{lt} \sin(\alpha) \cos(\beta)$ term is not zero under these constraints, Equation (3.16) is not simplified to the form expressed in Equation (D.1); additional constraints are required.

i. Set $z_{eq} = 0$; (implies $\beta = 0$)

The resulting system of two equations and two variables (x, y) is transcendental and cannot be solved.

ii. Set $z_{eq} \neq 0$; (implies $\beta \neq 0$)

The system of three equations and four variables (x, y, z, β) requires additional constraints to yield a distinct solution.

A. Set $\beta = \pm\pi/2$

Identical to 2.a

(b) Set $y_{eq} = 0$ i. Set $z_{eq} = 0$; (implies $\beta = 0$)ii. Set $z_{eq} \neq 0$; (implies $\beta \neq 0$)

E. MISCELLANEOUS ALGORITHMS

A variety of algorithms have been developed to support the analyses in this investigation. Several of the more complex algorithms are explained below to facilitate future research in the CR3BP+LT.

E.1. Distinct Equilibrium Point Computation

A set of distinct equilibrium points is parameterized by the system mass ratio, μ , and the low-thrust acceleration parameters, a_{lt} , α , and β . In this investigation, variations in the equilibrium solutions with the α angle are explored. Accordingly, the sets of equilibria, \mathbb{E}_i , are computed for fixed μ , a_{lt} , and β values; the α angle varies throughout each set. Once these sets, the zero acceleration contours (ZACs), are constructed, the distinct equilibrium solutions at a particular α angle may be computed. The processes to compute the ZACs and the distinct equilibrium points are described in detail below.

ZAC Computation via Continuation

To compute the ZACs, the μ , a_{lt} , and β parameters are first fixed. Depending on the value of these parameters, up to six or as few as two distinct ZACs may exist. The number of distinct ZACs for the specified μ , a_{lt} , and β values is available by comparing a_{lt} to the saddles in the ballistic gravitational acceleration magnitude field, as discussed in Section 3.2.5. However, computing the locations of these saddles can be difficult due to the topology of the acceleration magnitude field; the differential corrections schemes attempted thus far frequently fail to converge. To avoid this numerical difficulty, six *ZAC candidates* are constructed. To distinguish these candi-

dates from the true ZACs, the candidates are denoted $\tilde{\mathbb{E}}_i$, where i is the index of the candidate ZAC. A single point on each $\tilde{\mathbb{E}}_i$ structure is computed from the analytical and semi-analytical solutions derived in Sections 3.2.1, 3.2.2, and 3.2.3, as defined in the following list:

$\tilde{\mathbb{E}}_1$ is initialized at the collinear equilibrium point for $\alpha = 180^\circ$ and $\beta = 0^\circ$ that solves Equation (3.19)

$\tilde{\mathbb{E}}_2$ is initialized at the collinear equilibrium point for $\alpha = 180^\circ$ and $\beta = 0^\circ$ that solves Equation (3.20)

$\tilde{\mathbb{E}}_3$ is initialized at the collinear equilibrium point for $\alpha = 180^\circ$ and $\beta = 0^\circ$ that solves Equation (3.21)

$\tilde{\mathbb{E}}_4$ is initialized from the analytical solution described by Equation (3.42) for $\alpha = 180^\circ$ and $y > 0$

$\tilde{\mathbb{E}}_5$ is initialized from the analytical solution described by Equation (3.42) for $\alpha = 180^\circ$ and $y < 0$

$\tilde{\mathbb{E}}_6$ is initialized at the highly-out-of-plane point described by Equation (3.31) for $\alpha = 180^\circ$

Of these six initializations, only the points for the $\tilde{\mathbb{E}}_4$ and $\tilde{\mathbb{E}}_5$ structures are exact locations of equilibrium points. Thus, a differential corrections process is employed to solve for the location (x , y , and z) of a solution at the specified α , β , a_{lt} , and μ values for each candidate ZAC. In other words, the location variables are varied to satisfy the constraint Equations (3.15) – (3.17). In the systems explored in this investigation, namely the Earth-Moon and Sun-EMB systems, convergence from these initial solutions to exact equilibrium points is rapid regardless of the required β angle.

Once the initial solutions on each candidate ZAC are corrected, a pseudo-arclength continuation process is employed to construct an entire candidate ZAC. The location variables (x , y , and z) are varied, as is the α angle, while the β , a_{lt} , and μ values are held constant. It is frequently useful to limit the step size of the continuation process so that the change in α between subsequent solutions is reasonably small; in this work, a maximum angle change of 0.5° is used to supply a visually continuous

structure. Following the computation of the six candidate ZACs, the solutions may be concatenated into the true ZACs. In practice, this is not always necessary. For example, when plotting the ZACs to display the α angle, as in Figure 3.7, or stability properties, as in Figure 3.17, the points from the candidate ZACs may be plotted together; any overlap between the candidate ZACs is not apparent. However, when the ZACs must be identified as distinct structures, the concatenation process benefits by recognizing the following qualitative configurations:

1. All six candidate ZACs are distinct ZACs, i.e., $\mathbb{E}_i = \tilde{\mathbb{E}}_i$, as in Figure 3.7(a). This configuration generally corresponds to very small a_{1t} values or to β angles near $\pm 90^\circ$.
2. The three candidate ZACs initialized near L_3 , L_4 , and L_5 are merged into \mathbb{E}_3 , as in Figures 3.7(b) and 3.7(c), i.e.,

$$\mathbb{E}_1 = \tilde{\mathbb{E}}_1, \quad \mathbb{E}_2 = \tilde{\mathbb{E}}_2, \quad \mathbb{E}_3 = \left\{ \tilde{\mathbb{E}}_3, \tilde{\mathbb{E}}_4, \tilde{\mathbb{E}}_5 \right\}, \quad \mathbb{E}_4 = \tilde{\mathbb{E}}_6.$$

This configuration is generally available for non-large $|\beta|$ angles (e.g., below 60°) and moderate a_{1t} values (e.g., $7e-2$ in the Earth-Moon system or $1e-2$ in the Sun-EMB system)

3. The \mathbb{E}_1 and \mathbb{E}_2 ZACs together include $\tilde{\mathbb{E}}_i$ for $i = 1, \dots, 5$, and $\mathbb{E}_3 = \tilde{\mathbb{E}}_6$, as in Figure 3.7(d). This configuration corresponds to non-large $|\beta|$ angles and to large a_{1t} values (e.g., $5e-1$ in the Earth-Moon system or $3e-2$ in the Sun-EMB system)

In configuration 3, the \mathbb{E}_1 and \mathbb{E}_2 structures are composed of the first five candidate ZACs; no general algorithmic method to determine which candidate ZACs form the true ZACs has been identified, but they are straightforwardly sorted when viewed in configuration space.

Interpolation and Corrections

Following the computation of the candidate ZACs for a specified μ , a_{lt} , and β combination, a set of distinct equilibrium solutions may be identified for a particular α angle. First, an interpolation process computes all of the candidate equilibrium points on a single candidate ZAC at the desired α angle. Next, the candidate equilibrium points from all of the candidate ZACs are adjusted via differential corrections to the exact equilibrium solution given the required μ , a_{lt} , α , and β parameters. Finally, the locations of the converged solutions are compared to one another to identify the unique, i.e., distinct solutions. In this investigation, two points are deemed distinct if any of the position differences (i.e., Δx , Δy , or Δz) is greater than a small tolerance, $\epsilon > 0$

E.2. Mesh Refinement

To construct the apsis maps in Section 4.6, a large number of initial conditions are propagated to a set of stopping conditions. Each map is visualized by coloring the initial conditions by the “fate” of the resulting arc. Regions of distinct fate behaviors are identified and may be targeted to deliver different types of low-thrust trajectories. Because the fate metric is discrete, the number of computations is greatly reduced by employing a mesh refinement algorithm. In other words, only the boundaries between distinct regions need to be located; points within each region need not be evaluated. As mesh refinement algorithms are actively studied by other researchers, an existing algorithm has been employed in this investigation; the cell-based structured adaptive mesh refinement (CSAMR) algorithm described by Ji, Lien, and Yee [106] is selected.

The mesh is defined as a set of rectangular *cells*; the four corners of the cell are *nodes*, as displayed in Figure E.1. The size of a cell is denoted by its *level*. When a mesh is initialized, it consists of a single cell at level 0. In the example displayed in the figure, the level 0 cell has corner nodes at $(-1,-1)$, $(-1, 1)$, $(1, 1)$, and $(1, -1)$. Each node is evaluated to determine the mesh *metric* at the node location; in this example,

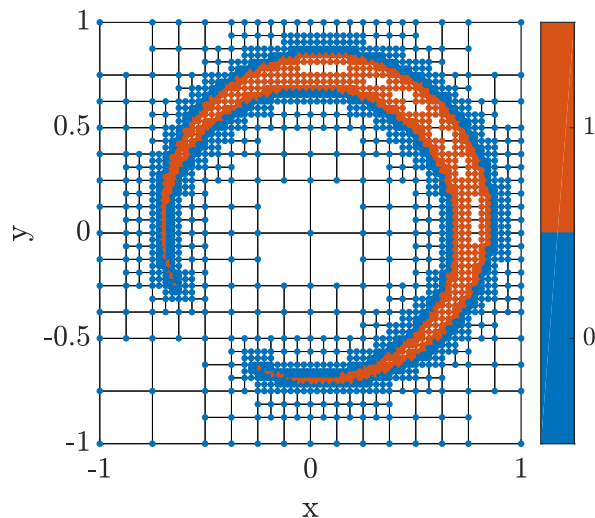


Figure E.1.: Example of a mesh; cells are marked by black squares and nodes are colored points

the metric is a simple binary value, but in the apsis map application, the metric is the fate of a trajectory propagated from the node location. If each of the four corners has the same metric value, the cell is *uniform*; otherwise the cell is non-uniform. The goal of the mesh refinement algorithm is to subdivide non-uniform cells to refine the location of the discontinuities between node metrics.

Several algorithmic parameters are required to tune the mesh refinement process. First, a minimum refinement level is specified. Every cell is subdivided, regardless of its uniformity, until this minimum level is reached. For example, consider the level 0 cell in Figure E.1. The four corners at $|x| = 1$ and $|y| = 1$ all yield the same metric; thus, the level 0 cell is uniform. However, the interior of the cell is not entirely uniform and additional refinement must occur to isolate the red, sickle-shaped region. Accordingly, the minimum level is set to three and the level 0 cell is subdivided three times, yielding $4^3 = 64$ equally-sized level 3 cells. The nodes associated with these smaller cells locate some of the red points in the figure, yielding non-uniform cells that are subdivided further to refine the boundary between the metric values. The second parameter specifies a minimum cell size to limit the duration of the refinement

process. Left unchecked, refinement will continue to subdivide the cells forever. Thus, the minimum cell size ensures that the refinement cannot proceed indefinitely.

With the aforementioned parameters selected for an analysis, the refinement algorithm begins. The refinement loop, represented by the orange box in Figure E.2, runs until a flag indicates that the refinement should halt. During the first few it-

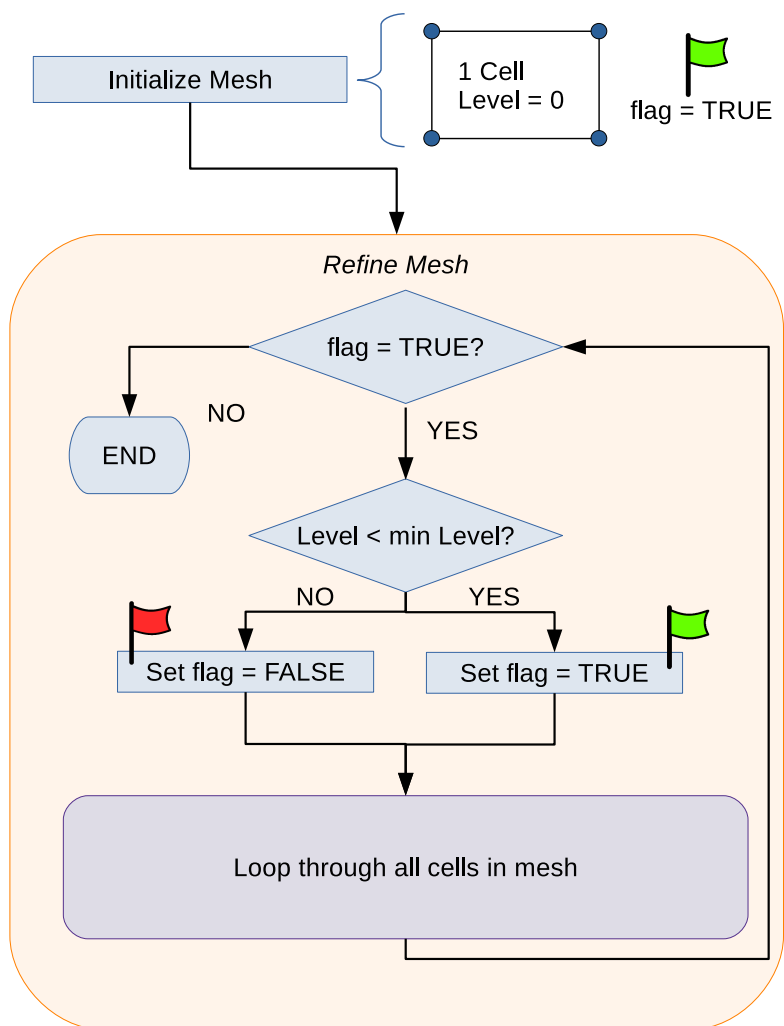


Figure E.2.: Mesh refinement algorithm

erations, the flag is set to true to ensure the minimum mesh level is reached. Once that threshold is surpassed, the flag remains true while new subdivisions are made. The bulk of the algorithm logic is contained within the loop through all of the cells

in the mesh, represented by the purple box in Figure E.2 and expanded in Figure E.3. Note that once the minimum level has been reached, the subdivision of a cell

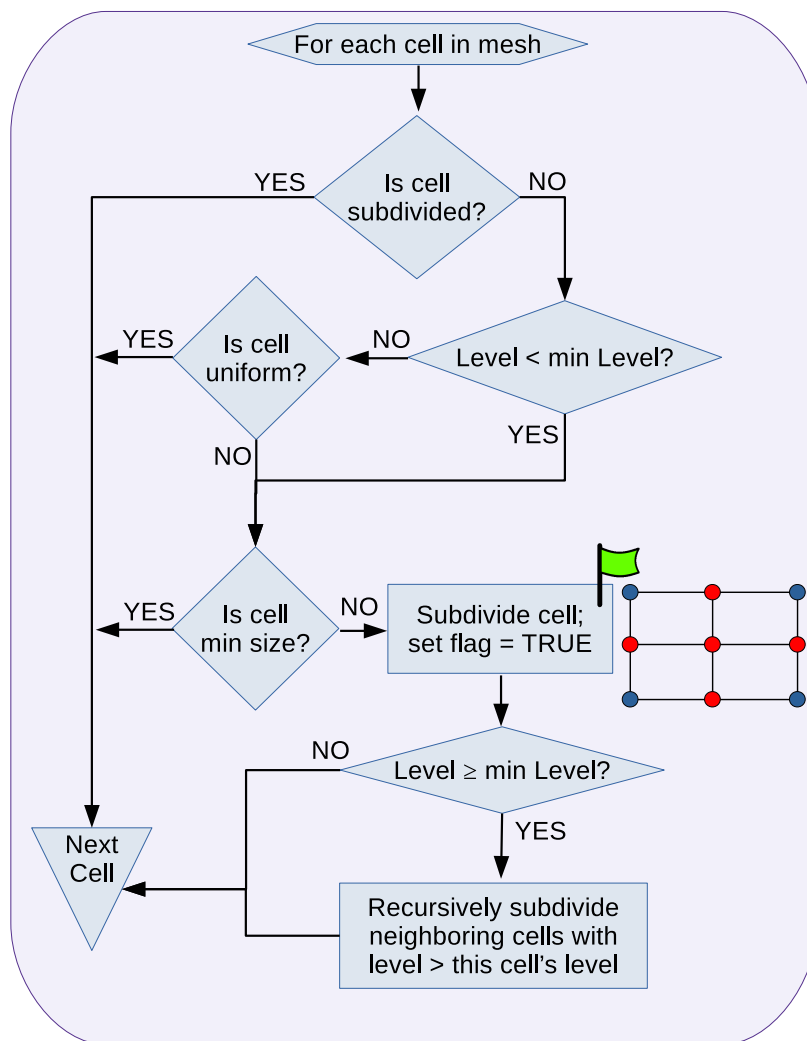


Figure E.3.: Inner loop through cells in mesh refinement

triggers the subdivision of neighboring cells, i.e., cells that share a (partial) edge with the cell being subdivided, until the relative level difference between the neighbors is at most 1. A clever process to quickly identify the parent, child, and neighbors of a cell reduces the computational cost of the refinement and is detailed in [106]. By applying this refinement algorithm, the number of numerical integrations is greatly reduced. For instance, a single-return ballistic apsis map at $H_{\text{nat}} = -1.59$ requires

36,854 propagations when a grid of initial states is employed but only 6,415 propagations when the mesh refinement algorithm is applied to the same region, a reduction of 82.6%. A problem-agnostic version of this algorithm is available on [GitHub](https://github.com/adcox/adaptive-mesh-refinement)¹.

¹<https://github.com/adcox/adaptive-mesh-refinement>

VITA

Andrew Cox graduated with his Bachelor of Science in Aeronautical and Astronautical Engineering from Purdue in May 2014. He joined Professor Kathleen Howell's Multi-Body Dynamics Research Group in August of that same year. During the first few years of grad school, Andrew studied an extended mission option for the LISA Pathfinder spacecraft, writing his thesis on the topic and graduating with a Master of Science degree in Aeronautical and Astronautical Engineering from Purdue in May 2016. After completing the M.S. degree, he began studying low-thrust trajectory design options as a NASA Space Technology Research Fellow. Throughout his undergraduate and graduate career, Andrew has completed internships at NASA's Armstrong Flight Research Center (2013), Goddard Space Flight Center (2014), and Jet Propulsion Lab (2016). Additionally, he has collaborated with researchers at NASA Goddard and the Jet Propulsion Lab during the summer months of 2015, 2017, 2018, and 2019. Following graduation, Andrew will join the Mission Design and Navigation section at the NASA/Caltech Jet Propulsion Laboratory.